Università degli Studi di Torino
Scuola di Dottorato in Scienza ed Alta Tecnologia

D^+ meson analysis at the LHC with ALICE

Giacomo Ortona

Università degli Studi di Torino
Scuola di Dottorato in Scienza ed Alta Tecnologia

Indirizzo di Fisica ed Astrofisica

D^+ meson analysis at the LHC with ALICE

Giacomo Ortona

Tutor: Massimo Masera

Discussant: Yves Schutz

Contents

1 The physics of QGP **5**

1.1 QCD and strong interactions 6

1.1.1 Confinement and deconfinement 13

1.2 The QGP quest at colliders 16

1.2.1 Dynamics of a collision 17

1.2.2 Probing the QGP 22

1.2.3 Hydrodynamics and collective flow 28

1.3 a charming way to probe QGP 34

1.3.1 Charm in proton-proton collisions 34

1.3.2 Charm in heavy ion collisions 35

2 A Large Ion Collider Experiment at the LHC **41**

2.1 The Large Hadron Collider 41

2.2 ALICE, a powerful tool 43

2.2.1 Inner Tracking System 46

2.2.2 Other Central Barrel detectors 50

2.2.3 Forward detectors 53

2.3 ALICE trigger and data acquisition system 55

2.3.1 Central Trigger Processor 55

2.3.2 Data AcQuisiton system 57

2.3.3 High Level Trigger 57

2.4 ALICE computing framework 58

2.4.1 Alice Offline Framework 58

2.4.2 The Grid 59

2.5 Event reconstruction 60

3 Have a look, it is charm! 65
3.1 Event reconstruction and filtering, from ESDs to AODs . . . 67
3.2 Data Quality . . . 70
3.3 Analysis Strategy . . . 72
3.3.1 PID . . . 76
3.4 Cut Optimisation . . . 80
3.5 Calculation of prompt D^+ corrected yield . . . 86
3.5.1 Efficiencies . . . 87
3.5.2 Feed-down subtraction . . . 89
3.6 Cross section extraction . . . 91
3.6.1 Normalization to cross section . . . 93
3.7 Systematic uncertainties . . . 97
3.8 Results at $\sqrt{s} = 7$ TeV . . . 104
3.8.1 Proton-Proton collisions at $\sqrt{s} = 2.76$ TeV . . . 106
3.8.2 Total charm production cross-section . . . 107

4 Charmed meson in Heavy Ion collisions 111
4.1 Analysis strategy for D^+ in Pb-Pb . . . 112
4.1.1 Centrality selection . . . 112
4.1.2 Cut selection . . . 115
4.2 R_{AA} . . . 116
4.2.1 Proton-proton reference . . . 120
4.2.2 Systematics in Pb–Pb . . . 121
4.2.3 Results . . . 125
4.3 Elliptic Flow of charmed mesons . . . 131
4.3.1 Event plane methods for v_2 extraction . . . 133
4.3.2 Method validation . . . 138
4.3.3 D^+ v_2 results . . . 141

5 Conclusions 147

A Rapidity and Pseudorapidity 149

List of Figures

1.1 Schematic representation of universe evolution according to Big Bang model. 6
1.2 The phase diagram of QCD matter 7
1.3 Quark masses 8
1.4 *Running* of the strong interaction coupling constant with transferred momentum 10
1.5 Chiral symmetry restoring and deconfinement phase transition from lQCD calculations 11
1.6 Evolution of the energy density as function of the temperature 13
1.7 Change of the phase transition behaviour and critical temperature depending of the quark masses value 14
1.8 Sketch representing the confinement mechanism using the string potential. 15
1.9 Debye screening of the colour charge 15
1.10 Geometry of a collision between two nuclei 18
1.11 Nucleus–nucleus collision evolution 19
1.12 Evolution of the Bjorken energy density in a central collision at RHIC 20
1.13 Evolution of an heavy–ions collision 20
1.14 1-σ confidence contour plot for the temperature and velocity boost parameters of the blast-wave fit on the identified particle spectra at RHIC (blue) and ALICE (red). 21
1.15 Jet creation in the medium 22
1.16 Azimuthal jet distribution at STAR (RHIC) 22
1.17 Di-jet asymmetry ratio in Pb-Pb events at CMS. 24
1.18 Inclusive charged hadron R_{AA} for central Au–Au collisions at RHIC 25

1.19 Nuclear modification factor of charged hadrons in ALICE. . . 25
1.20 Anomalous J/ψ suppression at SPS and RHIC 26
1.21 J/ψ R_{AA} at ALICE and RHIC. 26
1.22 Debye length dependence on the temperature. The different Debye length at which charmonium states dissociates are shown 26
1.23 Strangeness enhancement observed at ALICE compared to NA57 and STAR results. 28
1.24 Transverse mass spectra of pions, kaons and protons scaled to the particle specie's mass m_0 at STAR in proton–proton collisions 30
1.25 Directed flow as function of pseudorapidity at STAR for centrality 30%-60%. 32
1.26 Non central nucleus–nucleus collision 33
1.27 Azimuthal particles distribution at RHIC as function of centrality 33
1.28 Charged hadrons v_2 as a function of the centrality of the collision at ALICE measured using 2-particle correlations (blue) and multiparticle cumulants. 34
1.29 v_2 as a function of the energy available in the centre of mass of the collision. 34
1.30 non-prompt J/Ψ production differential cross section measured at CMS experiment. 36
1.31 Charm energy loss at RHIC 37
1.32 Charm elliptic flow at RHIC 38

2.1 CERN accelerating scheme (not in scale) 42
2.2 LHC 2010 delivered luminosity 43
2.3 The ALICE detector layout. 45
2.4 ALICE ITS layout 46
2.5 sketch of SDD detector and of charge production and collection. Coordinates are in the detector reference frame and not in the ALICE reference frame. 47
2.6 SDD module layout 48
2.7 Drift speed measured in four different SDD modules as a function of time during the LHC10c period 49
2.8 SDD resolution in the $r\phi$ plane before and after correcting for drift speed non-uniformities 49
2.9 dE/dx in the TPC as a function of particle momentum for Pb-Pb collisions at $\sqrt{s_{NN}} = 2.76$ TeV 51
2.10 TOF resolution for pions selected by the TPC in Pb-Pb collisions at $\sqrt{s_{NN}} = 2.76$ TeV. 52
2.11 Total number of triggered p-p events and Pb-Pb trigger efficiencies for 2010 data taking 56
2.12 Representation of AliRoot framework 58

2.13 TPC to ITS prolongation efficiency 60
2.14 Resolution on the D^+ secondary vertex. 61
2.15 Transverse momentum resolution 62
2.16 ALICE resolution on single track impact parameter. 63

3.1 Schematic representation of the $D^+ \to K^-\pi^+\pi^+$ decay channel. 65
3.2 Evolution of the fraction of pileup events over triggered events during the first month of 2010 p–p data taking at $\sqrt{s} = 7$ TeV 70
3.3 Evolution of the number of candidates for p–p minimum bias event for the first three months of 2010 data taking at $\sqrt{s} =$ 7 TeV. 71
3.4 p_t integrated distribution of $\cos\theta_{\rm point}$ for signal (red) and background (black) candidates in MonteCarlo simulations of proton-proton collisions at $\sqrt{s} = 7$ TeV. 73
3.5 p_t integrated distribution of σ_{vertex} for signal and background candidates in MonteCarlo simulations of proton-proton collisions at $\sqrt{s} = 7$ TeV. 75
3.6 dE/dx distribution of charged tracks inside ALICE TPC in p–p collisions at $\sqrt{s} = 7$ TeV. The lines are a parametrisation of the Bethe-Bloch curve 77
3.7 velocity of particles reaching TOF versus their momentum in p–p collisions at $\sqrt{s} = 7$ TeV. Different particles species are lines are clearly visible. 78
3.8 Effect of strong PID selection with respect to conservative PID approach 79
3.9 Distribution of the statistical significance in the cuts hyperspace for Pb–Pb collisions 81
3.10 Distribution of the statistical significance in the cuts hyperspace for p–p collisions 82
3.11 Invariant mass distributions corresponding to each cell of the histogram in figure 3.9. 83
3.12 Invariant mass distributions corresponding to each cell of the histogram in figure 3.10. 84
3.13 Invariant mass spectra for $D^+ \to K^-\pi^+\pi^+$ in bins of p_t. $2.64 \cdot 10^8$ pp events at $\sqrt{s} = 7$ TeV. 86
3.14 Reconstruction efficiencies in pp and Pb-Pb collisions from MonteCarlo simulations. 88
3.15 Efficiencies from simulated proton-proton collisions at $\sqrt{s} =$ 7 TeV 89
3.16 Cut variables distributions in data and MonteCarlo for p–p collisions at $\sqrt{s} = 7$ TeV 90
3.17 Cut variables distributions in data and MonteCarlo for Pb–Pb collisions at $\sqrt{s} = 2.76$ TeV 91
3.18 $f_{\rm prompt}$ fraction of prompt D^+ 92

3.19 D^+ corrected yield as function of p_t compared with FONLL predictions . . . 93
3.20 Ratio between the number of events with V0AND trigger and the number of minimum bias events for the LHC10b period. . 95
3.21 Ratio of number of candle events over V0AND events for the 2010 data taking period with p-p collisions at $\sqrt{s} = 7$ TeV. . 96
3.22 Relative systematic uncertainties on D^+ cross section in proton–proton collisions at $\sqrt{s} = 7$ TeV. . . . 97
3.23 Signal obteined from different fitting procedures. . . . 99
3.24 Effect of cut selection on raw yield and cross–section . . . 100
3.25 Comparison of D^+ raw invariant mass spectra without (first and second rows) and with (third and fourth rows) PID . . . 102
3.26 Comparison of the D^+ (left) and D^- (right) invariant mass spectra for $2 < p_t < 5$ GeV/c. . . . 103
3.28 prompt fraction of the D^0 raw yield as a function of p_t for the two FONLL-based methods to estimate the feed-down . . 105
3.29 D^+ production cross–section in proton–proton collisions at $\sqrt{s} = 7$ TeV compared with FONLL and GM–VFNS calculations . . . 107
3.30 D^+ production cross-section in p-p collisions at $\sqrt{s} = 2.76$ TeV. 108
3.31 Total charm production cross-section at ALICE and other experiments. The ALICE data point at $\sqrt{s} = 7$ TeV is in good agreement with analogue measurements made by ATLAS and LHCb. Lines are pQCD calculation at next to leading order (MNR). . . . 110

4.1 Distribution of the VZERO scintillators amplitudes compared to Glauber fit. . . . 113
4.2 Nuclear overlap function for the different centrality class. . . 113
4.3 Distribution of VZERO amplitude versus number of tracks in TPC. . . . 114
4.4 Distribution of VZERO amplitude per centrality intervals. . . 114
4.5 Fraction of events in 0-20% centrality with respect to the events in 0-80% centrality using V0M estimator . . . 115
4.6 D^+ invariant mass spectra from $3.19 \cdot 10^6$ central (0-20%) Pb-Pb collisions at $\sqrt{s_{NN}} = 2.76$ TeV for $6 < p_t < 8$ GeV/c (left), $8 < p_t < 12$ GeV/c (middle), $12 < p_t < 16$ GeV/c (right). . . . 118
4.7 D^+ invariant mass spectra from $6.9 \cdot 10^6$ peripheral (40-80%) Pb-Pb collisions at $\sqrt{s_{NN}} = 2.76$ TeV. . . . 119
4.8 Efficiencies for prompt (red triangles) and feed-down (blue circles) D^+ candidates in Pb-Pb central (left) and peripheral (right) collisions . . . 119

4.9 Ratio of D^+ cross-section at $\sqrt{s} = 2.76$ TeV and at $\sqrt{s} = 7$ TeV from FONLL with different parameter choices. Black line is the central value, yellow band is the resulting uncertainty for the D^+ with the $\sqrt{s} = 7$ TeV p_t binning. 122
4.10 Relative systematic uncertainties on D^+ yield extraction in central (left) and peripheral (right) Pb-Pb collisions at $\sqrt{s_{NN}} = 2.76$ TeV. 123
4.11 Different p_t shapes from FONLL (black) and PYTHIA (red), compared with D^+ prediction from FONLL (blue). 124
4.12 Ratio of D^+ measured cross-sections at $\sqrt{s} = 2.76$ TeVto the cross-section scaled from $\sqrt{s} = 7$ TeV. 124
4.13 Systematic uncertainty from the feed-down R_{AA} estimation as a function of the ratio $\frac{R_{AA}^{\text{feed-down}}}{R_{AA}^{\text{prompt}}}$. 125
4.14 D^+ corrected yields and proton-proton reference in Pb-Pb central and peripheral collisions. 127
4.15 D^+ R_{AA} for centrality classes 0-20% 128
4.16 D^+ R_{AA} for centrality classes 40-80% 129
4.17 D^+ R_{AA} compared to the R_{AA} of D^0 and D^* for central (left) and peripheral (right) Pb-Pb collisions. 130
4.18 R_{AA} of charged hadrons compared to the R_{AA} of D mesons . 130
4.19 Shadowing effect on the R_{AA} of D mesons. 130
4.20 Model predictions for charm R_{AA} at the LHC energies and comparison with ALICE data 132
4.21 Distribution of the event plane measured from charged tracks in the TPC with (red) and without (black)ϕ weights corrections 133
4.22 VZERO event plane distribution with (green) and without (yellow) channel equalization. 133
4.23 VZERO event plane correction factors 134
4.24 Event plane angle measured with the VZERO detector versus the one determined from the distribution of charged tracks in the TPC. 135
4.25 $\cos(2(\Psi^a - \Psi^b))$ from two sub-events obtained by randomly selecting TPC tracks from semi-peripheral (30-50% centraliy class) events. 136
4.26 v_2 obtained from asymmetried in the azimuthal distribution of candidates with respect to the event plane in MonteCarlo simulations 139
4.27 v_2 of pions measured using the D meson tools compared to ALICE measurement. 140
4.28 Invariant mass distributions for the D^+ candidates in-plane (top) and out-of-plane (bottom) for 3 p_t bins in the range $3 < p_t < 16$ GeV/c, for semi-peripheral events (30-50% centrality). 141
4.29 v_2 extraction using the fit of v_2 versus invariant mass method. 142

4.30 D^+ v_2 as a function of $p_t$in semi-peripheral and peripheral collisions. 143
4.31 D^+ p_t differential elliptic flow measurement in 30-50% centrality. 144
4.32 Centrality dependence of p_t integrated D^+ v_2. 145

A.1 Pseudorapidity distribution of charged particles in Pb-Pb collisions at $\sqrt{s_{NN}}$ = 2.76 TeV in ALICE measured with the SPD and V0 detectors 150

List of Tables

1.1 Quark families 8

3.1 D meson hadronic decay channels under study at ALICE. . . 67
3.2 Production cut values on the D^+ candidate triplets 69
3.3 PID requirements for identification/rejection of daughters in p–p collisions at $\sqrt{s} = 7$ TeV 80
3.4 Cut values for D^+ candidate triplets used in p-p collisions at $\sqrt{s} = 7$ TeV. 85
3.5 $D^+ + D^-$ raw yield measured in 5 nb^{-1} p-p collisions at $\sqrt{s} =$ 7 TeV. 87
3.6 D^+ cross-section in different p_t bins. 106

4.1 Average values of the number of participating nucleons, the number of binary collisions, and of the nuclear overlap function for the considered centrality classes, expressed as percentiles of the nuclear cross section from Glauber model. . . . 114
4.2 Cut values on the D^+ candidate triplets in Pb–Pb collisions at $\sqrt{s_{NN}} = 2.76$ TeV. 117
4.3 Cut values on the D^+ candidate triplets in Pb–Pb collisions at $\sqrt{s_{NN}} = 2.76$ TeV. 117
4.4 Summary of the relative systematic uncertainties on the D^+ R_{AA} measurement in central (top) and peripheral (bottom) collisions. 126

Introduction

This thesis describes the analysis of the D^+ meson in its purely hadronic decay channel $D^+ \rightarrow K^-\pi^+\pi^+$ performed at the Large Hadron Collider with A Large Ion Collider Experiment in proton-proton collisions at $\sqrt{s} =$ 2.76 TeV and $\sqrt{s} = 7$ TeV and in Pb-Pb collision at $\sqrt{s_{NN}} = 2.76$ TeV. The study of open charm meson (mesons made by one light quark and one charm quark) are an interesting tool to probe pQCD and the Quark-Gluon-Plasma properties.

The study of the open charm meson production cross section is an interesting test of QCD calculations based on factorization approach in an energy domain yet unexplored. Both at Tevatron and RHIC the comparison between these calculations and data suggests that the charm production might be underestimated by the central values of the theoretical computation parameters. At the LHC energies the measurement of the D meson cross section in the very low p_t region, possible thanks to the very good tracking, vertexing and PID capabilities of ALICE, is an excellent probe for the parton distribution function in the very low x regions, down to $x \sim 10^{-5}$. The small x region is dominated by the gluon component, that in this region might show effects of saturation. If this happens, then significant deviations from the cross section expectations obtained using the factorization approach should be observed. The measurement of the D meson production cross section at LHC, where the energy is more than three times higher than the energy available at Tevatron is therefore of high interest. The measurement of the charm production cross section is also an essential requirements in order to have a baseline to perform measurement in Pb-Pb collisions.

The heavy quark related measurements are among the most powerful tools to investigate the properties of the strongly interacting medium created in heavy ion collisions. These probes have been already studied at RHIC experiments (and to some extent at the SPS), but it is at the LHC,

where the charm and beauty production rate is several times larger than in any experiment before, that the study of charm and beauty production will be a really powerful tool. Due to their large mass heavy quarks are mainly produced at the very beginning of the collision in the scatterings between the partons of the colliding nucleons that are enough energetic to create a pair of heavy partons. The produced heavy quarks travel through the medium experiencing all the stages of the medium evolution and finally hadronize inside or outside the fireball. While they follow the fireball evolution their dynamical quantities experience several modifications and some of them are peculiar to heavy quarks. The main observables related to medium effects on the charm partons that will be presented in this thesis are the nuclear modification factor and the elliptic flow of open-charm mesons. Light hadron suppression is driven by gluon energy loss, while the suppression of open heavy flavour mesons is mainly due to the energy loss of the heavy quark. The comparison between open-charm meson and light hadrons energy loss can therefore probe the colour charge dependence of the energy loss in the medium. Being the charm quark much heavier than light partons, the study of charmed hadrons elliptic flow can provide insights about the Quark-Gluon-Plasma thermalization mechanism, charm dynamic in the medium and on the hadronization mechanism.

In the first chapter I introduce the main topics related to the physics of the Quark-Gluon-Plasma, presenting the main experimental observables and the measurement obtained at RHIC and SPS as well as last results from LHC experiments, including the observables related to the measurement of charm properties.
Chapter 2 describes the ALICE experimental apparatus and its main characteristics. Thanks to the very good tracking, vertexing and PID capabilities ALICE is very well suited for the open-charm studies. The main detectors used for the D^+ analysis are the Inner Tracking System, the Time Projection Chamber, the Time Of Flight and the VZERO detectors. All these detectors and their performances will be described in detail in this chapter and the ALICE computing framework will be introduced.
The description of the analysis strategy is given in chapter 3. Here I describe the D^+ meson reconstruction in proton-proton collisions and I give the details of cut selection strategy, signal extraction, particle identification and data quality selections. The ALICE open-charm results obtained in proton-proton collisions at centre of mass energies of $\sqrt{s} = 2.76$ TeV and $\sqrt{s} = 7$ TeV are also showed in chapter 3. I present the details of the cross-section measurements and the description of systematic uncertainties affecting it. The D^+ p_t differential cross-section and the total charm production cross-section compared to theoretical models (FONLL, GM-VFNS) and other LHC experiments (ATLAS, LHCb) measurements made at the centre of mass energy of $\sqrt{s} = 7$ TeV.
Chapter 4 presents the result of the D^+ measurements in Pb-Pb collisions

at $\sqrt{s_{NN}} = 2.76$ TeV. The main differences arising when analysing Pb-Pb data instead of proton-proton data (higher multiplicities, centrality selection) will be described. In the first part of this chapter I present the D^+ energy loss measured using the nuclear modification factor R_{AA} and a complete description of how this measurement is performed. The comparison of the D^+ nuclear modification factor as measured at ALICE with the one of light hadrons will be showed as well as with theoretical predictions from several different models. The second part of the chapter shows the preliminary results on D^+ elliptic flow in semi-peripheral Pb-Pb collisions. Although the 2010 statistics is not enough to allow us to make any conclusive statement on charm elliptic flow yet, the details of the analysis and prospects for the analysis of 2011 Pb-Pb data are given.

1

The physics of QGP

The Quark–Gluon–Plasma (QGP) is a state of matter whose existence is predicted by Quantum–Chromo–Dynamics (QCD), the theory of the strong interaction. One well known and studied feature of the strong interaction between partons (quark and gluons) is the confinement of the partons inside hadrons. Due to the fact that the coupling constant of the strong interaction gets stronger when two or more partons are pulled away, one has two effects: on one side when partons are very close to each other, i.e. when the energy and the density of the system are very high, they act freely and do not feel the presence of the others. On the other side, it is impossible to separate partons, because, once the distance starts to increase, the colour force becomes stronger and the energy needed to separate the partons increases. This behaviour leads to the phenomena of the *asymptotic freedom* and of *confinement*. The former is the fact that at high energies or densities, partons behave like free particles that suffer no interactions. The latter is the fact that single partons can never be observed but they are always confined into hadrons. If one can create a system where the energy or the density of the partons are extremely high, then the confinement can not be maintained and a state of matter of strongly interacting deconfined partons is created: this medium is what we call Quark–Gluon–Plasma. In the case of QGP the colour charge is screened by the quarks and gluons that are free to move over volumes much larger than the hadron size, so that we effectively obtain a plasma of QCD matter strongly interacting. It is predicted that QGP can occur when the temperature of the system goes above the *critical temperature* $T_c \approx 190$ MeV or when the barjonic density is higher than $\rho_c \approx 0.72 fm^{-3}$ (more than 5 times larger than nuclear density of $0.14 fm^{-3}$). At present days, such conditions are expected to exist in the core of neutron stars, that are extremely dense stars, or to be created, surviving for a few instants, in the heavy ion collisions at the big accelerator facilities on planet Earth. The cosmological models assume that the QGP was the state of all

the matter in the universe in the very first moments of its life and expansion, between 10^{-12} (electroweak symmetry breaking) and 10^{-6} seconds (hadron formation, see figure 1.1 and reference [1]). For this reason, the study of QGP properties allows us to obtain a better understanding of the history of our universe and it can help in building a theory to link quantum mechanics and cosmological models.

QGP was originally expected to be a perfect gas, as one would naively

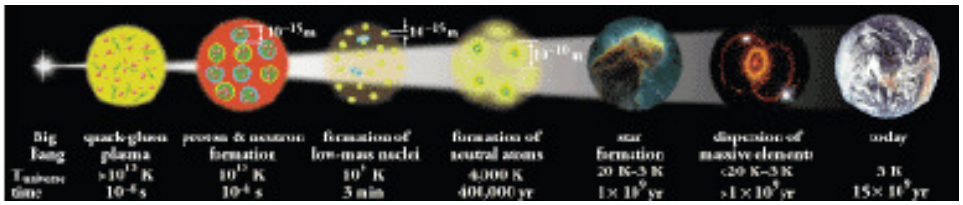

Figure 1.1: Schematic representation of universe evolution according to Big Bang model.

expect from asymptotic freedom, but the first measurements of QGP properties made at the Relativistic Heavy Ion Collider (RHIC) in 2005 [2] showed that QGP is better described as almost a perfect liquid, i.e. a strongly interacting fluid with extremely low viscosity.

As we will see in section 1.2, experimental studies of the QGP are carried out at the big heavy–ion accelerator facilities. Those are currently the only facilities that meet the demanding requirements needed not only to produce QGP but also to have it living enough time to allow us to study it and extract informations on its properties.

This chapter will be devoted to explain the main characteristics of the QGP and the experimental observables used to study its properties. Section 1.1 will discuss the theoretical calculations of the main QGP properties in the QCD and lattice QCD frameworks, with a particular emphasis on the probes related to the heavy flavours and charm quarks (1.3) and on the elliptic flow (1.2.3). The second part of this chapter, section 1.2, will describe how the experimental search for QGP is done at RHIC and at the LHC and will discuss the main experimental results obtained so far in the field of QGP study. Results from the Pb–Pb run at the LHC collected by ALICE, ATLAS and CMS will also be presented.

1.1 QCD and strong interactions

The strong interaction is one of the four fundamental forces in nature, alongside with gravity, electromagnetism and the weak interaction. Its existence was postulated in the 1970s, when the structure of the atomic nucleus was identified. Nowadays the strong interaction is described through the formalism of a Quantum Field Theory. The particular theory describing this force

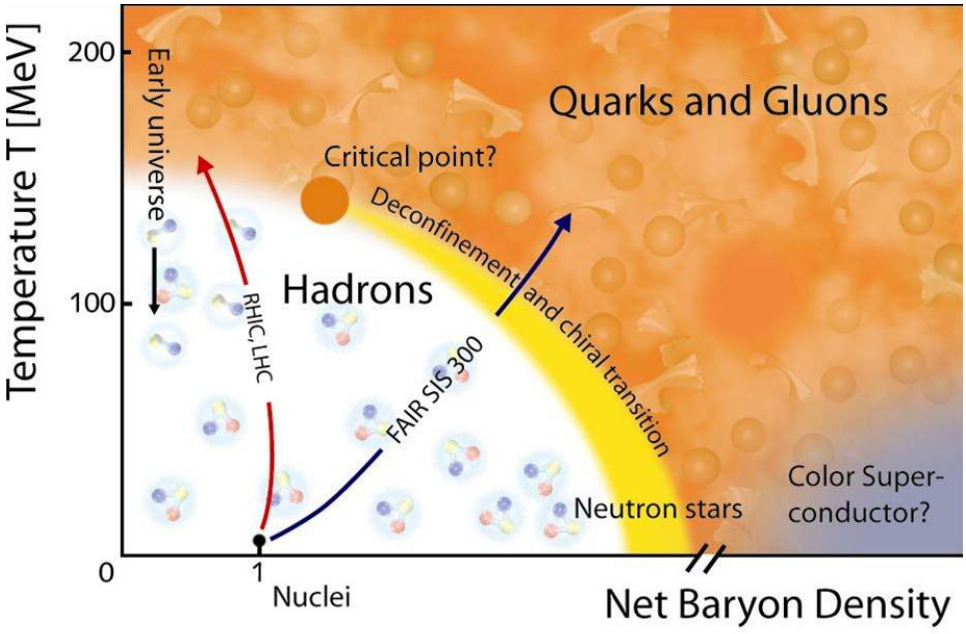

Figure 1.2: The phase diagram of QCD matter

is the Quantum Chromo–Dynamics (QCD), in analogy to the Quantum Electro–Dynamics (QED) that describes the electromagnetic interaction. The main features of the particles subject to the strong interaction have been explored mainly in experiments of hadronic spectroscopy and Deep Inelastic Scattering (DIS). The main properties of the Standard Model of particle physics can be summarised as following:

- The mediators of the strong interaction are partons called *gluons*. Differently to what happens in QED with the photons, gluons are coloured objects. So they can interact between them (and with quarks, of course) exchanging colour charges.

- the coupling constant α_s of the strong interaction becomes stronger when the distance among the coloured objects increases or when the transferred momentum decreases, so it behaves the opposite way with respect to the QED coupling. As already discussed in the previous section, two direct consequences of this behaviour are confinement and asymptotic freedom.

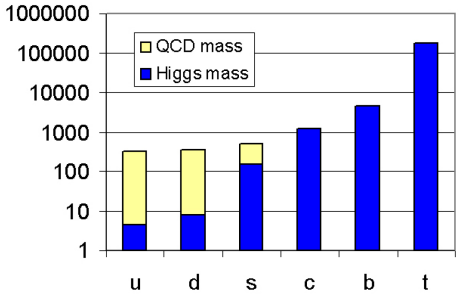

Figure 1.3: Quark masses. In yellow the contribution from chiral symmetry breaking, in blue the one from electroweak symmetry breaking.

Flavour	Mass (GeV)	Charge
u *up*	0.003	2/3
d *down*	0.006	-1/3
c *charm*	1.3	2/3
s *strange*	0.1	-1/3
t *top*	175	2/3
b *bottom*	4.8	-1/3

Table 1.1: Quark masses from PDG[3]. u, d and s masses are current masses and c and b the *running* masses calculated in the $\overline{\text{MS}}$ scheme at the scale $\mu \approx 2$ GeV.

The QED is described by the *abelian*[1] group $U(1)$ while the QCD is based on the non–abelian group $SU(3)$. Being described by $U(1)$, which has one generator and is abelian, QED has only one chargeless force mediator, the photon. The QCD structure is otherwise more complex. $SU(3)$ has 8 generators (the Gell–Mann matrices) and it is non–abelian, so QCD has 8 different kinds of gluons and they can carry colour charge. The Lagrangian of QCD can be written as follows:

$$\mathscr{L}_{\text{QCD}} = -\frac{1}{4}F^a_{\mu\nu}F^{\mu\nu}_a + \sum_q \overline{\psi}^i_q \gamma^\mu (D_\mu)_{ij} \psi^j_q - \sum_q m_q \overline{\psi}^i_q \psi_{iq} \qquad (1.1)$$

Where

$$F^a_{\mu\nu} = \partial_\mu G^a_\nu + \partial_\nu G^a_\mu - g_s f_{abc} G^b_\mu G^c_\nu$$

and

$$(D_\mu)_{ij} = \delta_{ij}\partial_\mu + i g_s \frac{\lambda^a_{ij}}{2} G_{a\mu}$$

In equation 1.1 $G^{a=1\ldots8}_\mu$ represents the 8 gluonic fields; ψ^i_q is the quark field of flavour q and colour i. g_s and m_q are the coupling constant and the mass term respectively[2] while the matrices λ^a are the 8 $SU(3)$ generators and f^{abc} their structure constants.
The first term of the QCD Lagrangian contains the kinetic term of the gluons and the interaction among 3 and among 4 gluons. The second term of equation 1.1 describes the kinetic evolution of quarks and the quark–gluon coupling with the only allowed interaction between 2 quarks and one gluon.

[1] An abelian group is a commutative group, a group where the result of the application of the group operation to two group members does not depend on their order

[2] g_s and m_q are not the same thing as the strong interaction and coupling constant α_s and the physical mass of the particle. To obtain the physical quantities we should apply to the QCD Lagrangian the *renormalisation* procedure. The discussion of this procedure is well beyond the topic of this chapter. To who might be interested, a description of this procedure can be found in [4]

The last term is the *constituent mass* term of the quarks. Since the quarks are subject to the interaction with the Higgs field in the QED Lagrangian they also have a *current mass* term, that is dominant for heavy quarks.
The Lagrangian contains all the information available in a system, but the way to extract this information might not be easy. The most common approach to the QCD Lagrangian analysis is to use the perturbative approach. This is usually referred as perturbative QCD or pQCD. This approach relies on the computation of the *path integrals*, a method developed by Richard Phillips Feynmann, at different order of their perturbative expansion. Feynmann also invented a graphic method, know as Feynmann diagrams, to evaluate rapidly (at least for the first order of the perturbative development) the matrix elements of the operators. The perturbative approach is valid only when the coupling constant has a small value, so when the transferred momentum is large, as shown in figure 1.4. Moreover, the method is practical only when the number of constituents of the system is small. When the conditions of the problem do not allow a pQCD approach, other methods are available: one of the most successful methods is the lattice–QCD (lQCD). In this approach the computation is made on a lattice with fixed space–time steps between the points of the grid. The lattice sites represents quarks while gluons are represented by the link connecting the different sites. Having a fixed minimum step helps in healing some divergences that appears in pQCD when the transferred momentum is very high (UV divergences). lQCD can provide precise predictions, but the computation usually requires large amount of time and computational resources. Finally, approaches based on approximated Lagrangians and approaches based on thermodynamical and hydrodynamical models can be developed. Those last ones are particularly helpful in heavy ion physics, where the QGP can be described as a thermalized medium. Some of the results obtained with lQCD that are strictly related with the heavy ion collision topic will be discussed later in this section.

Before moving to those topics, we can have a closer look to one detail of equation 1.1. It's easy to observe that if all the quarks have the same mass then the QCD Lagrangian is symmetric under the group $SU(N)$, where N is the number of quarks with the same mass present in the Lagrangian. This fact means that the strong interaction is only affected by the quark mass, but otherwise it can't distinguish between different flavours. This implies that, if the quark species are degenerate in mass, then it would be possible to switch from one flavour to another without implications for the physical system. If we go to the limit of all quarks without mass then the QCD Lagrangian is symmetric under action of the group $SU(N)_L \otimes SU(N)_R$, a symmetry called *chiral symmetry*. To understand what the chiral symmetry implies, we can simplify our Lagrangian to the case where only quarks *up*

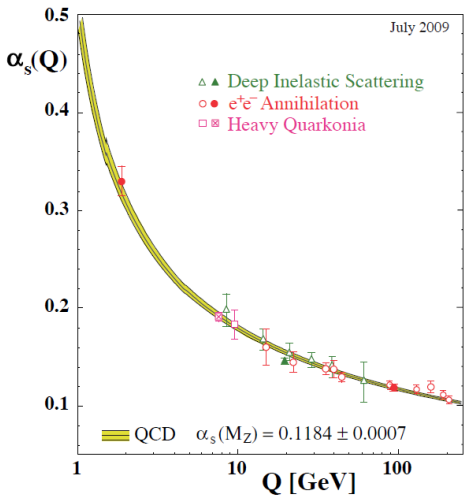

Figure 1.4: *Running* of the strong interaction coupling constant with transferred momentum [3]

and *down* are present. We can then write the quark field as

$$\psi = \begin{pmatrix} q_L \\ q_R \end{pmatrix} = \begin{pmatrix} u_L \\ u_R \\ d_L \\ d_R \end{pmatrix} \tag{1.2}$$

Having in mind this notation we can write the QCD Lagrangian as

$$\mathscr{L} = \overline{q}_L i\gamma^\mu D_\mu q_L + \overline{q}_R i\gamma^\mu D_\mu q_R + \mathscr{L}_{\text{gluons}} \tag{1.3}$$

If the quarks were massless then this implies that

$$\langle \overline{\psi}\psi \rangle = \langle \overline{\psi}_L \psi_R + \overline{\psi}_R \psi_L \rangle = 0 \tag{1.4}$$

The object $\langle \overline{\psi}\psi \rangle$ is usually referred to as *chiral condensate*. Its value in the empty space is known to be about $(235\text{MeV})^3$, and this means that the fundamental state of the system is not invariant under chiral symmetry. The chiral symmetry breaking adds a contribution to the quark masses. Even the residual symmetry under $SU(N)$, that is the flavour symmetry, is broken, due to the fact that quarks with different flavours have different masses. Even if the masses are different, at least for the three lightest flavours (u,d,s) the mass values are very close between the quarks and close to 0. This is reflected in the fact the the pions, that are Goldstone bosons associated to the chiral symmetry break down, have very similar and very small masses. The chiral symmetry is of particular interest in the study of QGP. According to lattice QCD calculations done at temperatures close to

the critical temperature, at which the state transition from normal matter to QGP occurs, a restoring of the chiral symmetry is expected. Chiral symmetry restoration introduces changes in the QCD vacuum state that bring the value of the chiral condensate down to a value close to 0. If this is the case, then the constituent masses of the quarks should vanish in the QGP. As we can see from figure 1.3 this effect is particularly important for light quarks. As an example the mass of the strange quark is expected to drop from about 500 MeV to just 150 MeV, thus making strangeness production more probable. Chiral symmetry restoration was suggested to be a possible explanation of the strangeness enhancement observed at the SPS accelerator [5]. Figure 1.5 shows lQCD calculations [6] (in a 2 flavour environment) for the chiral condensate and for the deconfinement phase transition calculated using the Polyakov loop, a loop that wraps around the lattice.

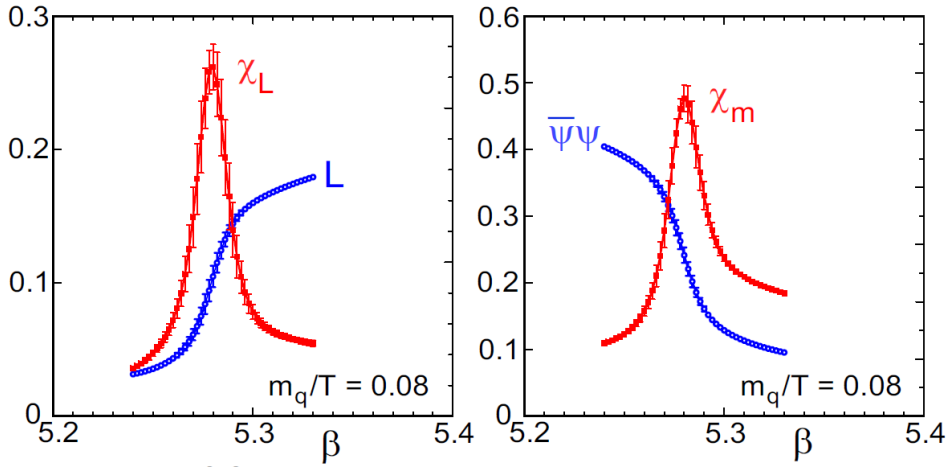

Figure 1.5: lQCD calculations for two dynamical quark flavors showing the coincidence of the chiral symmetry restoration marked by the rapid decrease of chiral condensate $\langle\overline{\psi}\psi\rangle$ (right) and deconfinement (left) phase transitions pointed by the Polyakov loop. Plots are shown as a function of the bare coupling strength β used in the calculations; increasing β corresponds to decreasing lattice spacing and to increasing temperature.

As already discussed, lattice QCD is a non–perturbative approach to QCD calculations whose main feature is to introduce a finite minimum distance between the points in the lattice that physically correspond to a discretization of the time–space. All distances that in the 4 dimension time–space are smaller then this minimum step are therefore ignored, providing a way to remove UV divergences from the QCD Lagrangian. Although lQCD is a powerful method to extract information from the QCD Lagrangian, it can be extremely expensive in terms of required resources (such as comput-

ing resources and time), so strong assumptions are often made to simplify the tasks. For many years the *pure gauge* approximation was used, where the only degrees of freedom in the calculation were the gluons, while quarks were considered as colour sources of infinite mass. lQCD calculations are also usually made in the case of chemical potential $\mu_B = 0$.
One of the most successful calculations of lQCD is the *partition function* $Z = \sum_{x_a} \langle x_a | e^{-\beta H} | x_a \rangle$, where $\beta = \frac{1}{T}$. The partition function, in analogy with the entropy in statistical mechanics, allows one to establish a correspondence between microscopical and macroscopical states of the system. Thermodynamical quantities such as pressure, energy density, volume and temperature can all be expressed in terms of the partition function. We report as an example the expressions for pressure and energy density:

$$P = T \left(\frac{\partial LnZ}{\partial V} \right)_T$$

$$\epsilon = \frac{T^2}{V} \left(\frac{\partial LnZ}{\partial T} \right)_V$$

If we continue with the analogy with statistical mechanics, Z represents the sum of the Boltzmann factor $e^{-\frac{E}{T}}$ over all the microstates. In QCD, it is possible to extend the concept of partition function establishing a connection with the Feynmann path integrals. Z can be written as a path integral in the form $< x_b | e^{i(Ht_a - t_b)} | x_a >$ under the following assumptions:

- A Wick rotation must be used, so $t = -i\tau$ and the relations $t_a = 0 \leq t \leq t_b = \beta$ must be true.
- there must be a periodicity condition such that $x(t_a) = x(t_b)$.

The most realistic conditions for available lQCD calculations are made at null barion density and with 3 flavours: 2 light (u, d) and 1 heavier (s). Those conditions can be used to explore the phase diagram of the hadronic matter, to understand where phase transitions occur and of what kind those transitions are[3]. Figure 1.6 shows the behaviour of the energy density as a function of the temperature. From these calculations the phase transition occurs around $T_c \sim 190$ MeV and it appears to be a *crossover*, a smooth transition instead then a critical and sudden change in the system properties. The behaviour of the phase transition can be studied by changing the system conditions, for example performing small perturbations around $\mu_B = 0$ or doing more complex lQCD calculations. Figures 1.6 and 1.7 show the results of this work, with different phase transitions occurring in different areas of the nuclear matter phase diagram. A qualitative picture of

[3] A phase transition of order N is characterised by the presence of a discontinuity in the order N derivative of the free energy G with respect to a thermodynamical variable. ϵ_{SB}/T^4 is the Stefan-Boltzmann limit for a free gluon gas

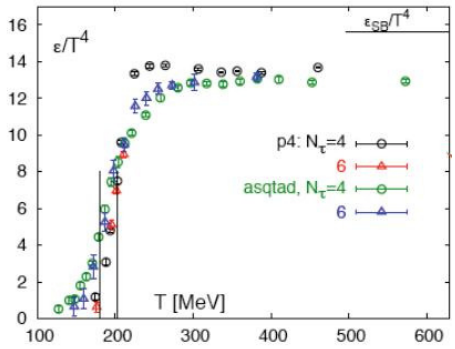

Figure 1.6: Evolution of the energy density as function of the temperature. Calculation made with 2 light (u, d) and one heavier flavour (s) at 0 barionic density. Phase transition occur at 192 ± 11 MeV (F. Karsch, [7]). open circles (triangles) are calculated using a lattice with 4 (6) steps in the time dimension. Black and red points are based on a 1-link plus 3 bended links terms fermion action. Blue and green points are calculated using a static quark potential [8]

the nuclear matter phase diagram is shown in figure 1.2. As we can see, the area explored at the LHC is well inside the region where the phase transition is expected to be a crossover. This means that the experimental search for signatures of the deconfinement is a more challenging task, as we can not expect some physical variable to suddenly change behaviour just beyond the phase transition border.

1.1.1 Confinement and deconfinement

We want to give here some details that can be helpful to understand the deconfinement mechanism. It was already commented in previous sections that the coupling constant α_s of the strong interaction gets stronger when the distance between the partons increases, as shown in figure 1.4. Going to the extremes, two partons at infinite distance must interact, while two partons next to each other will not feel the presence of the other quark (asymptotic freedom). But in practical terms there is no possibility to bring two partons at infinite distance, as when we start to separate them the strength of the interaction between the two rapidly increases, binding them together or filling the vacuum between them with enough energy to create a new quark–antiquark pair with one of the new partons close to each of the original ones, so that in practical terms there is no chance of having one free quark. The main method used to simulate this phenomenon is the *string model*, used for example in many MonteCarlo simulations. In this model the quarks are linked each other with a string (or pipe) through which a flux of colour charge flows from one parton to the other (actually being the flux a

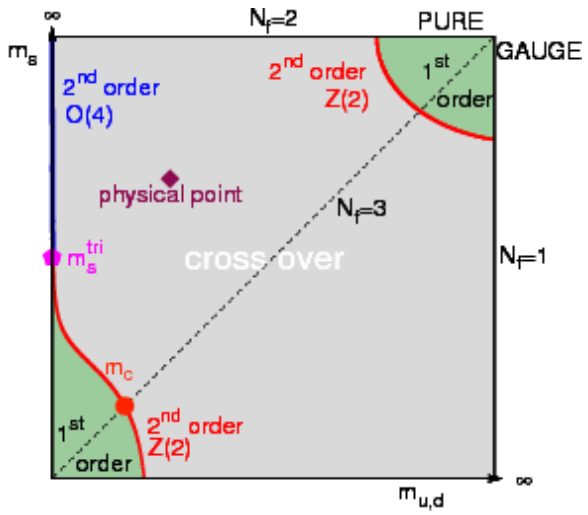

Figure 1.7: Change of the phase transition behaviour and critical temperature depending of the quark masses value. Calculation made on a 3 flavours lQCD[9]

representation of virtual gluons and quarks). The strength of the interaction binding the quarks increases with the distance and it is characterized by a potential of the kind

$$V_{\mathrm{QCD}}(r) = -\frac{4}{3}\frac{\alpha_s(r)}{r} + k \cdot r \tag{1.5}$$

where r is the distance between the quarks and k a constant called *string tension*. V_{QCD} is therefore the sum of a Coulombian term due to the gluon exchange and another term called *confinement potential*. It is straightforward from equation 1.5 that there is a value of r for which it becomes energetically convenient to create a new pair of quarks from the vacuum and reduce r, as sketched in figure 1.8.

We can use this picture of confinement to understand better the deconfinement mechanism. To do so, let us introduce the *Debye screening*. This is a behaviour already observed in classical physics for charges placed in a charged medium (such as electric charges in a water and ion solution). For those charges, the distance at which each charge can feel the interaction with the other is drastically reduced by the presence of the medium to a factor $e^{-\frac{r}{\lambda_D}}$, where the length λ_D called *Debye length* is the effective distance at which the charges still feel each other. Just to make an example, inside a 1M solution the Debye length is just 0.3 nm, meaning that at 1 nm of distance two electric charges are already completely screened.
If the temperature increases such that is possible to have enough energy to create a conspicuous number of $q\bar{q}$ pairs, we will have a situation similar to the one depicted in figure 1.9 where the colour charges are screened by the

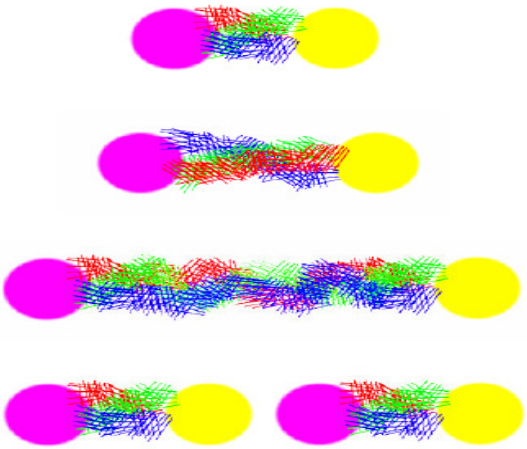

Figure 1.8: Sketch representing the confinement mechanism using the string potential. As the distance between the quarks increases (top, second rows) the string potential grows until (third row) it becomes energetically convenient to form a new $q\bar{q}$ pair and reduce the string potential (bottom).

presence of the medium. Equation 1.5 is then modified accordingly to the Debye term in the following:

$$V_{\mathrm{QCD}}(r) = -\frac{4}{3}\frac{\alpha_s(r)}{r}e^{-\frac{r}{\lambda_D}}. \tag{1.6}$$

The confinement potential vanishes and the Coulombian potential itself is strongly screened. In these conditions, the partons feel the presence of other partons only if they are closer than the Debye length λ_D. It is not possible anymore to claim that one quark belongs to a specific hadron, that therefore disappears and we have the formation of a strongly interacting medium: the QGP.

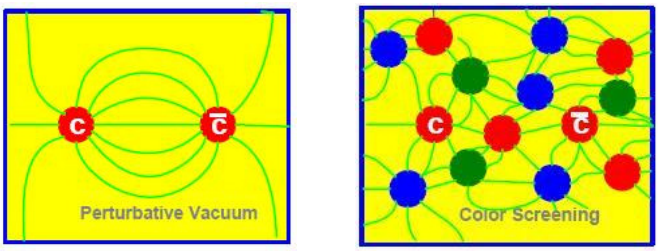

Figure 1.9: Debye screening of the colour charge

1.2 The QGP quest at colliders

Exploring experimentally the possible existence of QGP and studying its properties is a challenging task. Experimental conditions where values of energy density and temperature larger then the critical ones must be created to free the partons from hadron confinement. To create deconfined matter is necessary but not sufficient condition. To allow the study of such deconfined matter further requirements must be met. Obviously it is not possible to directly detect the deconfined partons, so the usage of macroscopic thermodynamical quantities is mandatory to address QGP properties. This means that the system must reach some kind of thermodynamical equilibrium for those quantities to be properly defined. Thus, the system must have a lifetime larger then the system relaxation time. The time it takes to a deconfined parton system to reach thermodynamical equilibrium depends on the strength of the interactions between partons and it is not known yet. It is commonly used as an approximation for the relaxation time of the system the value $\tau_0 = 1$ fm/c, that is the time needed for a particle to travel a 1 fm distance at the speed of light. Having a system that lives sufficiently long it is not enough: the system must also be an extended system so that the rescattering among the partons can maintain the equilibrium. This is because the equilibrium is conserved through multiple scatterings between the system components. To have a parton undergoing enough scatterings, the size of the system must be much larger then the mean free path of the parton in the medium. All those requirements are met when nuclei collide at relativistic speeds in the big accelerator facilities such as RHIC in Brookhaven and the Large Hadron Collider (LHC) at CERN[4]. The first attempt to create QGP was made at the Alternating Gradient Synchrotron (AGS) in Brookhaven, which was capable to reach a centre of mass energy of $\sqrt{s_{NN}} = 33$ GeV. After it the Super–Proton–Synchrotron at CERN could reach a centre of mass energy of $\sqrt{s_{NN}} = 17$ GeV for nucleon pair. Then the Relativistic–Heavy–Ion–Collider in Brookhaven started to deliver collisions in 2000 reaching energies as high as $\sqrt{s_{NN}} = 130$ GeV using gold beams. Finally, the Large–Hadron–Collider is currently delivering lead beams colliding at an energy of $\sqrt{s_{NN}} = 2.76$ TeV, half of the nominal energy, that will be reached after the next upgrade. The system created in a Pb–Pb collision can reach a volume in the order of 1000 fm^3, producing about 1000 hadrons and, already at the energies available at the SPS, an energy density 200 times larger then the atomic nucleus energy density.

[4]Conseil Européen pour la Recherche Nucléaire - European Organization for Nuclear Research

1.2.1 Dynamics of a collision

In this section the evolution of the collision between two heavy ions accelerated at ultra–relativistic speed is described. Before doing that, some geometrical definitions should be given. Since nuclei are extended objects, the geometry of the collision plays an important role, and most of the observables depend on the initial collision geometry. The *impact parameter* b, defined as the distance between the centres of the two colliding nuclei in the transverse plane, describes the geometry of the collision. Figure 1.10 provides a sketch that it is helpful to visualise this quantity. The volume of the overlap region between the two nuclei can be computed from the value of the impact parameter. The framework commonly used to describe the collision geometry is the *Glauber model*, discussed in detail in [10]. In this semi–classical model the nuclei are moving along the collision direction in a straight path. The main assumption of this model states that a collision between nuclei can be seen as the superposition of independent binary collision between nucleons. Nucleons that suffer at least one collision are called *participants*, while the other nucleons are called *spectators*. Nucleons are distributed inside a nucleon with a given density function. When the collision occurs, it is described in terms of single interactions between the constituent nucleons. The Glauber model allows to describe the features of the collision as the impact parameter, the number of participants and the number of binary collisions among participants[5]. The participant nucleons will transfer a fraction of their energy to the collision region, providing the energy needed to possibly create the QGP, while the spectators will simply continue their flight (almost) unaffected by the collision. If the impact parameter is small (central collisions), the overlap region between the nuclei is large. In this case, most of the nucleons are involved in the collision. This means that a large amount of energy will be transferred to the collision region and wherefrom matter, also called *fireball*, is created providing good chances of fulfilling the requirements for the creation of the QGP . Alternatively, if the impact parameter is large (peripheral collisions), most of the energy will be carried away by the spectators, leaving a small amount of energy to build the fireball.

If the behaviour of a physical observable is affected by the creation of the QGP, then when studying this observable as a function of the centrality of the collision it should change its behaviour moving from very peripheral collisions, where there is small energy available and so we do not expect QGP formation, towards central collision where QGP is formed. This feature will be described in detail for some physical observables in section 1.2.2 and 4.2. A good knowledge of the geometry is also important because many collec-

[5]Given the impact parameter b and the density function of the nucleus it is possible to compute the number of participants and the number of binary collisions without any other input.

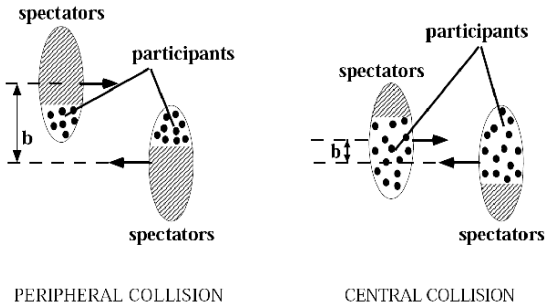

Figure 1.10: Geometry of a collision between two nuclei. Left: in a peripheral collision, with large impact parameter b the number of colliding nucleons (participants) is small, and most of the energy is carried away by the spectator nucleons that do not interact. Right: in a central collision with small impact parameter many nucleons are involved in the collision.

tive and hydrodynamical effects, such as collective motions, generally called *flows*, are strongly affected by the initial geometrical distribution of the colliding nucleons, as we will see in section 1.2.3.
The two colliding nuclei approach each other at relativistic speed and therefore are strongly Lorentz contracted. To understand the behaviour and evolution of the fireball it is useful to have a proper definition of the energy density available in the fireball at the beginning of the collision evolution. As it can be see in figure 1.11, that sketches the creation and evolution of the collision, the simple assumption of computing the energy density from the distribution function of the colliding nucleons it is not satisfactory as most of that energy will be taken away by the fragments that simply pass through the collision without interacting and so it will not be available for the fireball evolution. Bjorken built in 1983 an hydrodynamical model that proved to be useful to compute this value [11]. The Bjorken model is based on the reasonable assumption that the medium constituents are created in a very short time and in a region with very short longitudinal extension. Also, as the initial baryon contribution is carried away by the nuclei fragments, the net baryon density of the fireball, at least in a longitudinally limited region, is almost zero. This condition is known as *full transparency* and it is opposite to the *full stopping*, where the colliding baryons are stopped in the centre of mass of the system and possibly form a QGP with high baryonic content. It is useful to stress that in a full transparency regime the forward regions of the fireball (high rapidity) will have a high baryon number (as they will evolve together with the fragments), while the region at low rapidity will be almost baryon free.
If the assumption of limited longitudinal extension is correct, then most of the particles will be produced with momentum directed mainly in the trans-

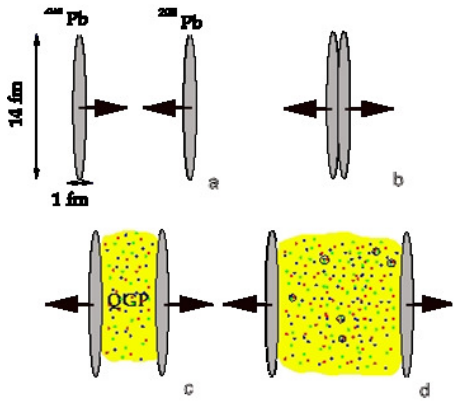

Figure 1.11: Collision of two nuclei and QGP creation. The two nuclei, Lorentz contracted due to their very high speed, approach each other (a) and collide (b). At the moment of the collision the energy of the system is concentrated in the central region, creating the fireball. Then the nuclei move away from the central region (c) where the QGP is created and starts to expand (d)

verse plane or, equivalently, at midrapity (see appendix A for the definitions of rapidity and pseudorapidity). This effect is known as *Dirac plateau*. We can define the initial energy density available in the collision according to the Bjorken model as

$$\epsilon_{\mathrm{Bj}} = \frac{1}{A\tau_f}\frac{dE_T(\tau_f)}{dy} \tag{1.7}$$

where τ_f is the fireball formation time, y the rapidity and A is the overlap area (that can be computed from the impact parameter b). We can now quantify the meaning of the Bjorken model assumptions checking which requirements are needed for equation 1.7 to be valid. The main assumption is that the incoming nuclei should free the interaction region before the fireball is formed, leaving a null net baryon density in it. This means that $\tau_f >> \frac{2R}{\gamma}$. Assuming an arbitrary value of τ_f of the order of 1 fm/c we can calculate that the condition is met for RHIC, while this is not completely true for the SPS. We can go on and insert in equation 1.7 the best estimations of τ_f for RHIC energies to compute the energy density available. At RHIC this is in the order of 15 GeV/fm^3 at formation time, much larger than the deconfinement threshold predicted by lQCD calculations. To have a QGP the energy density must be above the critical value not only at the fireball formation, but also when the system thermalizes, so that we have a medium composed of partons in thermodynamical equilibrium. We can still rely on equation 1.7 that is valid at any time provided that the fireball evolution is mainly longitudinal.

Data from elliptic flow at RHIC, that will be discussed in section 1.2.3, can

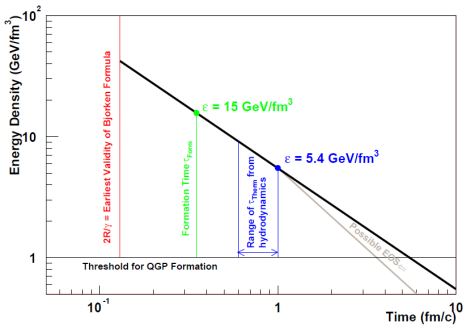

Figure 1.12: Evolution of the Bjorken energy density in a central collision at RHIC

be interpreted as containing signatures of an early thermalization between 0.6 and 1 fm/c [12]. For those values, as depicted in figure 1.12 the energy density is still around 5.4 GeV/fm^3 at RHIC energies, and at least three times higher at the LHC assuming similar thermalization time, well above the threshold for QGP formation. We can now have a closer look to the

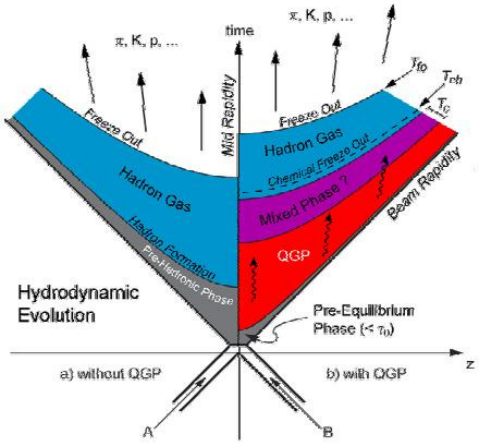

Figure 1.13: Evolution of an heavy–ions collision. Left: evolution without QGP creation. Right: Evolution with a QGP phase. Time goes from down to up, A and B are the colliding nuclei.

details of the fireball evolution, shown schematically in picture 1.13. After the collision, while the spectator nucleons continue their flight unaffected, the participant nucleons undergo to some scattering. The partons inside those nucleons are released altogether with a large amount of energy. Given the strongly Lorentz contracted structure of the colliding nuclei, the energy released in the collision and the newly created partons will be mainly oriented in the transverse plane. This creates a condition where in the central rapidity region many $q\bar{q}$ pairs and gluons are created from the large avail-

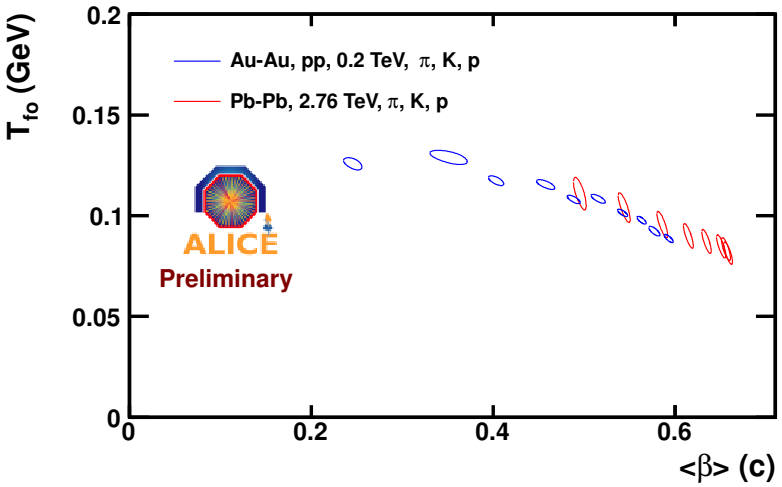

Figure 1.14: 1-σ confidence contour plot for the temperature and velocity boost parameters of the blast-wave fit on the identified particle spectra at RHIC (blue) and ALICE (red).

able amount of energy, producing a region with small net baryon number. In the meanwhile, the excess of baryon number carried by the freed partons of the participant nucleons will give rise to a region at high baryon number at forward rapidity.
The system then starts to expand and after a short interval of time (of the order of 1fm/c), local thermal equilibrium is reached. The mechanism allowing to reach this equilibrium in such a short time is not completely understood yet. Once the fireball reaches thermal equilibrium, the QGP is created.
The fireball continues to expand and cool down, until the moment when the critical temperature $T_c \sim 190$ MeV is reached. After this threshold the partons begin to hadronize and the fireball becomes a gas of hadrons and resonances, where constituents still undergo scatterings but without enough energy to deconfine the partons.

The abundances of particle species become fixed when no more inelastic collisions occur. This is the moment of the *chemical freeze–out*. Thermal fits on experimental data put this second threshold at about 175 MeV. The remaining elastic scatterings can be powerful enough to modify significantly the momenta of the particles in the successive phases of collision evolution. This situation stands until the *kinetic freeze–out*. At RHIC the kinetic freeze-out was measured to be around 120 MeV from fits of the low p_t particle momentum distributions based on blast-wave models. The same analysis

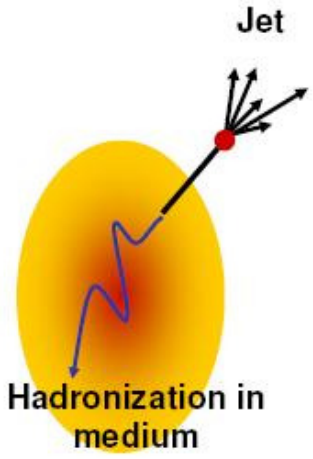

Figure 1.15: Jet creation in the medium

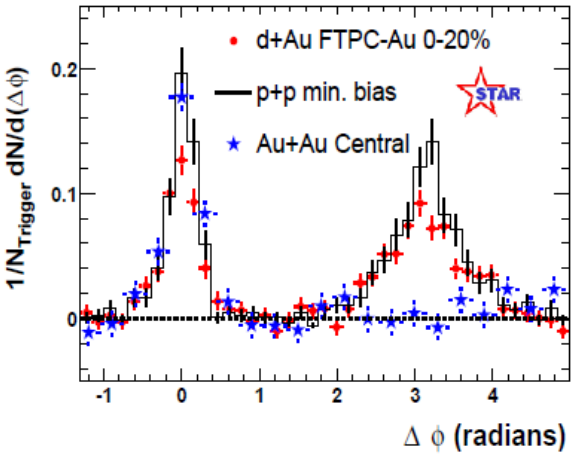

Figure 1.16: Azimuthal distribution of particles with respect to leading particle (jet) at STAR (RHIC) in p–p, d–Au and Au–Au collisions. The away side jet distribution is clear for p–p and d–Au systems, but it disappears in Au–Au collisions.

performed at ALICE shows an increase in the radial boost velocity β of the emitting source with respect to RHIC and a kinetic freeze-out temperature just below 100 MeV. This is shown in figure 1.14 where ALICE and RHIC kinetic freeze-out temperatures and source velocities are compared. After the kinetic freeze-out the few scattering still occurring are not energetic enough to change significantly the particle momentum distributions: the system is now made of free streaming particles that will continue moving towards the detectors.

1.2.2 Probing the QGP

Energy loss

Travelling through the QGP, a parton loses energy mainly because of collisional and radiative energy loss. The quantity of energy transferred by radiative energy loss from a parton to the medium depends on the medium properties. According to the BDMPS [13, 14] model it can be expressed as

$$\Delta E \propto \alpha_s C_R \hat{q} L^2. \tag{1.8}$$

In this formula C_R is the Casimir factor, which depends on the colour charge of the parton (4/3 for quark–quark scattering and 3 for gluon–gluon scattering), $\hat{q}$ is the medium transport coefficient, proportional to the gluon

density, and L is the distance travelled in the medium. If we try to feed in the formula some realistic values for the RHIC conditions, then a parton travelling the fireball length should lose 40 GeV, a huge amount of energy. Then if really there is a QGP medium we expect high p_t hadrons to be produced near the fireball border, because partons produced in the centre of the fireball will lose too much energy before escaping the fireball, as shown in figure 1.15. This means that while in p–p collisions jets are produced back to back, in heavy ions collisions we expect the away side jet to be likely absorbed in the medium. This was observed at RHIC, as we can see in figure 1.16 showing the jet distribution for Au–Au; d–Au and p–p collisions. The same effect is also observed at the LHC. Figure 1.17 shows the asymmetry ratio $A_j = (p_{t,1} - p_{t,2})/(p_{t,1} + p_{t,2})$ in the momentum of reconstructed jets measured at the CMS experiment [15]. The increase of the asymmetry with the centrality of the collisions shows that the away side jets lose more energy to the medium as the centrality of the collision increases. The energy of the away side jet is eventually recovered when increasing the radius used to reconstruct the jet momentum. A similar behaviour was also observed by the ATLAS experiment [16].

Due to the partons energy loss in the medium we expect the p_t distribution of produced particles to be softer when there is a medium and being harder when no medium is created, like in p–p collisions. This effect can be quantified using the *nuclear modification factor* $R_{\rm AA}$, defined by the ratio between the particle transverse momentum distribution in nucleus-nucleus and proton-proton collisions divided by the average number of binary collisions in a nucleus-nucleus collision $N_{\rm coll}$ (in a given centrality class).

$$R_{\rm AA}(p_t) = \frac{1}{< N_{\rm coll} >} \frac{dN_{AA}/dp_T}{dN_{pp}/dp_T} \tag{1.9}$$

From this definition, if a nucleus-nucleus is only the superposition of $N_{\rm coll}$ proton-proton collisions, then $R_{\rm AA} = 1$. The number of particles produced in a nucleus-nucleus collision is expected to be proportional to the number of participants at low p_t (according to the wounded nucleon model [17]) and to the number of nucleon-nucleon collisions at high p_t. If no QGP is created we would expect the value of $R_{\rm AA}$ to increase from a value around 1/6, more or less the ratio between participants and collisions, to a value close to 1 with increasing p_t. Initial state effects modify this expected behaviour. These effects can be estimated in proton–nucleus collision. The first of those effects is the *Cronin enhancement*, discovered at Fermilab in proton–nucleus collisions. For p_t larger then about 2 GeV it was observed the the value of R_{pA}[6] was larger than 1. This effect can be explained by the fact that before suffering the inelastic collision the partons in the projectile proton undergo some elastic scattering with some partons of the target acquiring a small

[6] that is the same as $R_{\rm AA}$ but in proton–nucleus collisions instead of nucleus–nucleus

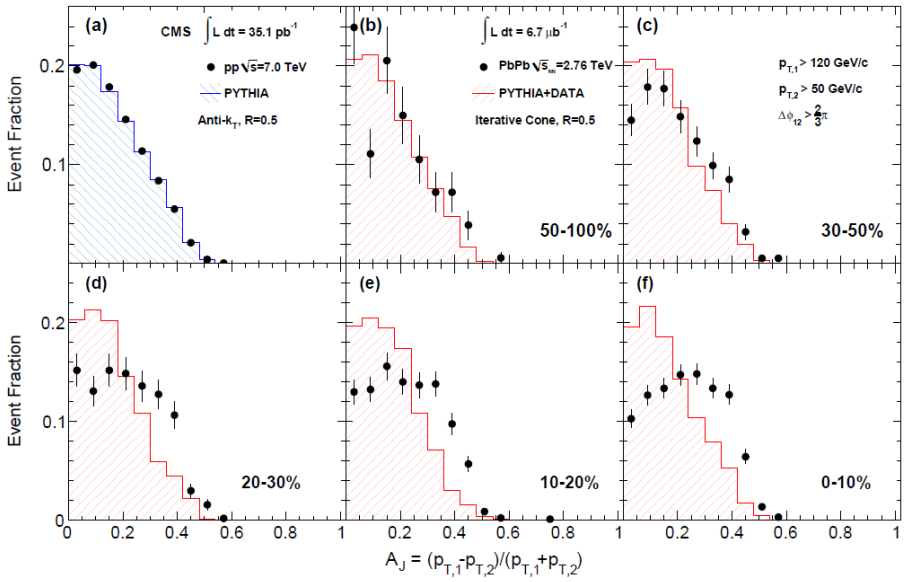

Figure 1.17: Di-jet asymmetry ratio in Pb-Pb events at $\sqrt{s_{NN}} = 2.76$ TeV with the CMS experiment [15]. Selected events have a leading jet with $p_{t,1} > 120$ GeV/c and subleading jet with $p_{t,2} > 50$ GeV/c and a separation between the two jets of $\Delta\phi_{12} > \frac{2\pi}{3}$. Panel (a) show the p-p reference data at $\sqrt{s} = 7$ TeV compared to PYTHIA simulations. Panels from (b) to (f) show Pb-Pb data in different centralities compared to true Pb-Pb events with embedded PYTHIA events. A clear increase of the asymmetry between the two jets while going towards central collisions is visible.

transverse momentum component. In this way when the hard scattering finally occurs particles will be produced with a small momentum contribution k_t that is, on average, different from zero. A second effect that needs to be estimated is the modification of parton distribution functions for nucleons in a nucleus (*shadowing* and *anti-shadowing*, that will be discussed in detail in chapter 4). The nuclear modification factor as a function of p_t observed for charged hadrons is visible for results from RHIC in figure 1.18 and from ALICE in figure 1.19. A final state effect pointing to the QGP creation is visible. The R_{AA} value goes asymptotically to the ratio between participants and collisions. An interesting possible interpretation of this feature is the following: the number of participants is proportional to the volume of the interaction region (i.e. to the volume of the fireball) while the number of collisions goes like $N_{\text{part}}^{4/3}$. So we have that

$$\frac{N_{\text{part}}}{N_{\text{coll}}} \propto \frac{V}{V^{4/3}} \propto \frac{1}{R_{\text{fireball}}} \tag{1.10}$$

That is a typical Volume/surface ratio.

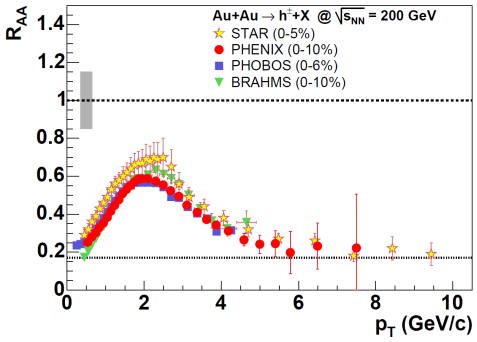

Figure 1.18: Inclusive charged hadron R_{AA} for central Au–Au collisions at RHIC

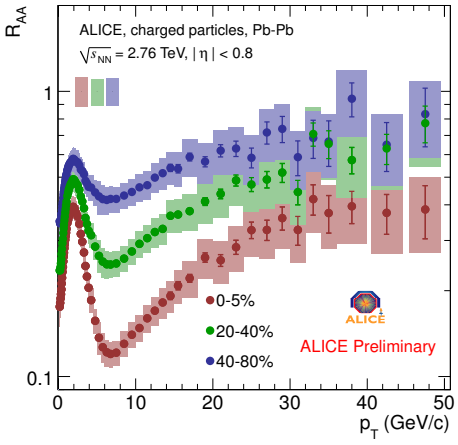

Figure 1.19: Nuclear modification factor of charged hadrons in ALICE as a function of $\mathrm{p_t}$ for three different centralities.

Quarkonium suppression

Heavy quarkonia are $c\bar{c}$ (charmonium) or $b\bar{b}$ (bottomonium) bound states. As c and b quarks are not present in the initial flavour content of the colliding nuclei, they must all be produced in pairs at the moment of the fireball creation. Due to their large mass, only in the initial phase of the collision the energy density is high enough to produce those partons abundantly. As we discussed in section 1.1.1, if the QGP is created the presence of the deconfined medium reduces the distance at which each parton of the pair feels the interaction with the other quark because of the *Debye screening*. In the QGP the distance at which the partons feel each other becomes very small and the two heavy quarks do not form a bound state. Since the amount of heavy quarks in the fireball is small (about 100 $c\bar{c}$ and 5 $b\bar{b}$ pairs in central Pb-Pb collisions [18]), the probabilities for the two partons to meet another heavy quark to combine with at the hadronization are small too, so that they will finally build up two hadrons each of them with only one heavy quark. These hadrons are called *open-charm* and *open-beauty* hadrons. This means that the quarkonium states will be suppressed in heavy–ion collisions, with respect to p–p collisions, if a QGP is formed. This effect is shown in figure 1.20 for the J/ψ particle at RHIC and SPS and it is one of the main evidence that SPS experiments managed to reach the energy threshold for deconfinement [19, 20]. Figure 1.21 shows the J/ψ nuclear modification factor measured at ALICE for Pb-Pb collisions at $\sqrt{s_{NN}}$ =

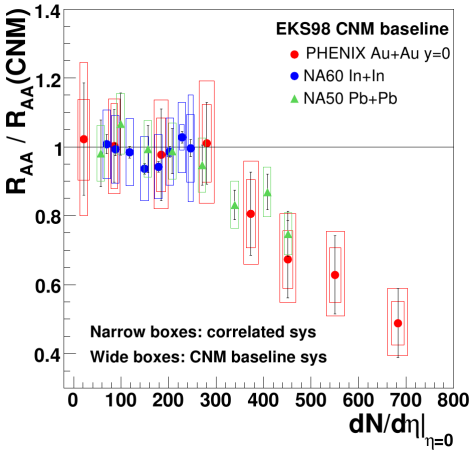

Figure 1.20: Anomalous J/ψ suppression at SPS and RHIC as function of the particle multiplicity for unit of pseudorapidity.

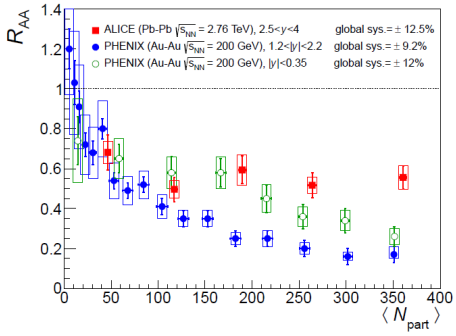

Figure 1.21: Inclusive J/ψ $R_{\rm AA}$ as function of the number of participating nucleons at ALICE in Pb-Pb collisions at $\sqrt{s_{NN}}$ = 2.76 TeV compared to PHENIX results at $\sqrt{s_{NN}}$ = 0.2 TeV.

2.76 TeV[7] compared to PHENIX results. The suppression of charmonium

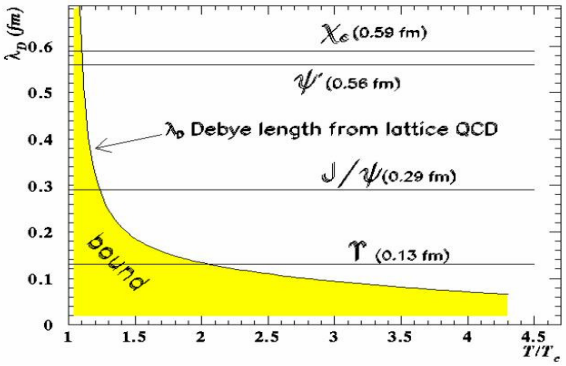

Figure 1.22: Debye length dependence on the temperature. The different Debye length at which charmonium states dissociates are shown. Temperature is in unit of the critical temperature.

and bottomonium states is expected to occur at different energies depending on the binding energy of the bound state, as shown in figure 1.22. This fact can provide a tool to estimate the QGP temperature measuring which resonances are suppressed and which other are conserved. J/ψ suppression has been observed at SPS, RHIC and the LHC. The size of the effect is comparable at the SPS and RHIC, while one would expect to observe much

[7] With the notation $\sqrt{s_{NN}}$ = 2.76 TeV we refer to the energy available in the binary collision between two nucleons of the colliding nuclei.

larger suppression at RHIC, where the larger amount of energy available in the centre of mass ($\sqrt{s}$) means that higher temperatures are reached. Moreover at RHIC the observed suppression is larger at forward rapidity than at central rapidity. An interpretation of this effect can be provided by the *recombination* mechanism: the $c\bar{c}$ production cross section increases steeply with $\sqrt{s}$, allowing more c quarks to find another one to combine with and create a J/ψ. While this explanation seems solving the puzzle, there is no evident reason why exactly at RHIC energies the recombination and the dissociation of the J/ψ reach the balance. The study of the J/ψ production at the LHC, where much more c quarks will be produced, allow us to answer this question: observing a J/ψ enhancement will be a compelling evidence of the fact that recombination can compete with dissociation. Also the study of bottomonium production will be helpful: as the number of b quark in the QGP is much smaller than c quarks, then recombination should be negligible in the case of bottomonium.

Strangeness enhancement

We have already seen in section 1.1 that one of the possible implications of the phase transition is the restoring of the chiral symmetry. If that happens then strange quark mass should reduce from ~ 500 MeV/c^2 to about 150 MeV/c^2. This makes more favourable the production of $s\bar{s}$ pairs in gluon fusion processes. The observation of strangeness enhancement *per se* would not be a sufficient condition to claim a medium effect. In fact, even in a hadron gas processes like $\pi + \pi \rightarrow K + K$ or $\pi + N \rightarrow \Lambda + K$ enhance the strangeness content. What is important is therefore the relative enhancement of strangeness for particles with different strange content. We can define the enhancement of the particle of specie X as $E(X) = \frac{(N_X/<N_{\rm part}>)_{AA}}{(N_X/<N_{\rm part}>)_{pp}}$. In a hadron gas it is relatively easy to produce kaons or Λ particles ($s = 1$) but creation of particles with higher strange content such as Ξ ($s = 2$) and Ω ($s = 3$) is much rarer, so that we can expect a hierarchy of the kind $E(\Omega) < E(\Xi) < E(\Lambda)$. At the opposite, in case of QGP creation, the creation of particles with higher strangeness is enhanced by the diminished strange mass and we should obtain that $E(\Omega) > E(\Xi) > E(\Lambda)$. This kind of behaviour was already observed by the WA97 [21] and NA49 [22] experiments at the SPS. The size of the effect decreases when the energy available in the collisions increases. As shown in figure 1.23 the effect observed is larger at the SPS with respect to RHIC [23] that is larger than LHC. A more precise description of this phenomenon can be obtained from statistical models [24, 25] that can try to estimate in which moment of the evolution the overproduction happens and can investigate if there are possible mechanisms to explain this effect other than the chiral symmetry restoration. In these models this effect is explained by the canonical suppression of the strangeness charge: in small systems (such as p-p collisions) the strangeness

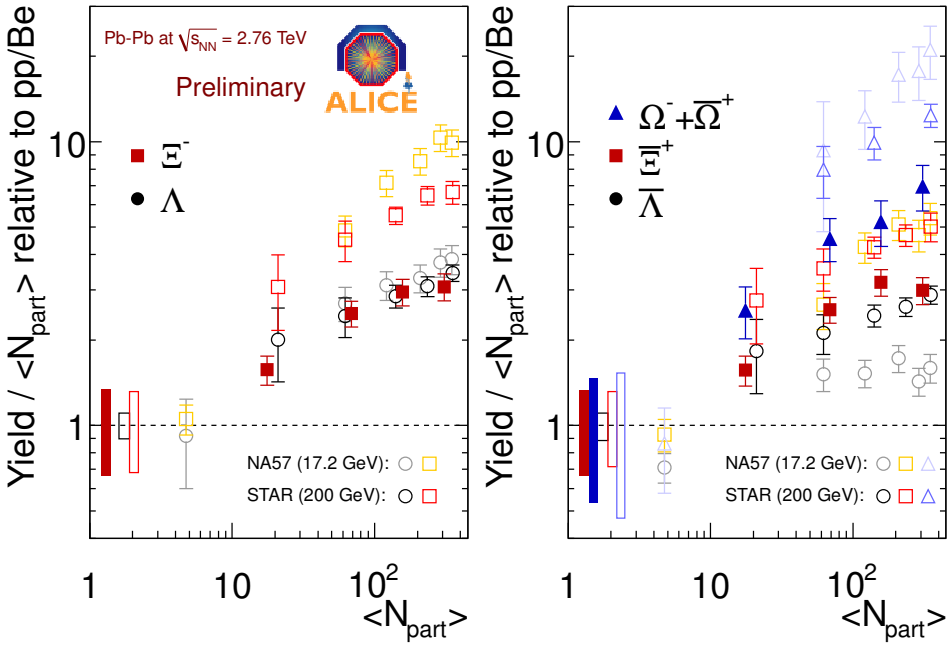

Figure 1.23: Strangeness enhancement observed at ALICE (full symbols) compared to NA57 and STAR measurements (open symbols). Left panel shows the enhancement of Ξ^- ALICE (full red squares) compared to NA57 and STAR Ξ^- (open yellow and open red squares respectively) and Λ (open grey and black circles). Right panel shows ALICE, NA57 and STAR measurements for $\bar{\Xi}^-$ (full red, open yellow and open red squares respectively for the three experiments) and Ω^+ and $\bar{\Omega}^-$ combined (full blue, open light blue and open blue triangles) and $\bar{\Lambda}$ measurement at NA57 (grey open circles) and STAR (black open circles).

production is suppressed by the fact that the charge must be conserved both exactly and locally.

1.2.3 Hydrodynamics and collective flow

Once the fireball is formed after the collision, the free partons start to move chaotically inside the QGP. But if the medium created is strongly interacting, then on top of this Brownian motion also collective behaviours can arise, generically called *flows*. Flows are generated by the presence of pressure gradients in the medium. The standard approach to the description of the flow is based on hydrodynamics which relies on the assumption that the system is thermalized and therefore it is possible to properly define a temperature and other thermodynamical variables (entropy, speed of sound in the medium and so on). As collective motion can only appear for a strongly interacting system, if the flow is established early enough in the collision,

when the pressure gradients are strong, then its presence is one of the most compelling evidences of QGP creation. The first evidence for the presence of collective behaviour was made at RHIC where in 2005 the creation of a perfect fluid (a fluid with viscosity close to zero) was claimed [2]. As it need the system to be thermalized, the hydrodynamical approach can only describe the fireball evolution from the moment of thermalisation to the moment of the thermal freeze-out. The different models available differ mainly on the following aspects:

- How they model initial conditions. Most of the models use Colour Glass Condensate or Glauber initial condition.
- How particles hadronize
- What is the equation of state of the system
- how many dimensions are used in the system. We will see most of the calculations can be made at midrapidity and therefore it would be possible to limit the computations to just 2 spatial dimensions.
- If they include or not viscosity. Viscosity is one of the main properties of QGP and it affects heavily the flow results. Models based on Anti de Sitter–Conformal Field Theory correspondence (AdS–CFT)[26] predict a minimum viscosity of $\frac{\hbar}{4\pi}$[27], even if this minimum is not necessarily the lowest bound[28]. Already at RHIC, where it was questioned whether the energy density was high enough to obtain a completely thermalized system, estimates of viscosity obtained from comparison of models and experimental data showed very low possible values for the viscosity, close to the $\frac{\hbar}{4\pi}$ limit.

The first to apply relativistic hydrodynamic to the study of heavy ions collisions was Landau in 1935 [29], well before QCD was developed, but it started to be commonly used only since the RHIC data, where the large particle number made hydrodynamic relatively easy to use compared to other methods, such as pQCD or lattice QCD. We will only give here the description of the collective flow, without discussing the hydrodynamical equations, for which a nice description can be found in [30]. We can distinguish two main flow categories: the radial flow, which is isotropic and originates from the fireball expansion, is measured from the particle production $\mathrm{p_t}$ (or m_T) spectra. Anisotropic flows are originated by asymmetries in the pressure gradients that act on the fireball and are measured from the particles azimuthal distribution.

Radial flow

A universal scaling, as shown in figure 1.24, appears in proton–proton collisions when the particle production yields are plotted as a function of the

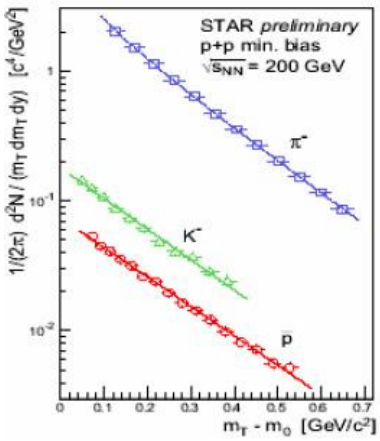

Figure 1.24: Transverse mass spectra of pions, kaons and protons scaled to the particle specie's mass m_0 at STAR in proton–proton collisions

transverse mass $m_T = \sqrt{m^2 + p_t^2}$. Hence the transverse mass distribution of produced particles can be written as

$$\frac{dN}{dm_T} \propto e^{\frac{m_T}{T}} \tag{1.11}$$

and it looks like the particles are emitted according to the Boltzmann law by a body at temperature T. In Pb-Pb collisions a possible interpretation of the parameter T is that it is the temperature at which the partons, created in the collision, hadronize and reach the thermal freeze–out.
The universal scaling of equation 1.11 is broken in collisions between nuclei. In this case the slope of the spectrum decreases with the mass of the particle specie. This behaviour can be understood assuming that the particles, before reaching the thermal freeze–out, were participating to some kind of collective expansion. If this is the case, then the slope would be dependent on the mass of the particles and on the speed of the collective expansion (the *radial flow*) in the form

$$T = T_{\text{fo}} + \frac{1}{2} m v_T^2 \tag{1.12}$$

where T_{fo} is the temperature of the thermal freeze-out.

Anisotropic flow

Anisotropic flow patterns are generally associated with asymmetries in the azimuthal distribution of particles. We can define as the longitudinal (z) axis the direction of the colliding nuclei and as the x axis the direction of the impact parameter vector. These two axis define the *reaction plane*. The true reaction plane is not directly measurable, so it must be estimated from the data collected in the single event. This estimation is called *event*

plane. Orthogonal to the event plane is the *transverse plane*, defined by the x and y axis. A sketch picturing this coordinate system is visible in figure 1.26. The azimuthal angle ϕ is defined as the angle with respect to the x axis in the transverse plane. Given these definitions, we can expand the azimuthal distribution of particles in the transverse plane with a Fourier series obtaining the following:

$$\frac{dN}{Nd\phi} = 1 + 2v_1 cos\phi + 2v_2 cos2\phi + 2v_3 cos3\phi + ... \tag{1.13}$$

The factors "2" are introduced to simplify following calculations. The usual methods to compute the event plane are based on the reconstruction of a symmetry plane from the distribution of the particles in one event. As this plane can be different for different harmonics, when computing each v_n coefficient the proper event plane should be used [31]. The determination of the event plane is not trivial and different techniques can be used. The main methods are based on building a event flow vector Q_n for the n^{th} harmonic, containing the information on the azimuthal distribution of the particles, defined by the relations

$$\begin{aligned} Q_n^X &= \sum_i w_i \cos(n\phi_i) \\ Q_n^Y &= \sum_i w_i \sin(n\phi_i) \end{aligned} \tag{1.14}$$

where the w_i coefficients are weights associated to each particle and ϕ_i are the particle azimuthal angles. The event plane angle Ψ_n for the n^{th} harmonic can be obtained as

$$\Psi_n = \frac{1}{n} \tan^{-1}\left(\frac{\sum_i w_i \sin(n\phi_i)}{\sum_i w_i \cos(n\phi_i)}\right). \tag{1.15}$$

Several corrections are often needed in order to have an isotropic azimuthal distribution of the event planes. Some examples of this procedure will be given in section 4.3, where the event plane determination for the D meson flow analysis is discussed.
Each of the v_n factors of equation 1.13, at least for the first coefficients, can have a different physical interpretation and are the quantification of what we call *flow*. The most interesting flows are

Directed flow v_1 Appears when the fireball is likely to shift towards one direction.

Elliptic flow v_2 Perhaps the most important flow, it is a preference of the system to emit particles inside or outside the reaction plane.

Triangular flow v_3 end higher harmonics $v_{n>2}$ are linked to fluctuation of initial energy density in the collision due to fluctuations in the geometrical configuration of the nucleons inside the colliding nuclei.

Before moving to a more detailed description of those coefficients, it useful to note that at midrapidity, for the collision of two identical nuclei, the system is symmetric along the z axis. This suppresses the odd terms leaving v_2 as the main flow in the midrapidity region.

Directed flow

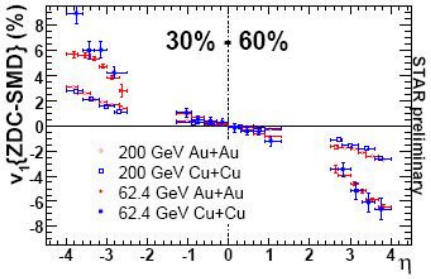

Figure 1.25: Directed flow as function of pseudorapidity at STAR for centrality 30%-60%.

v_1 represents a translation of the particle source in the transverse plane and its measurement at STAR, shown in figure 1.25, makes immediately visible the suppression of the odd flow coefficient at midrapidity. The fireball at midrapidity expands mainly in the transverse direction and all the new particles that are created are created with no preferred direction. But when going towards higher rapidity regions [32] the matter created in the collision is more likely to keep part of the momentum of the colliding nuclei and receives a momentum component from the bounce-off of the spectator nucleons on the target nucleus. Another component to the direct flow is the fact that the fireball is spinning due to the asymmetry of the collision [33]. This spinning is also pushing the direction of particles at high rapidity.

Elliptic flow

When two nuclei collide with large impact parameter (semi–peripheral collisions), as in figure 1.26, the interaction region is anisotropic in the transverse plane, assuming a characteristic almond shape, that can be reasonably parametrised with an ellipse. If the matter produced in the collision does have collective behaviour, then along the shorter axis of the ellipse, that is the axis in the direction of the impact parameter (x in figure 1.26, where z is the direction of the colliding nuclei) the pressure gradient will be stronger then along the long axis (y). The presence of different pressure gradients enhances the momentum component in the x direction, where pressure is stronger, while the y component is less pushed because of the lower pressure. During the fireball evolution the original spatial asymmetry is washed away

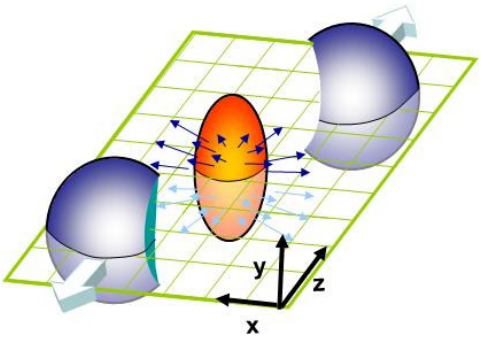

Figure 1.26: Non central nucleus–nucleus collision

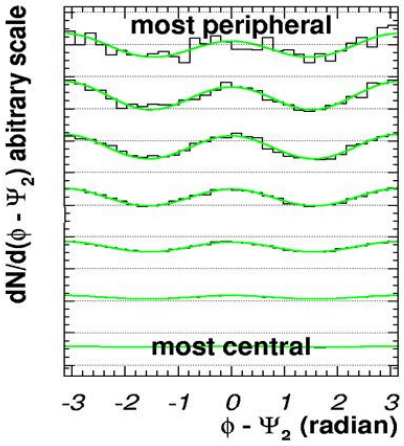

Figure 1.27: Azimuthal particles distribution at RHIC as function of centrality

by the action of the pressure gradients. The only surviving asymmetry is therefore the momentum asymmetry, generated mainly at the beginning of the collision when the pressure gradients are stronger and the energy density is maximum. This makes the elliptic flow a good test for the equations of state of the system in the early stages of its evolution. If the collision is at very high energy (close to the transparency regime) the net effect of this asymmetry is that there will be more particles emitted in the direction of the reaction plane (in–plane) than in the transverse plane direction (out of plane) as shown in figures 1.27 where the particles azimuthal distribution with respect to the reaction plane measured at RHIC is shown for different centralities, and in figure 1.28, that shows the v_2 coefficient measured at ALICE as a function of the collision centrality. It is visible that going towards collisions with small impact parameter the v_2 contribution tends to disappear, an effect of the decreasing initial asymmetry. When the speed of the colliding nuclei is not large enough for transparency to be achieved, than some of the nucleons are still in the impact region during the fireball build-up, stopping the fireball initial expansion and modifying the pressure gradients. The effect is that under these conditions the v_2 turns out to be negative, a behaviour observed at the AGS. The evolution of the v_2 value against the energy available in the centre of mass of the event is shown in figure 1.29. The value of v_2 increases continuously going from SPS to RHIC to LHC energies. Having measured the particle azimuthal distribution, we can extract the value of v_2 applying:

$$v_2 \equiv \int_0^{2\pi} d\phi \cos(2\phi) \frac{dN}{d\phi} \equiv \langle cos2\phi \rangle \tag{1.16}$$

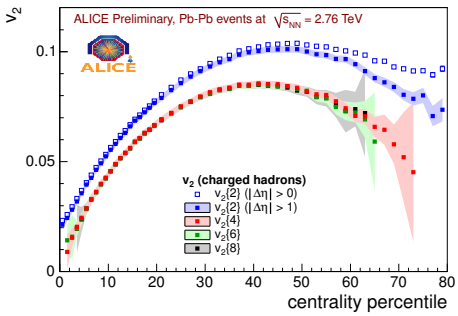

Figure 1.28: Charged hadrons v_2 as a function of the centrality of the collision at ALICE measured using 2-particle correlations (blue) and multiparticle cumulants.

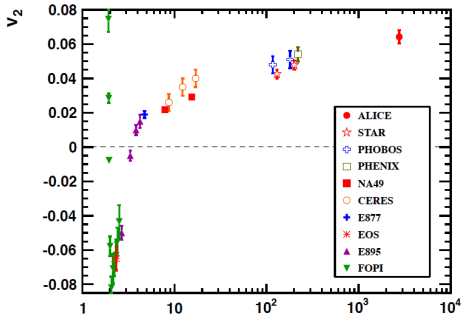

Figure 1.29: v_2 as a function of the energy available in the centre of mass of the collision. ALICE data is from Pb-Pb collisions ar $\sqrt{s_{NN}} = 2.76$ TeV in the centrality class 20-30% and it is compared to results from lower energies experiment at similar centralities.

So to measure v_2 we only need to average the azimuthal particle distribution over many particles and many events, a relatively easy measurement, where the tricky part of the measurement is basically the determination of the reaction plane, a topic that will be discussed in 4.3.

Triangular flow

The third coefficient of the Fourier expansion v_3 is called triangular flow. It should vanish at midrapidity but it was speculated [34, 35] that fluctuations of the geometrical nucleons distribution inside the colliding nuclei also produce asymmetries in the interaction region and that most of this anisotropy can be accounted by v_3 and higher order harmonics.

1.3 a charming way to probe QGP

1.3.1 Charm in proton-proton collisions

Chapter 3 will be dedicated to the analysis and results obtained by ALICE in the study of charm production in proton-proton collisions. The study of the open charm meson production cross section is an interesting test of QCD calculations based on the factorization approach [36] in an energy domain yet unexplored. In this approach to QCD processes the cross section is computed as the convolution of three independent terms:

- The parton distribution function (PDF) of the colliding protons

- The cross section of the partonic hard scattering, that can be computed with a perturbative approach
- The fragmentation function parametrizing the probability of the charm quark to hadronize in a particular D meson specie.

Putting these three ingredients together, we can write the D meson production cross section as:

$$\sigma_{pp\to Dx} = \mathrm{PDF}(x_a, Q^2) \cdot \mathrm{PDF}(x_b, Q^2) \times \sigma_{ab\to c\bar{c}} \times D_{c\to D}(z_c, Q^2) \quad (1.17)$$

Where *PDF* is the parton distribution function and depends on the fraction of momentum of the incoming proton carried by parton (x_i) and on the transferred momentum Q^2, and D is the fragmentation function of the c quark in a D meson carrying a fraction z_q of the quark momentum. These calculations describe well the beauty production measured at Tevatron [37] and at the LHC by the LHCb [38] and CMS experiments [39], for which the results are shown in figure 1.30. The charm production is also well reproduced and consistent within the theoretical and experimental uncertainties, however both at Tevatron [40] and RHIC [41] the comparison suggests that experimental data might be underestimated by the central values of the theoretical computation parameters. The measurement of the D meson production cross section at LHC, where the energy is more than three times higher than the energy available at Tevatron is therefore of high interest. At the LHC energies the measurement of the D meson cross section in the very low $\mathrm{p_t}$ region, possible thanks to the very good tracking, vertexing and PID capabilities of ALICE, is an excellent probe for the parton distribution function in the very low x regions, down to $x \sim 10^{-5}$. The small x region is dominated by the gluon component, that in this region might show effects of saturation. If this happens, then significant deviations from the cross section expectations obtained using the factorization approach should be observed [42].

The measurement of the charm production cross section is also an essential requirement in order to have a baseline to perform measurements in Pb-Pb collisions, as we will see in detail in the following chapters.

1.3.2 Charm in heavy ion collisions

The heavy quark related measurements are among the most powerful tools to investigate the properties of the medium created in heavy ion collisions. These probes have been already studied at RHIC experiments (and to some extent at the SPS), but it is at the LHC, where the charm and beauty production rate is several times larger than in any experiment before, that the study of charm and beauty will be a really powerful tool. In this section I will describe some of these measurements and the physical insight on the

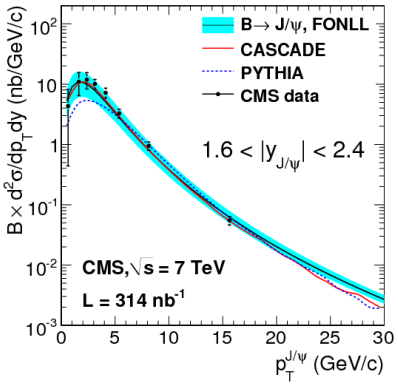

Figure 1.30: non-prompt J/Ψ production differential cross section measured at CMS experiment. Prompt and non-prompt candidates are separated with a fit to the decay length. CMS data points are compared to FONLL, PYTHIA and cascade models.

QGP properties they can provide. A special focus will be placed on the probes related to the study of open heavy flavours (hadrons made by one heavy quark and one or two light quarks) We will see in chapter 2 that the ALICE experiment is very well suited for those kinds of studies, while in chapters 3, 3 and 4 I will give details of the open heavy charm decaying in their hadronic channel analysis, as this is the main topic of this thesis.

Due to their large mass heavy quarks are mainly produced at the very beginning of the collision in the scatterings between the partons of the colliding nucleons that are energetic enough to create a pair of heavy partons. As these scatterings are very hard they mainly happen at the very beginning of the collision, before the medium creation, so they can be computed using perturbative QCD calculations. The produced heavy quarks travel through the medium experiencing all the stages of its evolution and finally hadronize inside or outside the fireball. While they follow the fireball evolution their dynamical quantities experience several modifications and some of them are peculiar to heavy quarks. Two of the most important observables regarding heavy quarks, whose experimental results at ALICE will be discussed in detail in chapter 4, are the energy loss and the elliptic flow, and more precisely the comparison of heavy quarks energy loss and flow with respect to what measured for light hadrons.

The first measurement we are going to discuss in this section is the heavy flavour energy loss. We have already seen that the energy loss of a given specie due to the presence of the strongly interacting medium can be quantified using the nuclear modification factor, defined in eq 1.9. We can then compute this factor for the D and B mesons, that are composed of one c

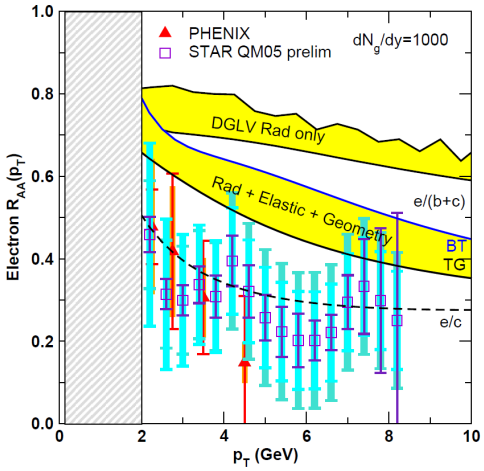

Figure 1.31: Nuclear modification factor of electrons from heavy-flavour decays as measured at PHENIX (triangles) and STAR (squares). Top yellow band shows theoretical calculation of energy loss with only contribution from radiative energy loss. The lower band includes elastic and inelastic energy loss too (calculations from Wicks, Horowitz, Djordjevic and Gyulassy[43]

or b quark and one light parton. If we suppose hadronization by the fragmentation mechanism then we should consider the fragmentation functions. As the fragmentation functions for D and B mesons are significantly harder than the ones for the light partons, the open-heavy flavour mesons will carry a larger fraction of momentum of the original c or b quark. So the measurement of the energy loss from the open heavy-flavour will be close to the one of the c quarks. If we recall equation 1.8 the energy loss in the QCD medium depends on the colour charge of the parton. In the case of the quarks the colour charge is 4/3, smaller then the colour charge of 3 of the gluons. This reflects the fact that a gluon is more likely to interact in the medium than a quark, a fact can be extrapolated from the QCD Lagrangian noticing that gluons have interaction with two quarks and with two or three gluons, while quarks only interact with one gluon and one quark. Most of the light hadrons come from hadronization of gluons, that at the LHC energies are much more abundant than quarks. This means that light hadron suppression is driven by gluon energy loss, while the energy loss of an open heavy flavour meson is close to the one of a quark, and therefore smaller. So the expectation on the energy loss of the D meson is that $R^{D}_{\rm AA} > R^{\pi}_{\rm AA}$[8]. We can move a step further and discuss the energy loss of the open beauty mesons.

[8]As most of the light hadrons are pions and because of the fact that the $R_{\rm AA}$ changes slightly at high p_t with the particle specie, we will use in this section as equivalent the notation $R^{\pi}_{\rm AA}$ (nuclear modification factor of pions) and $R^{h}_{\rm AA}$ (nuclear modification factor of charged hadrons.

The beauty quark have the same colour charge of the charm quarks, but much higher mass. In case of radiative energy loss that for the quarks is due to gluon emission (*Gluonstrahlung*) there is a predicted effect, called *dead cone effect*, described in [44]. The dead cone effect prevents the emission of gluon for small angles with respect to the direction of the quark momentum. This dead cone angle is proportional to ratio between the parton mass and its momentum. Being the mass of b quark significantly larger the the one of the c, the forbidden region is larger and therefore the b energy loss due to gluon emission is smaller. So that we expect a hierarchy of the nuclear modification factors of B and D mesons and light hadrons such that

$$R^{B}_{\mathrm{AA}} > R^{D}_{\mathrm{AA}} > R^{\pi}_{\mathrm{AA}} \tag{1.18}$$

The data sample collected in 2010 by ALICE is still not sufficient to include in this work the beauty energy loss, but as we will see in section 4.2 some important results are already available for the energy loss of charmed particles. Results on the heavy quarks R_{AA} measurements made at PHENIX [45] and STAR [41] using inclusive electronic decays are shown in figure 1.31. Those data show that already at RHIC energies a strong suppression was observable in the heavy flavour sector. The figure also shows that the suppression is larger than what predicted by theoretical models, even when taking into account not only the radiative energy loss contribution but also contirbutions from elastic and inelastic scatterings. The suppression of the heavy flavour at RHIC is smaller than the one of pions for low $\mathrm{p_t}$ values, but they start to approach each other for $p_t > 4$ GeV/c.

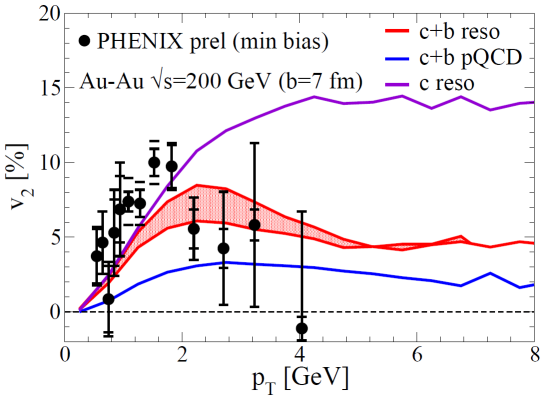

Figure 1.32: Elliptic flow from heavy flavour decays electrons measured at PHENIX. Predictions from Hees Greco and Rapp [46] are shown in comparison.

The second important observable we are going to discuss is the elliptic flow of D mesons measured at midrapidity. The general features of the elliptic flow were already discussed in the previous sections. We will just un-

derline here that with hydrodynamical models, for a completely thermalized system, in principle each fluid element is equivalent to all the others, with its behaviour only influenced by the local thermodynamical quantities such as temperature, energy density, entropy and so on. Under these conditions hydrodynamics predicts the pressure gradients to act in the same way on heavy and light partons, so that observed collective motion should present a mass hierarchy, with heavier particles showing smaller effects, an effect already observed at RHIC [47]. We should note that assuming the charm quark to be thermalized in the medium exactly in the same way as light partons does not look like a realistic assumption. If the main thermalisation mechanism is through scatterings or radiative energy loss then we would expect the charm to thermalize much later or even not to thermalize at all. There are available hydrodynamical models [46, 48] that try to treat separately heavy quarks in order to have a more realistic estimation or what we can expect for the elliptic flow of the open charm mesons. What I want to stress is that qualitatively we should expect the elliptic flow of the charm at midrapidity to have an upper limit slightly below the light hadrons v_2 (because of the mass hierarchy effect) reached in case of a complete thermalisation of charm in the medium and a lower limit in case of charm quark not thermalized just above 0, because there is a contribution from the light parton in the case of hadronization by recombination mechanism. If any of the two extreme values is reached at LHC it would come out as a surprise on this observable. In the first case, if $v_2^c \lesssim v_2^h$ then the thermalisation mechanism is really extremely strong and fast, while if $v_2^c \gtrsim 0$ it would mean that the thermalisation mechanism is not strong enough to thermalize heavy objects. We should also notice that at high $\mathrm{p_t}$ a non-zero v_2 contribution is expected due to the path length dependence of the energy loss. Figure 1.32 shows the measured elliptic flow of electrons produced in heavy flavour decays [49]. The flow looks similar to the one of light hadrons at low $\mathrm{p_t}$ while data at higher $\mathrm{p_t}$, where the beauty contribution is dominant, are affected by large statistical errors. This is compatible with a picture where low $\mathrm{p_t}$ partons are thermalized in the medium. Experimental data are well reproduced by hydrodynamical models that include the presence of c and b resonances and hadronization by a combination of coalescence fragmentation, while are underestimated when only pQCD (non resonant) processes are considered [46].

2

A Large Ion Collider Experiment at the LHC

A Large Ion Collider Experiment (ALICE) is one of the four experiments located at the Large Hadron Collider (LHC) facility at CERN. In this chapter I will give an overview of the ALICE experimental setup. I will describe with particular attention those detectors on which we rely most for the open charm analysis: the Time Projection Chamber (TPC), the Time Of Flight (TOF) and the Inner Tracking System (ITS). I will also focus on the Silicon Drift Detector (SDD) which is part of the ALICE Inner Tracking System, since I worked directly for this detector operation and maintenance. An introduction to ALICE computing model, to the analysis framework and to the computing interface (the GRID) will be given in section 2.4.

2.1 The Large Hadron Collider

The Large Hadron Collider is the largest accelerator at CERN and at the present status it is the most powerful accelerator facility in the world [50]. The accelerator is installed in a 26.7 km long tunnel originally built for the Large Electron-Positron collider (LEP) that was dismissed in 2000. It lies between 45 and 170 metres below the Jura mountains across the border between France and Switzerland. LHC is designed to accelerate and collide proton bunches at a centre of mass energy of 14 TeV and heavy ion (lead) bunches at 5.5 TeV per nucleon pair. Currently the LHC is running at half of the nominal energy, providing proton-proton collisions at $\sqrt{s} = 7$ TeV and Pb-Pb collisions at $\sqrt{s_{NN}} = 2.76$ TeV. Proton-ion collisions are also in the capabilities of the LHC and the first p-A collisions are expected for November 2012.

The LHC is the last step of a complex accelerating procedure involving several machines. The particles to be accelerated are extracted from a source (an hydrogen tank for protons and a piece of isotopically enriched lead heated to 500°C for lead atoms, subsequently ionized using an electric

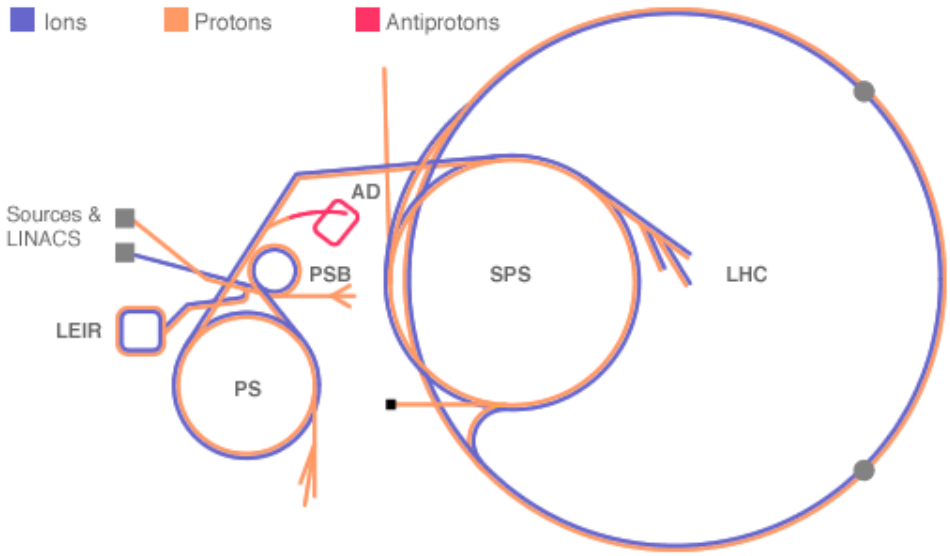

Figure 2.1: CERN accelerating scheme (not in scale)

field) and then injected in the Linear Accelerator 2 (Linac2) where they are accelerated to an energy of 50 MeV. From this they pass to the Proton Synchrotron Booster (PSB); then to the Proton Synchrotron (PS) and after the PS to the Super Proton Synchrotron (SPS) acquiring more energy at each step. When they are extracted from the SPS to be injected in the LHC the particles have an energy of 450 GeV. Then the LHC accelerates them to the final energy: 3.5 TeV for protons and 1.38 TeV per nucleon for Pb ions. This accelerating chain is sketched in figure 2.1.

The LHC accelerator hosts four experiments: A Toroidal Large Acceptance Solenoid (ATLAS) [51] and the Compact Muon Solenoid (CMS) [52] are two big multi purpose experiments. Their main research goal is the detection of the Higgs boson and the study of Standard Model physics and beyond, such as signatures of SuperSimmetry (SUSY). Both of them also have a research program for Pb-Pb collisions. LHCb [53] is an experiment focused on B physics and CP violation and it only collects proton-proton and proton-Pb collisions. They have recently released important physical signatures of CP-violation observed in the D^0 decay channels [54]. A Large Ion Collider Experiment (ALICE) [55] is an heavy-ion experiment with the goal of studying QGP properties. It also has a rich proton-proton program. A detailed description of ALICE will be given in section 2.2

The nominal luminosity of LHC is $\mathscr{L} = 10^{34}\text{cm}^2\text{s}^{-1}$ for proton-proton collisions and $\mathscr{L} = 10^{27}\text{cm}^2\text{s}^{-1}$. The first beam were circulated in the LHC ring on September 10^{th}, 2008 but after 10 days the LHC suffered a severe malfunctioning [56] that brought to the decision of running the LHC at half

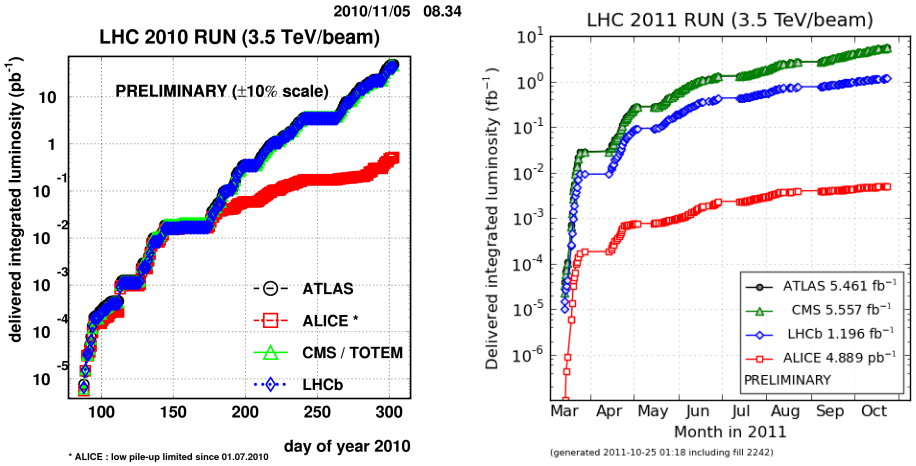

Figure 2.2: LHC 2010 delivered luminosity for p-p collisions (left) and Pb-Pb collisions (right) for ATLAS (black), CMS (green) ALICE (red) and LHCb (blue) experiments. LHCb did not participated in the Pb-Pb runs.

of the nominal energy for the 2010-2012 period: 3.5 TeV for protons and 1.38 TeV per nucleon for lead ions. The data presented in this thesis were collected at these energies. In addition to this, the LHC delivered proton-proton collisions at a centre of mass energy $\sqrt{s}$ = 900 GeV in November 2009 and $\sqrt{s}$ = 2.76 TeV in April 2011. In 2013-2014 a 15 months long shutdown is foreseen in order to upgrade the machine and allow it to run safely at the designed energies.
During the 2010 proton-proton collisions the LHC reached a peak luminosity of $\mathscr{L} = 2 \cdot 10^{32}\text{cm}^2\text{s}^{-1}$ [57] for an integrated luminosity of 45 pb^{-1} delivered to ATLAS and CMS. In the same period ALICE collected 1 pb^{-1}. This is due to the fact that ALICE requires lower luminosity in order to deal with the pile up in its TPC. In order to reduce the luminosity, the LHC beams are displaced before the ALICE interaction point. In the 2010 Pb-Pb period all the experiments collected $10\mu\text{b}^{-1}$, with a peak luminosity of $\mathscr{L} = 30 \cdot 10^{24}\text{cm}^2\text{s}^{-1}$. These results are summarized in figure 2.2. In 2011 LHC improved its performances reaching a peak luminosity for p-p collisions of $\mathscr{L} = 3.5 \cdot 10^{33}\text{cm}^2\text{s}^{-1}$ (just a factor 3 below the nominal value) that allowed to deliver more than 5 fb^{-1} to ATLAS and CMS and about 5 pb^{-1} to ALICE.

2.2 ALICE, a powerful tool

A Large Ion Collider Experiment [55] is a general purpose heavy-ion experiment with the main goal of exploring the characteristics of the strong

interacting medium produced in heavy ion collisions at the LHC and it is designed in order to be able to investigate the majority of the experimental observables for the medium characterization (electrons, hadrons, muons and photons). ALICE is capable of tracking charged particles in a wide transverse momentum range (from 0.1 GeV/c to 100 GeV/c) and has excellent particle identification capabilities in a wide p_t range and it is designed to operate in a high charged particle multiplicity environment. To provide good tracking performances ALICE relies on high granularity detectors. As some of the tracking detectors are based on drift technologies, they are slower then the detectors operated by the other LHC experiments but can work at the nominal LHC ion beam rate of 10kHz.

ALICE, whose setup is sketched in figure 2.3, can be divided in three different parts: a set of detectors covering the central rapidity region called the *central barrel*, the muon arm at forward rapidity and the forward rapidity detectors for triggering and event characterization.
The central barrel detectors are installed inside a solenoid built for the L3 experiment at LEP (with the exception of ACORDE, placed on the top of the solenoid). The solenoid can provide a 0.5 T magnetic field, uniform within a 2% level in the volume of the detectors. It includes, moving from the beam pipe to the outside: the Inner Tracking System (ITS) made of six layers of high resolution silicon detectors with three different technologies (pixels, drift, strips); the Time Projection Chamber (TPC), that is the main tracking detector; the Transition Radiation Detector (TRD); a Time-Of-Flight detector (TOF). While ITS, TPC, TRD and TOF cover the full azimuthal angle for $|\eta| < 0.9$, in the central barrel there are also three detectors covering a smaller pseudorapidity (η) and azimuthal angle (ϕ): the High Momentum Particle Identification Detector (HMPID) which is an array of ring imaging Cherenkov detectors; the Photon Spectrometer used to measure photons and neutral pions, and the Electro-Magnetic CALorimeter (EMCAL).
In the forward region there is the Muon Spectrometer (or *muon arm*) used for muon reconstruction and covering the range $-4 < \eta < -2.5$. It is made of 10 planes of tracking chambers, four planes of trigger chambers and an hadron absorber which is installed inside the L3 magnet to reduce the background from hadrons produced in the collision.
The set of forward detectors used for event characterization and triggering is made by The Photon Multiplicity Detector (PMD); the Forward Multiplicity Detector (FMD); two neutron and proton calorimeters placed on both sides of the interaction point at a distance from it of about 116 metres to make the Zero Degree Calorimeter (ZDC); the VZERO detector and two scintillators counters (T0).

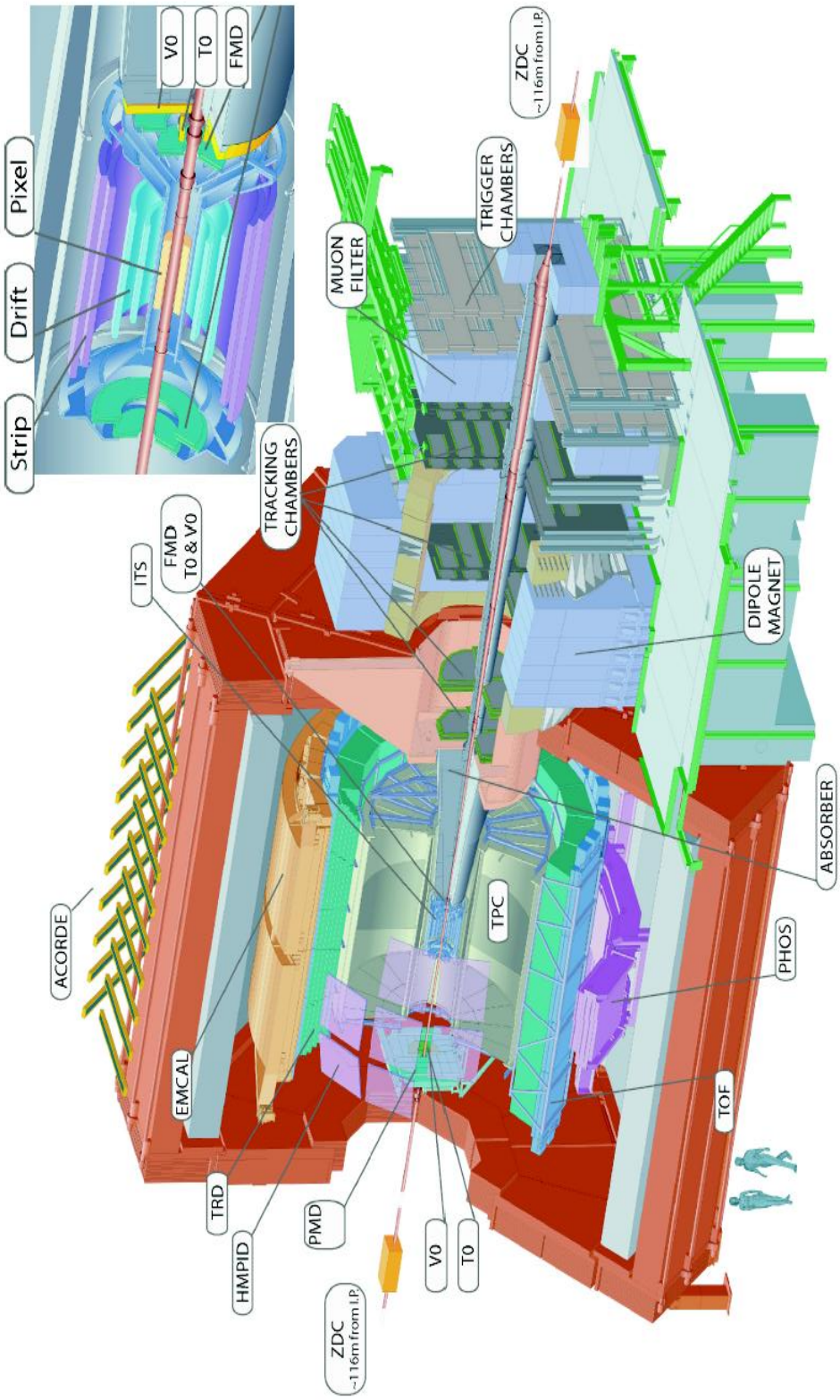

Figure 2.3: The ALICE detector layout.

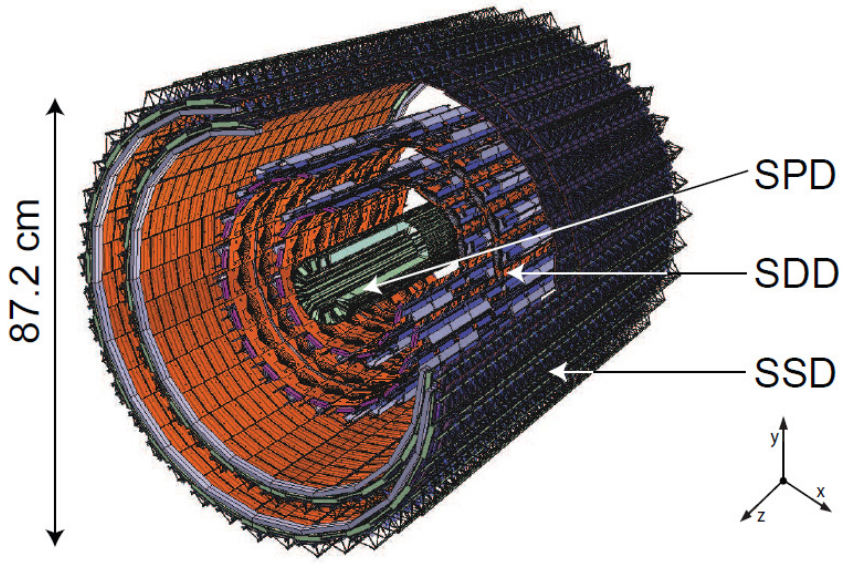

Figure 2.4: ALICE ITS layout

2.2.1 Inner Tracking System

The Inner Tracking System, depicted in figure 2.4, is the closest detector to the vacuum tube. It is composed of six layers of silicon detectors, with a radius ranging from 3.7 cm for the innermost layer to about 44 cm for the outermost. The first two layers are made of fast and high-granularity pixel detectors (SPD), the two intermediate layers are the Silicon Drift Detector and the two outermost layers are made of silicon strips (SSD). The ITS is designed to keep good tracking efficiency in high multiplicity environment, as those produced in Pb-Pb collisions at the nominal LHC energies where some models predicted up to 8000 charged particles per rapidity unit at the time of ALICE design. The ITS performance is crucial to provide a high spatial resolution (better than 100 μm) on the primary vertex of the collision and on the secondary vertices (like those from heavy flavour decays) and on the track impact parameter and momentum. The ITS can track and identify low momentum particles (down to $p_t \sim 70$ MeV/c). The particle identification is provided by the energy loss information from the 4 outermost layers. Also, ITS hits are used to improve the tracking from the TPC, allowing to prolong TPC tracks towards the primary vertex of the event.

SPD

The first two layers of the ITS are made Silicon Pixel Detectors (SPD). The SPD plays a fundamental role in reconstructing the primary vertex and identifying the secondary vertices from the decays of heavy flavour particles:

its high space point resolution and its small distance from the beam pipe and the small material budget are all relevant to obtain excellent tracking resolution. Each pixel cell measures 50 μm in the $r\phi$ direction and 425 μm in the z direction. Pixels are arranged in two dimensional matrices of 256×160 cells, for a total of more than $9.8 \cdot 10^6$ pixels. The signals from the matrices are read by a set of five front end chips, each one reading a sub-matrix of 256×32 cells. The innermost pixel layer is as close as possible to the beam pipe, with an average radius of 3.9 cm, while the outer layer is placed at 7.6 cm from the interaction point. The SPD detector provides a binary information for each pixel. The spatial resolution of the SPD is determined by the cells size, by the track angle with respect to the cell orientation and by the detector thresholds applied in the readout. The spatial resolution measured during beam tests was found to be 12 μm in the $r\phi$ direction and 100 μm along the z axis. The SPD is also one of the ALICE trigger detectors, and its response was used to trigger minimum-bias events both in the proton-proton and Pb-Pb data taking. Each SPD front-end chip give a fast trigger signal when fired (Fast-OR).

SDD

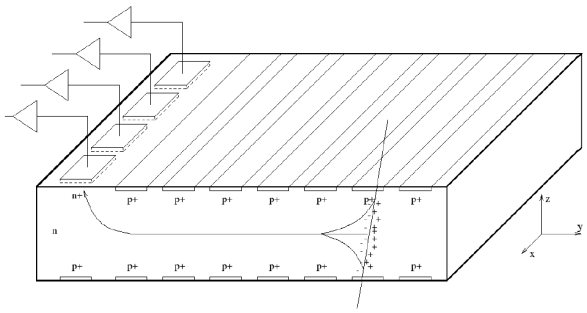

Figure 2.5: sketch of SDD detector and of charge production and collection. Coordinates are in the detector reference frame and not in the ALICE reference frame.

The Silicon Drift Detector equips the two intermediate layers of the ITS. The inner layer is placed at an average radius of 15.03 cm while the outer layer at a radius of 23.91 cm. Both layers cover a pseudorapidity range of $|\eta| < 0.9$. The basic building block of the ALICE SDD is a module that covers an active region of 7.017×7.526 cm^2. Each module is divided into two drift regions by a central cathode strip. Both drift regions have 256 anodes with 294 μm pitch and 291 cathode strips with 120 μm pitch on both sides of the detector. The cathodes fully cover the detector volume and generate a drift field obtained by gradually scaling down the voltage applied to the cathode when moving from the central one towards the anodes allowing

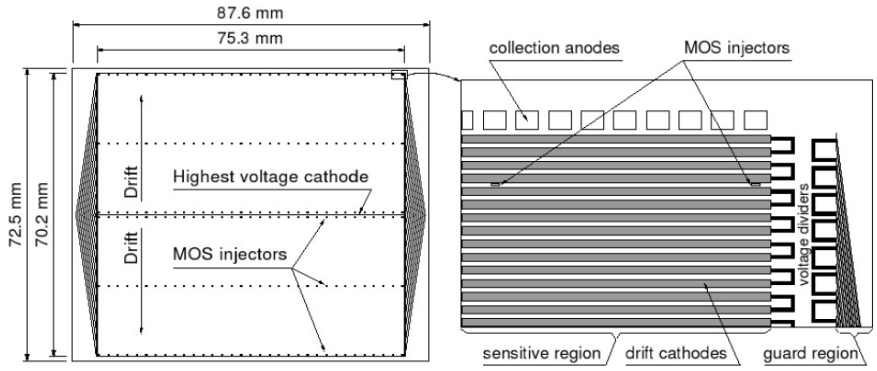

Figure 2.6: Layout of an ALICE SDD module. The sensitive area (left) is split in two drift regions by the central highest-voltage cathode. On the side of each drift region there is a row of 256 collection anodes and three rows of 33 point-like MOS charge injectors. In the right panel is visible a zoom on the anodes region of the module.

electrons to move in opposite directions under the effect of the drift field. A Metal Oxide Semiconductor (MOS) structure, made of 3 lines of MOS for each drift region, is capable to inject a defined amount of charge at a known distance from the anodes. By this mean, it is possible to check the drift speed during the data taking. This tool to control the drift speed is called *Injectors*. The layout of an SDD module is visible in figure 2.6. The read out front-end electronics chips are on both sides of the module. The SDD modules are mounted on linear structures called ladders. There are 14 ladders with six modules each on the inner SDD layer, and 22 ladders with eight modules each on the outer SDD layer. When a charged particle crosses one SDD module active region it creates electron-holes pairs. The electrons, driven by a 1800 V potential that generates an electric field of $\sim$ 500 V/cm, drift from the generation point to the collecting anodes. The measure of the time necessary to collect all the electrons produced by the crossing particle allows to determine one coordinate (along $r\phi$ in the ALICE coordinate system) of the point where the particle crossed the detector, while the other coordinate (along the beam direction z) is given by the centroid of the collected charge distribution. A scheme of the detector and of this mechanism is shown in figure 2.5. The amount of collected charge is proportional to the energy deposit of the particle in the silicon, and this information can be used for particle identification. The drift collection time of the SDD is of 5,5 μm, while the SDD read out time is 1023 μs. An optimal reconstruction of the ϕ coordinate requires to know with good precision the drift velocity and the time-zero, which is the measured drift time for particles with zero drift distance. The drift velocity is strongly dependent on

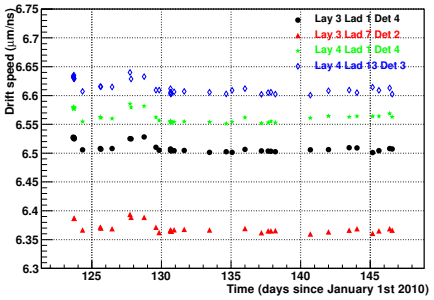

Figure 2.7: Drift speed measured in four different SDD modules as a function of time during the LHC10c period

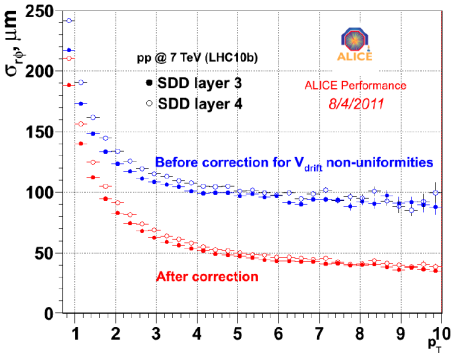

Figure 2.8: SDD resolution in the $r\phi$ plane before (blue) and after (red) correcting for drift speed non-uniformities in the detector on layer 3 (full) and 4 (open)

temperature, following a relation $v_{\text{drift}} \propto T^{-2.4}$, and it is therefore sensitive to temperature gradients in the SDD volume and to temperature variations with time. As the temperature can vary even on a short time scale, the detector was designed with the capabilities to calibrate it frequently during the data taking. The improvement of the resolution in the $r\phi$ coordinate obtained with the injector measurement is shown in figure 2.8. The data collected from injector runs during the first year of data taking show that the drift speed is stable over several days. Figure 2.7 shows the drift speed measured from injectors in four different SDD modules during the LHC10c data taking period. During the 2011 data taking period the calibration procedure to measure the drift speed has been automatized and it is now performed every time the LHC beam ramp up. The SDD detector can achieve a spatial resolution of 35 μm along the drift direction and of 25 μm in the anode coordinate.

SSD

The two outermost layers of the ITS are composed of Silicon Strip Detectors (SSD). SSD, being the closest detector to the TPC, plays a crucial role in the prolongation of tracks from the TPC to the ITS. The basic building block of the ALICE SSD is a module composed of one double-sided strip detector. Strips are almost parallel (the stereo angle being 35 mrad) to the beam axis in order to provide the best resolution, of 20 μm on the $r\phi$ coordinate. The resolution along z is $\sim 800\mu$m. The SSD working mechanism is based on the collection on each strip side of the electron/holes pairs created by a charged particle crossing the detector. As the SDD, the SSD measures the particle specific energy loss (dE/dx) to perform particle identification.

2.2.2 Other Central Barrel detectors

TPC

The Time Projection Chamber is the main tracking detector of ALICE. It is designed to track charged particles up to $p_t = 100$ GeV/c and it can identify particles using their measured energy loss in the TPC volume. It covers a rapidity range of $|\eta| < 0.9$ over the full azimuth. It has an inner radius of 85 cm, an outer radius of 250 cm and an overall length of 500 cm for a total active volume of about 88 m^3. The inner radius was designed in order to limit the particle density in a high multiplicity environment but still providing good tracking and momentum determination capabilities, while the outer radius is defined by the path length needed to reach a good resolution on the energy loss of particles inside the volume. The TPC material budget is kept as low as possible to limit multiple scattering, the radial thickness of the TPC is 3.5% of a radiation length X_0 in the central region, increasing towards the edges. The volume is filled with a mixture made of 90% of Ne and 10% of CO_2. The TPC cage is divided in two sections by a high voltage electrode, that forces the electrons freed by the crossing particle to drift with a speed of 2.7 cm/μs for a maximum total drift time of 88 μs, which sets the limit for the TPC event rate capabilities. The PID is based on comparing the crossing particle energy loss in the TPC volume dE/dx with a Bethe-Bloch function, with parameters tuned on data, under the mass assumption for a given specie to determine whether the particle is compatible with that specie or not. An example of the particles dE/dx in the TPC as a function of particle momentum for Pb-Pb collisions at $\sqrt{s_{NN}} = 2.76$ TeV is shown in figure 2.9, where the separation among different species is clearly visible. The TPC readout is based on multi-wire proportional chambers with cathode-pad read-out.

TOF

The particle identification used for this thesis work is provided by the TPC and TOF detectors. TOF provides PID for particles up to transverse momentum $p_t \sim 2.5$ GeV/c for pions/kaon separation and can separate protons up to $p_t \sim 4$ GeV/c. The detector is made of Multigap Resistive Plate Chamber strips (MRPC) covering an area of 150 m^2 filled with a mixture composed of 90% of $C_2H_2F_4$, 5% of C_4H_{10} and 5% of SF_6. Each MRPC is made by a ten layer double-stack detector with a time resolution of about 40 ps. The MRPCs are organized in 18 sectors placed in a cylindrical shell with an inner radius of 3.7 m. It covers the same pseudorapidity region as the TPC and the ITS ($|\eta| < 0.9$) and the full azimuth. The TOF works together with the Time0 (T0) detector in order to provide the time of flight of the particles reaching the detector. The overall TOF resolution is around 85 ps in Pb-Pb events (as shown in figure 2.10) and 100 ps in proton-proton

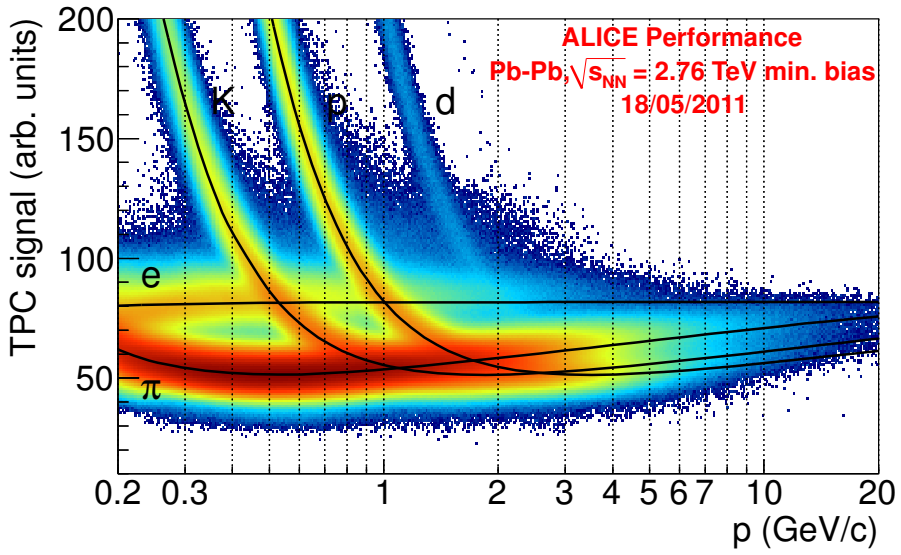

Figure 2.9: dE/dx in the TPC as a function of particle momentum for Pb-Pb collisions at $\sqrt{s_{NN}} = 2.76$ TeV. Black lines are Bethe-Bloch lines for different species.

collisions, where there is a larger systematic uncertainty on the determination of the event time zero. TOF is able to disentangle pions from kaons up to 3 GeV/c and kaon from protons up to 5 GeV/c. Assuming that the distance L travelled by a particle to reach the TOF is knows with good precision (assumption that needs a good precision on the primary vertex), then the velocity of the particle will be $v = L/t$ where t is the time needed by the particle to reach the TOF. From this, and knowing the particle momentum p, the mass of the particle can be determined by the equation

$$m = p\sqrt{\frac{1}{v^2} - \frac{1}{c^2}} = \frac{p}{c}\sqrt{\frac{c^2t^2}{L^2} - 1}. \tag{2.1}$$

TRD

The electron identification in the central barrel is provided by the Transition Radiation Detector, which identifies electrons and positrons with $p_t > 1$ GeV/c, where the separation between electrons and pions with the TPC becomes too small. The TRD, thanks to the $e^{\pm}$ identification capabilities can improve the reconstruction of light and heavy vector meson. As it reconstructs a set of space points with good spatial resolution ($\sim 600\mu$m) the TRD allows to prolong tracks outside the TPC, therefore improving the resolution on the track momentum. The TRD is composed of 540 modules

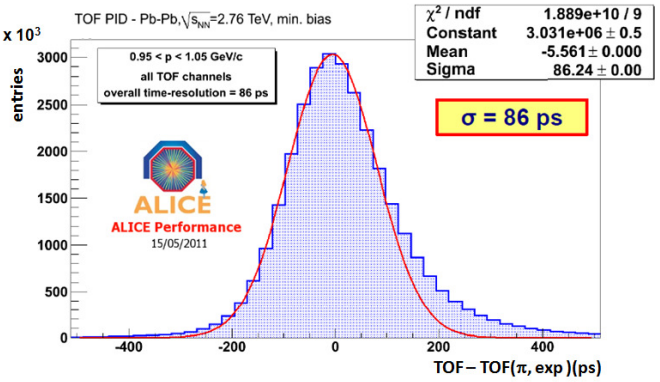

Figure 2.10: TOF resolution for pions selected by the TPC in Pb-Pb collisions at $\sqrt{s_{NN}} = 2.76$ TeV.

organized in 18 sectors (or super-modules), each module consisting of a 4.8 cm thick radiator and a multi-wire proportional chamber. It covers the full azimuth in the mid rapidity region ($|\eta| < 0.84$) and thanks to its fast response time can provide a trigger for charged particles. During the 2009 data taking, the TRD was working with 4 super-modules out of 18. Three more were installed in 2010 and three others were installed during the December 2011 shutdown. The TRD is crucial for heavy-flavour analysis based on inclusive semi-leptonic decay [58].

HMPID

The aim of the High Momentum Particle Identification Detector is to extend the ALICE PID capability for charged hadrons at high p_t increasing the useful range for the π/K separation up to 3 GeV/c and the K/proton separation up to 5 GeV/c. The HMPID consists of an array of proximity-focusing Ring Imaging CHerenkov counters (RICH) and covers a pseudorapidity range of $|\eta| < 0.6$ and 58 degrees of azimuthal angle. The particle transverse momentum threshold in the HMPID RICH is $p_{\mathrm{min}} = 1.21m$ where m is the particle mass.

EMCAL

The EMCAL is the last detector added to the ALICE layout. Its construction started in 2008. The EMCAL is a lead scintillator sampling calorimeter that covers an azimuthal angle range of 107° in the rapidity interval $|\eta| < 0.7$ at a radial distance of about 4.5 metres from the vacuum tube. The EMCAL is designed for the study of jet-physics and can provide trigger signals for hard jets, photons and electrons.

PHOS

The Photon Spectrometer is a high resolution electromagnetic calorimeter aimed at providing photon and neutral meson identification, the latter being reconstructed through their decay in two photons. The direct photons, coming directly from the medium produced in the heavy ion collisions are an extremely interesting probe as they (almost) do not interact with the medium once produced and thus can provide direct insight in the medium properties. The PHOS is placed partially opposite to the EMCAL and covering a rapidity range $|\eta| < 0.14$ and an azimuthal angle of 110°, made of highly segmented electromagnetic calorimeter of lead-tungstenate ($PbWO_4$, PbWO) crystals with a radiation length of $20X_0$ and a charged particle veto detector consisting of a Multi-Wire Proportional Chamber with cathode-pad read-out.

2.2.3 Forward detectors

Muon spectrometer

The ALICE muon spectrometer is designed to detect muons in the rapidity range $-4 < \eta < -2.5$. It allows to perform a rich physics program covering quarkonia, heavy quarks and low masses vector mesons ($J/\Psi, \Upsilon, \phi, \ldots$) studied through their dimuon decays and semi-leptonic decays of charmed and beauty particles. The muon spectrometer is composed of a high granularity system of 5 stations each made of two tracking planes, 4 planes of trigger chambers, each one placed after a muon filter wall, a large dipole magnet producing a strong magnetic field perpendicular to the beam axis and an hadron absorber placed inside the L3 magnet to reduce contamination from large rapidity hadrons coming from the interaction vertex.
The tracking chambers are designed to achieve a spatial resolution of 100 μm, that is enough to reach an invariant mass resolution of 100 MeV/c^2 at the Υ mass. Presently the resolution is limited by the precision of the alignment, measured using cosmic rays and collision data, and it is estimated to be 450 μm in the bending direction and 650 μm in the non-bending direction. The muon trigger system is made of four Resistive Plate Chambers (RPC) placed in two different stations 1 metre from each other at about 16 metres from the interaction point. Each station consists of two planes of 18 single-gap RPCs, placed behind an iron absorber (muon filter). The muon filters are 120 cm thick and combined with the front absorber they prevent efficiently pions from reaching the trigger chambers. Also muons with momentum $p_t < 4$ GeV/c are stopped by the muon filters.

FMD

The Forward Multiplicity Detector is a silicon strip detector divided in five modules surrounding the beam pipe and placed at distances between 42 and 225 cm on both sides of the interaction point. It is designed to measure charged particle multiplicity in the forward and backward rapidity regions and it covers a pseudorapidity range $-1.7 < \eta < -3.4$ and $1.7 < \eta < 5.0$ and full azimuth. Together with SPD it allows the measurement of charged particle multiplicity measurements in a wide η range.

PMD

The Photon Multiplicity Detector (PMD) measures the multiplicity and the spatial distribution of photons in the forward rapidity region ($2.3 < \eta < 3.7$) to provide estimation of the collision reaction plane event-by-event. The large particle density that is possible to have in the forward region makes difficult to use calorimeter technique to determine this multiplicity. The PMD is hence a pre-shower detector. A $3X_0$ thick converter is placed between two planes of gas proportional counters. The first plane is used as charge particle veto, while the second is used for photon identification.

T0

The T0 detector is used to determine the time at which the collision occurs, used as the starting time for the TOF detector. It is also used as trigger detector and for on-line luminosity monitoring purposes. It is made of two arrays of 12 Cherenkov counters. The arrays are placed on both sides of the interaction point, at 72.7 cm on the C side (T0-C) and at 375 cm on the A-side[1] (T0-A). The rapidity coverage of the T0-C detector is $-3.28 < \eta < -2.97$ while the T0-A coverage is $4.61 < \eta < 4.92$. The time resolution of the T0 detector is 50 ps and it can determine the interaction vertex with a resolution of 1.5 cm. It can also estimate particle multiplicity providing a centrality determination for Pb-Pb collisions.

VZERO

The VZERO detector is a small angle detector designed to provide the centrality information in Pb-Pb collisions by measuring the charged particle multiplicity in the forward rapidity region. It is also used, altogether with the timing information of the collision, for the rejection of beam-gas interactions and it is possible to use it to have a determination if the event plane.

[1] The A and C sides are used to define ALICE geometry. The A-side is the side closer to ATLAS detector and corresponds to positive values of the z coordinate, while C-side is closer to CMS detector and corresponds to negative z. To better orient, the muon spectrometer is on the C-side.

Being a fast detector, the VZERO is used for the proton-proton and Pb-Pb minimum bias triggers, and for the centrality trigger in Pb-Pb collisions. It consists of two arrays of scintillators counters placed on both sides of the interaction point, at 90 cm on the C-side and 340 cm on the A-side, covering a rapidity region of $2.8 < \eta < 5.1$ (V0A) and $-3.7 < \eta < -1.7$ (V0C). Each array consists of 32 individual scintillators distributed in four rings.

ZDC

Another detector, besides VZERO, TPC and FMD that can be used to perform centrality determination is the Zero Degree Calorimeter, that measures the energy carried by the spectator nucleons. The ZDC can also give an estimate of the reaction plane in nucleus-nucleus collisions and it is very important to reject parasitic collisions both in pp and Pb–Pb. The ZDC consists of two pairs of calorimeters, each one is placed about 116 m from the interaction point on the two sides of the vacuum tube. Each pair is made of one neutron calorimeter (ZN) and one proton calorimeter (ZP) to measure deflected spectator protons. They are placed on different sides of the vaccum tube in order to use the nucleons deflection driven by the beam magentic fields. Fragments with a charge to mass ration similar to the one of the beam are carried away with the beam and can not be detected by the ZDC. The ZN and ZP are installed on lifting platform, so that they can be displaced when they are not in use in order to preserve them from high levels of radiations. The ZDC are made of heavy materials, tungsten for neutrons and brass for protons, and quartz fibres for the detection of the Cherenkov light emitted y charged particles in the hadronic shower. Quartz was chosen for the higher radiation damage resistance with respect to traditional scintillators materials: during Pb-Pb operations, the estimated daily dose for the ZDCs is in the order of 100 Gy. The ZDC is complemented by two electromagnetic calorimeters (ZEM) placed at 7 m from the interaction point on the A side which allow to resolve ambiguities in the determination of the centrality due to the unknown number of fragments which have not been detected by the ZN and ZP. The ZEM is made of lead and quartz-fibres.

2.3 ALICE trigger and data acquisition system

2.3.1 Central Trigger Processor

The trigger signals from the detectors are collected and managed by the ALICE Central Trigger Processor (CTP), designed to select events having a variety of different features and rates and to manage these rates with bandwidth requirements of the Data AcQuisition system (DAQ). It also has to deal with signals from many different detectors which are busy for widely different periods following a valid trigger. The first trigger signal, called

Level 0 (L0) and made of 24 L0 inputs, arrives 1.2μs after the collision. The L0 signals from the fastest detectors, such as the SPD, VZERO, T0 and the muon trigger, are treated with a three states logic (asserted, not relevant, negated) and combined to select the desired class of events, which is defined by the logical combination of the triggers and by the detectors required in the readout (detector clusters). The information from the detectors that are not fast enough to be collected by the L0 trigger is used to create a Level 1 trigger signal (L1) that is dispatched after 6.5 μs. The ALICE trigger system has implemented a past-future protection that looks for other events of requested types in a time window around the collision under investigation: this helps the rejection of pile-up events in the TPC and the good read out of the detectors. To grant enough time for the past-future protection to work, the last level of trigger, Level 2 (L2), waits for the past-future protection and its signal is dispatched after 88μs from the collision that is the maximum drift time in the TPC detector. The CTP data are stored both in the raw data stream and in dedicated scalers and it is possible to keep track of the number of events passing each stage of the trigger (L0, L1, L2).

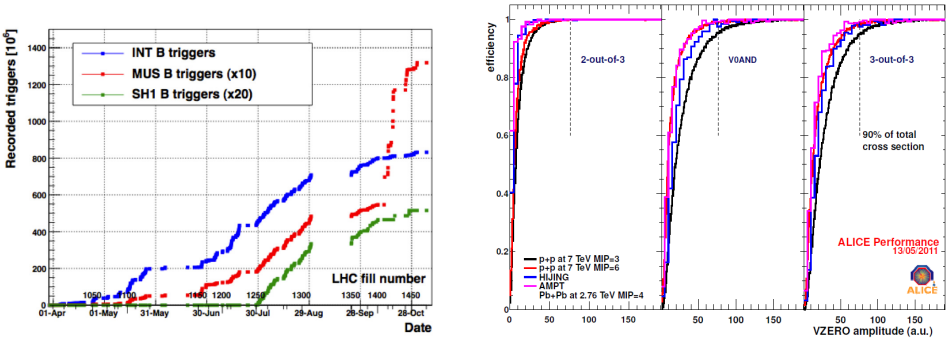

Figure 2.11: Left: Total number of triggered events for minimum bias (blue), muon (red) and high-multiplicity (green) p-p collisions for the 2010 data taking. Muon (high-multiplicity) is multiplied by a factor 10 (20). Right: trigger efficiencies for the VZERO-OR (left), VZERO-AND (middle) and VZERO-A AND VZERO-C AND SPD (right) configurations in 2010 Pb-Pb data taking.

In p-p 2010 data taking, the ALICE minimum bias trigger was defined by the presence of at least one hit in either of the two VZERO sides, or by one fired fast-or chip of the SPD. Starting from August 2010 also an high multiplicity trigger was introduced. In this case the signal trigger was given by at least 65 fast-or chips fired in the SPD outer layer. In parallel with the minimum bias trigger, a muon trigger based on the presence of signal in at least one of the muon trigger chambers was running. At the beginning of 2010 Pb-Pb data taking, the minimum bias trigger was defined in

the same way as p-p minimum bias trigger to avoid any risk of rejection of ultra-peripheral events. Then, to reduce the fraction of background from electromagnetic processes, the trigger condition was tightened to require at least two signals out of the three triggering detectors (VZERO-A, VZERO-C and SPD). In the last part of the data taking, an AND logic among the two sides of the VZERO scintillators (called VZERO-AND) was the requirement for the minimum-bias trigger. The total number of p-p triggered events and Pb-Pb trigger efficiencies for 2010 data taking are shown in figure 2.11. The trigger efficiency in Pb-Pb collisions was studied applying the Pb–Pb trigger selection to the p-p data, under the assumption that the p-p minimum bias trigger is totally efficient after beam background rejection, and then compared to MonteCarlo simulations. The overall selection efficiencies ranges between 97% to 99% with a 100% purity in all but the most peripheral events.

2.3.2 Data AcQuisiton system

The ALICE DAQ system must cope with extremely challenging conditions: on one hand the large interaction rate in proton-proton collisions with a relatively small event size and on the other hand the smaller Pb-Pb collision rate but a huge amount of data, up to 4 GB/s. Its design has been also driven by the requirement of sharing the resources between different clusters of detectors: these clusters are set up to study different observables that have different cross sections and, consequently, different trigger rates. Once the CTP has decided to acquire a particular event, the trigger signal is dispatched to the front-end read-out electronics (FERO) of the involved detectors. The data are then injected in the Detector Data Link (DDL, an ALICE-standard, in ALICE there are more than 450 optical DDLs) and sent to a farm of computers, called Local Data Concentrators (LDC), that do sub-event building from the event fragments they receive from the front-end electronics. The sub-events are than shipped through an event building network to the Global Data Collectors (GDC) that take all the sub-events from the various LDCs and build the full event and, depending on the High Level Trigger decision, send it to the storage facilities.

2.3.3 High Level Trigger

The rate of data collected by the different ALICE detectors can reach the impressive amount of 25 GB/s for central Pb-Pb collisions, where the data size of the single event can top 70 MB. The bandwidth of the DAQ system is limited to 4 GB/s. The High Level Trigger (HLT) is responsible of the acceptance or rejection of an event on the basis of an online analysis and, in case of positive decision, compress the amount of collected data (without any loss of physical information) using specific algorithms in order to reduce

the data rate to a value acceptable by the DAQ and by the storage elements. The High Level Trigger collects raw data from the LDCs, performs a local pattern recognition and fast tracking, as well as primary vertex localization, and builds up the global event. The trigger decision, the Event Summary Data of the event and the compressed data are then sent back to the DAQ via the HLT DDL output. In order to perform all these calculations on a short time scale the HLT relies on a farm of 1000 multi-processor computers.

2.4 ALICE computing framework

2.4.1 Alice Offline Framework

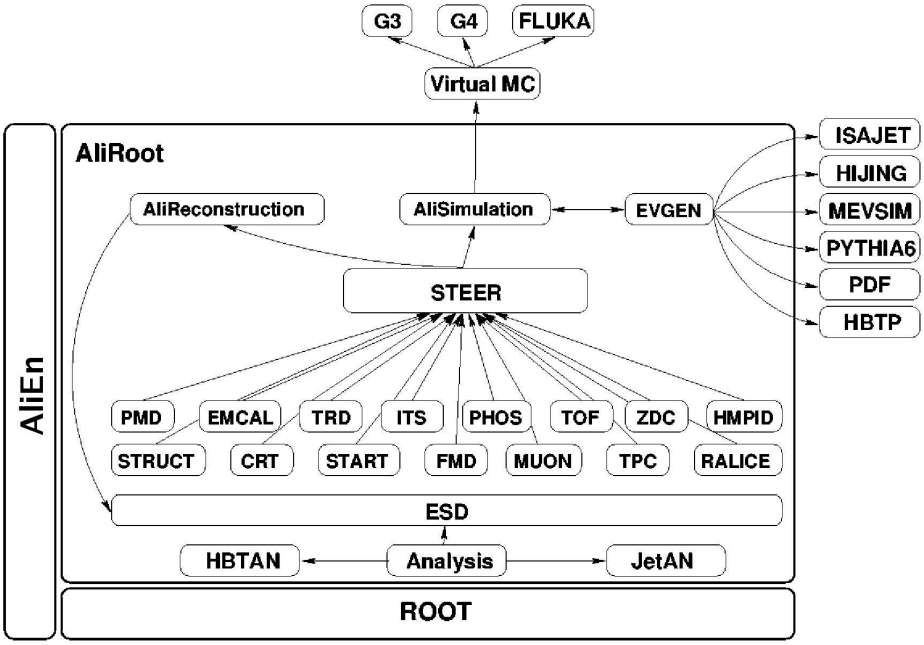

Figure 2.12: Representation of AliRoot framework

The development of the ALICE offline framework, AliRoot [59], started in 1998. This framework is completely developed using Object Oriented technologies and it is entirely written in C++. As described in figure 2.12, the AliRoot architecture is based on the ROOT framework [60] and it is designed to be modular. The STEER module provides steering, run management, interface classes and base classes. The detector code is divided in independent modules and provides code for the simulation and the reconstruction of the events. The analysis code is continuously developed and progressively added to the framework. A detailed and up-to-date description of detector conditions, shape, alignment and structures on a run-by-run basis

(Offline Calibrations DataBase, OCDB) is also part of the offline framework. AliRoot is designed to easily interface with external MonteCarlo modules for the event generation and the particle transport through the detector geometry. The MonteCarlo generator used in the collaboration are mainly PYTHIA [61], HIJING [62] and PHOJET [63] while the transport code used to simulate interactions with the material are GEANT3 [64], GEANT4 [65] and FLUKA [66].

2.4.2 The Grid

ALICE recorded on tape 1.8 PB of data in 2010 and about 2 PB in 2011 [67]. As it is not possible to concentrate all the computing resources needed to store and analyze such a huge amount of data, they have to be distributed around the countries of the ALICE collaboration. More than 60 computing centres in 20 different countries contribute to the ALICE computing resources. All these computing centres must deal with very different kind of analysis tasks sent by a large number of different users. In addition to this, as the local resources are administrated by the single computing centre, they can be organised using a large variety of technologies. To build a tool flexible enough to answer all these demands, the Grid computing project was started in 2000. The ALICE production ENvironment (AliEn) interface [67] provides the tools to access Grid data and computing resources via the offline framework.

All the LHC experiments are member of an international program coordinated by the Worldwide LHC Computing Grid (WLCG). This infrastructure, based on the MONARC model, is hierarchical and its levels are called Tiers. Data from the experiments are stored at the CERN computing centre, the Tier 0. Data are then replicated in regional large computing centres, that are the Tier 1 level. Tier 1 centres also participate in storage and reconstruction of MonteCarlo data. Large computing facilities at universities or other instutions compose the Tier 2 level. They do not have storage capabilities but contribute significantly to the computing power needed by the users to analyze data and participate in MonteCarlo productions, up to 50% of the total computing power out of CERN for ALICE for example, and can be shared among experiments. The coordination between all these different facilities is possible thanks to the Grid middleware. Through the AliEn User Interface (UI) the user can interact with the Grid, access and store files, send analysis tasks or simulations (jobs) and monitor their progress. AliEn also provides a global file system for data storage and can manage the job distribution mechanism. When a task is launched on the Grid, AliEn takes care of copying the necessary files and loading the required libraries to the Working Nodes (WN), that are the machines where the program can run. During the program execution these machines access to the Storage Elements (SE), which are responsible for the physical data

storage and access.

2.5 Event reconstruction

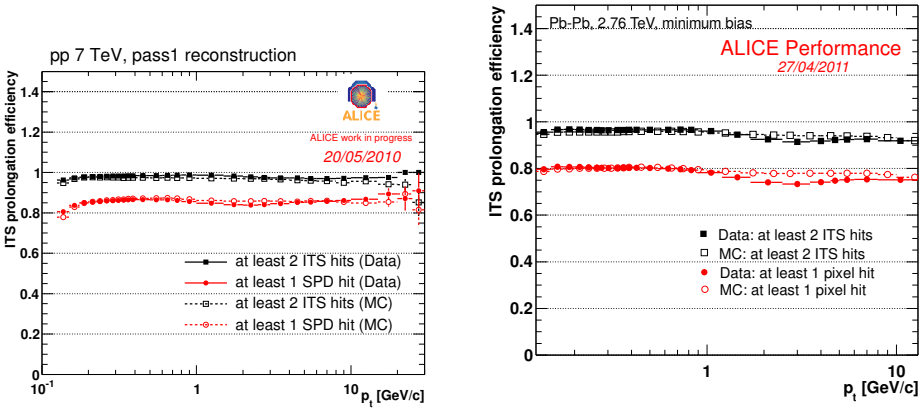

Figure 2.13: TPC to ITS prolongation efficiency in p-p collisions at $\sqrt{s} =$ 7 TeV (left) and Pb-Pb collisions at $\sqrt{s_{NN}} = 2.76$ TeV (right). Data (full symbols) are compared to MonteCarlo simulations (open symbols). The efficiencies are computed requiring two points in the ITS (black) and two points in the ITS out of which at least one in the SPD (red).

When a particle crosses the sensitive area of a detector, it release a signal in it, recorded as a *digit*. The digit is then associated to the information on the physical location of the digit in the detector: these information are the *raw data* of the detector. The raw data are the starting point for the event reconstruction both in real data and MonteCarlo simulations. In the event reconstruction, the physical information of an event is computed from the raw data. At first the information within each detector is rationalized, for example to reduce the random noise, groups of contiguous digits in each detector, which are the results of the signal released by a single crossing particle, are combined in *clusters* (*cluster finding*). The clusters are used to compute tracks coordinates and other observables (such as dE/dx, time-of-flight) that are detector specific. The second step in the reconstruction is to find the position of the primary vertex of the events and to find the particles direction and momentum (*tracking*) and other properties, including also particle identification.

The tracking procedure developed for the ALICE relies on the Kalman filter method [68]. The Kalman filter is used to perform track finding and fitting simultaneously and being a local method allows to extract the optimal estimate of the geometrical parameters of each track point-by-point. For

this reason it is an ideal method when it is needed to prolong tracks from one detector to another, the typical situation we have in the central barrel. The method also takes into account multiple scattering and energy loss. The track reconstruction is a sequential procedure. A first estimation of the primary vertex position is performed using pairs of hits in the SPD (tracklets) and it is used as a starting point for the track finding. The track finding algorithm is ran starting from the hits at the outer radius of the TPC and prolonging the trajectories towards the inside. The outermost TPC pad rows and the primary vertex position are used as seeds. When tracks are prolonged to the inner radius of the TPC, the algorithm is called for the ITS. TPC tracks are matched to points in the outermost SSD layer and then prolonged to inner ITS layers until the first SPD layer. Next step is back propagation and refit of the tracks outward in the ITS and then in the TPC. Once the outer radius of TPC is reached, tracks are prolonged and matched to the TRD at first and then to the other detectors of the central barrel (TOF, HMPID, PHOS, EMCAL) for particle identification. At this point the tracks are again propagated inward down to the ITS and to the primary vertex as computed in the first step. Finally the final position of the primary vertex is computed from the reconstructed tracks to obtain the optimal resolution. The prolongation efficiency from TPC to ITS is shown in

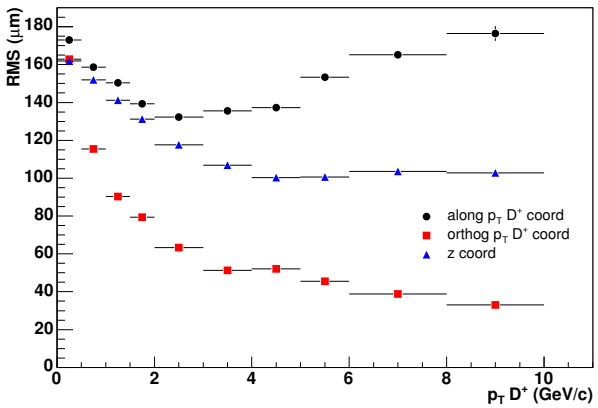

Figure 2.14: Resolution on the D^+ secondary vertex. Black points is the resolution along the direction defined by the D^+ particle transverse momentum, red points is the direction orthogonal to the D^+ p_t in the transverse plane, blue points the resolution along the z axis.

figure 2.13 as a function of the track transverse momentum, for p-p collisions at $\sqrt{s} = 7$ TeV and Pb-Pb collisions at $\sqrt{s_{NN}} = 2.76$ TeV. The efficiency is more than 97% when requiring at least two points in the ITS and 85% when asking two points in the ITS and at least one point in the SPD. This drop can be explained by the presence of dead modules in the SPD. MonteCarlo

simulation reproduces well the data, with a discrepancy smaller than 2% for tracks with $p_t < 10$ GeV/c. The prolongation efficiency has also been studied in Pb-Pb data and the results are compatible with the p-p ones for all centralities. The same procedure can be applied to the reconstruction of secondary vertices, e.g. the D^+ decay vertices. A precise determination of the D^+ decay vertex is of high importance for the $D^+ \to K^-\pi^+\pi^+$ analysis, as many topological cuts we applied to select our candidates depend on it. The resolution on the D^+ secondary vertex is shown in figure 2.14.

The transverse momentum resolution of the global TPC+ITS ALICE tracking reaches 20% for tracks with $p_t \sim 100$ GeV/c, and goes down to $\sim 3\%$ for tracks with $p_t = 10$ GeV/c and to 1% for tracks with $p_t = 1$ GeV/c, as shown in figure 2.15 for Pb-Pb collisions at $\sqrt{s_{NN}} = 2.76$ TeV.

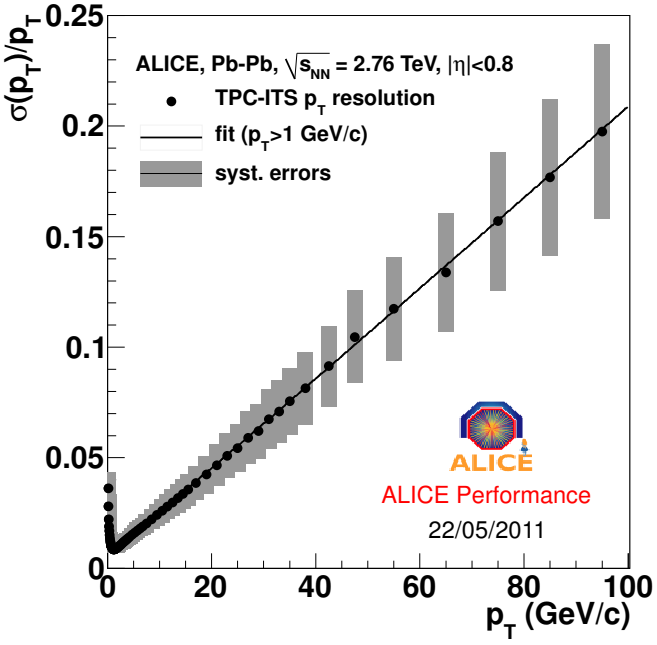

Figure 2.15: Transverse momentum resolution for TPC+ITS combine tracking obtained from covariance matrix in Pb-Pb collisions at $\sqrt{s_{NN}} = 2.76$ TeV.

Thanks to the low material budget and to the fact that the inner SPD layer is close to the vacuum tube, ALICE has the specific feature to have a good resolution on the track impact parameter d_0, defined as the distance of closest approach between the track itself and the primary vertex of the event. The impact parameter resolution was estimated by a three components fit that takes into account the primary vertex resolution, the tracking and the multiple scattering due to the material budget. To compute it primary tracks with one hit in both the SPD layers were used. For each track, its impact parameter was estimated with respect to the primary vertex reconstructed

without using the selected track. The impact parameter resolution includes the convolution of the track position and primary vertex resolution, and it is shown in figure 2.16 for p-p and Pb-Pb collisions and compared to MonteCarlo simulations. The impact parameter resolution in proton-proton collisions is of the order of 60μm for tracks with $p_t \sim 1$ GeV/c, and goes as low as 30μm for tracks with $p_t \sim 10$ GeV/c, and similar results are obtained in heavy ion collisions.

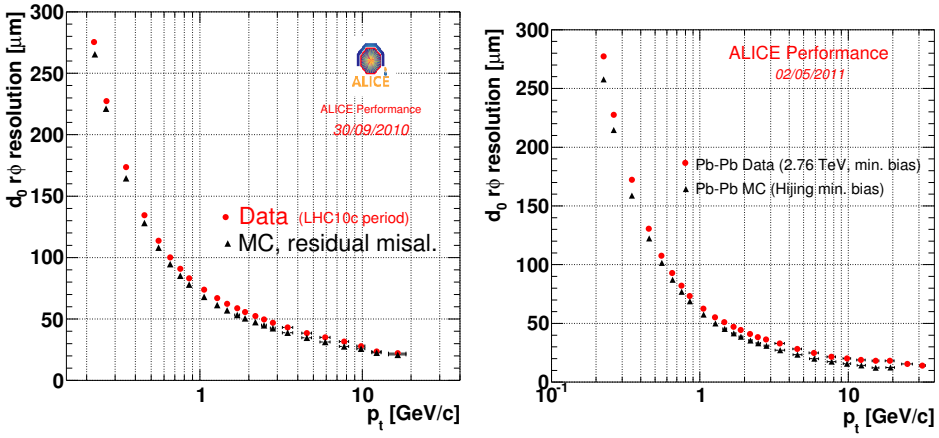

Figure 2.16: ALICE resolution on single tracks impact parameter in data and MC for p–p collisions (left) and Pb–Pb collisions (right).

The output of the reconstruction is stored in the Event Summary Data (ESD), a file containing all the physical informations needed for the analysis both at track and event level plus informations relevant for checking the quality of the reconstruction for each detector. Since the ESD contains more information than what is needed for the analysis, Analysis Object Data have been developed. These files are smaller and can reduce the computational needs of the analysis providing the user with faster access to the data. The production of AOD files from the ESDs is called *filtering*. The AOD files can also contain some first analysis steps, such as the combinatorial of a particular kind of tracks. The details of the filtering for the case of the D meson analysis will be described later in section 3.1.

3

Have a look, it is charm!

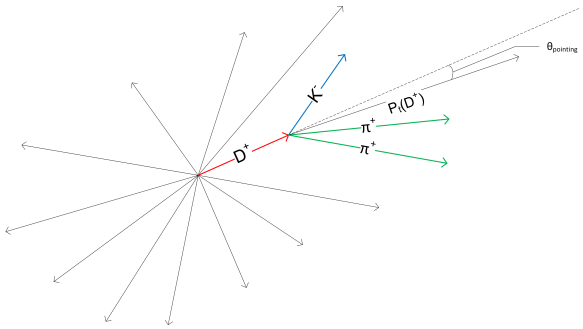

Figure 3.1: Schematic representation of the $D^+ \to K^-\pi^+\pi^+$ decay channel.

As already discussed in section 1.3 open charm is a powerful probe for the properties of Quark Gluon Plasma. ALICE has excellent capabilities for charm studies both in proton-proton and Pb-Pb collisions at the different energy domains explored at the LHC, that in 2010 provided ALICE with proton–proton collisions at $\sqrt{s} = 7$ TeV and $\sqrt{s} = 2.76$ TeV and Pb–Pb collisions at a centre of mass energy $\sqrt{s_{NN}} = 2.76$ TeV.
Open heavy-flavours are studied at ALICE in the mid–rapidity region through semi–leptonic decays [58], with open-charm being also studied through fully reconstructed hadronic decays, which is what will be discussed in this thesis. In its main aspects the analysis strategy based on hadronic decays is common to all the open charm particles studied at ALICE: D^+, D^0, D^*, D_s and Λ_c. These particles are studied using decay topologies that are fully reconstructed in the detector. A list of the decay channels currently studied in ALICE with their main properties is available in table 3.1. For the reconstructed candidates the invariant mass distribution is built and then fitted in the region of the hadron mass value to extract the yields of signal

and background. To improve the fit results, the candidates must pass several analysis cuts. The general cut strategy is based on the maximisation of statistical significance[1], although for certain analyses, especially the elliptic flow, some special effort is done in order to have a high purity in the sample. The open charm measurements at ALICE are performed both in proton–proton and Pb–Pb collisions. The main goal of the D^+ study in proton–proton collision is to extract the charm production cross section in the unexplored energy domain available at the LHC. This measurement provides also an essential reference to explore the QGP properties in Pb-Pb collisions, for example the measurement of the energy loss, described in section 4.2 requires a precise measurement of the D^+ production in proton–proton collisions. In Pb–Pb the main observable under study are the D mesons $R_{\rm AA}$, which is sensitive to the charm energy loss in the medium, and the elliptic flow. Open-charm would also be the best normalization for charmonium studies. Both $R_{\rm AA}$ and elliptic flow were already discussed in section 1.3.
In this chapter a description of the D^+ analysis in proton-proton collisions at $\sqrt{s} = 7$ TeV with ALICE will be given. We will describe in detail the operations performed to measure the D^+ cross–section (3.6) and we will describe the systematics errors affecting this measurement (3.7). Finally, the results obtained in the proton–proton colliding system at $\sqrt{s} = 7$ TeV will be given in section 3.8 and the results obtained will be presented in section 3.8. Although experimental conditions are different, the analysis strategy and most of the analysis software tools are common between proton–proton and Pb–Pb analysis. Whenever possible I will discuss in this chapter also the main strategy of the Pb-Pb collisions analysis, whose results will be presented in the following chapter.
LHC proton–proton program provided ALICE not only with $\sqrt{s} = 7$ TeV collisions but also with a short period of proton-proton collisions at $\sqrt{s} = 2.76$ TeV taken at the beginning of 2011. This run has the special feature that the energy available in the centre of mass is the same as in Pb–Pb collisions. This means that the results of this special run can be used as reference for the Pb–Pb collisions without applying any energy rescaling of the results. Unfortunately the statistics collected at this energy is not enough to use it in the investigation of the D^+ $R_{\rm AA}$, but nevertheless the measurement of the charm production cross–section at this energy is a test for pQCD calculations and the results obtained at this energy provide a precious cross–check for the energy rescaling procedure applied to the results obtained in the $\sqrt{s} = 7$ TeV collisions that is described in chapter 4. The results for the $\sqrt{s} = 2.76$ TeV run are described in section 3.8.1 at the end of this chapter.

[1] statistical significance: the ratio between signal and the square root of signal plus background. $S = \frac{s}{\sqrt{s+b}}$

Meson	Decay channel	$c\tau$	BR
D^0	$D^0 \to K^-\pi^+$	$(122.9 \pm 0.5)\mu m$	$(3.87 \pm 0.05)\%$
D^0	$D^0 \to K\pi\pi\pi$	$(122.9 \pm 0.5)\mu m$	$(8.07^{+0.21}_{-0.19})\%$
D^+	$D^+ \to K^-\pi^+\pi^+$	$(311.8 \pm 2.1)\mu m$	$(9.13 \pm 0.19)\%$
D_s^+	$D_s^+ \to K^+K^-\pi^+$	$(149.9 \pm 2.1)\mu m$	$(5.49 \pm 0.27)\%$
D^{*+}	$D^{*+} \to D^0\pi^+$		$(67.7 \pm 0.5)\%$
Λ_c	$\Lambda_c \to pK^-\pi^+$	$(59.9 \pm 2.8)\mu m$	$(5.0 \pm 1.3)\%$

Table 3.1: D meson hadronic topologies under study at ALICE. Life time $c\tau$ and branching ratios (BR) are from [3]

3.1 Event reconstruction and filtering, from ESDs to AODs

The first step of the track reconstruction procedure in the ALICE central barrel detectors starts with the determination of the position of the primary vertex of the proton-proton or Pb-Pb collision, done by correlating hit pairs (tracklets) in the two layers of the SPD. As those are also the ITS innermost layers, they provide most of the resolution on the vertex position. In proton-proton collisions, if there are tracklets that do not point to the found primary vertex, the same algorithm is used to search for vertices from pile–up collisions. An event is rejected due to pile-up if a second interaction vertex is found with at least 3 associated tracklets and separated from the first one by more than 8 mm. The remaining undetected pile–up, estimated from MonteCarlo simulation and beam characteristics, is negligible. The fraction of pile–up events recorded is shown in figure 3.2. As discussed in section 2.5, once the primary vertex of the event has been reconstructed, it is used to reconstruct tracks, with a Kalman filter method [68]. Tracks are built starting from the points on the outer pad of the TPC and prolonged towards this first estimate of the interaction vertex position, using also informations from the space points in the TPC and then hits in the six layers of the ITS. The resulting tracks are then propagated outward in order to associate signals in the large-radius detectors that perform particle identification (mainly the TOF for what concerns the analysis under discussion here). Finally, all tracks are propagated again with the Kalman filter in the inward direction. The relative p_t resolution at the primary vertex for this procedure is about 1%. The last step of the event reconstruction is the re–determination of the primary vertex position from the accepted tracks [69]. The primary vertex coordinates and covariance matrix are obtained via χ^2 minimisation applied to the tracks approximated by straight lines after propagation to their common point of closest approach. The algorithm is then repeated excluding the tracks that are incompatible with the assumption of being produced by

primary particles to reconstruct secondary vertices. The primary vertex position in the transverse plane is constrained by the position and spread of the luminous region, determined from the distribution of primary vertexes averaged over the run and stored in the database of experimental conditions run-by-run during the full data-taking period. The resolution on the position of the primary vertex reconstructed from tracks depends on the number of tracklets $N_{\rm tracklets}$ measured in the collision. In proton-proton collisions it was measured to be $\sigma_z(\mu m) \sim 430/N^{0.7}_{\rm tracklets}$ in the longitudinal direction and $\sigma_{xy}(\mu m) \sim min(\sigma^{\rm luminous}_{xy}, 600/N^{0.9}_{\rm tracklets})$ in the transverse coordinates by fitting its dependence on the number of tracklets in the SPD. The spread of the luminous region was measured by the distribution of the reconstructed interaction vertexes and it was found to be $\sigma^{\rm luminous}_{xy} \sim 35 - 50\mu$m in the transverse plane and $\sigma^{\rm luminous}_{z} \sim 4 - 6$cm along the longitudinal direction for p–p collisions and of $50 - 60\mu$m in the transverse plane and of about 6 cm in the longitudinal direction in during the Pb–Pb data taking. Taking those values into account the transverse position of the vertex in proton–proton collisions has a resolution that ranges from 40 μm in events with less than 10 charged particles per unit of rapidity to about 10 μm in events with a multiplicity of about 40.

In the ALICE computing framework [70] the output of the event reconstruction, which includes global event observables, tracks, vertices, response of PID detectors and calorimeters, and information relevant for checking the quality of the reconstruction for each detector are stored in an object called Event Summary Data (ESD). The amount of data can be reduced using a *filtering* procedure, that performs a selection of the data that are needed for the analyses and compacts them in a smaller object, the Analysis Object Data (AOD). While filtering the ESDs files, it is possible to perform some preliminary analysis steps, in order not to have to perform such steps at the analysis level and save CPU time. For the D^+ analysis the three tracks combinatorial is performed while filtering the ESDs files. This analysis-specific output is stored in a special AOD object called *delta AOD*. When building the D meson combinatorial some cuts are applied on the track quality and on the candidates that are built, in order to keep the size of the data, the CPU time required by the filtering and the number of combinations at a level to which the final analysis can be performed fast on the ALICE computing resources. As the combinations rejected in this process will not be anymore available for the analysis, this is a delicate task and there was a carefully tuning of the cuts applied in the filtering (that will be equivalently referred to as production cuts or filtering cuts in the following sections) in order to be sure that the smallest amount of signal was rejected in this procedure and that this selection does not bias our sample. Different analyses may need different cuts when producing the AODs. For each period of data taking

Variable	cut
Invariant Mass [GeV]	0.2
$\mathrm{dist}_{1\text{-}2}$	0.01
σ_{vertex}	0.06
Dec. len.	0.02
$\cos\theta_{point}$	0.85

Table 3.2: Production cut values on the D^+ candidate triplets

and for each MonteCarlo simulation it is therefore possible to have different *AOD productions* made with different configurations of the filtering. In the D^+ analysis we used minimum bias MonteCarlo productions but also productions enriched charm and beauty contents to study the cut efficiencies and the B feed-down. In the Pb-Pb analysis it was made an AOD production for the non-central events only in order to allow for looser filtering cuts. If not explicitly said, then the production used are the proton–proton and Pb–Pb data and MonteCarlo simulations without any special correction.

A vertexing procedure has to be used also to reconstruct the secondary vertices of D^+ candidates to be stored in the delta AOD. These were reconstructed using combinations of tracks having $|\eta| < 0.8$; $p_t > 0.4$ GeV/c for p–p collisions; $p_t > 0.8$ GeV/c for Pb–Pb central collisions or $p_t > 0.5$ GeV/c for non–central Pb–Pb collisions (more details on this requirement will be available in section 4.3); at least 70 associated space points (out of a maximum of 159) and $\chi^2/\mathrm{ndf} < 2$ in the TPC, and at least one hit in either of the two layers of the SPD (or at least 2 hits in the ITS and one hit in the SPD for Pb–Pb collisions). The combination of tracks built from the tracks passing the basic cuts just discussed, with their associated decay vertex, still have to pass very loose selection on the decay topologies that are meant to find a compromise between CPU time, AOD size and the need to keep as much signal as possible. As D^+ are not the only 3–prongs decay channel under study in ALICE (D_s^+ and Λ_c are also analysed) the information whether the triplet passed the D^+ cuts or it was more likely a different candidate is stored. Looping only over the interesting candidates speeds up the following analysis significantly. The selection of the candidates in the filtering is based on the invariant mass difference between the candidate and the D^+ PDG [3] mass value, the tracks $\mathrm{p_t}$, the dispersion of the tracks around the secondary vertex (σ_{vertex}), the distance of closest approach among a pair of decay tracks ($\mathrm{dist}_{1\text{-}2}$), the candidate decay length and the angle between the D^+ meson flight line and its momentum. These cuts will be discussed in detailed in section 3.3. The values of these topological cuts applied in the filtering are listed in table 3.2.

We can provide some examples to give an idea of the effect of the track

rejection at the filtering level. Assuming that in a large enough event the number of positively charged tracks is more or less the same as the amount of negatively charged tracks ($n^+ \sim n^- \sim \frac{n}{2}$) then we can expect a number of combinatorial three–prong decay candidates of about $2 \times \frac{(n/2)!}{2!(n/2-2)!}\frac{n}{2}$, with the factor 2 coming from the fact that we want to keep both D^+ and D^- particles. In proton–proton collisions at $\sqrt{s} = 7$ TeV events with as much as 400 tracks have been observed, but out of the about 8 millions expected combinations for such events less then one thousand survives the selection applied at the filtering level. In central Pb–Pb collisions the effect is much stronger. The bulk of central events (0-10% centrality class, for the definition of the centrality see chapter 4) have about 9500 tracks but again the number of surviving combinations is around one thousand while even in the largest events, with 14000 tracks or more, the number of three–prong combinations rarely reaches 1000.

3.2 Data Quality

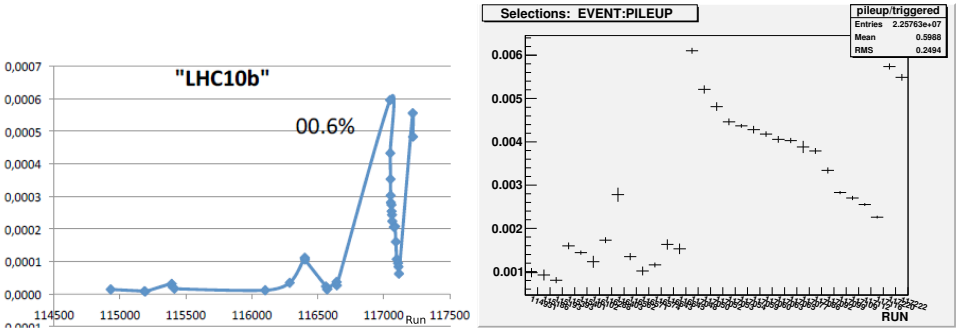

Figure 3.2: Evolution with respecto to the run number of the fraction of pileup events over triggered events during the first month of 2010 p–p data taking at $\sqrt{s} = 7$ TeV (right) compared to the pileup probability (left).

The data taking at ALICE is divided in *runs*. Each run corresponds to a period of data taking lasting a few hours and in principle in each run the experimental conditions might be different, for example the temperature in the experimental hall might be different, or some detector configurations could have been modified. Some of the runs are already discarded before we even analyse them in the quality assurance checks. The runs of each month of data taking are grouped into periods. The data used in this analysis were collected in the periods LHC10b, LCH10c, LHC10d and LHC10e, corresponding roughly to April, May, July and August 2010 for the proton-proton data taking and the period LHC10h, corresponding to November, 2010 for the Pb-Pb data taking. An important cross–check on the quality of

the data is to control that the basic properties of the events do not depend on the run, or if they do, that the effect is known and understood. To do so, when analysing our data samples, some basic quantities are stored in a class called *AliNormalizationCounter* as a function of the run number. Even if its main usage is to compute the number of events we need to use to normalise the charm cross section (see 3.6, where this procedure is explained in details) this class also stores information about basic properties of the events, such as the presence of at least a track passing a standard sets of requirements (*candle*) or the number of D^+ candidates per event. We can then measure the stability of these quantities as a function of the run number. As an example, figure 3.2 shows the fraction of pile-up events during the LHC10b period, and in figure 3.3 is shown the number of D^+ candidates for events.

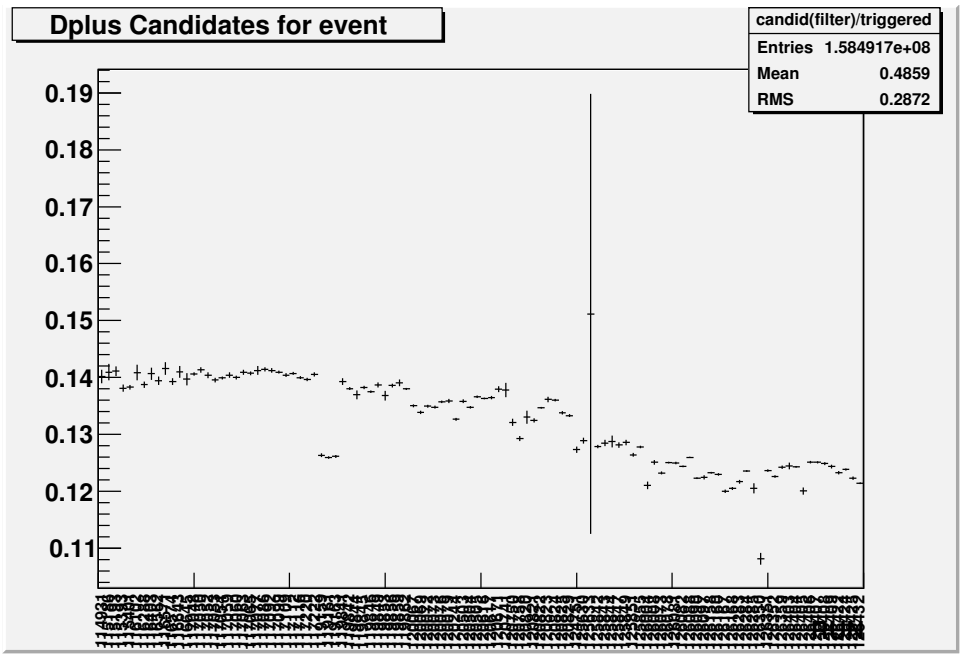

Figure 3.3: Evolution of the number of candidates for p–p minimum bias event for the first three months of 2010 data taking at $\sqrt{s} = 7$ TeV. Changes in the slope are compatible with the evolution of the SPD efficiency.

Another control of the data quality, a Quality Assurance (QA) step dedicated to D meson candidates and performed on the AOD and Delta AOD files, is done on the whole set of data measured and is meant to spot problems in the reconstruction of the events or some issues with detector configuration. This analysis controls the distribution of several variables and the performance of the main detectors related to D^+ analysis: ITS, TPC and TOF. Some quantities kept under control among the others are the number

of clusters in each ITS layer; the energy loss distribution in the TPC and the time of flight distribution measured by the TOF; the centrality distribution of the events in Pb–Pb collisions; the number of reconstructed tracks as a function of the centrality of the events; the distribution of the tracks impact parameters.

3.3 Analysis Strategy

The D^+ meson is studied at ALICE in its hadronic decay channel $D^+ \rightarrow K^-\pi^+\pi^+$. All the daughter particles created in this decay channel can be reconstructed in the ALICE central barrel, and therefore the strategy is to extract the signal yield by fitting the invariant mass distribution of the reconstructed candidates with proper charge sign combinations. This is done by fitting first the distribution in the side bands to estimate the background contribution and in the full available mass range $[1.669, 2.069]$ GeV/c^2 in order to quantify the amount of signal candidates available in our data. The side bands are the invariant mass region where we expect only background to be present, and are defined as the region more than four times the signal distribution standard variance away from the signal peak. For the first iteration, where no information on the signal is available, the D^+ mass from the PDG [3] is assumed as central value, and the invariant mass ranges of the side bands are $[1.669, 1.717]$ GeV/c^2 for the low mass side band and $[1.917, 2.069]$ GeV/c^2 for the high mass side band. To fit the invariant mass distribution of the candidates, an exponential shape is assumed for the background distribution, while the signal is assumed to be described by a Gaussian shape. To perform the fit, the parameters of the exponential are obtained fitting the invariant mass distribution in the side bands region, and then performing a fit minimising the χ^2 function in the full region. The number of signal and background candidates is then obtained integrating the background and the signal in the mass region with a width of 3σ around the mean of the gaussian peak, σ being the gaussian width of the signal from the fit. Several cross–checks have been made to address possible systematics arising from the assumptions on the background shape and on the fitting technique. They will be explained in detail in section 3.7.
Being a 3–body decay the channel $D^+ \rightarrow K^-\pi^+\pi^+$ is affected by a huge combinatorial background that needs to be reduced with a careful setting of the selection cuts applied to the reconstructed topologies in order to have a visible peak in the invariant mass distribution. Some features of this decay channel can help improving the selection: for example the large decay length of $\sim 310\mu$m and the information that the kaon is always opposite sign with respect to the mother D^+. This information turns out to be extremely powerful when combined with the very good performances of ALICE PID allowing an effective background rejection. The topological cuts applied to

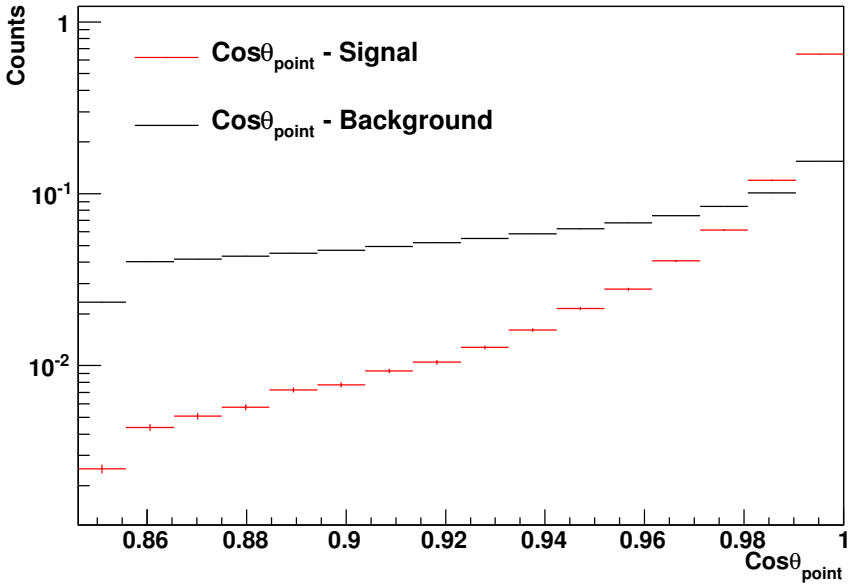

Figure 3.4: p_t integrated distribution of $\cos\theta_{\rm point}$ for signal (red) and background (black) candidates in MonteCarlo simulations of proton-proton collisions at $\sqrt{s} = 7$ TeV.

the D^+ candidates are summarised in table 3.4. Two of the most important cuts we apply are the cuts on the *pointing angle* and on the tracks impact parameter, defined as the distance of closest approach between the track itself and the primary vertex of the event in the $r\phi$ plane. The cut on the pointing angle, sketched in figure 3.1 is based on the fact that for signal candidates the D^+ reconstructed momentum should point to the primary vertex of the event. The cut is done on the cosine of the angle $\theta_{\rm point}$ between the D^+ meson flight line and the line passing through the primary and decay vertex. For signal candidates the distribution of $\cos\theta_{\rm point}$ is peaked at 1, while the distribution of background is flatter. A comparison among these two distributions is shown in figure 3.4. In the D^+ analysis in proton-proton collisions the cut on the track impact parameter is not applied at the single track level. Although this cut proves to be extremely important for two prong decay channels (e.g. the D^0), the presence of a third daughter makes this cut difficult to apply to the D^+. As an example, about 20-25% (estimated from MonteCarlo simulations) of D^+ signal candidates at low p_t have an impact parameter $|d_0| < 100\mu$m. During the filtering of Pb-Pb events a cut on the tracks impact parameter of $|d_0| > 100\mu$m is applied to tracks with $p_t > 2$ GeV/c. A detailed description of the cut variables is following.

Invariant mass This cut selects the mass window where the analysis is performed. The typical width of the D^+ mass peak is around 0.012 GeV/c^2 while the default mass windows used is of 0.4 GeV/c^2 centered on the the D^+ mass from the PDG. This width is large enough to allow us to use side bands to fit the background.

p_t^K It is the cut on the minimum p_t of the daughter track with opposite charge with respect to the candidate D. In the decay channel considered the opposite sign daughter is always a kaon for signal candidates.

p_t^π It is the cut on the minimum p_t of the two daughter tracks with the same charge as the candidate.

d_0^k Cut on the minimum impact parameter in the $r\phi$ plane with respect to the primary vertex of the daughter with opposite charge sign with respect to the D^+ candidate.

d_0^π Cut on the minimum impact parameter in the $r\phi$ plane with respect to the primary vertex of the daughters with same charge sign as the D^+ candidate. In the current analyses this cut has the same value as the cut on d_0^k.

$\text{dist}_{1\text{-}2}$ Cut on the distance between the reconstructed vertex of two of the three daughters and the primary vertex.

σ_{vertex} Cut on the dispersion of the tracks around the secondary (decay) vertex. In principle, for signal candidates, all the daughters are coming from the same vertex this dispersion should be close to 0. In realistic conditions this value is determined by the resolution that we have on the tracking so the distribution of σ_{vertex} is peaked at values close to 0, while the background, as visible in figure 3.5, has a broader distribution peaked at larger values.

DCA Cut on the maximum Distance of Closest Approach between each pair of decay tracks.

Decay length Cut on the distance between the primary vertex of the event and the decay vertex of the D^+. The D^+ has a $c\tau \sim 310\mu m$, so this cut is one of the most effective to separate background from signal. As particles at high p_t are also affected by a significant Lorentz boost, the value of this cut can reach values as high as 0.19 cm.

p_t^{max} Cut on the minimum value of p_t of the daughter with the highest p_t.

$\cos\theta_{point}$ Cut on the cosine of the pointing angle. Defining the flight line of the D^+ as the line passing through both the primary and the decay vertex, the pointing angle is the angle between the reconstructed D^+

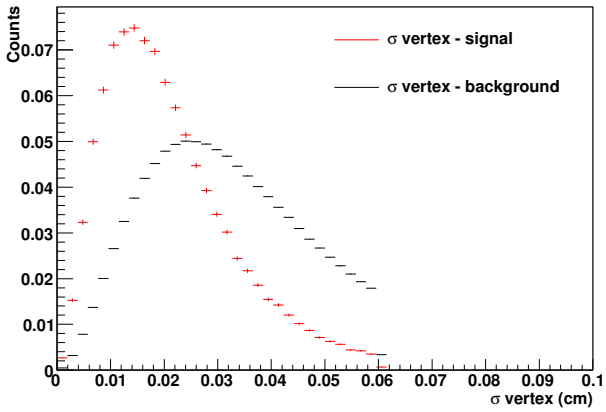

Figure 3.5: p_t integrated distribution of σ_{vertex} for signal and background candidates in MonteCarlo simulations of proton-proton collisions at $\sqrt{s}$ = 7 TeV.

momentum and the flight line. Figure 3.1 shows a graphical example of this variable. For signal candidates the two lines should be close and therefore $\cos\theta_{point} \sim 1$.

$\sum d_0^2$ Cut on the sum of the squared impact parameters of the decay tracks as defined before. Even if the impact parameter of the single track can be misleading due to the topology of the decay, their sum proved to be a much more useful cut.

Decay length XY It is a cut on the decay length in the transverse plane normalized to its error, i.e. a cut on the minimum distance between the primary and the secondary vertices in the the transverse plane. This cut was introduced to help the Pb–Pb analysis and it will be explained in detail in section 4.1.2.

$\cos\theta_{point}^{XY}$ Cut on cosine of the pointing angle in the transverse plane. This cut was introduced to help the Pb–Pb analysis and it will be explained in detail in section 4.1.2.

The 2010 data analysis is performed on minimum bias events both for what concerns proton–proton and Pb–Pb data. In proton–proton collisions the minimum bias trigger is defined by the requirement of registering at least one hit in either the VZERO counters[2] or in the SPD in coincidence with the arrival of the proton bunches from both sides of the interaction region. This trigger configuration is estimated to be sensitive to about $\approx$ 87% of

[2]As a general notation, the presence of a hit in either the VZERO scintillators is called VZEROOR, while the presence of hits in both VZERO sides is called VZEROAND

the p–p inelastic cross section and it was verified using the PYTHIA Monte-Carlo generator that the minimum bias trigger is 100% sensitive for events containing D mesons with $p_t > 1$ GeV/c and $|y| < 0.5$. To further remove beam induced background at the analysis level, a tighter event selection was applied taking into account the timing of the VZERO scintillators and the correlation between the number of hits and of track segments (*tracklets*) measured in the SPD detector. The ALICE luminosity in proton–proton collisions was limited to $0.6 - 1.2 \times 10^{29}\text{cm}^{-2}\text{s}^{-1}$ by displacing the beams in the transverse plane by about 3.8 times the r.m.s. of the beam profile in the transverse plane. This allowed us to keep the interaction probability below 10% and the pileup probability below 5%. The evolution of the pileup probability for a fraction of the 2010 p–p data taking is shown in figure 3.2 in section (3.2) where the data quality is discussed. Only events in the range $|z_{\text{vertex}}| < 10$ cm from the centre of the barrel are kept for the analysis. In total about 314 millions p–p events passed the selection criteria.

In the first period of Pb–Pb data taking the minimum bias events were triggered by the presence of signal in at least two detectors out of SPD, VZERO-A and VZERO-C. In the second part of the data taking coincidence between the VZERO signals was required to trigger an event. The offline event selection was based on the timings of the VZERO and neutron ZDC detectors. Again, events with $|z_{\text{vertex}}| > 10$ cm were rejected from the analysis, but no pileup rejection was applied on this data sample. A total of 17 millions Pb–Pb events passed these selection criteria. Pb–Pb events are classified according to their centrality. The details of the centrality selection will be discussed in chapter 4.

3.3.1 PID

Particle IDentification (PID) plays an important role in background rejection. The two ALICE detectors used for particle identification in the $\text{D}^+ \to \text{K}^-\pi^+\pi^+$ analysis are the TPC and TOF (we gave a short description of these detectors in chapter 2). The signal in the TPC is given by the energy loss suffered by the particle while passing through the detector. One can compare the measured dE/dx value with the value of a Bethe-Bloch function that gives the expected energy loss. The Bethe-Bloch function depends on the mass of the particle and the ALEPH functional form was used:

$$\frac{dE}{dx}(m,p) = \left[[1] - \beta^{[3]} - \log\left([2] + \frac{m}{p}^{[4]}\right)\right] \frac{[0]}{\beta^{[3]}} \tag{3.1}$$

The five free parameters [0]...[4] were determined, for each data sample, by a fit to the data. The distribution of the energy loss versus charged particle momentum is shown in figure 3.6. If the particle lies inside a certain amount of σs from the expected mean value of the Bethe-Bloch for the given specie, then we say that the particle is compatible or, if it is very close to the

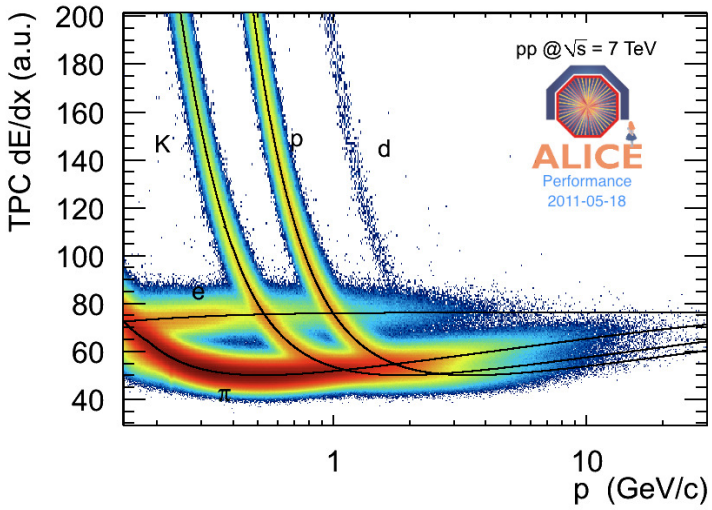

Figure 3.6: dE/dx distribution of charged tracks inside ALICE TPC in p–p collisions at $\sqrt{s} = 7$ TeV. The lines are a parametrisation of the Bethe-Bloch curve

mean value, that is identified as a particle of that specie. The number of σ required for identification, compatibility or exclusion depends on the particle momentum and is reported in table 3.3. The TPC resolution on the particle dE/dx is 5.5% in proton-proton collisions and Pb-Pb peripheral collisions, while decrease to 6.5% in central Pb-Pb collisions as an effect of the larger occupancy in the detector.
The TOF identifies particles from the time they needed to fly from the interaction vertex until the detector. The time of flight is given by the time difference registered between TOF and T0 detectors. A particle is identified in the TOF if the measured time of flight is compatible within 3σ with that expected on the basis of particle momentum and track length for a given mass hypothesis, where σ is the resolution of the TOF (around 160ps in p–p collisions). Figure 3.7 shows particles velocity versus momentum as measured by the TOF.
TPC and TOF results are then combined together. Table 3.3 summarizes the requirements we ask for rejection, compatibility and identification of tracks reconstructed as pions, kaons and protons.
In the $D^+ \to K^-\pi^+\pi^+$ decay channel we can use the information that the kaon has always opposite charge sign with respect to the mother particle. The PID strategy is thus based on the fact that the opposite sign particle must be compatible with a kaon, while the other two daughters must be compatible with pions. The strategy is designed in order to avoid as much as possible any signal rejection. As it is possible to see in figures 3.14a and 3.14b the efficiency of the PID selection for the signal candidates is almost

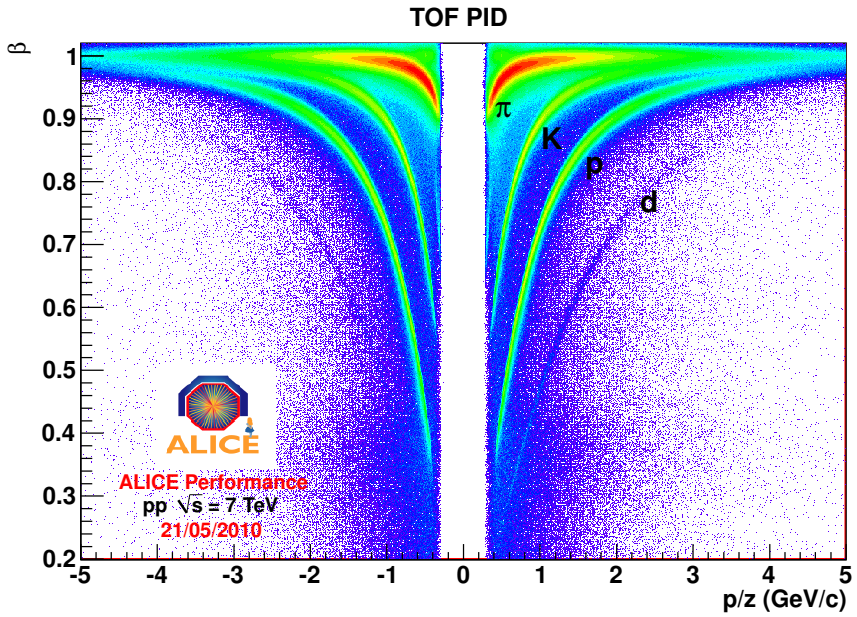

Figure 3.7: velocity of particles reaching TOF versus their momentum in p–p collisions at $\sqrt{s} = 7$ TeV. Different particles species are lines are clearly visible.

1, while in proton-proton collisions about half of the background candidates are rejected by PID selection. This means that we have almost no signal rejection because of the PID. A candidate is rejected when signals in both TPC and TOF are not compatible with the kaon signal for the opposite charged daughter or with the pion signal for the other two daughters. A more tight selection, that asks to positively identify the kaon at low p_t ($p_t^K < 1.5$ GeV/c) has been studied too. A particle is positively identified when it is identified (and not only compatible) as the desired specie, according to the requirements listed in table 3.3. Even if these requirements have proved to be effective in increasing the statistical significance, especially at low p_t, as shown in figure 3.8, the final results we will present in this thesis will be made with the conservative PID approach. This because the application of the strong PID selection results in an increase of the systematic errors on our measurement. For this reason we decided to maintain the conservative approach whenever it was possible to obtain a good statistical significance without asking for stricter PID requirements.

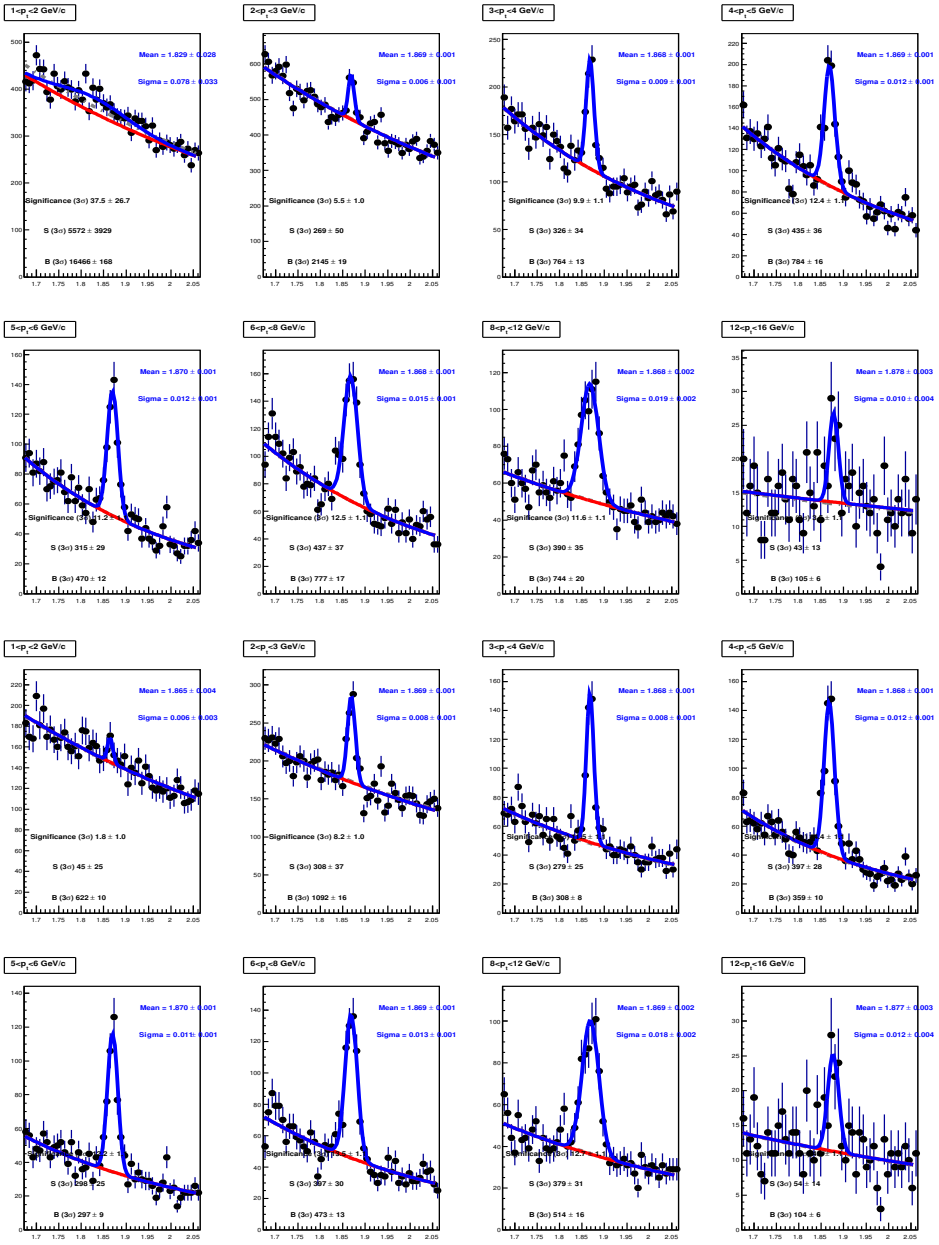

Figure 3.8: The figure shows the effect of asking strong PID requirements. In the two top panels is shown the invariant mass spectra for 252M p–p events ad $\sqrt{s} = 7$ TeV obtained using conservative PID approach. Bottom panels show the invariant mass spectra obtained from the same 252M events asking positive identification for tracks with $p_T < 2$ GeV/c. A not negligible gain in significance is observable in most of the p_t bins.

TPC	$p_t < 0.6 GeV/c$	$0.6 < p_t < 0.8 GeV/c$	$p_t > 0.8 GeV/c$
$< 1\sigma$	IS K/π		K/π COMPATIBLE
$1 < \sigma < 2$	IS K/π	K/π COMPATIBLE	
$2 < \sigma < 3$	K/π COMPATIBLE		
$> 3\sigma$	K/π EXCLUDED		

TOF	$p_t < 1.5 GeV/c$	$p_t > 1.5 GeV/c$
$< 3\sigma$	IS K/π	K/π COMPATIBLE
$> 3\sigma$	K/π EXCLUDED	

Table 3.3: PID requirements for identification/rejection of daughters in p–p collisions at $\sqrt{s} = 7$ TeV

3.4 Cut Optimisation

Studying a 3–prong decay such the $D^+ \to K^-\pi^+\pi^+$ channel means having to deal with a huge combinatorial background, a careful tuning of selection cuts is therefore mandatory. The strategy is meant to identify a combination of cuts for which the statistical significance is high. One of the possible problems of optimising the selection cuts on data is that there is a chance that they are affected by background fluctuations. If such a fluctuation occurs, it can enhance the background under the peak region faking a large signal. This would lead us to overestimate the number of raw signals we are counting, introducing a bias in our measurements. Such effect would affect all our measurement as the raw signal is the starting point of the D^+ cross section computation. In order to minimise the chances of picking up a statistical fluctuations, several requirements are applied besides the naive "maximum statistical significance" one. The selected point in the cut hyperspace should not only have a large (the best would be if it is the maximum) significance, but also be sitting in the middle of a region where signal is more or less stable against cut variation. Moreover, the position of the Gaussian peak, that is also affected by statistical fluctuations, should be compatible with the mass of the D^+ meson from the PDG (reported in table 3.1) and a reasonable width. In the case of Pb–Pb collisions we ask the σ of the Gaussian to be compatible with the resolution observed in proton–proton collisions and with the MonteCarlo one. We also want our cuts to change smoothly with the candidate's p_t and, if possible, we avoid to use too tight cuts even if this increases the statistical significance or improves the yield extraction. This because a low selection efficiency produces a high statistical uncertainty on the selection efficiency itself, that we extract from the MonteCarlo, and introduce a systematic uncertainty due to possible discrepancies between the detector description in the MonteCarlo and in

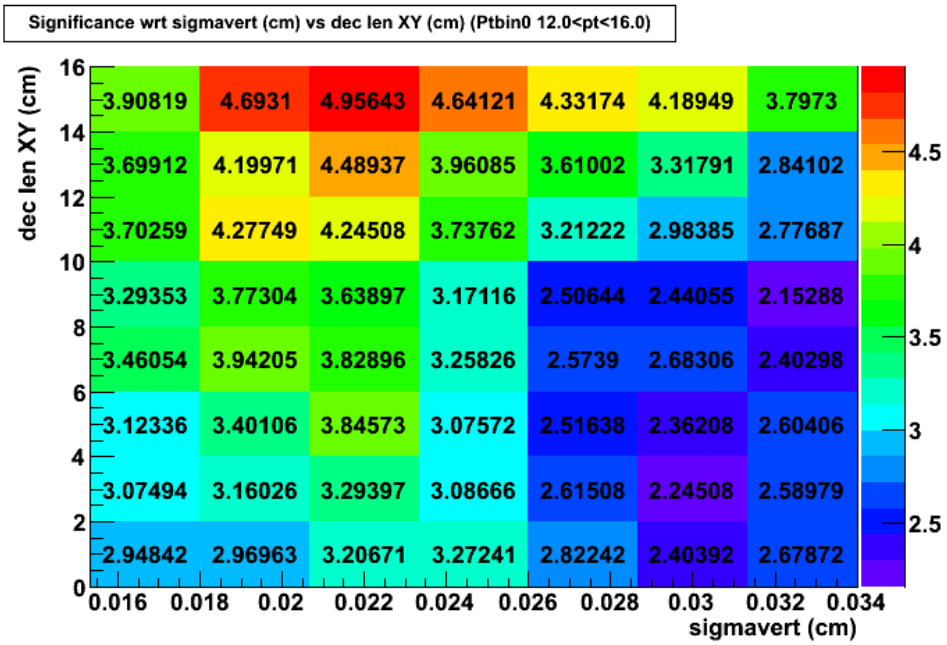

Figure 3.9: Distribution of statistical significance as a function of the decay length in the transverse plane and the tracks dispersion around the secondary vertex in Pb-Pb collisions for high p_t ($12 < p_t < 16$ GeV/c) candidates. figure 3.11 shows the invariant mass distributions corresponding to each cell of the histogram.

real data. Also tight cuts improve the fraction of candidates coming from B decays inside our sample, and if the fraction of feed-down candidates is high this will require larger corrections to estimate this effect. All these requirements reduce the chance of being affected by a statistical fluctuation. As a further cross–check. as we will see in section 3.7, we also control that the signal we obtain after correcting for the selection efficiencies is compatible among different sets of cuts.

Many cuts variables are applied (listed in table 3.4) to identify suitable candidates. These cuts depend on the candidate's p_t. At high p_t the cuts can be loosened because there is less background, but the higher Lorentz factor γ means that separation cuts (such as the cut on the candidate decay length) can be tightened. Also the PID is effective mainly at low p_t. The optimization procedure was focused on the cuts on the pointing angle; on the tracks dispersion around the secondary vertex and on the candidate decay length that proved to be the most effective candidates for the $D^+ \to K^-\pi^+\pi^+$ channel. Most of the cut variables are correlated, so the method we use to identify the best combination of cuts is to build a cut variable hyperspace with one variable for each axis and let all the variable vary in this space. For

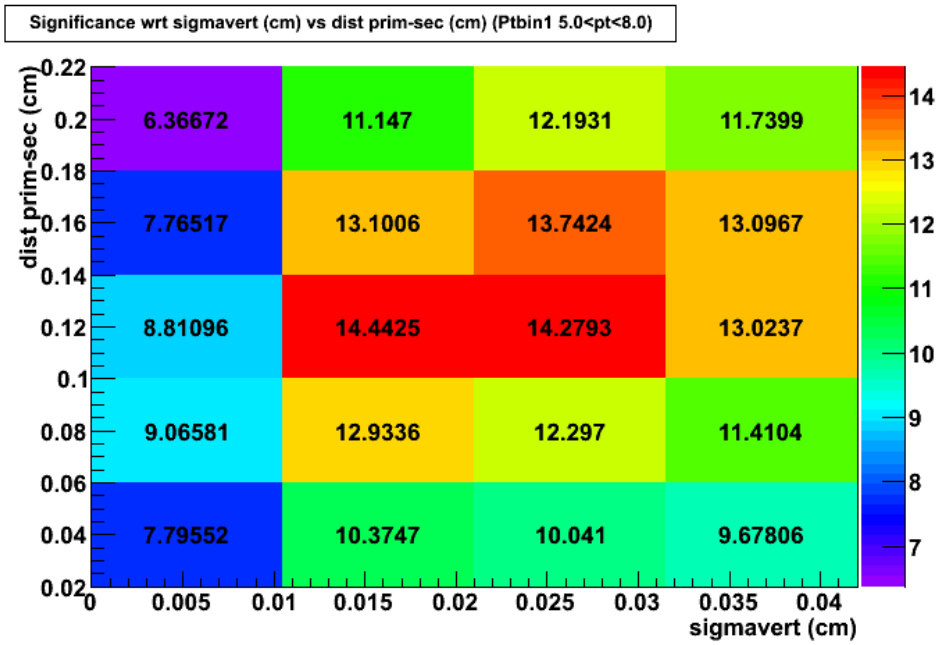

Figure 3.10: Distribution of statistical significance as a function of the decay length and the tracks dispersion around the secondary vertex in p-p collisions at $\sqrt{s} = 7$ TeV for candidates with $5 < p_t < 8$ GeV/c. figure 3.12 shows the invariant mass distributions corresponding to each cell of the histogram.

computational reasons the number of variables considered at a time usually ranges from 2 to 6, and the number of evaluated combinations is generally kept below 10,000 for a single run. For each cell of the cut hyperspace an histogram with the invariant mass distribution for that specific cut combination is produced. A dedicated task, called *AliAnalysisTaskSESignificance*, has been developed to run on the ALICE grid and store all the invariant mass histograms. The task loops over all the candidates and for each candidate it checks which are the cut combinations that it satisfies then it fills the corresponding mass histograms. Once all the events have been analysed, a macro loops over the content of each cell of the hyperspace, i.e. on each set of cuts, and all the histograms are fitted using the procedure described in section 3.3 to estimate the number of signal and background candidates that are kept after the application of the cuts. We then have a correspondence between each cut combination and the statistical significance we can obtain with it. As the fitting procedure also estimates the position of the invariant mass peak and its width, we also know mass and σ corresponding to each cut combination and we can selected those cells for which the cuts combination give optimal results. An example of the output of such a task is shown in figures 3.9 and 3.10 for Pb–Pb and proton–proton collisions respectively.

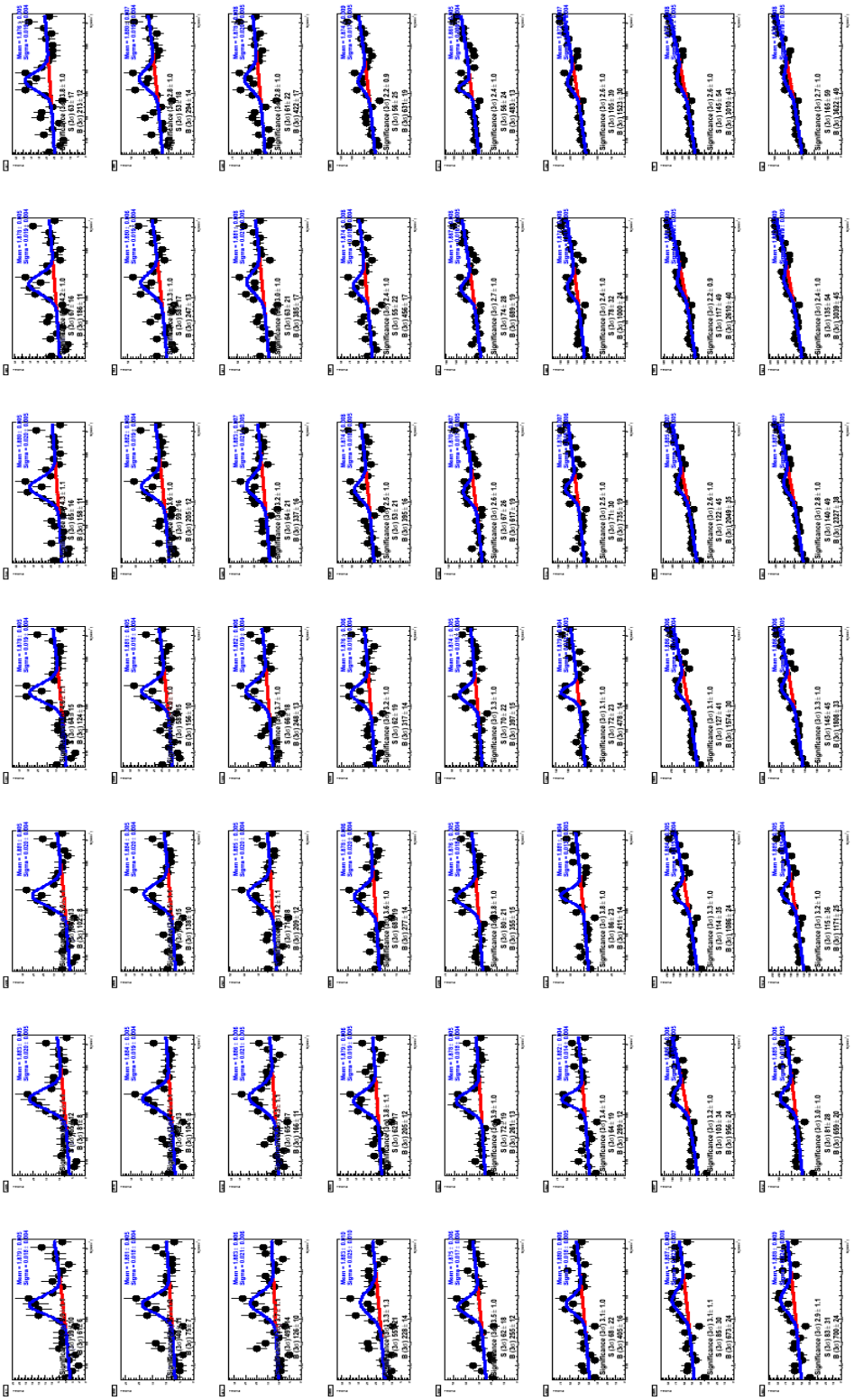

Figure 3.11: Invariant mass distributions corresponding to each cell of the histogram in figure 3.9.

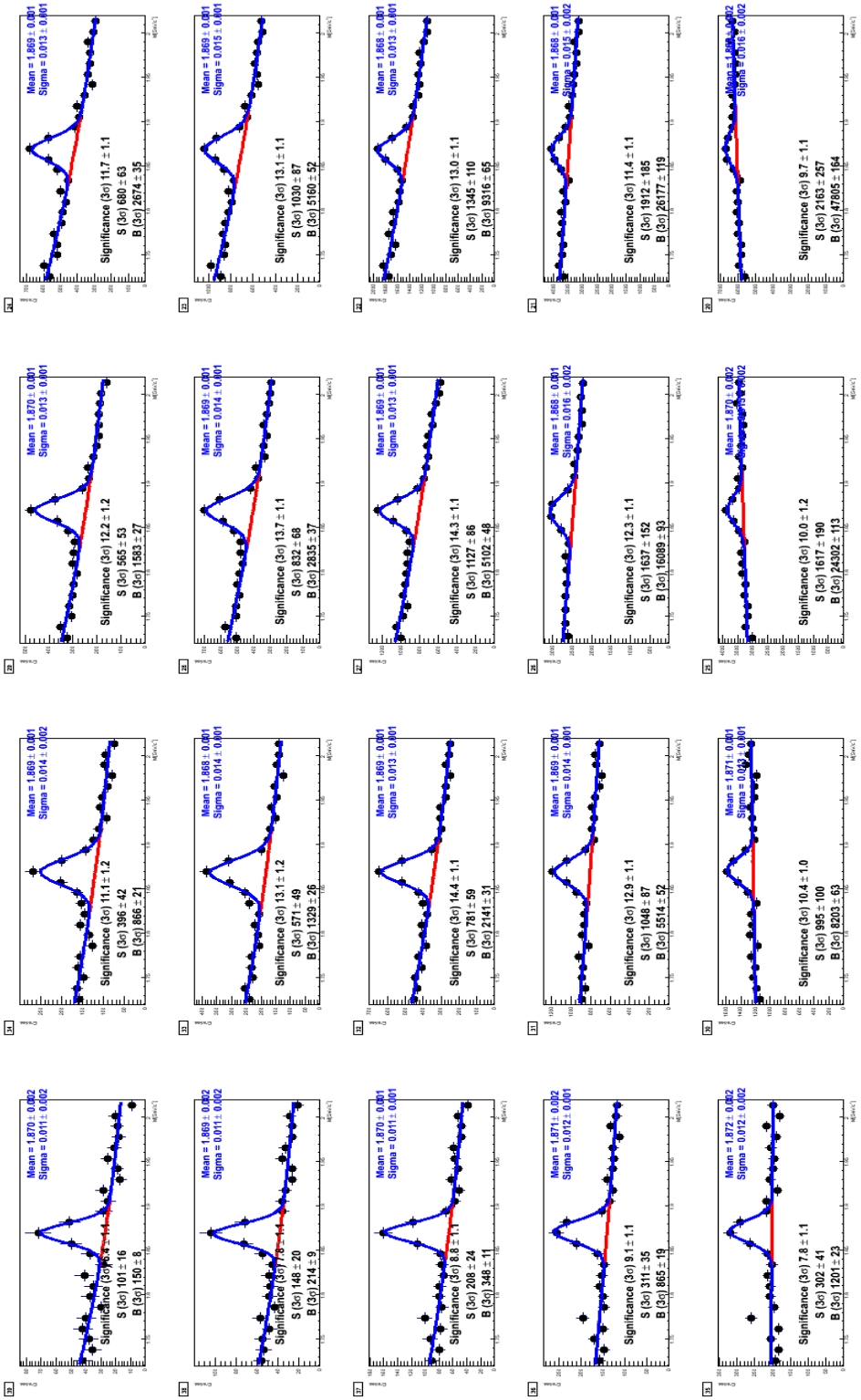

Figure 3.12: Invariant mass distributions corresponding to each cell of the histogram in figure 3.10.

p_t [GeV/c]	1 <p_t< 2	2 <p_t< 3	3 <p_t< 5	5 <p_t< 9	p_t> 9
Inv. Mass [GeV]	0.2	0.2	0.2	0.2	0.2
p_t^K [GeV/c]	0.4	0.4	0.4	0.4	0.4
p_t^π [GeV/c]	0.4	0.4	0.4	0.4	0.4
d_0^k [cm]	0	0	0	0	0
d_0^π [cm]	0	0	0	0	0
$\mathrm{dist}_{1\text{-}2}$[cm]	0.01	0.01	0.01	0.01	0.01
σ_{vertex} [cm]	0.0221	0.034	0.0207	0.0233	0.0233
Dec. len. [cm]	0.08	0.09	0.095	0.115	0.115
p_t^{max} [GeV/c]	0.5	1	0.5	0.5	0.5
$\cos\theta_{point}$	0.94	0.95	0.95	0.92	0.9
$\sum d_0^2$ [cm^2]	0.0055	0.0028	$8.83 \cdot 10^{-4}$	$8.83 \cdot 10^{-4}$	$8.83 \cdot 10^{-4}$
DCA [cm]	10^{10}	10^{10}	10^{10}	10^{10}	10^{10}

Table 3.4: Cut values for D^+ candidate triplets used in p-p collisions at $\sqrt{s} = 7$ TeV.

After few iterations of the procedure, it was clear that the cut variables that are most effective in maximising the significance are $\cos\theta_{point}$, σ_{vert}, the decay length and $\sum d_0^2$.

After several iterations, the best set of cuts we could identify for p–p collisions at $\sqrt{s} = 7$ TeV is reported in table 3.4. This set of cuts was identified performing the procedure on the first available data samples (LHC10b and LHC10c), corresponding to about 1/3 of the final 2010 statistics, and was then applied to the total data sample. These cuts provides high enough significance over different p_t bins but keeping the selections efficiency high enough to allow us to trust our results.

Having chosen a set of cuts that provides high enough significance, we can analyse our data sample and obtain the invariant mass spectra, that are the distributions of invariant mass of the candidates passing our selection cuts and are reported in figure 3.13 for proton-proton collisions at $\sqrt{s} = 7$ TeV.

The measurement of the raw yields (for particle and antiparticle), reported in table 3.5 is the first step in the procedure to compute the production cross section of the D^+. The amount of signal that we measure from the fit to the invariant mass spectra must be corrected for the experimental acceptance and efficiency, including the efficiency of the applied selections, the efficiencies ($\epsilon_{\mathrm{prompt}}$) of selection and reconstruction of the candidates and detector acceptance. This topic is discussed in section 3.5.1.

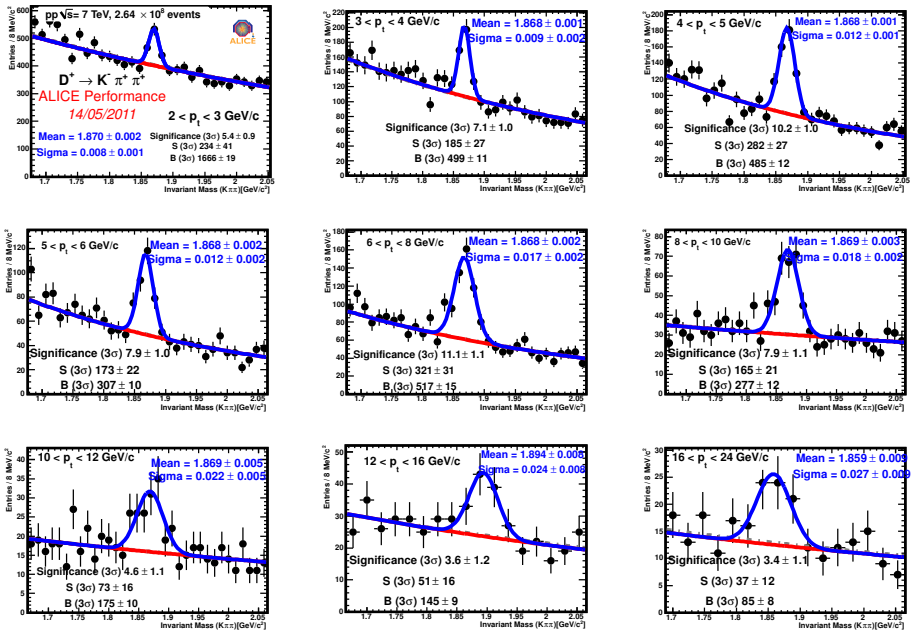

Figure 3.13: Invariant mass spectra for $D^+ \to K^-\pi^+\pi^+$ in bins of p_t. $2.64 \cdot 10^8$ pp events at $\sqrt{s} = 7$ TeV.

3.5 Calculation of prompt D^+ corrected yield

Different corrections are applied in order to go from the raw number of signal events obtained by fitting the invariant mass distributions to the number of mesons produced D^+ mesons in the sample. Each step of the analysis and each correction and normalization factor that we apply are affected by a systematic uncertainty that must be evaluated. We will discuss later in section 3.7 how this evaluation is done in each step of the analysis. The task we use to measure the invariant mass spectra of the D meson candidates provides also the most significant cross checks on the data quality. Among the other features, the task computes the number of analysed and rejected events; it allows us to use different PID features and to build the invariant mass spectra of particles (D^+) and antiparticles (D^-) separately. Another feature that was implemented but not used in this analysis is the possibility to estimate the background from the combinations of tracks all carrying the same charge (*like sign* background). The most important items will be discussed in detail in this section.

p_t (GeV/c)	$N^{D^+} \pm stat. \pm syst.$
$1 < p_t < 2$	$122 \pm 23 \pm 30$
$2 < p_t < 3$	$390 \pm 57 \pm 97$
$3 < p_t < 4$	$405 \pm 40 \pm 101$
$4 < p_t < 5$	$516 \pm 38 \pm 46$
$5 < p_t < 6$	$361 \pm 31 \pm 33$
$6 < p_t < 7$	$294 \pm 30 \pm 15$
$7 < p_t < 8$	$213 \pm 27 \pm 1$
$8 < p_t < 12$	$434 \pm 30 \pm 22$
$12 < p_t < 16$	$89 \pm 20 \pm 9$
$16 < p_t < 24$	$52 \pm 14 \pm 5$

Table 3.5: $D^+ + D^-$ raw yield measured in 5 nb^{-1} integrated luminosity p-p collisions at $\sqrt{s} = 7$ TeV. The systematic uncertainty is discussed in section 3.7.

3.5.1 Efficiencies

To compute the number of $D^+ \to K^-\pi^+\pi^+$ decays occurred in the analysed data sample the measured raw yield of D^+ mesons obtained from the invariant mass fit has to be corrected for the detector acceptance and efficiency, and the efficiency of the track and candidate selection cuts.
To correct for the number of lost decays, the efficiency of our reconstruction and selection is computed using MonteCarlo simulations. Those simulations are performed keeping into account the realistic conditions of the experimental apparatus during the data taking. The same analysis framework is used to treat real and MonteCarlo events. In this way, knowing how many D^+ mesons have been generated in the MonteCarlo productions it is possible to compute our reconstruction efficiency that is then used to correct the number of measured D^+. The MonteCarlo productions used for such a study in proton-proton collisions are based on PYTHIA [61] event generator with the Perugia-0 tuning [71] with one $c\bar{c}$ or $b\bar{b}$ pair for event. In Pb-Pb collisions the MonteCarlo simulations are based on HIJING event generator [62] to reproduce the minimum bias event. On top of it, PYTHIA events are added in order to enhance the number of $c\bar{c}$ and $b\bar{b}$ pairs produced in the event, the latter being used for the estimation of the feed-down contribution. The number of PYTHIA events added on top of each HIJING event depends on the event multiplicity and it is tuned to do not introduce any significant bias in the event mixing multiplicity. To increase the number of candidates that can be used for this analysis, and so to reduce the error on the efficiency estimation, both in proton-proton and Pb-Pb collisions all the D^+ mesons produced in PYTHIA events are forced to decay in the $D^+ \to K^-\pi^+\pi^+$ channel. The first step to compute the efficiency is to compute the ratio

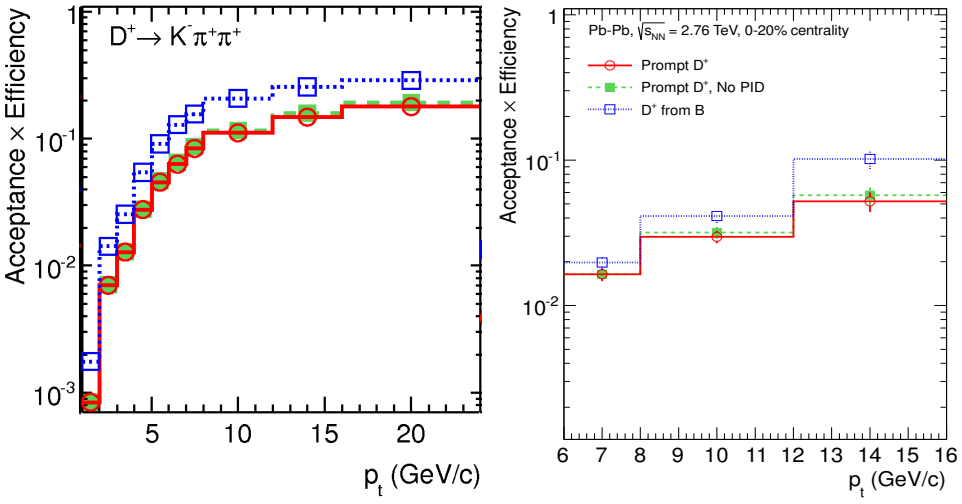

Figure 3.14: Acceptance times reconstruction and selection efficiencies in pp (left) and Pb-Pb collisions computed from MonteCarlo simulations. Blue line is the efficiency for D^+ coming from B decays, red (green) is the prompt efficiency with (without) PID selection.

between the D^+ generated in the fiducial acceptance of the central barrel (depending on the meson p_t and η) and the D^+ generated at midrapidity ($|y| < 0.5$), that is the region where we want to measure our cross-section. This factor is then multiplied by the ratio between the number of selected and reconstructed D^+ and the number of D^+ generated in the fiducial acceptance, obtained from a charm enriched sample in order to have a large enough number of D^+ passing our selection cuts. This is our selection and reconstruction efficiency. These two ratios are shown in figure 3.15 for both prompt and feed-down candidates. The tools that have been developed to compute these efficiencies (the *Correction Framework*) compute the number of D^+ fulfilling a chain of several requirements. In this way it is possible to control the efficiency of many selection steps: acceptance; fiducial acceptance; event selection; track quality selection; reconstruction; selection and PID selection.

The reconstruction and selection efficiencies found in this way, multiplied by a fiducial acceptance factor that varies smoothly from $|y| < 0.5$ at low p_t to $|y| < 0.8$ for $p_t = 5$ GeV/c are shown in figures 3.14a (for proton–proton collisions) and 3.14b (for Pb–Pb events).
As this correction relies on MonteCarlo simulations, it depends on the description of the experimental apparatus and of the D^+ meson in the MonteCarlo, and is therefore possible that a bias is introduced in our analysis. a way to check that our MonteCarlo describes correctly our apparatus is to compare the cut variables distributions between data and MonteCarlo. As

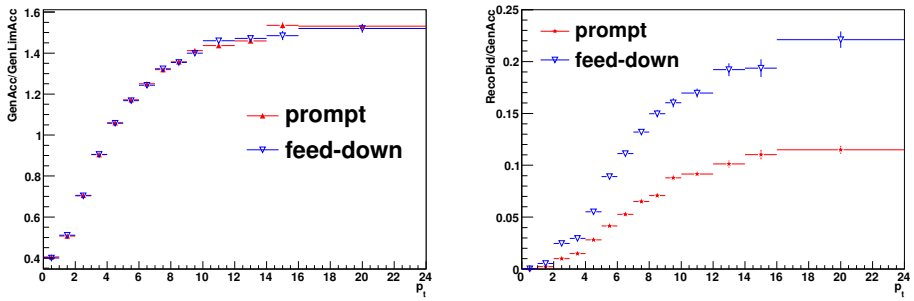

Figure 3.15: Efficiencies from simulated proton-proton collisions at $\sqrt{s}$ = 7 TeV. Left: ratio between the number of D^+ generated in the p_t and η fiducial acceptance of the central barrel and those generated in $|y| < 0.5$ from minimum bias MonteCarlo. Right: ratio between the number of reconstructed and selected D^+ and the number of D^+ generated in $|y| < 0.5$ from charm enriched Montecarlo. Red are prompt D^+, blue are feed down.

our data samples are dominated by the distribution background this comparison is in practice not sensitive to the signal candidates distribution. The distributions of some of the cut variables are shown in figure 3.16 and 3.17 for p-p and Pb-Pb collisions respectively. One can see that the agreement among data and MonteCarlo is satisfactory. The small discrepancies between data and MonteCarlo might be due to some residual misalignment of the detectors.
Another cross–check is to perform the analysis (e.g. the charm production cross–section in proton–proton collisions) using different sets of cuts that have significantly different efficiency. Discrepancies among the measurements can then be used to estimate the uncertainty of the efficiency estimation. Further details on this issue will be given in the section dedicated to the systematic studies in this chapter (section 3.7).

3.5.2 Feed-down subtraction

We are interested to move from the measured yield to the production cross section of prompt charm. To do this we have to remove the contribution due to the B meson decay feed-down from the measured yield. These are candidates coming from the decay of open beauty mesons following the decay chains $B \to X + D^+ \to K^-\pi^+\pi^+$ or $B \to X + D^{*+} \to X + D^+ \to K^-\pi^+\pi^+$. The beauty cross-section is smaller than the charm cross-section but at the LHC energies this contribution is not negligible. Moreover secondary D^+ are more displaced from the primary vertex and are more likely to satisfy our cut selection requirements. This fact is already visible in figure 3.14a where the efficiency of feed-down D^+ mesons is higher than the one of primary D^+.

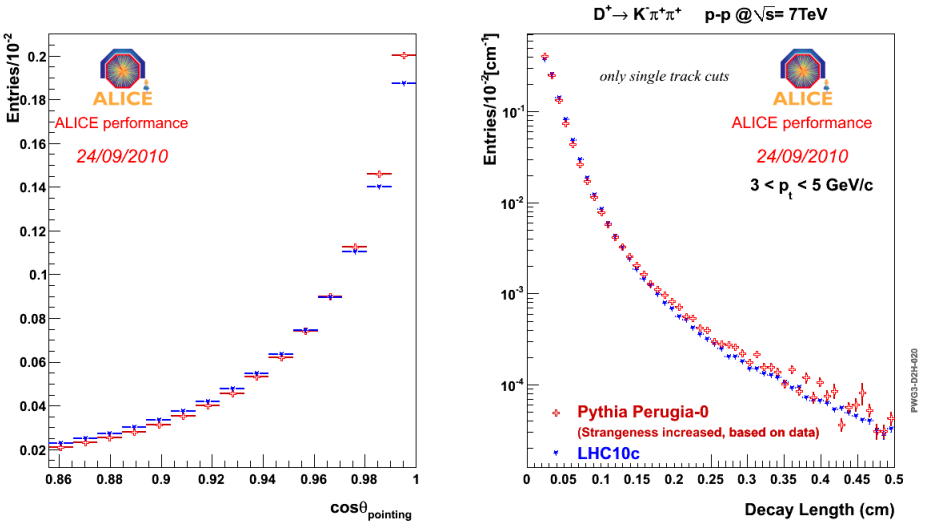

Figure 3.16: Distribution of the cosine of the candidate pointing angle (left) and of the decay length (right) of the $D^+ \to K^-\pi^+\pi^+$ candidates in proton-proton collisions. Very loose topological cuts are applied. In blue the distribution of data (May 2010), red is PYTHIA minimum bias simulation with Perugia-0 tuning [71]. Strangeness in the MonteCarlo sample is enhanced in order to reproduce the strangeness production observed at the LHC for p–p at $\sqrt{s} = 7$ TeV collisions.

This higher efficiency actually enhance the feed down contribution in our measured sample, that reaches a value of $\approx 20\%$ at high p_t. We estimate the feed down contribution starting from pQCD calculations and MonteCarlo simulations. We decided to use FONLL pQCD calculations [36] to have an estimate of the feed down particle yield. These calculations describe well beauty production at Tevatron [37] and LHC [38, 39]. The efficiency $\epsilon_{\text{feed–down}}$ was estimated from MonteCarlo simulations where we could trace D mesons coming from B decays. We can then define our prompt charm fraction f_{prompt} as:

$$f_{\text{prompt}} = 1 - \frac{\mathrm{N}^{D^\pm \text{raw}}_{\text{from B}}}{\mathrm{N}^{D^\pm \text{raw}}_{\text{all}}} \tag{3.2}$$

where, having defined the integrated luminosity $\mathscr{L}_{\text{int}}$ as the ratio of minimum bias events over the minimum bias cross–section ($\mathscr{L}_{\text{int}} = \frac{N^{\text{mb}}}{\sigma^{\text{mb}}}$), the factor $\mathrm{N}^{D^\pm \text{raw}}_{\text{from B}}(p_{\text{t}})\Big|_{|y|<y_{\text{acc}}}$ can be written as:

$$\mathrm{N}^{D^\pm \text{raw}}_{\text{from B}}(p_{\text{t}})\Big|_{|y|<y_{\text{acc}}} = \frac{d\sigma^{D^+ \text{from B}}_{\text{FONLL}}}{dp_{\text{t}}} \cdot 2 \cdot 2y_{\text{acc}} \Delta p_{\text{t}} \epsilon_{\text{feed–down}} \text{BR} \mathscr{L}_{\text{int}} \tag{3.3}$$

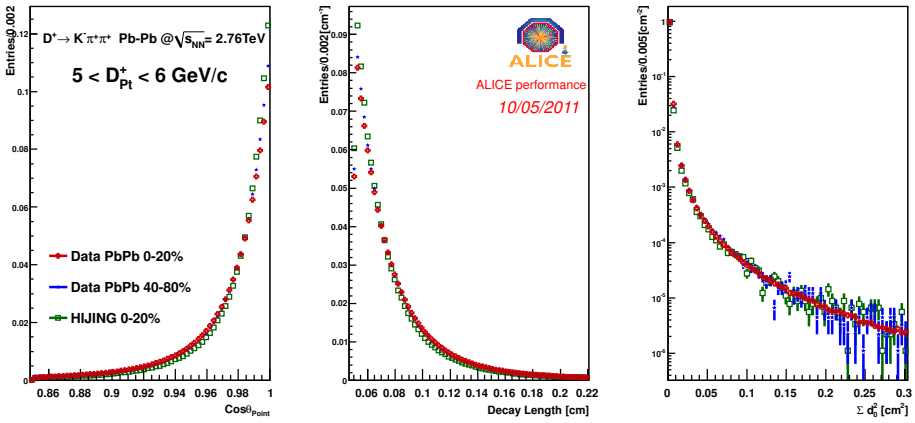

Figure 3.17: Distribution of cut variables for $D^+ \to K^-\pi^+\pi^+$ channel in Pb–Pb collisions at $\sqrt{s} = 2.76$ TeV. Very loose topological cuts are applied. The figure shows the distribution of the candidate cosine of pointing angle (left), decay length (centre) and the squared sum of the daughters' impact parameters d_0 (right). In blue the data for semi–peripheral Pb–Pb collisions (40-80% centrality) are shown, in red central (0-20%) Pb–Pb collisions and in green the results from HIJING MonteCarlo.

As shown in figure 3.18 the fraction of prompt D^+ is larger at low p_t, where it is more than 88% and then decreases towards higher p_t reaching 75% for $p_t > 8$ GeV/c. After applying the corrections for prompt D^+ efficiency and for the feed–down subtraction, we can have a first comparison of the corrected yield with the pQCD predictions. Figure 3.19 shows the corrected yield of D^+ compared to FONLL predictions in arbitrary units. The FONLL distribution was normalized to the integral of data in order to have a comparison of the FONLL slope with the data.

3.6 Cross section extraction

The goal of the study of the D^+ meson in p–p collision is to measure its production p_t differential cross section. To do this the raw yield of D^+ extracted from the fits to the invariant mass spectra in intervals of p_t must be corrected by the acceptance, reconstruction and selection efficiencies and be normalized to the cross section. The formula we use to obtain the full

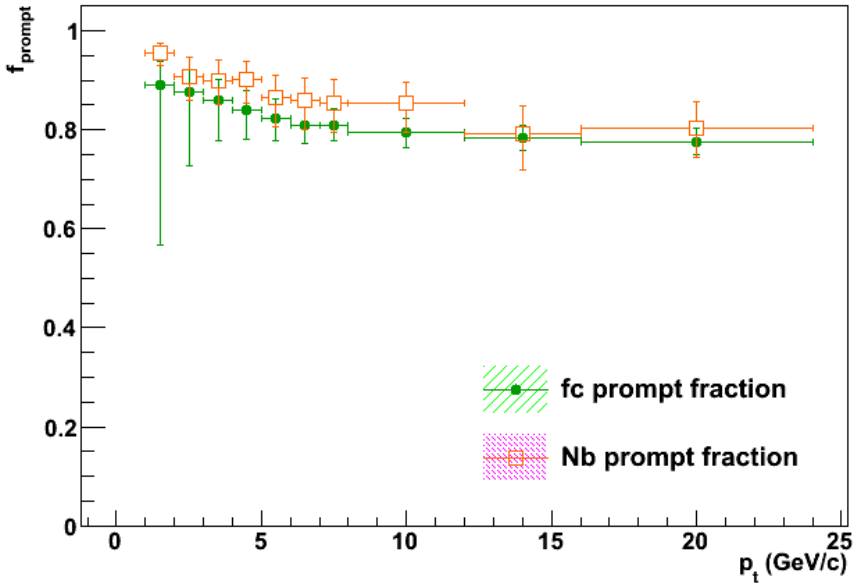

Figure 3.18: $f_{\rm prompt}$ fraction of prompt $\rm D^+$ computed accordingly to equation 3.3 (green circles) compared to the fraction $f_{\rm prompt}$ obtained following the method of equation 3.7 (red squares) for proton-proton collisions at $\sqrt{s} = 7$ TeV as a function of $\rm p_t$.

cross section is:

$$\frac{d\sigma^{D^+}(p_{\rm t})}{dp_{\rm t}}\,|_{|y|<0.5} = \frac{1}{2}\frac{1}{\Delta y(p_{\rm t})}\frac{f_{\rm prompt}(p_{\rm t})}{({\rm Acc}\times\epsilon_{\rm prompt})}\frac{N^{D^\pm}_{\rm raw}(p_{\rm t})|_{y<\Delta y}}{({\rm BR})\Delta p_{\rm t}}\frac{\sigma^{mb}/\sigma^{\rm V0AND}}{N^{\rm mb}}\sigma^{\rm V0AND} \tag{3.4}$$

where:

N^D_{raw} is the raw yield as obtained directly from the invariant mass spectra

$\Delta y(p_{\rm t})$ is the acceptance where we measure our signal. A cut varying smoothly with $\rm p_t$ is applied to select the fiducial acceptance region. This cut ranges from $\Delta y = 1$ at low $\rm p_t$ to $\Delta y = 1.6$ for $p_t > 5$ GeV/c.

BR: is the branching ratio of the decay $\rm D^+ \to K^-\pi^+\pi^+$ ($9.13 \pm 0.19\%$ [3]).

$f_{\rm prompt}$ is the prompt charm fraction that we use to estimate the contribution from feed down (see section 3.7)

$({\rm Acc}\times\epsilon_{\rm prompt})$ is the correction for the efficiencies times the acceptance.

σ^{mb} and $\rm N^{mb}$ are the minimum bias cross section and the number of collected minimum bias events respectively, where minimum bias events are triggered by the logical OR of the SPD and the VZERO detector.

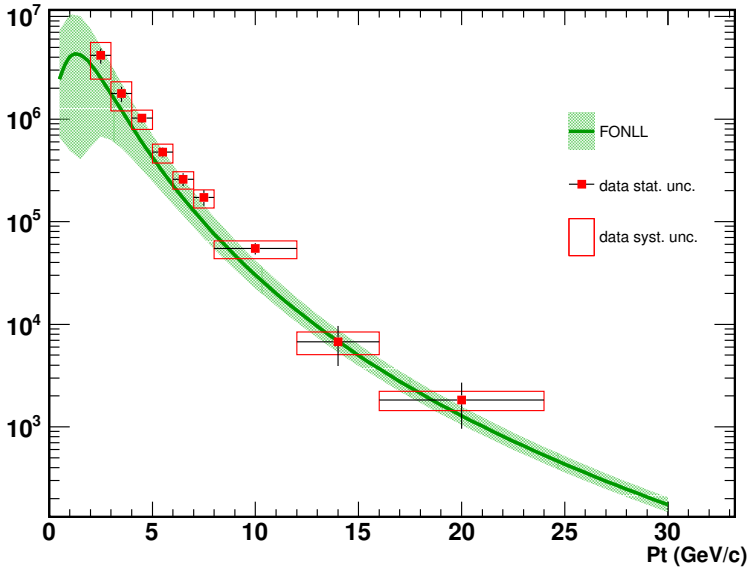

Figure 3.19: Primary D^+ corrected yield as function of p_t compared with FONLL predictions, where the FONLL distribution was rescaled to the integral of the data. The y–axis is the p_t differential corrected yield in arbitrary unit.

$\sigma^{V0_{AND}}$ is the cross section for events with one signal on both sides of VZERO detector (V0A and V0C). We use this cross section as reference cross section for normalization. The V0AND cross section is measured directly during the Van Der Meer scans.

the $\frac{1}{2}$ factor comes from the fact that we are counting particles and antiparticles together. We verified that the number of $D^+$and D^- produced are compatible (see figure 3.26).

This section will be devoted to give a detailed description of the terms of equation 3.4. Finally the total D^+ production cross section is obtained by extrapolating the cross section measured at ALICE, which is limited over a certain range of p_t ($p_t > 1$ GeV/c) and acceptance ($|y| < 0.5$), to the full acceptance and down to $p_t \sim 0$ GeV/c. This procedure is based on FONLL theoretical predictions and it is explained later in this chapter.

3.6.1 Normalization to cross section

Two basic quantities needed in order to have a measurement of the prompt charm cross section are the number of D^+ mesons per event (that we can obtain correcting properly the measured raw yield) and the cross section of

the events that we accept in our analysis (*good events*). The requirements we apply on the triggered events were discussed in section 3.3. The number of minimum bias events N^{mb} that we have to consider in the normalisation procedure is not just the number of analyzed events that pass our vertex quality requirements (we remind here that among the other requirements a "good" event should have a reconstructed vertex and its z coordinate must be closer than 10 cm from the coordinate origin). The V0AND cross-section measurements accounts for vertexing efficiency, so we have to normalize to the number of events with and without vertex. As our efficiencies are relative to the event sub sample with $|z_{\rm vertex}| < 10$ cm we need to remove the number of events outside the 10 cm region also from the event counting. This number is not known but the distribution of the vertexes z coordinate was verified to be Gaussian and its σ was measured during the data taking as a function of the run number. The number of minimum bias events we should use in equation 3.4 is given by

$$N^{mb} = N^{good} + N^{noVtx} - N^{noVtx} \cdot f^{vtx>10} \tag{3.5}$$

where N^{good} is the number of events passing our requirements, N^{noVtx} is the number of events without reconstructed primary vertex and $f^{vtx>10}$ is the fraction of events with $|z_{\rm vertex}| > 10$ cm. It is easy to recognise that if we assume that the distribution of $z_{\rm vertex}$ is the same for events for which we could and could not reconstruct the vertex, then equation 3.5 is just the sum of the number of good events plus the number of events with $|z_{\rm vertex}| < 10$ cm for which the vertex was not reconstructed. The minimum-bias cross section, that we want to use to normalise our measured yield, was not measured directly. Hence we must use some process for which the cross section is known or can be measured and refer to that process. The reference cross section that was used in our analysis is the cross section of a V0AND event. An event satisfy the V0AND condition when it gives signals in both sides of the VZERO scintillator detector [55]. The cross–section of the V0AND events was measured with the Van–der–Meer technique[3] [72]. Three short periods of data taking dedicated to Van–der–Meer scans [73], were performed in order to have a precise measurement of the V0AND cross–section. The ratio $\frac{\sigma_{pp}^{\rm V0AND}}{\sigma_{pp}^{\rm mb}}$ was found to be ≈ 0.87, stable within 1% over the period of data taking we are considering in this thesis. This value was cross-checked measuring the ratio between the number of V0AND and minimum bias events run by run, as shown in figure 3.20 for the LHC10b period. From the

[3] In this technique the two colliding beams are moved in the transverse plane one across the other. While the beams move, the rate of a reference process (V0AND in our case) can be measured as a function of the beams separation. The head-on luminosity L can be measured from the head-on reference process rate R, beam properties (number of bunches, revolution frequency, number of proton per bunch) and the size of the scanned area. The reference process cross section can be computed from the head-on rate and the head-on luminosity as $\sigma_R = \frac{R}{L}$.

$\frac{\sigma_{pp}^{\mathrm{V0AND}}}{\sigma_{pp}^{\mathrm{mb}}}$ ratio and the measurements performed during the Van–Der–Meer scans we can finally obtain $\sigma_{pp}^{\mathrm{mb}} = 62.3$ mb with negligible statistical error and 3.5% systematic uncertainty. This error comes from a 3.5% systematic uncertainty in the determination of the $\sigma_{pp}^{\mathrm{V0AND}}$ cross section and it is mainly due to uncertainties on the beam intensities. Thus the factors that are directly measured in equation 3.4 are $\frac{\sigma_{pp}^{\mathrm{V0AND}}}{\sigma_{pp}^{\mathrm{mb}}}$ and $\sigma_{pp}^{\mathrm{V0AND}}$.

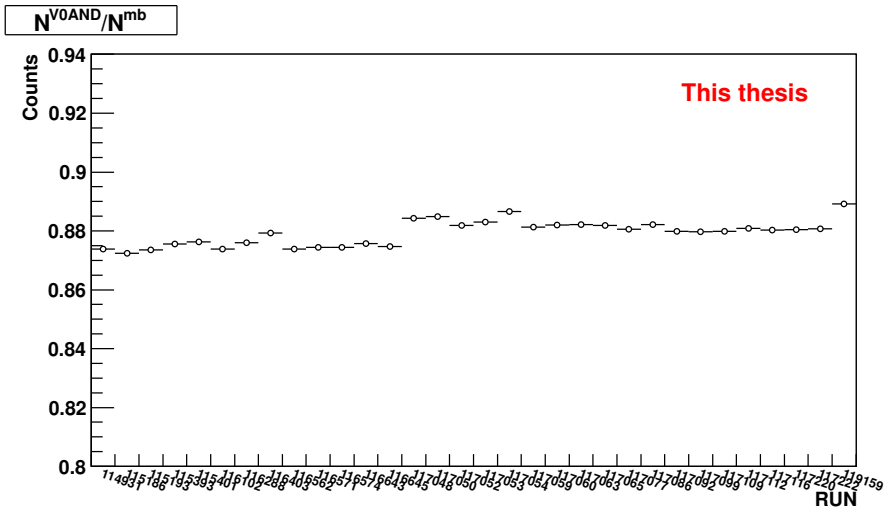

Figure 3.20: Ratio between the number of events with V0AND trigger and the number of minimum bias events (computed accordingly to equation 3.5) for the LHC10b period.

Normalization to the candle

A different normalization procedure that we currently use as a cross–check method is what we call *normalization to the candle*. In this method we identify a reference process (the candle), for example an event containing at least one track of at least a certain momentum, that identifies an event as *event with candle*. We can measure the candle cross section in a run with the configuration as close as possible as the one used in the Van-Der-Meer scans (*golden run*) and, assuming that the ratio of events with candle over the minimum bias events is stable over time we can extract the cross section of D^+ production as

$$\left.\frac{d\sigma^{\mathrm{D}^+}(p_{\mathrm{t}})}{dp_{\mathrm{t}}}\right|_{|y<0.5|} = \frac{N^{\mathrm{D}^+}}{N_{mb}}\sigma_{mb} = \frac{N^{\mathrm{D}^+}}{N_{candle}}\,\sigma_{candle} \tag{3.6}$$

where N_{candle} represent the number of events with candle in the same sample where N^{D^+} D^+ have been counted and σ_{candle} is the candle cross-section

measured in the golden run. N^{D^+} is the number of prompt D^+ corrected for the efficiencies.
We decided to use as candles signals that are by construction required to detect a D meson: for example as we are requiring our daughter tracks to have $p_{\mathrm{t}} > 0.3$ GeV/c one good candle process is to have at least one (or two) tracks with $p_{\mathrm{t}} > 0.3$ GeV/c. Also having a track with at least 70 cluster in the TPC can be used as candle, as this is also a requirement we have on our daughter tracks. What happens with those candles is that we can have a small fraction of events that have a candle, but without the V0AND. In any case the fraction of those events is very small, and the fraction of events of this kind that also have D mesons candidates is even smaller, so we can consider any bias due to this, if any exists at all, as negligible.
We keep record of the number of events with V0AND and different candle processes, as well as the number of minimum bias events analyzed, in a special object (*AliNormalizationCounter*) that keeps also record of the run number to which any event corresponds.

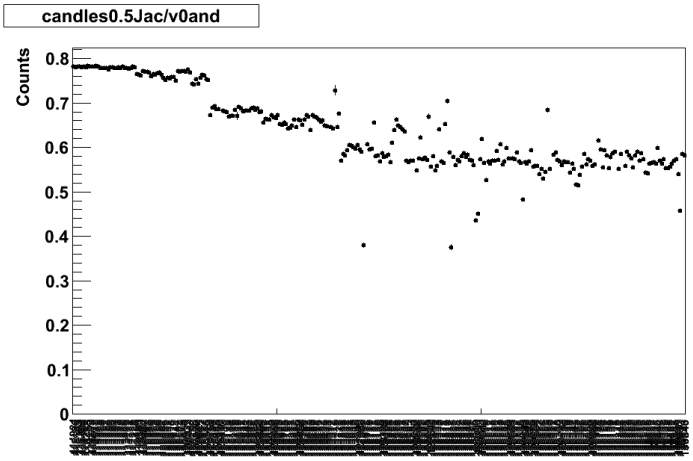

Figure 3.21: Ratio of number of candle events over V0AND events as a function of the run number for the 2010 data taking period with p-p collisions at $\sqrt{s} = 7$ TeV. Candle is defined as an event with a reconstructed vertex with $|z_{\mathrm{vertex}}| < 10$ cm, at least one track with $p_t > 0.5$ GeV/c and $|\eta| < 0.8$, at least 70 clusters in the TPC, two points in the ITS of which at least one in the SPD.

The candle process we decided to use to cross-check the normalization to cross-section is an event with a reconstructed vertex with $|z_{\mathrm{vertex}}| < 10$ cm with at least one track with $p_t > 0.5$ GeV/c and $|\eta| < 0.8$, at least 70 clusters in the TPC, two point in the ITS of which at least one in the SPD. As a further requirement to remove secondaries, the track should have a distance of closest approach to the primary vertex of the event $|d_{xy}| < 0.0182 + 0.035 p_t^{-1.01}$ cm in the transverse plane and $|d_z| < 2$ cm in the longitudinal

direction. This candle was chosen because it was also fitting the needs of other ALICE analyses, and in this way it is possible to cross-check its behaviour over different analyses. Figure 3.21 shows the ratio of this candle process over the number of collected V0AND events as a function of the run number. The steps visible in coincidence with the different periods can be correlated to changes in the LHC filling scheme and detectors efficiency. Using this candle as a reference we obtained a discrepancy with respect to the standard normalization procedure of about 3.5-4.5% (depending on the period of the analysis) for the D^+ cross section. This discrepancy is still under investigation and it may be due to the computation of candle reconstruction efficiency, but the final result is in any case compatible within the systematic uncertainties.

3.7 Systematic uncertainties

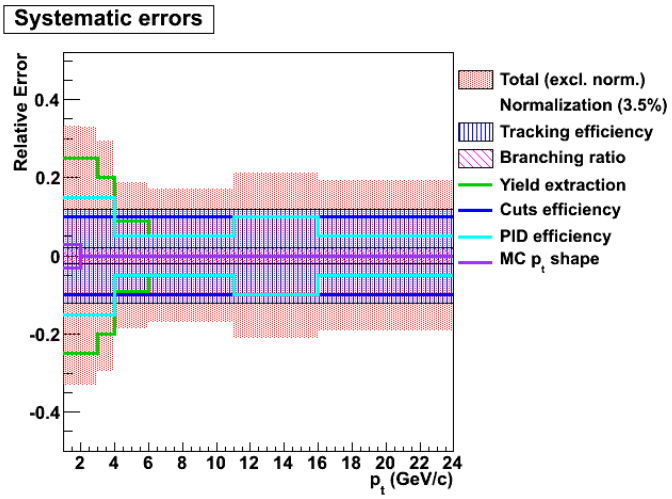

Figure 3.22: Relative systematic uncertainties on D^+ cross section in proton–proton collisions at $\sqrt{s} = 7$ TeV.

We have described until now all the ingredients needed to compute the charm cross section starting from equation 3.4. Before presenting the results obtained with the proton-proton data sample collected by ALICE in 2010, I describe here the systematic uncertainties that affect our measurement and how we computed them. Figure 3.22 shows the size of the different systematic error sources affecting our cross section measurement for the p_t intervals used in the analysis. As shown in figure 3.22 some sources are strongly p_t dependent. At low p_t the largest contribution (25%) comes from the systematics from the yield extraction, while at intermediate and high p_t the major sources of systematic error are tracking (12%) and PID (15%)

efficiencies. Being the analysis strategy very similar between proton–proton and Pb–Pb collisions, most of these sources are the same, although the size of the effects can be largely different for the two systems. Among these sources of systematics there are systematics on the raw yield extraction; systematics due to the tracking efficiency in ALICE detectors and the track quality cuts; systematics related to the topological selection cuts applied to isolate the signal; systematics originating from PID efficiency and contamination; the uncertainty induced by the assumption on the $p_{\rm t}$ shape of the D meson spectra in the MonteCarlo; systematics coming from the treatment of the B feed–down; and systematics from the uncertainty on the D^+ decay branching ratio and the normalization.

The first source of systematic uncertainty is related to the yield extraction: we have decided to use an exponential function to fit the distribution of the background candidates and a gaussian for the D meson line shape. Many settings of the fit can have an effect on the resulting number of signal candidates. By default we interpolate the background over a region of ± 0.2 GeV/c around the D^+ mass peak (1.869 GeV/c) and we divide the region in 102 bins. To estimate the effect of these choices we varied the binning of the histogram; we changed the edges of the fitting region (moving it by a few bins) and we changed the background function using a linear and parabolic shape instead of an exponential. Furthermore the signal is also estimated using a *bin counting* technique. In this method, the background is subtracted from a fit in the side bands of the invariant mass distribution. The signal is not estimated from a fit but by counting the entries contained in the bins of the histogram in the signal region after the background subtraction. The maximum spread between the results obtained with the default settings and the results obtained with all those changes is then quoted as a systematic uncertainty. Figure 3.23 shows the different values of signal and significance as a function of $\rm p_t$ obtained with the various settings in proton–proton collision. After all these possible signal extraction methods have been applied, the systematic uncertainty turns out to be of the order of 25% at low $\rm p_t$, then reaches a minimum of 5% at intermediate $\rm p_t$ and 10% at high $\rm p_t$ in proton-proton collisions. This behaviour can be explained by the fact that the fitting procedure is critical at low $\rm p_t$ where there is a large amount of background and therefore the significance is low, at intermediate $\rm p_t$ the maximum significance is reached and it decrease again at high $\rm p_t$ where there are a few signals, increasing again the raw yield extraction uncertainty.

The tracking efficiency is one of the main sources of systematic uncertainty affecting our analyses. It accounts for a 12% (18%) systematics in proton-proton (Pb-Pb) collisions, and and it includes effects coming from the track finding procedure in the TPC, from the track quality selection and from the prolongation efficiency from the TPC to the ITS. This is due to the fact that the signals collected in the ITS and in the TPC should be matched

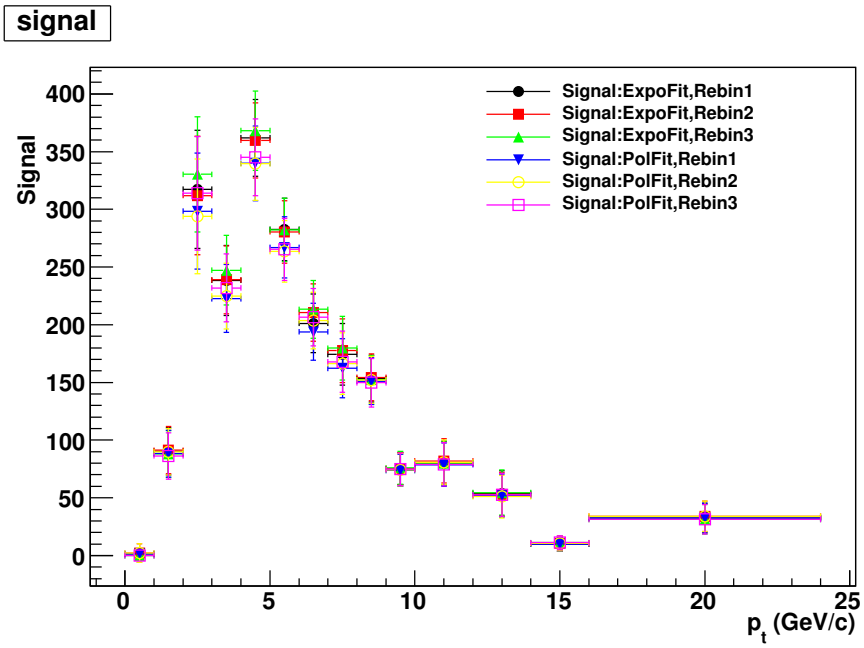

Figure 3.23: Signal obtained using different fitting procedures. Exponential fit is performed to obtain black, red and green markers while blue, yellow and magenta are obtained fitting with a polynomial function. Black and blue markers show a fit performed dividing the mass window in 102 bins, red and yellow dividing the mass window in 51 bins and green and magenta in 34 bins. Black markers are the default settings. Data from $2.66 \cdot 10^8$ minimum bias events at $\sqrt{s} = 7$ TeV.

when the tracks are reconstructed. As we ask in our analysis for tracks with at least one point in the SPD detector, a track found in the TPC track may be lost if it was not seen by the SPD detector. The estimation of this effect was done by data comparison and from MonteCarlo simulation with realistic description of the detector. This uncertainty does not depend on the properties of the meson but only on the number of daughters in the decay channel under investigation. For the D^0 decay in two prongs the effect is of the order of 8%, while it amounts to 12% for the $D^+ \to K^-\pi^+\pi^+$ channel (a 4% effect on each track) for proton-proton collisions. In Pb-Pb collisions the effect is larger and it amounts to a 6% effect for each track.

The applied D^+ selection cuts have a big effect on the amount of signal and background available. If the MonteCarlo we use for correction does not reproduce exactly cut variable distribution in the data, we can have a systematic effect. In order to estimate this contribution two other sets of cuts were defined in order to have at least a 20% signal variation with respect to the standard set of cut for $p_t < 8$ GeV/c. Figure 3.24a shows

the measured raw yield as a function of p_t with the different sets of cuts and figure 3.24b its effect on the D^+ corrected yield. The differences in the final corrected yields values where included as systematic uncertainty on the selection cuts. The final value of the cross-section was at most 10% different from what we quoted as final result. This 10% systematic was assumed constant over p_t.

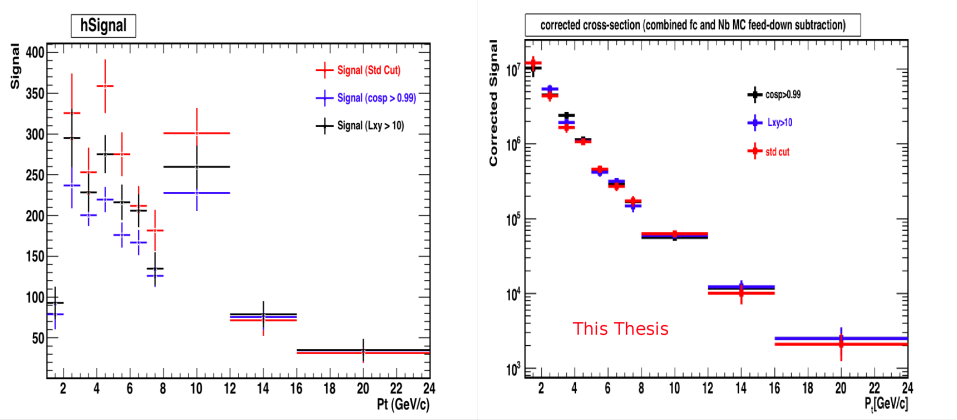

(a) (b)

Figure 3.24: Number of signal candidates extracted from the invariant mass fit (left) and the measured cross–section (right) for standard cuts (red); standard cuts with $\cos\theta_{\rm point} > 0.99$ (black) and for standard cuts with longitudinal decay length > 10 (blue). The relative difference between the cross–section measured with standard cuts and the cross–sections measured with the other two sets is taken into account as systematic error on cut selection.

The PID strategy we applied is designed in order to be conservative, that is to avoid as much as possible loss of signal due to the PID. Tests done on MonteCarlo simulations with realistic detector conditions show that the used PID selection keep 100% of the signal in all p_t bins. The systematic uncertainties related to Particle Identification (PID) are addressed in proton–proton collisions by performing the analysis without any PID information and using stricter requirements on the track identification, i.e. asking for 2σ compatibility instead of 3σ. The invariant mass spectra obtained with and without particle identification are shown in figure 3.25 and they demonstrate that the signal yield extracted in each p_t bin is compatible in the two cases. Even if compatible, the results are not exactly the same, so a conservative systematic error quoting the discrepancy between analyses with and without PID was introduced. This effect is of 15% at low p_t, 5% at intermediate p_t and then rise again to 10% for the high p_t region. The larger size of the systematic uncertainty at low p_t is reasonable because, as

shown in table 3.3 and figures 3.6 and 3.7 PID is used to identify particles at low p_t, while at higher p_t the only information we use from PID is the exclusion of particles outside the 3σ compatibility band. The separation in the TPC dE/dx and in time of flight of the different particle species is well reproduced in our MonteCarlo simulations, as it is well reproduced the fraction of particles that reaches the TOF detector. The effect at high p_t, where the PID contribution is less important being applied only on tracks with $p_t < 1.5$ GeV/c, can be explained by the fact that the systematic uncertainty is estimated using the yield extraction and therefore this estimation is affected by systematic contribution from yield extraction. In Pb–Pb collisions, where it is not possible to perform the D^+ analysis without PID, this estimation was done on the $D^0 \to K\pi$ channel.

The correct description of the detector conditions evolution, which can affect tracking, PID and reconstruction, was verified by analysing separately different sub–samples of data taken in different conditions and with different magnetic field orientation. The results where found to be compatible.
A further check, shown in figure 3.26 is that p_t differential raw yields extracted separately for D^+ and D^- are in agreement within statistical errors, and also the corrected yield obtained using the particle is compatible with the corrected yield obtained from the antiparticle, as shown in figure 3.27.

If the signal p_t shapes in data and MonteCarlo are different then inside a single p_t bin the efficiency corrections might be biased. When we simulate D^+ mesons in our MonteCarlo generators we make assumptions on the p_t shape of their spectrum. To quantify how much this assumption can affect our results, we calculated the MonteCarlo efficiencies, using realistic detector conditions, with two different inputs for the D^+ meson production p_t shape. The first generator we used was PYTHIA [61] with Perugia–0 [71] tuning. As a second set we used FONLL pQCD calculation[74]. At high p_t the production of D mesons follows a $\frac{dN}{dp_t} \propto p_t^{-2.5}$ trend when using PYTHIA Perugia–0, while FONLL predicts a $\frac{dN}{dp_t} \propto p_t^{-4.8}$. Although these two models predict largely different behaviour for the D mesons production, this discrepancy only produce a relative systematic error on D mesons selection efficiency of 3% at low p_t (p_t smaller then 2 GeV/c) and of 1% at higher p_t.

The estimation of the feed–down contribution to the raw yield and its subtraction is also a source of systematic uncertainty. A first way to estimate this contribution is to evaluate the uncertainty on the FONLL calculation and consider it as a systematic uncertainty on the results. As suggested in [75] this can be done by varying the b quark mass and the normalisation and factorisation scales. To evaluate the error the factorisation μ_F and renormalisation μ_R scales were varied independently in the range $0.5 < \mu/m_t < 2$ under the constrain $0.5 < \mu_F/\mu_R < 2$ where the transverse mass of the charm quark is defined as $m_t = \sqrt{p_t^2 + m_c^2}$ and the mass of the b quark was

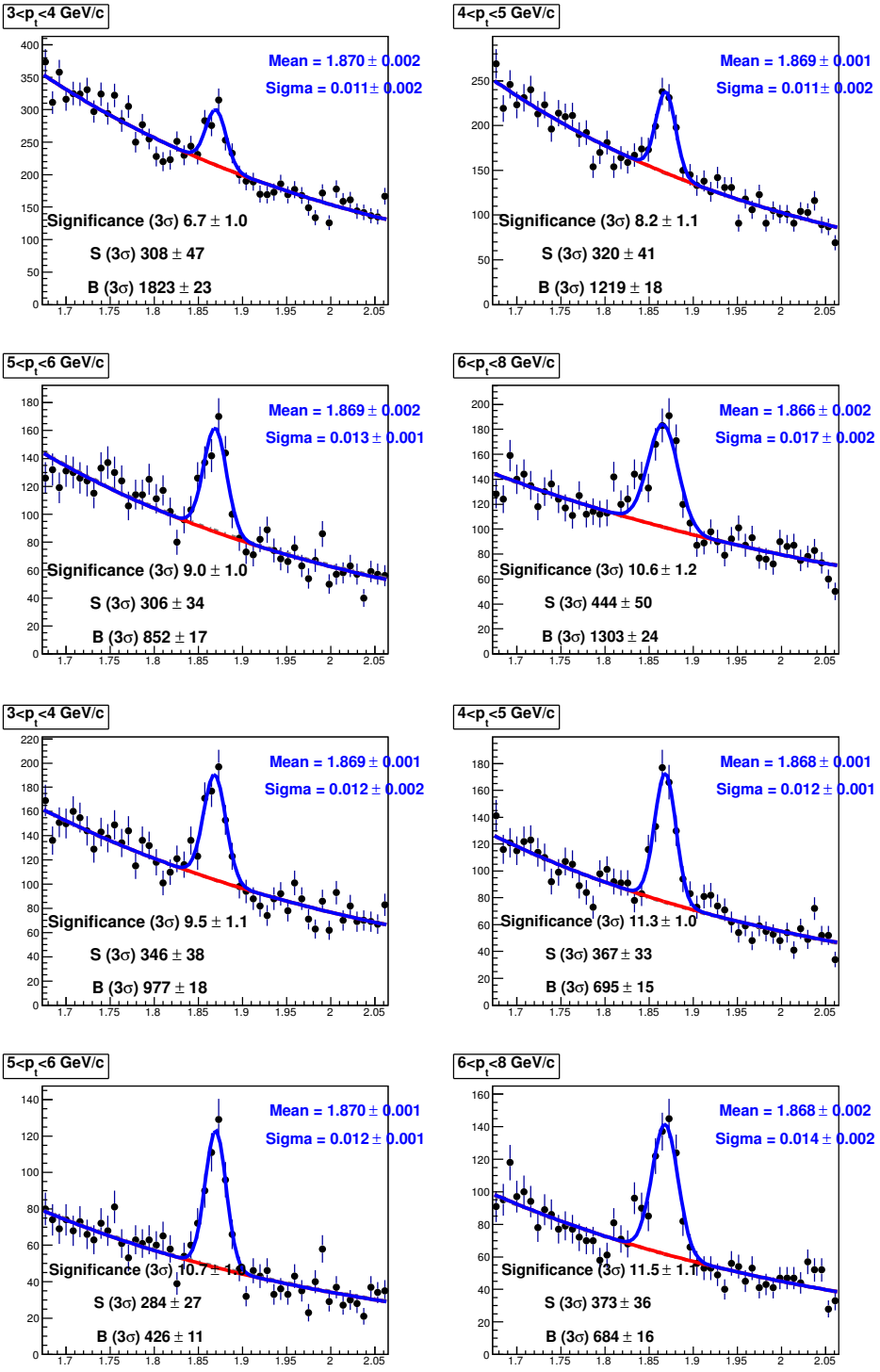

Figure 3.25: Comparison of D^+ raw invariant mass spectra without (first and second rows) and with (third and fourth rows) PID

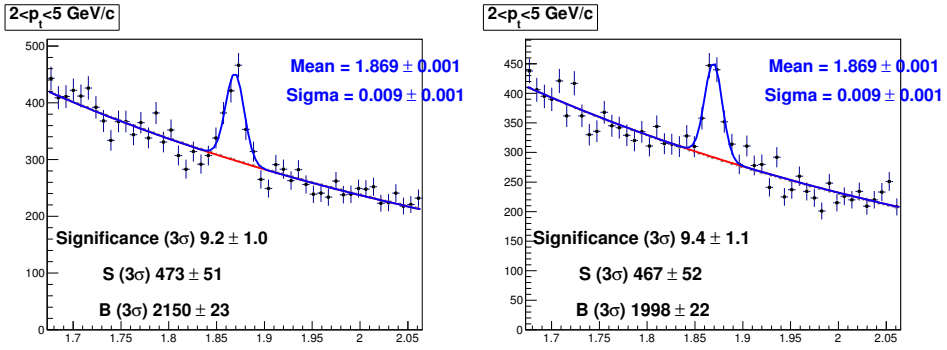

Figure 3.26: Comparison of the D^+ (left) and D^- (right) invariant mass spectra for $2 < p_t < 5$ GeV/c.

allowed to vary in the range $4.5 < m_b < 5$GeV.
Another approach consists in a different way to estimate the prompt fraction $f_{\rm prompt}$. We can use directly the prompt and feed–down fractions as predicted by FONLL calculations with their respective MonteCarlo efficiencies to obtain:

$$f_{\rm prompt} = \left(1 + \frac{\epsilon_{\rm from\ B}}{\epsilon_{\rm prompt}} \frac{\left. \frac{d\sigma^{D^+ \rm from\ B}_{\rm FONLL}}{dp_{\rm t}} \right|_{|y|<0.5}}{\left. \frac{d\sigma^{D^+}_{\rm FONLL}}{dp_{\rm t}} \right|_{|y|<0.5}} \right)^{-1} \tag{3.7}$$

The difference between this approach and the one summarised in equations 3.2 and 3.3 was included in the systematics and it is shown in figure 3.28.
It is possible to estimate the feed-down contribution also using data driven methods, as done by the CDF collaboration [40]. This possibility was implemented and studied at ALICE and is based on fitting the impact parameter distributions of prompt and secondaries D mesons in MonteCarlo simulations, and then using the obtained distributions to evaluate the contribution from the feed-down to our sample. Given the available MonteCarlo statistics this approach is not enough accurate to be used for the feed-down subtraction, but it is ready and it was tested for the D^0 candidates [76]. The prompt fraction estimated with data-driven methods is shown in figure 3.28 and compared to the value obtained using FONLL based methods.

Other small sources of systematic uncertainty, that are completely correlated in each p_t bin, are the uncertainty on the $D^+ \to K^-\pi^+\pi^+$ branching ratio from the PDG [3], that list for this decay a branching ratio of $(9.13 \pm 0.19)\%$ that accounts for a 2.1% systematic uncertainty and a 3.5% systematic error comes from the uncertainty on the minimum-bias proton-proton cross-section.
The tables summarising the different contribution to the total systematic

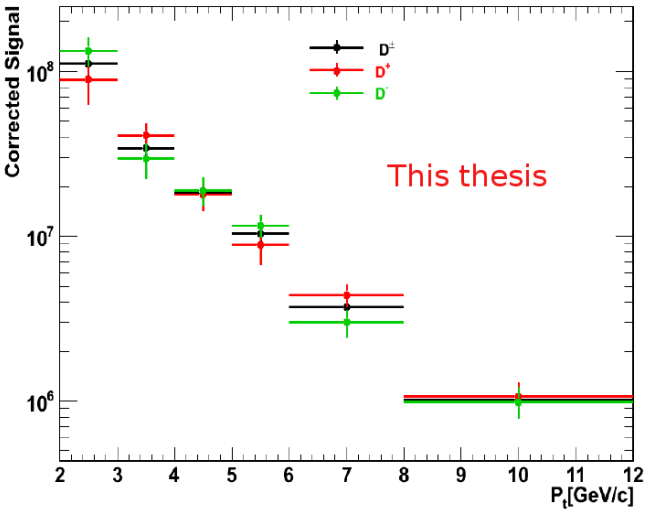

Figure 3.27: Corrected yield of D^+ (red), D^- (green) and $D^{\pm}$ (black) as a function of p_t.

uncertainty are reported in sections 3.7 and 4.2.2 for p–p and Pb–Pb respectively, while figure 3.22 shows the main contributions to the systematic uncertainty in the different p_t bins considered for the analysis.

3.8 Results at $\sqrt{s} = 7$ TeV

In the previous sections I described the procedures we used to extract the invariant mass spectra that are shown in figure 3.13 and which corrections we apply to the raw yields we extract by fitting the mass spectra in order to obtain the cross section. Also, the systematic uncertainties on the cross–section measurement were addressed. We can finally combine all these informations in order to extract the D^+ production cross–section at the LHC in proton–proton collisions at $\sqrt{s} = 7$ TeV. The value of the cross-section for the different p_t bins we used in the analysis is listed in table 3.6. The average value of the candidates p_t for each bin was computed and is reported as reference. The average p_t differs from the centre of the bin starting from $p_t > 8$ GeV/c, where the bins are larger than at lower p_t. Figure 3.29 shows the D^+ production cross-section for p-p collisions at $\sqrt{s} = 7$ TeV, compared with theoretical predictions made by FONLL [74] and GM-VFNS [77]. Both calculations used CTEQ6.6 parton distribution functions [78]. The error on the calculation was computed varying the renormalization scales μ_F and μ_R independently in the range $0.5 < \mu/m_t < 2$ under the constrain $0.5 < \mu_F/\mu_R < 2$ where the transverse mass of the charm quark is defined as $m_t = \sqrt{p_t^2 + m_c^2}$. In the FONLL calculation the charm quark mass is

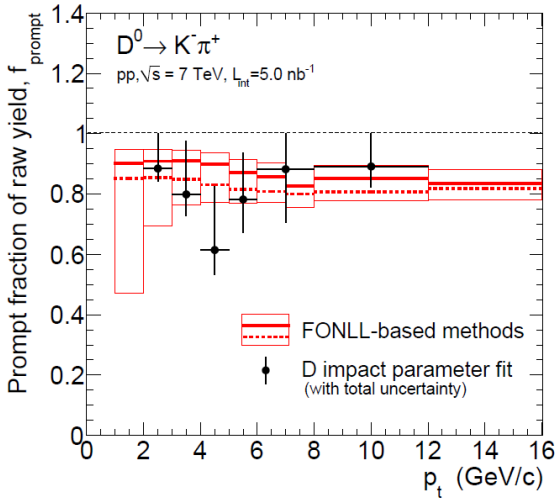

Figure 3.28: prompt fraction of the D^0 raw yield as a function of p_t for the two FONLL-based methods (solid: central value, from Eq. 3.2; dashed: alternative method,3.7) and for the impact parameter fit method (circles); the boxes show the envelope of the uncertainty bands of the two FONLL-based methods; the error bars show the total uncertainty from the impact parameter fit, including the statistical and systematic contributions.

varied in the range $1.3 < m_c < 1.7$ GeV/c^2. To compare our measurements to the theoretical models, we computed the integral of the theory in the same p_t bins we measured. Our measurement agrees with both theoretical calculations within the given uncertainties. The comparison with FONLL calculations shows that the central value of the model systematically underpredicts the positions of the cross-section, a feature already observed at lower energies at Tevatron by the CDF experiment [40] and at RHIC by the PHENIX [79] and STAR [80] collaborations. The GM-VFNS model shows an opposite behaviour, as the central values from this model are systematically above our data points, while the model was generally in good agreement with CDF data [81]. The p_t range of the visible (directly measured) cross section down to $p_t = 1$ GeV/c corresponds to probing the gluon distribution function in a x region of the order of 10^{-4} but due to the current uncertainties it is not yet possible to draw a conclusion concerning gluon saturation effects.

The total D^+ production cross-section in proton-proton collisions at $\sqrt{s} = 7$ TeV, can be obtained extrapolating the results in the region where the cross-section was measured down to $p_t = 0$ GeV/c. This was done using the ratio of the total FONLL cross-section to the FONLL cross-section in the

p_t (GeV/c)	$< p_t >$ (GeV/c)	$\frac{d\sigma}{dp_t}\|_{\|y\|<0.5} \pm stat. \pm syst.$ (μb/GeV/c)
$1 < p_t < 2$	1.5 ± 0.3	$117 \pm 23^{+39}_{-61}$
$2 < p_t < 3$	2.5 ± 0.2	$37.7 \pm 6.1^{+12.6}_{-14.5}$
$3 < p_t < 4$	3.5 ± 0.1	$20.1 \pm 2.2^{+6}_{-6.5}$
$4 < p_t < 5$	4.5 ± 0.1	$11.51 \pm 0.96^{+2.2}_{-2.64}$
$5 < p_t < 6$	5.5 ± 0.1	$4.72 \pm 0.47^{+0.92}_{-1.00}$
$6 < p_t < 7$	6.5 ± 0.1	$2.76 \pm 0.32^{+0.49}_{-0.5}$
$7 < p_t < 8$	7.4 ± 0.1	$1.50 \pm 0.22^{+0.27}_{-0.29}$
$8 < p_t < 12$	9.4 ± 0.3	$0.575 \pm 0.056^{+0.103}_{-0.115}$
$12 < p_t < 16$	13.8 ± 0.9	$0.085 \pm 0.026^{+0.019}_{-0.020}$
$16 < p_t < 24$	$17.0^{+2.0}_{-1.0}$	$0.020 \pm 0.007 \pm 0.004$

Table 3.6: D^+ cross-section in different p_t bins.

visible sector ($p_t > 1$ GeV/c). The total D^+ cross-section in proton-proton collisions at $\sqrt{s} = 7$ TeV was measured to be

$$\frac{d\sigma^{D^+}}{dy} = 248 \pm 30(\text{stat.})^{+52}_{-92}(\text{syst.}) \pm 9(\text{lumi.}) \pm 5(\text{BR})^{+57}_{-18}(\text{extr.})\mu\text{b}. \quad (3.8)$$

As we can see the systematics and extrapolation uncertainties are the main sources of uncertainty on this measurement. The main contributions to the systematic uncertainty come from the raw yield extraction at low p_t and from the tracking efficiencies. The systematic uncertainties contributions described in section 3.7 were added in quadrature, with the exception of the correlated uncertainties on the branching ratio and on the normalization.

3.8.1 Proton-Proton collisions at $\sqrt{s} = 2.76$ TeV

In April 2011 the LHC delivered a short period of proton-proton collisions at an energy of $\sqrt{s} = 2.76$ TeV. This run was meant to be used as a reference for the heavy ions runs, where the centre of mass energy is of $\sqrt{s} = 2.76$ TeV for nucleon pair. The data taking at this energy lasted 35 hours in which more than 90 million minimum bias collisions were recorded. Of these, 58 million events passed our requirements for the analysis. This statistics was not enough to use this run as a direct reference for the D meson Pb-Pb analyses, but was fundamental to cross–check our procedures to scale the cross-section measured at $\sqrt{s} = 7$ TeV to $\sqrt{s} = 2.76$ TeV, that will be explained in detail in section 4.1 and allowed us to measure the charm production cross section in an energy range in between of what was already measured at previous colliders (such as RHIC and Tevatron) and what we measured at LHC for the charm production cross section at $\sqrt{s} = 7$ TeV.

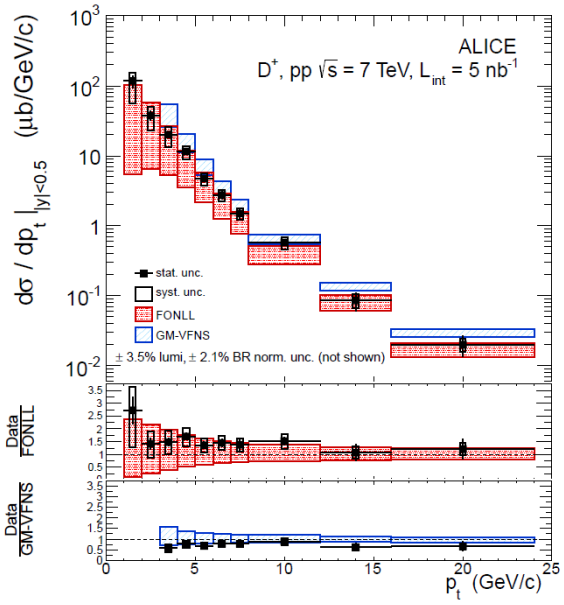

Figure 3.29: The top panel shows the D^+ production p_t differential cross–section in proton–proton collisions at $\sqrt{s} = 7$ TeV compared with predictions from FONLL [74] and GM-VFNS [77] calculations. Boxes are the total systematic uncertainty while the error bars represent the statistical error on the measurement. The data point are placed in the centre of each p_t interval. Red boxes are FONLL predictions and blue boxes are GM-VFNS calculations. 3.5% systematic uncertainty from minimum bias cross section and 2.1% uncertainty from the branching are not shown. Middle (bottom) panel shows the ratio of data over FONLL (GM-VNFS) cross-section.

The statistics available allowed us to extract signal in 4 p_t bins in the range $2 < p_t < 12$ GeV/c.

We can compute the D^+ production cross-section at $\sqrt{s} = 2.76$ TeV using the same equation (3.4) we used to compute the cross-section at $\sqrt{s} = 7$ TeV. The p_t differential cross-section is shown in figure 3.30. As for the $\sqrt{s} = 7$ TeV collisions, the comparison with theoretical models shows that both FONLL and GM-VFNS predictions are compatible with our measurement within the errors, but also that, while the central value for the FONLL prediction is systematically below data, the one from GM-VFNS calculation is systematically above.

3.8.2 Total charm production cross-section

From the measured p_t differential cross-section using the branching fraction of the c quark to D^+ mesons we can compute the total charm cross-section, integrated over p_t and rapidity. The integral of the D^+ p_t differential cross-

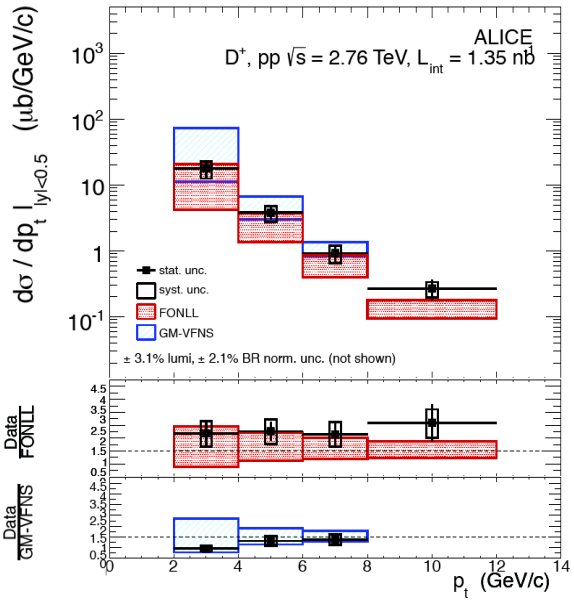

Figure 3.30: D^+ production cross-section in p-p collisions at $\sqrt{s} = 2.76$ TeV.

section computed accordingly to equation 3.4 in the pseudorapity and p_t range where we can directly measure it ($|y| < 0.5$ and $p_t > 1$ GeV/c) is what is generally called *visible cross-section*. It is possible to obtain the *total* production cross-section by extrapolating the visible cross-section by some means to the full p_t range and rapidity phase space. Most of the cross-section is given by the low p_t region. This computation was made using the ratio of the total FONLL cross-section to the FONLL cross-section in the visible sector

$$\frac{d\sigma_{\mathrm{FONLL}}}{dy}/\sigma^{\mathrm{vis}}_{\mathrm{FONLL}} = 1.25^{+0.29}_{-0.09}. \tag{3.9}$$

Assuming that this ratio is the same as the ratio between total and visible cross-sections, we can use it to extrapolate the hidden part of the cross section down to $p_t = 0$ GeV/c. For the extrapolation to the full rapidity we used FONLL to estimate the missing part of the cross-section. The total charm production cross-section was computed separately for the three mesons reconstructed with ALICE (D^0 and D^{*+}) and the final total charm cross-section is computed as the weighted average of the three. The result is

$$\sigma^{2.76\mathrm{TeV}}_{tot,c\bar{c}} = 4.10 \pm 0.43(\mathrm{stat.})^{+0.82}_{-.0.75}(\mathrm{syst.}) \pm 0.10(\mathrm{lumi.})^{+0.96}_{-0.93}(\mathrm{extr.})\mathrm{mb} \tag{3.10}$$

for the proton-proton collisions at $\sqrt{s} = 2.76$ TeV and

$$\sigma^{7\mathrm{TeV}}_{tot,c\bar{c}} = 8.48 \pm 0.48(\mathrm{stat.})^{+1.03}_{-.2.34}(\mathrm{syst.}) \pm 0.24(\mathrm{lumi.})^{+1.30}_{-0.29}(\mathrm{extr.})\mathrm{mb} \tag{3.11}$$

for collisions at $\sqrt{s} = 7$ TeV. These results are compared in figure 3.31 to the results obtained at lower energies as well to results from LHCb and ATLAS experiments at $\sqrt{s} = 7$ TeV. The results obtained by the three LHC experiments at $\sqrt{s} = 7$ TeV are in nice agreement within the uncertainties while ALICE is the only experiment that has measured the charm production cross-section at $\sqrt{s} = 2.76$ TeV so far. Looking at the comparison between experimental and pQCD NLO [36] results can be observed that results are compatible within the theoretical uncertainties and that the energy dependence of the charm production is well described by the theory over a very large range of energies, although the data points always lie on the upper edge of the theoretical band.

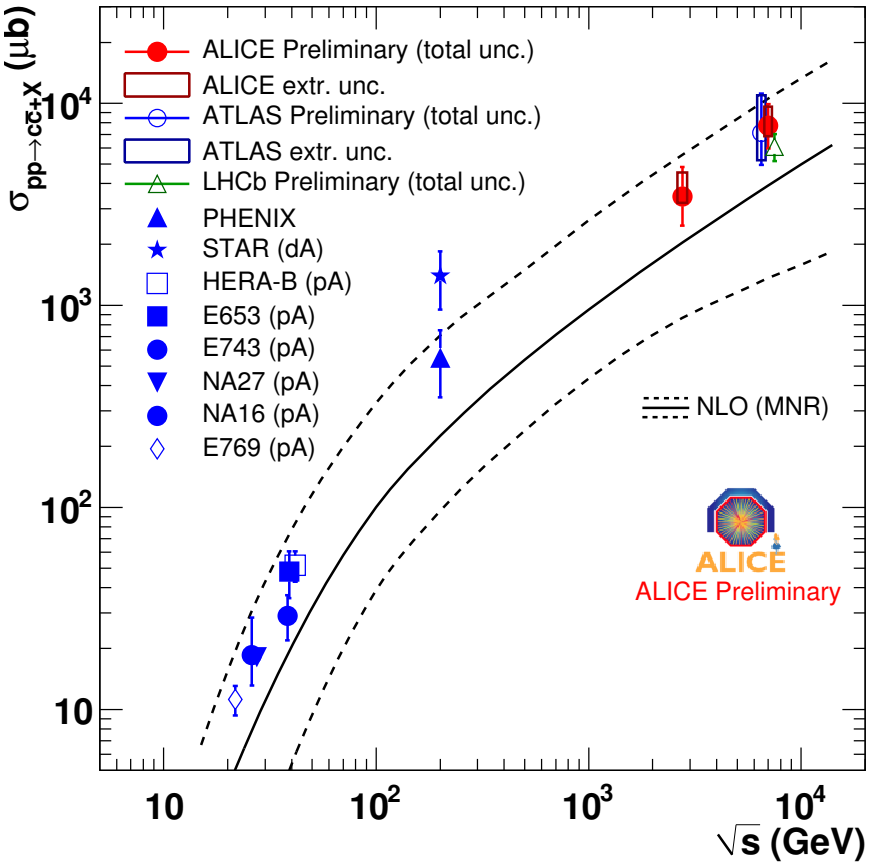

Figure 3.31: Total charm production cross-section at ALICE and other experiments. The ALICE data point at $\sqrt{s} = 7$ TeV is in good agreement with analogue measurements made by ATLAS and LHCb. Lines are pQCD calculation at next to leading order (MNR).

4

Charmed meson in Heavy Ion collisions

Charm quarks are among the most powerful probes for QGP medium. Having a large mass they are mainly produced at the very beginning of the collision in the scattering among the colliding partons (with a smaller fraction produced later in the medium) and they experience all the stages of the medium evolution. In this chapter, I will present the D^+ energy loss and the elliptic flow analyses results from Pb-Pb collisions at $\sqrt{s_{NN}} = 2.76$ TeV. The data sample used in the analyses is composed of $\sim 17 \cdot 10^6$ minimum bias triggers collected by ALICE in November 2010 (period LHC10h). In the first section (4.1) I will discuss the differences between the strategy used for the Pb-Pb analyses and the one used in p-p and described in chapter 3. Among these differences there is the cut selection, which has to be tighter to deal with a much larger combinatorial background (section 4.1.2) and the selection of the collision centrality, discussed in section 4.1.1. The main physics observables that will be discussed are the D^+ nuclear modification factor $R_{\rm AA}$ and its elliptic flow, that are treated in sections 4.2 and 4.3 respectively.
The nuclear modification factor allows to study the energy loss of the charm quark in the medium. To perform such a study, the D^+ production cross-section in proton-proton collisions at $\sqrt{s} = 7$ TeV, discussed in chapter 3, after scaling it to the energy of the collision between two nucleons of incoming Pb ions ($\sqrt{s_{NN}} = 2.76$ TeV) is used as reference. The proton-proton reference scaling is described in section 4.2.1, while in section 4.2.2 the systematic uncertainties affecting the $R_{\rm AA}$ measurement are discussed.
The study of the elliptic flow of the charmed mesons can provide useful information on the medium thermalisation. We will give the details on its measurement for the D^+ meson in section 4.3. The 2010 Pb-Pb statistics is not enough to provide a conclusive statement on this measurement, but the analysis tools are ready and they have been tested against MonteCarlo simulation and on the light hadron elliptic flow. These tests are described

in section 4.3.2.

4.1 Analysis strategy for D^+ in Pb-Pb

One important difference between proton-proton and heavy ion collisions is that the heavy ion collisions can be classified accordingly to the impact parameter, a number that characterise the collision *centrality*. The centrality estimation is an important criterium for the study of QGP properties, as medium size and density depend on it. The centrality has a strong correlation with the multiplicity of particles produced in the collision, on the number of reconstructed D^+ candidates and on the D^+ production, which being mainly a hard process scales with the number of nucleon-nucleon (binary) collisions $N_{\rm coll}$. It is also useful to remind that the nuclear modification factor, defined in chapter 1 (equation 1.9) is directly dependent on the centrality, and that the elliptic flow, being originated by initial spatial asymmetries in the colliding nuclei overlap region, is expected to reach its maximum value at intermediate and semi-peripheral centrality values.
The strategy used for the D^+ analyses in Pb-Pb collisions is similar to what is done in the proton-proton collision analysis. The raw signal yield is obtained by fitting a gaussian plus exponential shape to the invariant mass distribution of D^+ candidates. Those candidates must pass a set of topological selection cuts, reported in table 4.2 and 4.3 as a function of the candidate p_t for central and peripheral events respectively. These cuts have been optimized in order to have at the same time a good statistical significance, enough statistics in the MonteCarlo simulations to estimate the efficiencies with small uncertainties, a gaussian peak from the fit to the invariant mass distribution with a gaussian mean compatible with the PDG value of D^+ mass and a σ compatible with what obtained in the MonteCarlo simulations and what observed in proton-proton collisions for the same p_t range. As in Pb-Pb collisions the combinatorial background is much larger than in proton-proton, due to the larger number of tracks produced in the Pb-Pb collisions, much tighter selection cuts have to be applied to the candidates and at the filtering level to keep the CPU processing time at a reasonable level. This, and the limited statistics, prevented us from reaching the same low p_t region reached in proton-proton collisions at $\sqrt{s} = 7$ TeV. The $R_{\rm AA}$ analysis requires to compute the corrected yields, with a procedure analogue to what is done for proton-proton collisions analysis for the efficiencies correction and feed-down subtraction, while the elliptic flow measurement uses directly the measured raw yields.

4.1.1 Centrality selection

It is possible to perform the centrality estimation in ALICE using different detectors [83]. The collision geometry for the centrality analysis was stud-

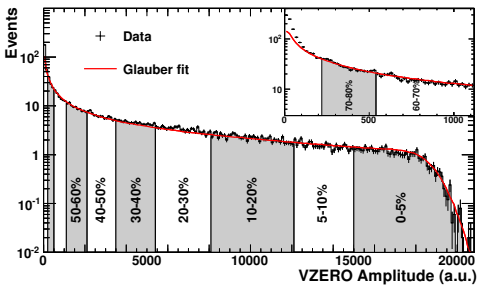

Figure 4.1: Distribution of the VZERO scintillators amplitudes sum for event compared to Glauber fit [82].

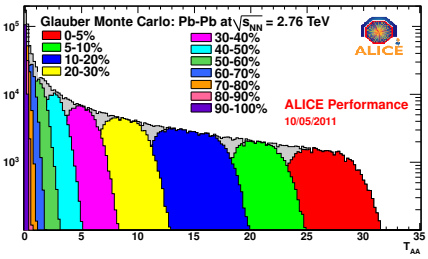

Figure 4.2: Nuclear overlap function for the different centrality class.

ied using the Glauber model, already described in section 1.2.1, assuming a Woods-Saxon distribution for the nucleon density profile inside the colliding nuclei. The integral of the convolution of the two distributions in the overlap geometrical region is called *nuclear overlap function* T_{AA} [84]. Some centrality classes in the range 0-80% with their corresponding values of average T_{AA}, N_{part} and N_{coll} evaluated in a pure Glauber model are reported in table 4.1. The centrality information can be obtained experimentally by the multiplicity in the VZERO scintillators, the number of tracks in the TPC, the number of clusters in the SPD layers or the number of tracklets in the SPD, the multiplicity in the FMD, the energy deposited in the ZDC calorimeters by the spectator nucleons, which for central events (up to 40% centrality) is correlated with the energy deposited in the ZEM electromagnetic calorimeters to remove bias from nuclear fragments. For the D^+ analyses the centrality estimation was done mainly using the multiplicities from the VZERO scintillators (abbreviated as V0M). The distribution of the VZERO signal amplitude, that is proportional to the recorded multiplicity, is shown in figure 4.1 for minimum bias events, where the centrality percentiles are also indicated. The centrality percentile 0-5% contains the 5% most central events. The shape of the distribution is typical for most centrality observables, with a large number of entries at low VZERO amplitudes corresponding to the most peripheral collisions that are contaminated by electro-magnetic background and trigger inefficiencies, a slowly decreasing region corresponding to semi-central events and then the edge of the distribution whose shape depends on the characteristics of the used detector and its resolution. The VZERO distribution is compared to Glauber MonteCarlo simulation convoluted with a negative binomial distribution that models the relation between the number of produced particles $N_{primary}$, the number of participants N_{part} and collisions N_{coll} according to the rule

$$N_{primary} = f \cdot N_{part} + (1 - f)\, N_{coll} \tag{4.1}$$

where the parameter $f = 80.6\%$ quantifying the relative contributions of N_{part} and N_{coll} is extracted from the fit. The number of participants per centrality class obtained as percentile of the geometrical cross section from a Glauber MonteCarlo is shown in figure 4.2.

Centrality class	$\langle N_{part} \rangle$	$\langle N_{coll} \rangle$	$\langle T_{AA} \rangle$ (mb^{-1})
0–20%	308 ± 3	1211 ± 131	18.93 ± 0.74
40–80%	46 ± 2	77 ± 8	1.20 ± 0.07
0–10%	357 ± 4	1503 ± 170	23.48 ± 0.97
10–20%	261 ± 4	923 ± 100	14.43 ± 0.57
20–40%	157 ± 3	439 ± 44	6.85 ± 0.28
40–60%	69 ± 2	128 ± 13	2.00 ± 0.11
60–80%	23 ± 1	27 ± 2	0.42 ± 0.03

Table 4.1: Average values of the number of participating nucleons, the number of binary collisions, and of the nuclear overlap function for the considered centrality classes, expressed as percentiles of the nuclear cross section from Glauber model.

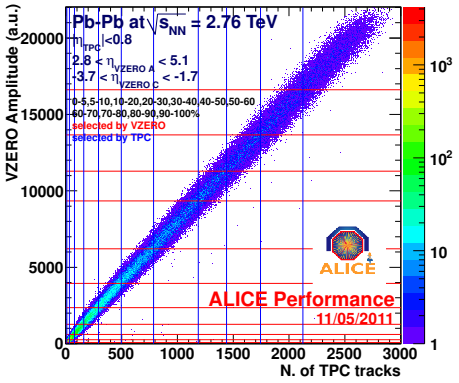

Figure 4.3: Distribution of VZERO amplitude versus number of tracks in TPC. Red lines show centrality percentiles selected by VZERO, blue lines from TPC.

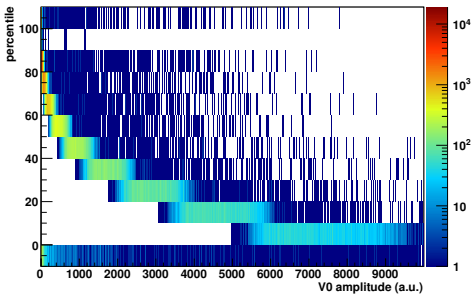

Figure 4.4: Distribution of VZERO amplitude per centrality intervals. Events with centrality$<$ 0 are outliers. Events with centrality$=$ 100% are showed in the upper bin.

In the open-charm analyses we define as *central events* the events in the centrality class 0-20% and *peripheral* events those in the 40-80% centrality class. I will also define a *semi-peripheral* class of events for the centrality class 30-50% that will be used for the elliptic flow study. We study events up to 80% centrality. The results presented in this chapter are from $3.19 \cdot 10^6$ central events and $6.9 \cdot 10^6$ peripheral events, for a total $\sim 13 \cdot 10^6$

events collected in 0-80% centrality, corresponding to an integrated luminosity of $2.12 \pm 0.07 \mu b^{-1}$[1]. The performance of the V0M centrality estimator is studied on a run-by-run basis and cross-checked against the centrality estimated from the number of tracks in the TPC. Events that are more than 7 σ away from the distribution of TPC tracks versus V0M centrality are rejected at the analysis level as outliers. The correlation between number of TPC tracks and VZERO amplitudes is shown in figure 4.3. Due to binning reasons, ultra-peripheral events with centrality 100% are showed in the top percentile, while outliers events are stored in the centrality smaller than 0 bin. The distribution of VZERO amplitudes as a function of centrality for the events selected in our analysis is shown in figure 4.4. Figure 4.5 shows the fraction of events collected in the 0-20% centrality class over the number of events in the 0-80% centrality class for the different run analysed. We decided to normalize to the number of events in 0-80% instead of 0-100% as this is the centrality range we consider for our analyses.

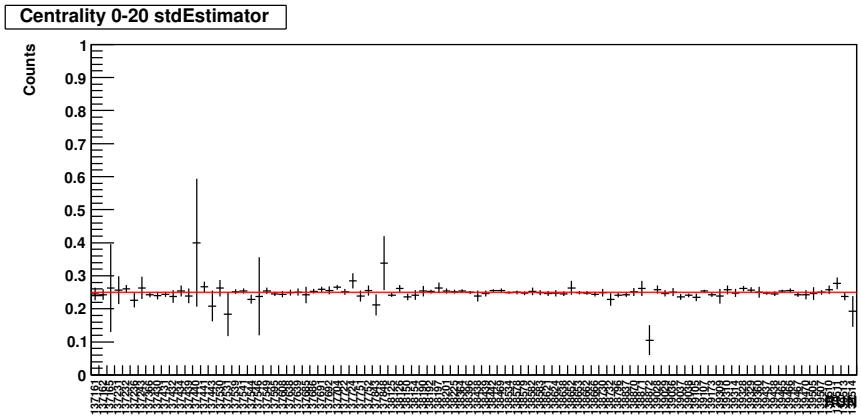

Figure 4.5: Fraction of events in 0-20% centrality with respect to the events in 0-80% centrality using V0M estimator. Red line shows the ratio 0.2/0.8

4.1.2 Cut selection

In Pb-Pb collisions, and especially in central Pb-Pb collisions, there is a much larger combinatorial background than in proton-proton collisions. To keep an acceptable CPU time in the filtering procedure, tighter filtering cuts are applied with respect to the cuts applied in proton-proton collisions. In central events a cut on the single track impact parameter $|d_0| > 75 \mu$m is applied on tracks with $p_t < 2$ GeV/c, the minimum p_t of the tracks

[1]Given the hadronic cross-section in 0-100% centrality $\sigma = 7.654 \pm 0.25$ b and the number of events N^{0-20} collected in 0-20% for our analyses, the luminosity is estimated as $N^{0-20}/0.2/\sigma$. The electromagnetic contamination is negligible and the trigger efficiency is almost 100%.

has to be $p_t > 0.7$ GeV/c and the minimum candidate p_t has to be $p_t > 3$ GeV/c. A large fraction of candidates with $p_t < 3$ GeV/c (more than 80% for candidates with $p_t \sim 3$ GeV/c from simple MonteCarlo simulations) would be in any case rejected by the track minimum p_t cut. As for the proton-proton analysis, the candidate selection cuts in Pb-Pb collisions are optimised in each p_t bin in order to reach a good statistical significance, high enough efficiencies and gaussian mean of the signal peak compatible with the D^+ mass from the PDG. Moreover, the gaussian σ is required to be compatible with what observed in proton-proton collisions in the same p_t bin and with MonteCarlo simulations. The topological candidate selection cuts have also been tightened with respect to the proton-proton analysis. This was required by the need of rejecting a larger fraction of combinatorial background. Tables 4.2 and 4.3 list the selection cuts applied to candidates in central and peripheral events respectively. For non-central events, where the multiplicity is lower, it was possible to release the minimum track p_t cut in the filtering down to $p_t > 0.5$ GeV/c and the impact parameter cut to $|d_0| > 25\mu$m for the tracks with $p_t < 2$ GeV/c. The cuts on the decay length in the transverse plane normalized to its error (normalized decay length XY) and the cut on the cosine of the pointing angle in the transverse plane $\cos\theta^{XY}_{point}$ are not applied in proton-proton analysis and were introduced to increase the significance in the Pb-Pb analysis. An effect of the large combinatorial background is that the p_t range in which the D^+ signal was observed with the 2010 statistics for central Pb-Pb collisions at $\sqrt{s_{NN}} = 2.76$ TeV is limited to $6 < p_t < 16$ GeV/c, with the signal observed in three p_t bins ($6 < p_t < 8$ GeV/c, $8 < p_t < 12$ GeV/c, $12 < p_t < 16$ GeV/c). The efficiencies are lower than the proton-proton ones, as tighter cuts have been applied. For peripheral collisions it was possible to measure the D^+ in the range reach $3 < p_t < 12$ GeV/c. The invariant mass distributions of D^+ candidates measured in the different p_t bins is shown in figure 4.6 and 4.7 for central and peripheral Pb-Pb collisions respectively. The analysis of 2011 data should allow to enlarge the p_t range towards lower values in central events and towards higher values in peripheral collisions.

4.2 R_{AA}

We define the D^+ nuclear modification factor $R_{\rm AA}$ as

$$R_{\rm AA}(p_t) = \frac{1}{\langle T_{\rm AA}\rangle} \cdot \frac{dN_{\rm AA}/dp_t}{d\sigma_{\rm pp}/dp_t}, \tag{4.2}$$

where $dN_{\rm AA}/dp_t$ is the corrected prompt D^+ p_t spectra measured in Pb-Pb collisions at $\sqrt{s_{NN}} = 2.76$ TeV and $d\sigma_{\rm pp}/dp_t$ is the D^+ production cross-section in proton-proton collisions. This was obtained from the one at $\sqrt{s} = 7$ TeV scaled down to $\sqrt{s} = 2.76$ TeV. $\langle T_{\rm AA}\rangle$ is the average of the nuclear

p_t [GeV/c]	6 <p_t< 8	8 <p_t< 12	12 <p_t< 16
Inv. Mass [GeV]	0.2	0.2	0.2
p_t^K [GeV/c]	0.8	0.8	0.8
p_t^π [GeV/c]	0.8	0.8	0.8
$\lvert d_0^k \rvert$ [μm]	75	75	75
$\lvert d_0^\pi \rvert$ [μm]	75	75	75
$\mathrm{dist}_{1\text{-}2}$[cm]	0.01	0.01	0.01
σ_{vertex} [cm]	0.0233	0.0233	0.0233
Dec. len. [cm]	0.14	0.0995	0.1265
p_t^{max} [GeV/c]	2	0.5	0.5
$\cos\theta_{point}$	0.995	0.99	0.98
$\sum d_0^2$ [cm^2]	$8.83 \cdot 10^{-4}$	$8.83 \cdot 10^{-4}$	$8.83 \cdot 10^{-4}$
DCA [cm]	10^{10}	10^{10}	10^{10}
Norm. Dec. len. XY	10	6	14
$\cos\theta_{point}^{XY}$	0.997	0	0

Table 4.2: Cut values on the D^+ candidate triplets in Pb–Pb collisions at $\sqrt{s_{NN}} = 2.76$ TeV.

p_t [GeV/c]	3 <p_t< 4	4 <p_t< 6	6 <p_t< 8	8 <p_t< 12
Inv. Mass [GeV]	0.2	0.2	0.2	0.2
p_t^K [GeV/c]	0.5	0.5	0.5	0.5
p_t^π [GeV/c]	0.5	0.5	0.5	0.5
$\lvert d_0^k \rvert$ [μm]	25	25	25	25
$\lvert d_0^\pi \rvert$ [μm]	25	25	25	25
$\mathrm{dist}_{1\text{-}2}$[cm]	0.01	0.01	0.01	0.01
σ_{vertex} [cm]	0.0207	0.0233	0.0287	0.0233
Dec. len. [cm]	0.14	0.19	0.113	0.122
p_t^{max} [GeV/c]	0.5	2	0.5	0.5
$\cos\theta_{point}$	0.99	0.99	0.957	0.966
$\sum d_0^2$ [cm^2]	$8.83 \cdot 10^{-4}$	$8.83 \cdot 10^{-4}$	$8.83 \cdot 10^{-4}$	$8.83 \cdot 10^{-4}$
DCA [cm]	10^{10}	10^{10}	10^{10}	10^{10}
Norm. Dec. len. XY	12	12	8	8
$\cos\theta_{point}^{XY}$	0.993	0.993	0	0

Table 4.3: Cut values on the D^+ candidate triplets in Pb–Pb collisions at $\sqrt{s_{NN}} = 2.76$ TeV.

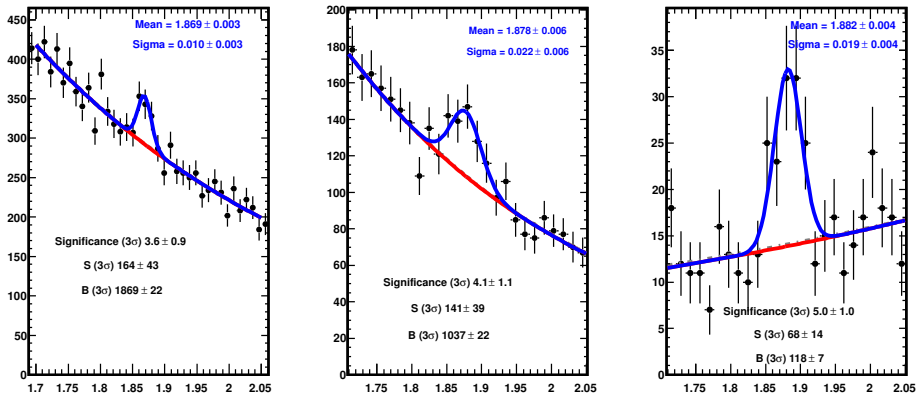

Figure 4.6: D^+ invariant mass spectra from $3.19 \cdot 10^6$ central (0-20%) Pb-Pb collisions at $\sqrt{s_{NN}} = 2.76$ TeV for 6 <p_t< 8 GeV/c (left), 8 <p_t< 12 GeV/c (middle), 12 <p_t< 16 GeV/c (right).

overlap function in the centrality range considered for the calculation. The scaling procedure is discussed in section 4.2.1. The D^+ R_{AA} is an interesting probe for QGP properties. The charm is expected to be suppressed by the presence of a medium because of parton energy loss occurring via gluon radiation and collisions with partons.

The efficiencies have been computed using charm-enriched MonteCarlo simulations, as in the proton-proton analysis. Minimum bias Pb-Pb collisions at $\sqrt{s_{NN}} = 2.76$ TeV were simulated using HIJING event generator and GEANT3 transport code. To enrich the charm and beauty content of the MonteCarlo, on top of each minimum bias event, proton-proton events from PYTHIA v6.4.21 event generator where added, with each injected events having at least one $c\bar{c}$ or $b\bar{b}$ pair and D mesons forced to decay through their hadronic channels. The number of PYTHIA events added to each minimum bias event was tuned on the basis of the HIJING event centrality. 20 PYTHIA events are added to HIJING events with an impact parameter $b < 5$ fm, while for the other HIJING collisions the number of events is determined according to the formula $N = \frac{80}{3}(1 - \frac{b}{20})$. The efficiencies were computed in each centrality class using simulated events that reproduced the charged particle multiplicity and detector occupancy in that centrality class. They have in any case been tested to be almost independent from the centrality for the D^0 analysis. The factor of acceptance multiplied by efficiencies for each p_t bin is shown in figure 4.8 for both Pb-Pb central and peripheral collisions. The differences between the central and peripheral collisions, visible in figure 4.8 is due to the different cut selection we apply in the two cases. The fiducial acceptance range increases smoothly from

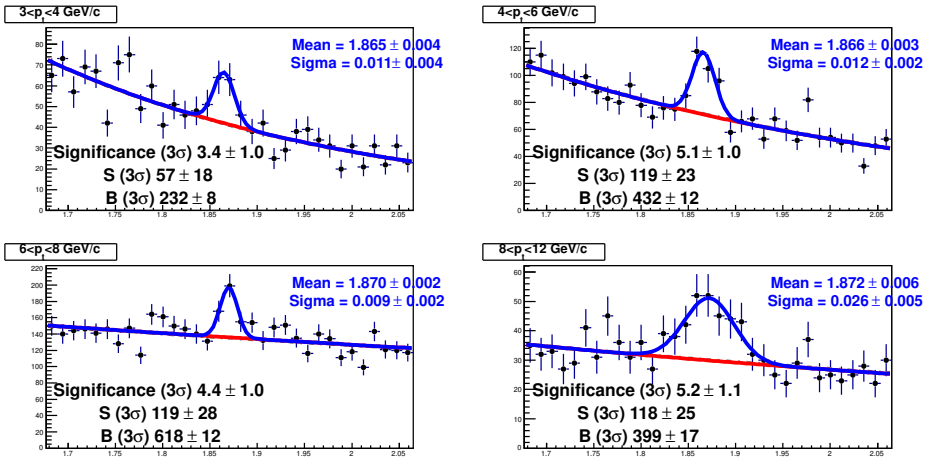

Figure 4.7: D^+ invariant mass spectra from $6.9 \cdot 10^6$ peripheral (40-80%) Pb-Pb collisions at $\sqrt{s_{NN}} = 2.76$ TeV.

$|y| < y_{\rm fid} = 0.5$ at low p_t to $|y| < y_{\rm fid} = 0.8$ for $p_t > 5$ GeV/c. As expected, the efficiency for feed-down D^+ is higher than the one of the prompt candidates.

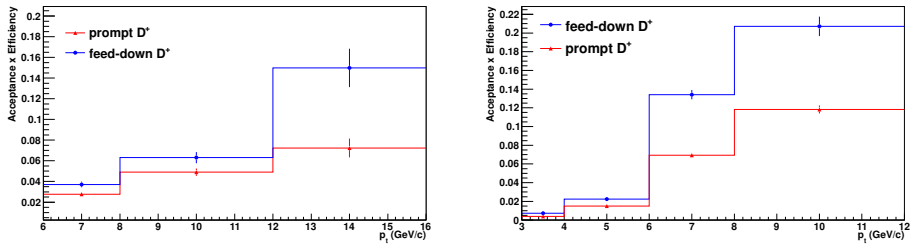

Figure 4.8: Efficiencies for prompt (red triangles) and feed-down (blue circles) D^+ candidates in Pb-Pb central (left) and peripheral (right) collisions

The feed-down subtraction was performed using the same method described in section 3.5.2 for the proton-proton collisions at $\sqrt{s} = 7$ TeV, and using equation 3.2 to define the prompt fraction $f_{\rm prompt}$. Hence the number of D^+ candidates coming from beauty decays is computed starting from the beauty cross-sections from FONLL calculations. The kinematics of the B→D decay was taken from the EvtGen [85] package and the feed-down meson efficiency was obtained from MonteCarlo simulations with realistic detector conditions. The feed-down cross-section was estimated by scaling, in each centrality class, the FONLL feed-down cross-section in proton-proton collisions at $\sqrt{s} = 2.76$ TeV by the average of the nuclear overlap function $\langle T_{\rm AA} \rangle$. As the beauty can be suppressed in Pb-Pb collision by the presence

of the medium, the feed-down cross-section was corrected also by the beauty nuclear modification factor in the medium $R_{\rm AA}^{\rm feed\text{-}down}$ of the $\rm D^+$ meson coming from B decays. The prompt fraction $f_{\rm prompt}$ can therefore be written as:

$$f_{\rm prompt} = 1 - \frac{N_{\rm raw}^{\rm feed\text{-}down}}{N_{\rm raw}^{\rm prompt}} = \\ = 1 - \langle T_{\rm AA} \rangle \cdot \left(\frac{d^2\sigma}{dydp_t} \right)_{\rm FONLL}^{\rm feed\text{-}down} \cdot R_{\rm AA}^{\rm feed\text{-}down} \cdot \frac{({\rm Acc} \times \epsilon)^{\rm feed\text{-}down} \Delta y \Delta p_t ({\rm BR}) N_{\rm evt}}{N_{\rm raw}/2} \tag{4.3}$$

where the $\rm p_t$ dependence symbol has been omitted for brevity. As the beauty suppression in the medium is not known, $R_{\rm AA}^{\rm feed\text{-}down}$ is a parameter of the calculation. The central values for the results of prompt $\rm D^+$ $R_{\rm AA}$ and corrected yield presented in this chapter are obtained under the assumption that $R_{\rm AA}^{\rm feed\text{-}down} = R_{\rm AA}^{\rm prompt}$. The systematic uncertainty related to this assumption was estimated letting the ratio between feed-down and prompt nuclear modification factors to vary in the range $\frac{1}{3} < R_{\rm AA}^{\rm feed\text{-}down}/R_{\rm AA}^{\rm prompt} < 3$. The implications and tests of this hypothesis are discussed in section 4.2.2.

The corrected $\rm D^+$ yield measured from $N_{\rm evt}$ analysed events in a given centrality class can be obtained in the same way as it was done for the proton-proton case using the formula

$$\left. \frac{{\rm d}N^{\rm D^+}}{{\rm d}p_{\rm t}} \right|_{|y|<0.5} = \frac{1}{2} \frac{1}{\Delta y \, \Delta p_{\rm t}} \frac{f_{\rm prompt}(p_{\rm t}) \cdot N^{\rm D^\pm \ raw}(p_{\rm t})\Big|_{|y|<y_{\rm fid}}}{({\rm Acc} \times \epsilon)_{\rm prompt}(p_{\rm t}) \cdot {\rm BR} \cdot N_{\rm evt}}. \tag{4.4}$$

4.2.1 Proton-proton reference

To evaluate the $R_{\rm AA}$ both the numerator and denominator of the fraction in eq. 1.9 must be taken at the same energy. In the case of the $\rm D^+$ analysis at ALICE the center of mass energy for a Pb-Pb collision is $\sqrt{s} = 2.76$ TeV per nucleon-nucleon pair, while the proton-proton collisions data are taken at a centre of mass energy of $\sqrt{s} = 7$ TeV. Therefore the $\sqrt{s} = 7$ TeV data have to be rescaled to the proper energy value. LHC delivered also a period of proton-proton collisions at $\sqrt{s} = 2.76$ TeV, but due to limited statistics it could not be used as a reference for the $\rm D^+$ $R_{\rm AA}$. The estimation of the rescaling factor was based on FONLL pQCD calculations, and is obtained as the ratio of the FONLL cross-section at the two energies [86], so that the reference rescaled cross-section at $\sqrt{s} = 2.76$ TeV is:

$$\sigma^{D^+}(p_t; 2.76) = \frac{\sigma^{\rm FONLL}(p_t; 2.76)}{\sigma^{\rm FONLL}(p_t; 7)} \sigma^{D^+}(p_t, 7) \tag{4.5}$$

where $\sigma^{D^+}(p_t; 7)$ is the cross-section measured in the $\rm p_t$ bin p_t at $\sqrt{s} = 7$ TeV and $\sigma^{\rm FONLL}(p_t; X)$ is the integral of the FONLL cross-section in the same $\rm p_t$

bin at the energy X. To evaluate the uncertainty on this ratio, the FONLL factorization (μ_F) and renormalization (μ_R) scales and the charm quark mass (m_c) were varied in the ranges $0.5 < \frac{\mu_F}{m_T} < 2$, $0.5 < \frac{\mu_R}{m_T} < 2$ (being m_T the parton transverse mass) and $1.3 < m_c < 1.7$ GeV under the constraint $0.5 < \frac{\mu_F}{\mu_R} < 2$. The central values for the calculation are assumed to be

$$\frac{\mu_F}{m_T} = \frac{\mu_R}{m_T} = 1$$

and $m_c = 1.5$ GeV. The spread of the ratio $\frac{\sigma^{\mathrm{FONLL}}(p_t;2.76)}{\sigma^{\mathrm{FONLL}}(p_t;7)}$, when varying the parameters coherently for the FONLL cross-section at $\sqrt{s} = 2.76$ TeV $\sigma^{\mathrm{FONLL}}(p_t;2.76)$ and he one at $\sqrt{s} = 7$ TeV $\sigma^{\mathrm{FONLL}}(p_t;7)$, is considered as systematic uncertainty on the scaling. The total uncertainty on the rescaled cross-section is then given by the rescaling uncertainty and by the original uncertainty on the measured cross-section. The value of the scaling factor in the $\sqrt{s} = 7$ TeV $\mathrm{p_t}$ binning for different combinations of the FONLL parameters is shown in figure 4.9. The rescaling procedure has been cross-checked with three independent methods. The first method is to perform the extrapolation down to the Tevatron center of mass energy ($\sqrt{s} = 1.76$ TeV) where the charm-cross section was measured by the CDF experiment. The rescaled cross-section was found to be compatible with the one measured by CDF in all $\mathrm{p_t}$ bins. As a second cross-check, the interpolation was done using GM-VFNS computations for the theoretical cross-section instead of FONLL. Also in this case the results are compatible within errors. Finally, the rescaled cross-section was compared with the $\mathrm{D^+}$ cross-section measured in proton-proton collisions at $\sqrt{s} = 2.76$ TeV. Figure 4.12 shows the ratio between the measured $\mathrm{D^+}$ cross-section at $\sqrt{s} = 2.76$ TeV and the rescaled $\sqrt{s} = 7$ TeV cross-section for three $\mathrm{p_t}$ bins. For both the mesons, results are compatible with 1 within the errors.

4.2.2 Systematics in Pb–Pb

The relative systematic uncertainties for the $\mathrm{D^+}$ yield extraction in central and peripheral Pb-Pb collisions are shown in figure 4.10 while table 4.4 summarise the systematic uncertaintied on the $\mathrm{D^+}$ R_{AA}. Some of the sources of systematic uncertainty affecting the corrected yield extraction were already described in section 3.7.

The uncertainty on the yield extraction was estimated fitting the invariant mass spectra in each $\mathrm{p_t}$ bin varying the binning, the fit range and using a parabola instead of an exponential for the background distribution. Also, a method based on counting the signal after background subtraction, instead of performing a fit to the signal peak, was used as comparison. The half difference between the maximum and minimum values for the yield is quoted as systematic uncertainty and its value ranges from a maximum of 20% for

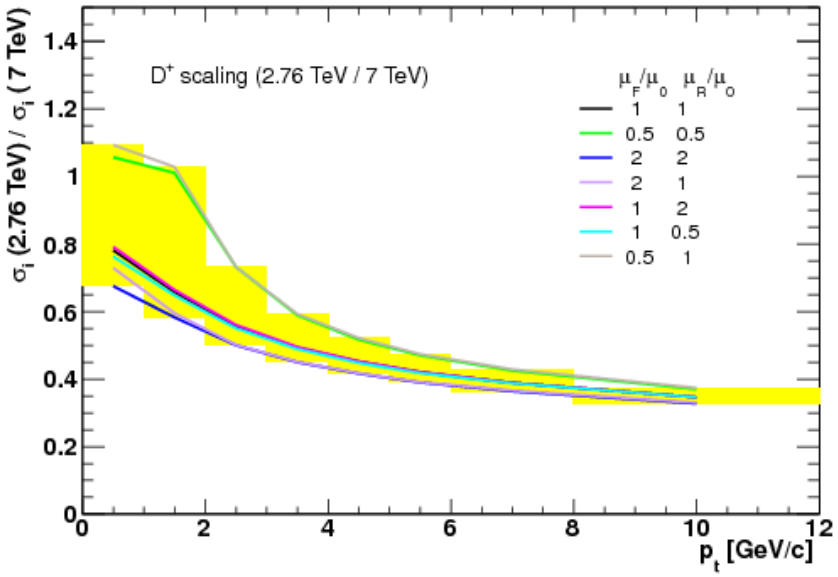

Figure 4.9: Ratio of D^+ cross-section at $\sqrt{s} = 2.76$ TeV and at $\sqrt{s} = 7$ TeV from FONLL with different parameter choices. Black line is the central value, yellow band is the resulting uncertainty for the D^+ with the $\sqrt{s} = 7$ TeV p_t binning.

the lowest p_t bin in central collisions ($6 < p_t < 8$) to a minimum of 5% for the intermediate p_t bin in peripheral events. This source of systematic uncertainty strongly depends on the fit quality, and is therefore minimum in conditions of high significance, as in the intermediate p_t in 40-80% centrality, while it increases when the significance is low, as it is the case for the 0-20% centrality at low p_t.

The systematic uncertainty on the tracking efficiency was estimated comparing the efficiencies of track finding in the TPC and track prolongation from the TPC to the ITS between data and MonteCarlo simulations and changing the track quality selection. The efficiency of track prolongation towards the ITS was found to be described by MonteCarlo at a level of 3%, while the cut quality selection accounts for a 4% effect, giving a total 5% systematic uncertainty per track, stable against p_t and centrality. The total tracking efficiency systematic uncertainty for the $D^+ \to K^-\pi^+\pi^+$ (three-prong) amounts therefore to 15%.

The systematic uncertainty due to the cut selection was estimated by extracting the D^+ corrected yield using different sets of cuts, and taking as a systematic uncertainty the difference between the central value and the ones obtained with the different cuts. This systematic uncertainty also

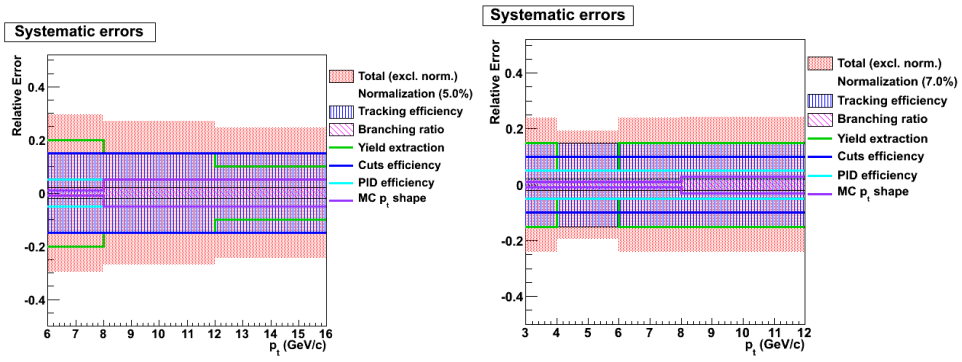

Figure 4.10: Relative systematic uncertainties on D^+ yield extraction in central (left) and peripheral (right) Pb-Pb collisions at $\sqrt{s_{NN}} = 2.76$ TeV.

includes effects due to residual misalignment of the ALICE detectors. To have an indication of how big this effect can be, it is possible to compare the cut variable distributions between data and MonteCarlo, as in figure 3.17 for the cosine of the pointing angle, the decay length and the sum of the square of the daughters' impact parameters. This study is done releasing the cuts as much as possible, hence the distributions are dominated by background candidates, but nevertheless they show good agreement between data and MonteCarlo and no centrality dependence for the cut variable distributions is observed. The cut variation systematic uncertainty is estimated to be of 15% and 10% for central and peripheral collisions respectively.

The PID is crucial for background rejection in Pb-Pb events, and it was not possible to repeat the D^+ analysis without applying PID selection, but this study is possible for the D^0 candidates, which have a systematic uncertainty of 5% for both central and peripheral Pb-Pb events in the p_t range where the D^+ is measured. This value was assumed to hold for D^+ analysis, as the PID strategy is similar for the two analysis.

The effect of possible discrepancies between the D^+ transverse momentum distribution simulated in the MonteCarlo and the one of the data was estimated comparing MonteCarlo simulations with different p_t shapes as input, as shown in figure 4.11. The effect was found to be about 1% at low p_t and about 3-5% at high p_t for peripheral and central Pb-Pb collisions respectively.

The feed-down subtraction systematic uncertainty was estimated changing the range of the factorization and renormalization scales as well as the masses of the charm and beauty quark as proposed in [75]. In addition to this, a second method to compute the prompt fraction, based on the ratio of the FONLL prompt and feed-down production cross-sections was imple-

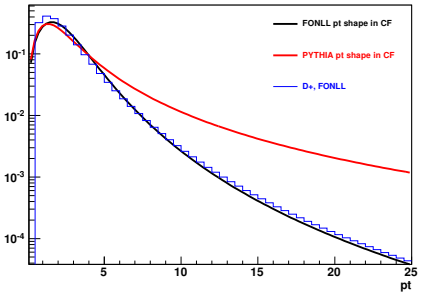

Figure 4.11: Different p_t shapes from FONLL (black) and PYTHIA (red), compared with D^+ prediction from FONLL (blue).

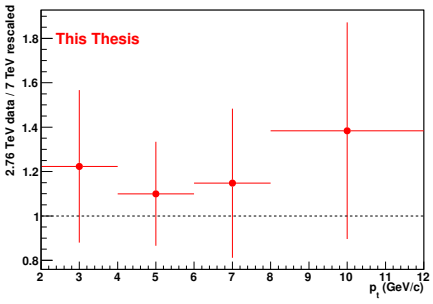

Figure 4.12: Ratio of D^+ measured cross-sections at $\sqrt{s} = 2.76$ TeVto the cross-section scaled from $\sqrt{s} = 7$ TeV.

mented. In this method the prompt fraction is obtained from the equation

$$f_{\text{prompt}} = \left(1 + \frac{\epsilon_{\text{feed-down}}}{\epsilon_{\text{prompt}}} \frac{\left.\frac{d\sigma^{D^+\text{feed-down}}_{\text{FONLL}}}{dp_t}\right|_{|y|<0.5}}{\left.\frac{d\sigma^{D^+}_{\text{FONLL}}}{dp_t}\right|_{|y|<0.5}} \cdot \frac{R_{\text{AA}}^{\text{feed-down}}}{R_{\text{AA}}^{\text{prompt}}} \right)^{-1} \tag{4.6}$$

This equation is analogue to equation 3.7 used for proton-proton collisions with the addition of the term accounting for the hypothesis on feed-down D^+ energy loss. The overall systematic uncertainty on the B feed-down subtraction is evaluated as the envelope of the results obtained with the two methods when varying the parameters in the given range. To evaluate the possible effect of different energy loss between prompt and feed-down D mesons, the ratio $\frac{R_{\text{AA}}^{\text{feed-down}}}{R_{\text{AA}}^{\text{prompt}}}$ was varied in the range $\frac{1}{3} < \frac{R_{\text{AA}}^{\text{feed-down}}}{R_{\text{AA}}^{\text{prompt}}} < 3$ for both the feed-down subtraction methods described in equations 4.3 and 4.6. This range is justified both by theoretical predictions on the size of charm and beauty R_{AA} [87, 88] and by recent results by CMS collaboration on the R_{AA} of non-prompt J/ψ [89]. Figure 4.13 shows the systematic uncertainty due to the feed-down R_{AA} estimation as a function of the ratio $\frac{R_{\text{AA}}^{\text{feed-down}}}{R_{\text{AA}}^{\text{prompt}}}$ for three p_t bins in central collisions.

The last source of systematic uncertainty on the yield extraction is a 2.1% uncertainty on the D^+ branching ratio (9.13 ± 0.19), that cancels out with the the corresponding uncertainty from proton-proton collisions when computing the D^+ R_{AA}.

In addition to the systematic sources on the yield extraction, other sources affect the R_{AA} measurement, namely the uncertainties on the proton-proton cross-section scaled reference and the uncertainty on the average nuclear overlap function for each centrality class.

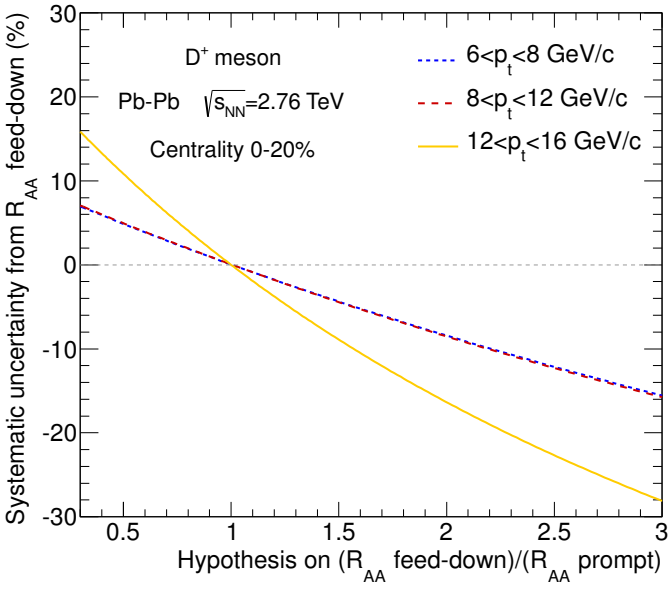

Figure 4.13: Systematic uncertainty from the feed-down $R_{\rm AA}$ estimation as a function of the ratio $\frac{R_{\rm AA}^{\rm feed\text{-}down}}{R_{\rm AA}^{\rm prompt}}$ for the $\rm D^+$ in central (0-20%) collision for three $\rm p_t$ bins: $6 < p_t < 8$ GeV/c (blue-dotted line), $8 < p_t < 12$ GeV/c (red-dashed line) and $12 < p_t < 16$ GeV/c (yellow line).

The uncertainties on the $\rm D^+$ production cross-section in proton-proton collisions at $\sqrt{s} = 7$ TeV were discussed in section 3.7 and are summarised in table 3.6, and the scaling procedure described in section 4.2.1 introduces an additional uncertainty of the order of 10-30% depending on the centrality and on the $\rm p_t$ bin.
The systematic uncertainties from proton-proton and Pb-Pb yields are added in quadrature to obtain the total systematic uncertainty, with the only exception of the feed-down contribution as it partly cancel in the ratio. The systematic uncertainty from the feed-down contribution to the $R_{\rm AA}$ was evaluated by computing the $R_{\rm AA}$ using the two methods for $f_{\rm prompt}$ varying the FONLL parameters but keeping the same parameters between proton-proton and Pb-Pb.

The total systematic uncertainties on the $R_{\rm AA}$ measurement are summarised in table 4.4.

4.2.3 Results

The corrected Pb-Pb yield for central and peripheral events, compared to their proton-proton reference cross-section, is shown in figure 4.14. A strong

	p_t interval (GeV/c)	6–8	8–12	12–16
0–20% centrality	Pb-Pb data syst.	30%	33%	27%
	p-p data syst.	13%	17%	21%
	p-p ref. scaling	$^{+6}_{-10}$%	$^{+5}_{-8}$%	$^{+4}_{-6}$%
	Feed-down subtraction	$^{+12}_{-18}$%	$^{+16}_{-28}$%	$^{+17}_{-28}$%
	FONLL feed-down	$^{+3}_{-2}$%	$^{+3}_{-2}$%	$^{+2}_{-1}$%
	$R_{AA}^{\text{feed-down}}/R_{AA}^{\text{prompt}}$	$^{+7}_{-16}$%	$^{+7}_{-16}$%	$^{+16}_{-28}$%
	Normalization	5.3%	5.3%	5.3%

	p_t interval (GeV/c)	3–4	4–6	6–8	8–12
40–80% centrality	Pb-Pb data syst.	25%	28%	29%	24%
	p-p data syst.	30%	20%	13%	17%
	p-p ref. scaling	$^{+8}_{-19}$%	$^{+7}_{-13}$%	$^{+6}_{-10}$%	$^{+5}_{-8}$%
	Feed-down subtraction	$^{+10}_{-18}$%	$^{+11}_{-24}$%	$^{+14}_{-11}$%	$^{+15}_{-25}$%
	FONLL feed-down	$^{+4}_{-1}$%	$^{+2}_{-1}$%	$^{+1}_{-1}$%	$^{+2}_{-1}$%
	$R_{AA}^{\text{feed-down}}/R_{AA}^{\text{prompt}}$	$^{+6}_{-14}$%	$^{+6}_{-13}$%	$^{+10}_{-20}$%	$^{+10}_{-20}$%
	Normalization	6.9%	6.9%	6.9%	6.9%

Table 4.4: Summary of the relative systematic uncertainties on the D^+ R_{AA} measurement in central (top) and peripheral (bottom) collisions.

suppression in central collisions is clearly visible from the figure, while, as expected, in peripheral collisions the suppression is visible but less pronounced. The suppression is visible over the whole p_t range considered for the analysis. The D^+ R_{AA} as a function of p_t is shown in figures 4.15 and 4.16 for events in centralities 0-20% and 40-80% respectively. In the figures are also explicitly reported the systematic uncertainties contributions coming from the data, from B feed-down subtraction and from the feed-down R_{AA} estimation. The results indicate a $R_{AA} \approx 0.3$, in the whole measured p_t range ($p_t > 6$ GeV/c) for central collisions. As in this p_t region the shadowing effect is expected to be small, as shown in figure 4.19, this is a signature of medium-induced energy loss. For peripheral (40-80%) collisions, $R_{AA} \approx 0.61$ was measured in the intermediate p_t region. The D^+ nuclear modification factor is smaller for central than for peripheral events, a behaviour in agreement with the assumption that the energy loss is a medium induced effect. The R_{AA} of the open-charm mesons has been measured also for the D^0 and D^* candidates in the same centrality range as for the D^+. The results from the 3 mesons are in agreement within the uncertainties

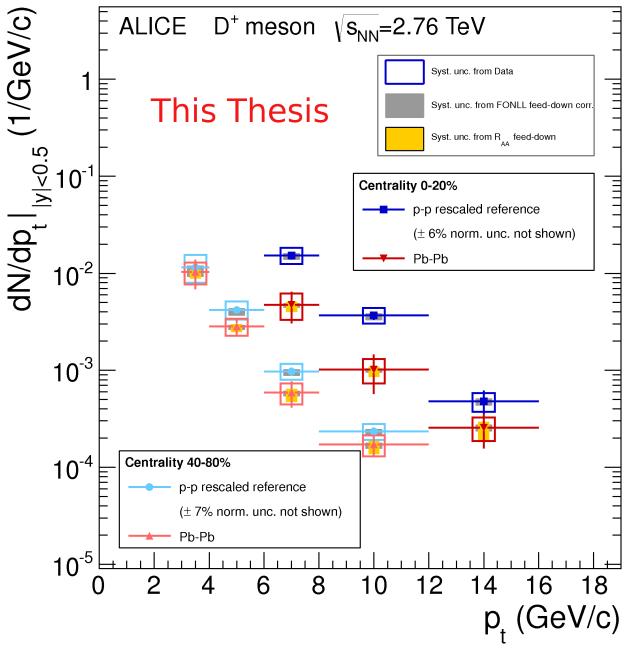

Figure 4.14: The figure shows the D^+ corrected yields in Pb-Pb central (dark colours) and peripheral (light colours) collisions as a function of p_t. The Pb-Pb corrected yields (blue) are compared with the proton-proton scaled reference (red). Boxes are uncorrelated systematic uncertainties, grey band represents the systematic uncertainty on B feed-down subtraction, yellow band the systematic uncertainty on the R_{AA} of feed-down for Pb-Pb only. The uncertainties on the proton-proton cross-section and on the branching ratio are not shown.

in all p_t bins for both centralities classes, as shown in figure 4.17. To verify that the observed R_{AA} is really an effect due to the presence of a strongly interacting medium, we must estimate possible initial state effects. Modifications of the parton distribution functions of the nucleons due to the presence of the other nucleons inside the colliding ions can modify the initial parton scattering probability and therefore the production of charm quarks. The *shadowing*, a relative reduction of the PDF in a nucleus with respect to that of the proton for partons with $x < 10^{-2}$ is the main expected initial state effect. To estimate this effect we used pQCD at the next to leading order calculation from Mangano, Nason and Ridolfi (MNR-NLO) [18] with parton distribution function from CTEQ6M [90] with EPS09 parametrization [91] for their nuclear modification. The uncertainty on this calculation comes mainly from the uncertainty on the EPS09 functions. The effect of the shadowing is shown in figure 4.19 and it is compared to the weighted

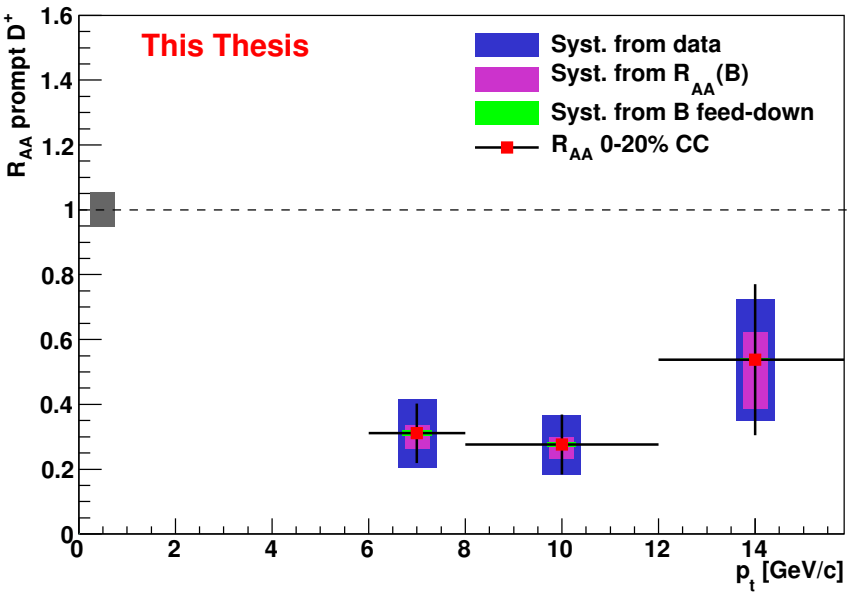

Figure 4.15: D^+ R_{AA} for centrality classes 0-20%. Error bars are statistical uncertainties, blue area is the systematic uncertainties from data (yield extraction, p-p cross-section), the purple band represents the systematic uncertainty due to feed-down R_{AA} and the green band the uncertainty on feed-down subtraction.

average of the R_{AA} for D^0, D^+ and D^*. It is clear from the figure that shadowing can not explain the large suppression observed in the data.
With three independent measurements for the charm R_{AA} it is possible to combine these results, weighting the contribution by their statistical uncertainties. Being the $D^0 \to K^-\pi^+$ the channel with the highest significance, the averaged results are closer to the D^0 points than to D^+ and D^* ones. The average R_{AA} of the three D mesons in the 0-20% centrality class is compared to the R_{AA} of charged hadrons (that are dominated by light flavours) measured by ALICE in the same centrality range in figure 4.18. The charged hadron R_{AA} coincides with the pion R_{AA} for $p_t > 5$ GeV/c while it is $\sim 30\%$ lower for $p_t = 3$ GeV/c [92]. The averaged D meson R_{AA} is compatible with the one of light hadrons in the whole p_t range where the analysis is performed, but we can observe that the central value of the D R_{AA} are always above that of the charged hadron ones. If we also take into account that systematic uncertainties are not fully correlated among the different p_t bins, we have a hint for the expected hierarchy $R^D_{AA} > R^\pi_{AA}$. Many theoretical models make predictions about the D meson R_{AA} at the LHC energies, with some of them also providing predictions for the charged hadron nuclear

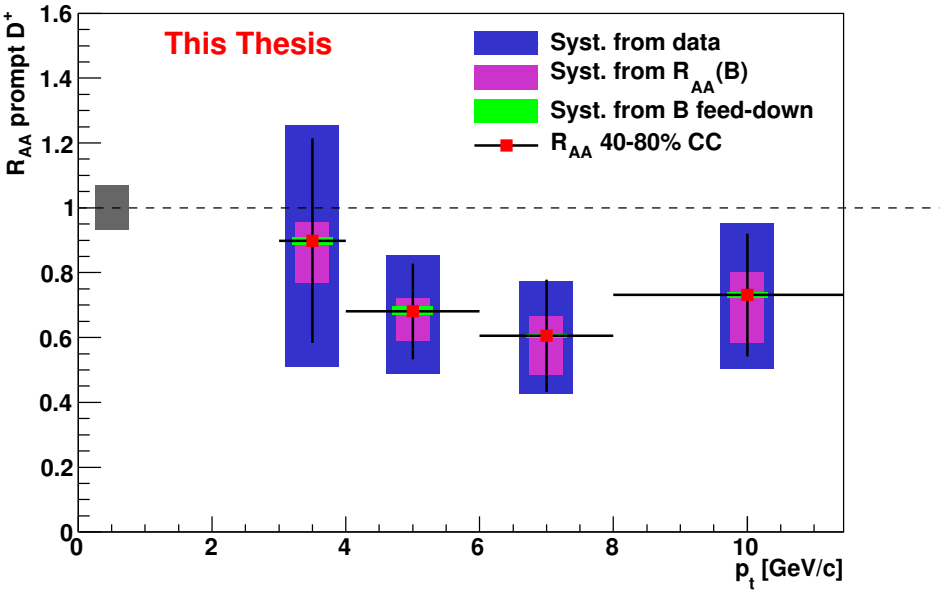

Figure 4.16: D^+ R_{AA} for centrality classes 40-80%. Error bars are statistical uncertainties, blue area is the systematic uncertainties from data (yield extraction, p-p cross-section), the purple band represents the systematic uncertainty due to feed-down R_{AA} and the green band the uncertainty on feed-down subtraction.

modification factor:

I Model from Sharma, Vitev and Zhang [93] is based on factorized pQCD calculations and takes into account radiative energy loss in the medium and accounts also for the energy loss of D and B meson that are created and decay in the medium (radiative plus D dissociation).

II Horowitz and Gyulassy propose pQCD calculations [94] based on WHDG energy loss model [43] that includes elastic, inelastic and path length fluctuations contributions (radiative plus collisional).

III Instead of using pQCD, that is weakly-coupled, a strong coupled theory based on AdS/CFT with heavy quark drag [95] has been suggested.

IV Many properties of the QGP are studied using hydrodynamical models. The energy loss of charm quark has been predicted using Langevin hydrodynamical equations [96].

V The model described in [97] predicts charm energy loss from radiative and collisional energy loss and from path length fluctuations (collisional plus LPM).

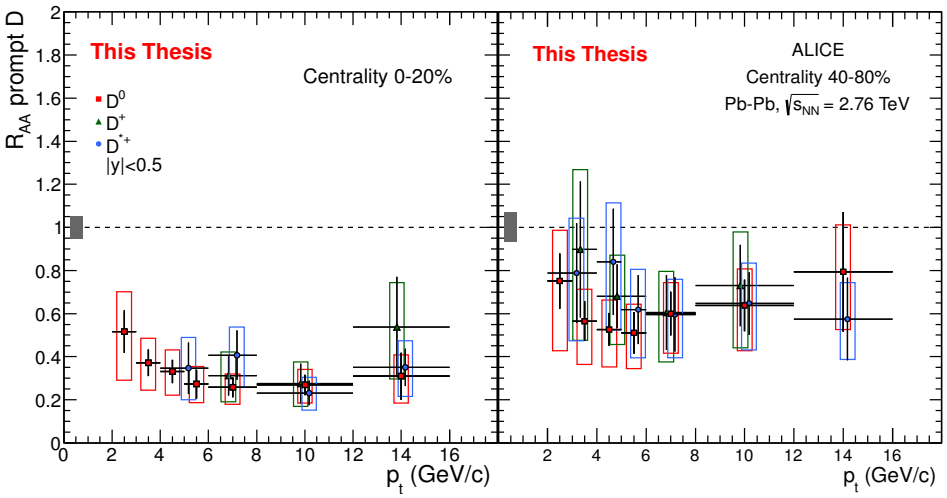

Figure 4.17: D^+ R_{AA} (green triangles) compared to the R_{AA} of D^0 (red squares) and D^* (blue circles) for central (left) and peripheral (right) Pb-Pb collisions. Error bars are statistical uncertainties, boxes systematic uncertainties.

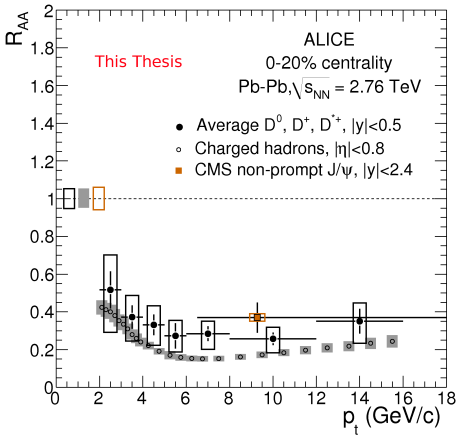

Figure 4.18: R_{AA} of charged hadrons (grey) compared to the R_{AA} of D mesons (black). The D meson R_{AA} is obtained by averaging the R_{AA} of D^+, D^0 and D^* weighted with their statistical uncertainty. The brown point shows the measurement of non-prompt J/ψ from CMS experiment [89].

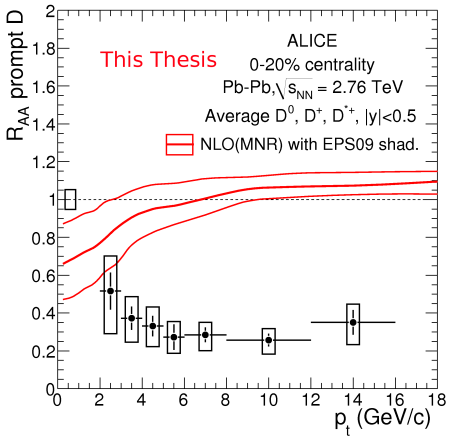

Figure 4.19: R_{AA} of D mesons (black) obtained by averaging the R_{AA} of D^+, D^0 and D^* weighted with their statistical uncertainty compared to the effect of the shadowing on the D meson R_{AA} obtained from MNR-NLO pQCD calculations.

VI A partonic transport model based on a Boltzmann Approach to Multi-Parton Scattering (BAMPS) has been suggested in [98]. Binary interaction in the model are computed with pQCD calculation and energy loss is calculated using 3+1 dimension simulations. To obtain agreement with RHIC results the model has also to include radiative processes.

VII Predictions are also available with the CUJET1.0 MonteCarlo simulator [99].

VIII Finally, the ADSW [88] model predictions, based on radiative energy loss and with a BDMPS transport coefficient $\hat{q} = 25$, were also considered (BDMPS-ADSW).

The comparison between the predictions of the different models and the D meson $R_{\rm AA}$ measured by ALICE is shown in figure 4.20. Radiative energy loss with D dissociation in the medium, CUJET1.0 and radiative and collisional energy loss with WHDG predict fairly well both D meson energy loss and charged hadrons, with the two latter methods slightly underestimating the value of the charged hadrons. This can be due to the fact that while the radiative model is tuned on jet suppression at the LHC, the other two are extrapolated from RHIC data. The AdS/CFT with charm quark drag model significantly underestimates the charm nuclear modification factor, although no model can be definitively ruled out with the current experimental uncertainties.

4.3 Elliptic Flow of charmed mesons

The study of D meson elliptic flow can probe the degree of thermalization of c quarks in the medium. Being the charm quark much more massive than lighter quark species it is expected that it will be much more difficult for it to thermalize. Assuming hadronization via recombination mechanism, depending on the strength of medium thermalization, the elliptic flow of open-charm meson can range from small values (few percent) if the charm quark did not thermalize and the v_2 only comes from the light quark contribution, up to 20%, a value slightly smaller with respect to the light hadrons elliptic flow v_2^h, in case of complete thermalization of the charm quark that participate as any other fluid particle to the medium collective motion. The remaining difference between v_2^D and v_2^h would be due to the mass hierarchy of v_2 [100]. With a precise value of charm elliptic flow it will be possible introduce constraints on the medium equation of state [101].

Two strategies to study the D meson elliptic flow have been implemented at ALICE. The main strategy is based on computing v_2 from the azimuthal distribution of signal (extracted with fit to the invariant mass distribution)

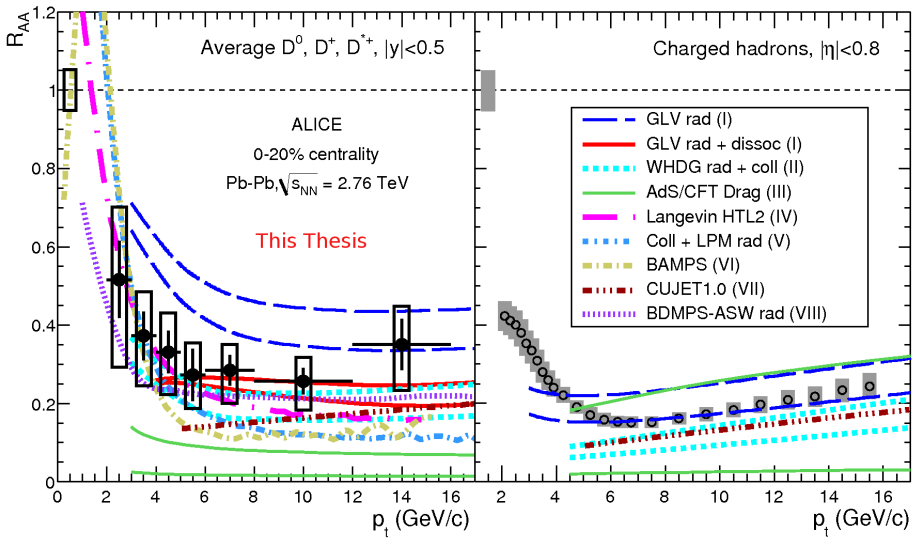

Figure 4.20: Left: model predictions from [93, 94, 95, 96, 97, 98, 99, 88] for charm R_{AA} at the LHC energies and comparison with ALICE data for the 0-20% centrality class. The right panel shows the comparison between charged hadron R_{AA} and theoretical predictions for those models that also provide calculation for light flavour particle R_{AA}

with respect to the symmetry plane of the event (*event plane*). The preliminary results obtained for the D^+ v_2 measurement using the event plane method are presented in section 4.3.3. The event plane determination is performed from the azimuthal distribution of tracks in the TPC and from the amplitudes recorded by the VZERO detector. The methods to reconstruct the event plane are discussed in section 4.3.1. Our analysis tools have been validated with MonteCarlo simulations and also by applying them to light hadrons analyses and comparing with ALICE published results. These tests validation are described in section 4.3.2.
The second strategy, that has not been applied to the D^+ analysis yet, is based on the Q-cumulants [102] method for D meson candidates. The Q-cumulants method is based on building the 2 or 4 particle correlators (second or fourth order cumulants) from the Q-vector of the event (defined as in equation 4.7). In a first step, the flow is computed for an ensemble of particles called *Reference Particles* (RP). This *reference flow* is then used as baseline to compute the flow of the *Particle Of Interest* (POI), in our case the D^+ candidates. The two ensembles might also overlap, but as we estimate the v_2 for the POI ensemble, a high purity in the D^+ sample is needed to reduce systematic uncertainties coming from this strategy. The possibility of using 4 particles cumulants has the advantage of allowing the

removal of non-flow contribution from the v_2, but due to the limited statistics it was not possible to use this method for the D^+ analysis with 2010 Pb-Pb data. A strategy similar to the event plane approach is to divide each event in two sub events and then compute the *scalar product* of the Q-vectors of the two sub-events for the POI and RP.

4.3.1 Event plane methods for v_2 extraction

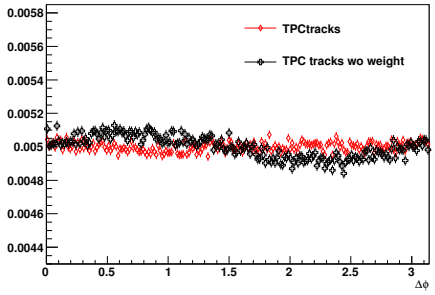

Figure 4.21: Distribution of the event plane measured from charged tracks in the TPC with (red) and without (black)ϕ weights corrections

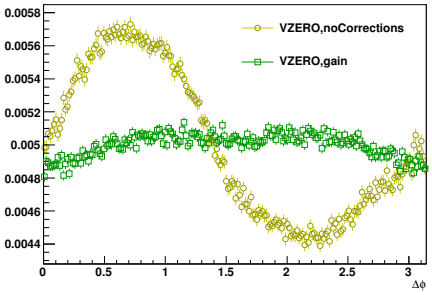

Figure 4.22: VZERO event plane distribution with (green) and without (yellow) channel equalization.

In the D^+ analysis we use information from track distribution in the TPC and amplitudes in the VZERO detector sectors to estimate the event plane in two independent ways. The TPC is used in order to have a more complete azimuthal coverage with respect to SPD. From the azimuthal distribution of tracks in the TPC it is possible to compute the two dimensional Q-vector, in particular the second harmonic, which we use for the measurement of v_2. The longitudinal and transverse components of the Q-vector are defined as

$$\begin{aligned} Q^X &= \sum_i w_i \cos(2\phi_i) \\ Q^Y &= \sum_i w_i \sin(2\phi_i) \end{aligned} \tag{4.7}$$

and from the vector the second harmonic event plane can be obtained as

$$\Psi = \frac{1}{2}\tan^{-1}\left(\frac{Q^Y}{Q^X}\right). \tag{4.8}$$

In these formulas ϕ_i is the azimuthal angle of the i^{th} track reconstructed in the TPC, the sum goes through all the TPC tracks and the w_i are weights associated to the azimuthal position of the track. As different TPC sectors

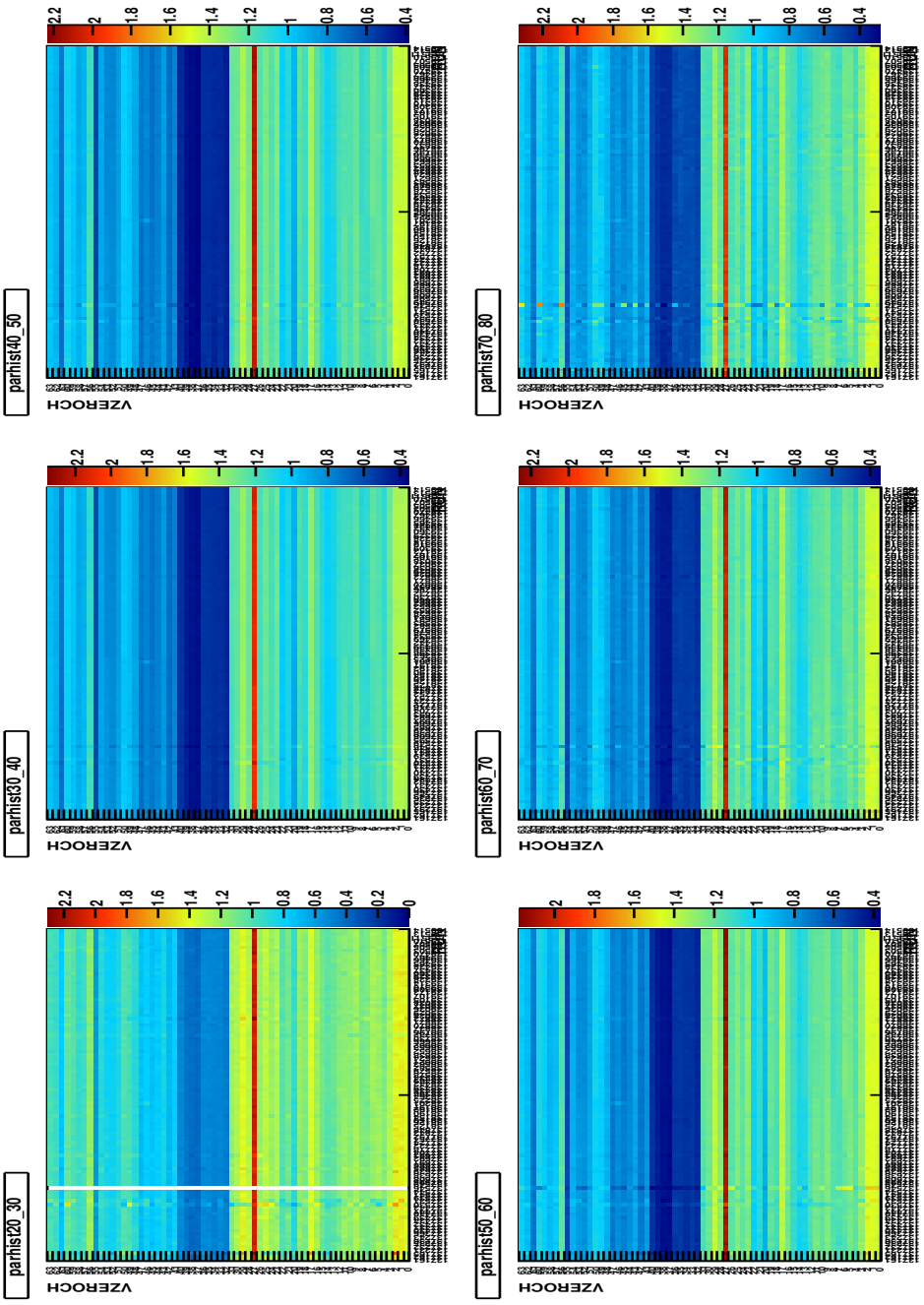

Figure 4.23: Correction factors for the VZERO event plane in 6 centrality classes (from 20-30% to 70-80%). For each VZERO channel and each run the corrected VZERO amplitude is obtained dividing the measured amplitude by the corresponding factor. The weights are computed in order to be flat inside each run and each centrality bin.

can have different efficiencies, assuming all weights to be equal introduces bias in the distribution, favouring the most efficient sectors over the less efficient. For each run of the Pb-Pb data taking period, the weights are computed and optimized in order to have a flat event plane distribution. To avoid possible auto-correlations, for each candidate D^+ the event plane is computed after removing the contributions to the Q-vector of the three tracks from which the candidate is built. The event plane distributions obtained with and without applying the weights are shown in figure 4.21.
The procedure to extract the event plane from the VZERO detector amplitudes is also based on equations 4.7 and 4.8 but in this case the angle ϕ_i is the azimuthal position of the centre of each of the 64 VZERO sectors. The 64 weights associated to the sectors are the sectors occupancies properly corrected in order to take into account their different efficiencies for each run in classes of centrality width of 10%. For each run the correction factors to equalize are normalized to 1. The centrality dependence of the correction factors is smooth, and can be observed in figure 4.23, where the weights applied in the different centralities classe are shown as a function of the run number. Even after this correction the VZERO event plane distribution, visible in figure 4.22, is not flat. Residual fluctuations can be removed using recentering and flattening procedures. Recentering accounts for the fact that the mean values of Q^X and Q^Y over the collected events are not centred in 0. If this happen, these mean values are subtracted from the X and Y Q-vector components of each event.
The correlation between the TPC and VZERO event planes after corrections is shown in figure 4.24. The agreement between the two reconstructed event planes is good.

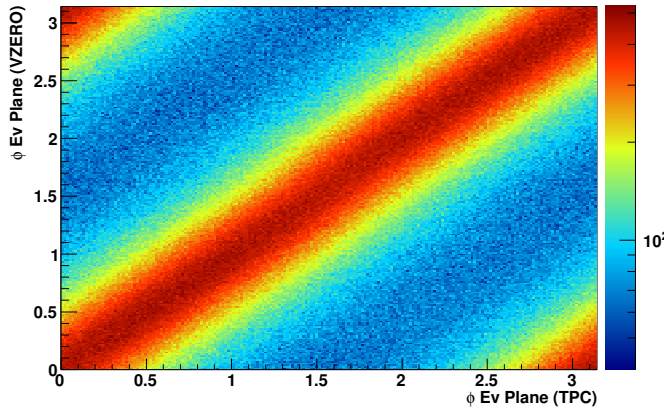

Figure 4.24: Event plane angle measured with the VZERO detector versus the one determined from the distribution of charged tracks in the TPC.

The elliptic flow extracted using the event plane methods must be cor-

rected for the event plane resolution [31], that dependends on the event multiplicity and the anisotropy of the azimuthal distribution of particles used for its estimation. To do this, the measured $v_2^{\rm obs}$ coefficient is divided by the event plane resolution, so that $v_2 = v_2^{\rm obs}/\sigma_{\rm EP}$. The methods we use to measure v_2 are discussed later in this section. The event plane resolution is measured in each event dividing the tracks in two sub-events of similar multiplicity [31]. The event plane is computed for both the sub-events and we build the distribution of $\cos(2(\Psi^a - \Psi^b))$, where $\Psi^{a,b}$ are the event plane angles of the two sub-events. Assuming that the non-flow correlations between particles of different sub-events are negligible, the resolution correction factor on the full data sample analyzed is then equal to the average of this distribution. When using the TPC event plane the two sub-events can be obtained dividing the tracks randomly between the two sub-events, or accordingly to their pseudorapidity. For example, one sub-event can contain all the track with positive pseudorapidity and the other with negative η. For the VZERO event plane, the most natural choice is to use each VZERO disc (VZERO-A and VZERO-C) as sub-event, even if the two discs do not cover the same rapidity region, and therefore the two sub-events have different multiplicity and v_2. The distribution of $\cos(2(\Psi^a - \Psi^b))$ in the 30-50% centrality class obtained by randomly selecting the TPC tracks associated to each sub-event is shown in figure 4.25. The corresponding resolution correction factor is $\sigma_{\rm EP} \sim 0.91\%$. For peripheral events (40-80%) the resolution drops to $\sigma_{\rm EP} \sim 0.78\%$, as an effect of the lower multiplicity.

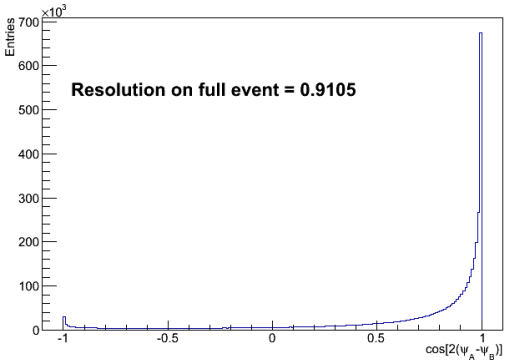

Figure 4.25: $\cos(2(\Psi^a - \Psi^b))$ from two sub-events obtained by randomly selecting TPC tracks from semi-peripheral (30-50% centraliy class) events.

AliAnalysisTaskSEHFv2, the analysis task that has been developed for the v_2 analysis based on the event plane stores for each 5% width centrality class the invariant mass distribution of $\rm D^+$ candidates divided in bins of $\rm p_t$ and in bins of the candidate azimuthal angle with respect to the measured event plane $\Delta\phi = \phi - \Psi$. The two-dimensional distribution of invariant mass versus $\cos(2\Delta\phi)$ is also stored in bins of $\rm p_t$ and centrality class. We have

foreseen 4 different methods to extract v_2 from the task output. 2 of them are based on the signal extraction from fits to the invariant mass spectra in intervals of $\Delta\phi$ and the other 2 are based on fits of the 2D distribution of invariant mass and $\cos(2\Delta\phi)$.
It is possible to build the distribution of the number of D^+ versus $\Delta\phi$ using the fit to extract the signal from the invariant mass distribution of each p_t and $\Delta\phi$ bin. Assuming for simplicity that any contribution except v_2 is negligible, the v_2 coefficient can be obtained by fitting the signal versus $\Delta\phi$ distribution with the following function:

$$\frac{dN}{d\phi} = k \cdot (1 + 2v_2 \cos(2\Delta\phi)) \tag{4.9}$$

where k is a normalization constant. The distribution of signal candidates is not flat inside the single $\Delta\phi$ bin, but it has a distribution that depends on v_2. If the $\Delta\phi$ bin are too wide, placing the point in the centre of the bin introduce a bias in the analysis. Given the statistics available in the 2010 Pb-Pb data sample, it is not possible to divide the statistic in many $\Delta\phi$ intervals, and we used at most 4 bins in the interval $[0, p_t)$.
A possibility to avoid this bias is to divide the candidates in only two $\Delta\phi$ regions: the *in-plane* region and the *out-of-plane* region. We define the in-plane region (centred on the event plane) as the region $\left(0, \frac{\pi}{4}\right] \cup \left(\frac{3\pi}{4}, \pi\right]$ and the out-of-plane as $\left(\frac{\pi}{4}, \frac{3\pi}{4}\right]$. Reducing the splitting in $\Delta\phi$ to only two bins allows to improve the statistics for each invariant mass fit. Resolving equation 4.9 for the number of signals measured in the in-plane and out-of-plane regions separately we obtain

$$\begin{aligned} N_{\text{in-plane}} &= k \int_{\text{in-plane}} 1 + 2v_2 \cos(2\phi) d\phi = k' \cdot (\pi + 4v_2) \\ N_{\text{out-plane}} &= k \int_{\text{out-plane}} 1 + 2v_2 \cos(2\phi) d\phi = k' \cdot (\pi - 4v_2) \end{aligned} \tag{4.10}$$

and therefore it is possible to compute v_2 from the relative difference between the number of signal observed in-plane and out-of-plane.

$$v_2 = \frac{\pi}{4} \frac{N_{\text{in-plane}} - N_{\text{out-plane}}}{N_{\text{in-plane}} + N_{\text{out-plane}}} \tag{4.11}$$

The first method based on the two-dimensional distribution of the invariant mass and the $\cos(2\Delta\phi)$ is based on a fit of the v_2 of candidates versus the invariant mass. At first, the usual invariant mass fitting procedure is performed on the projection of the 2D histograms on the invariant mass axis (thus recovering the full invariant mass distribution). From this fit it is possible to build the distributions of the signal and background fractions $\frac{S}{S+B}$ and $\frac{B}{S+B}$ as a function of the invariant mass value. Then for each

invariant mass bin, the total v_2 is computed from the $\cos(2\Delta\phi)$ distribution obtained in that bin as $v_2 = \langle \cos(2\Delta\phi) \rangle$. This allows to extract the candidate v_2 depending of invariant mass. To disentangle the signal and background contributions, the v_2 versus mass distribution is fitted using the function

$$v_2 = v_2^{\text{signal}} \frac{S}{S+B} + v_2^{\text{background}} \frac{B}{S+B} \tag{4.12}$$

where the invariant mass dependence of the terms of the equation is omitted for brevity, v_2^{signal} is the signal contribution to the total v_2 and $v_2^{\text{background}}$ is a function linearly depending on the mass. The different steps of this procedure are summarised in figure 4.29.
The second method, based on side band subtraction of the background contribution, is done by projecting the two-dimensional histogram on the $\cos(2\Delta\phi)$ axis instead of the invariant mass axis. Having defined a signal region and two side bands regions sufficiently displaced (n times the gaussian σ of the invariant mass fit), the distribution of $\cos(2\Delta\phi)$ is built for the signal region, the two side bands regions and then for the average of the two side bands. A linear fit is performed to estimate the background $\cos(2\Delta\phi)$ shape and then it is used to normalize the background in the signal region. The difference between the $\cos(2\Delta\phi)$ distribution in the signal region and in the side band average provides the distribution of $\cos(2\Delta\phi)_{\text{signal}}$ for the signal (under the assumption that the elliptic flow of the background is similar in the two side bands). Having this distribution the signal elliptic flow can be computed simply as

$$v_2^{\text{signal}} = \langle \cos(2\Delta\phi)_{\text{signal}} \rangle \tag{4.13}$$

4.3.2 Method validation

Our analysis tools have been tested to check that they are not biased, and that if they are used on a sample for which the elliptic flow value is known they provide the correct results. Such test have been performed on MonteCarlo simulations, where a v_2 contribution is added to the simulated particles, and analysing light hadrons instead of D mesons, for which the v_2 measured at ALICE with completely independent methods is available [103].

MonteCarlo test with the afterburner

The elliptic flow is not present in the MonteCarlo productions used for the D meson analysis. Therefore to test the quality of our methods on simulated data, we had to introduce the flow in the simulation using an *afterburner*, that introduces an azimuthal modulation in the generated particles. As D mesons and background particles should have different v_2 coefficients, the afterburner introduces different elliptic flow anisotropies for D mesons and for background tracks. The v_2 of kaons and pions is sufficiently similar that

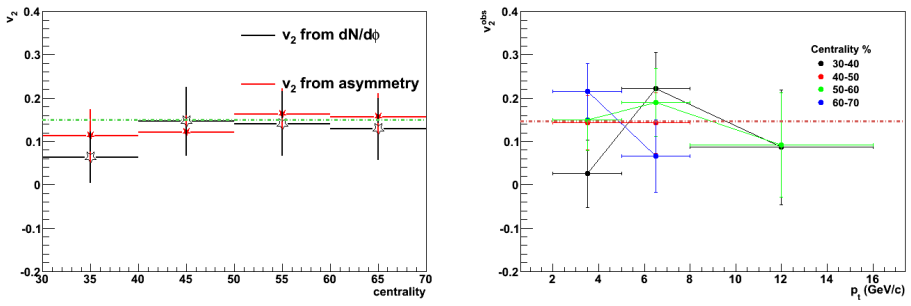

Figure 4.26: Left panel: v_2 versus centrality obtained fitting in 4 bins the candidate $\Delta\phi$ distribution (eq. 4.9) in black and using the in-plane versus out-of-plane anisotropy (4.11) in red for different centrality classes in MonteCarlo simulations with input $v_2 = 0.15$ (green line). Right panel: v_2 of D meson candidates for different values of p_t obtained using the anisotropy method in MonteCarlo simulations with input $v_2 = 0.15$ (red line). Missing points means that the fit quality was not satisfactory in that bin.

the effect of assuming $v_2^K = v_2^\pi$ for the background tracks is negligible. When our analysis task is ran on MonteCarlo data, for each event the afterburner generates randomly the event plane direction and then for each D^+ candidate in the event it checks whether it is a real D meson or background. If it is a real D^+, then its azimuthal angle ϕ with respect to the randomly generated event plane Ψ is set by the afterburner solving numerically the following recursive condition:

$$\phi_{i+1} = \frac{\phi_i - \left(\phi_i + v_2^{\text{signal}} \sin\left(2(\phi_i - \Psi)\right) - \phi_0\right)}{1 + 2v_2^{\text{signal}} \cos(2(\phi_i - \Psi))} \tag{4.14}$$

where the starting point ϕ_0 is the D^+ azimuthal angle as generated in the MonteCarlo and v_2^{signal} is the v_2 value associated to signal candidates. If there is the need to speed up significantly the analysis, it is possible to use an approximated version of the formula above, that can be solved analytically:

$$\phi = \phi - v_2^{\text{signal}} \sin(2(\phi - \Psi)), \tag{4.15}$$

but as pointed out in [104] this approximation can only be used for small values of v_2.
For background candidates, the $v_2^{\text{background}}$ coefficient should be applied to daughter tracks, according to their origin. For each of the three D^+ daughter the azimuthal angle is computed using equation 4.14, using the v_2^{signal} coefficient if the particle was coming from a D meson decay (of any D meson specie), or using $v_2^{\text{background}}$ in any other case. The ϕ angle of the background

candidate is then calculated starting from the new momentum components of the daughter tracks. The ϕ shift of each daughter is deterministic and it only depends on whether the real mother is a D meson or not. Therefore even if a track belongs to two different candidates it will receive always the same shift. The afterburner was checked for different values of v_2^{signal} and $v_2^{\text{background}}$. In figure 4.26 is reported the v_2 obtained using the in-plane versus out-of-plane anisotropy and splitting the $\Delta\phi$ distribution in 4 bins for different centrality values, and the dependence on p_t of the anisotropy method, using a value of v_2 equal to 15% and 25% respectively for signal and background. These extreme values were chosen to see clearly any possible deviation from the expected results. As shown in the figure, the reconstructed v_2 values are in good agreement with those introduced in the MonteCarlo.

Elliptic flow of charged hadrons

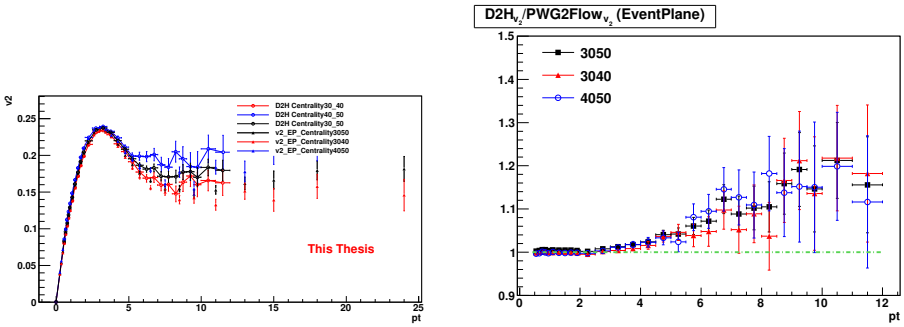

Figure 4.27: Left: v_2 of pions measured using the D meson tools (open circles) compared to the ALICE measurement (filled triangle) for the centrality classes 30-50% (red), 40-50% (blue) and 50-60% (black). The ratio of the two measurements for the three centrality classes is shown in the right panel.

Our tools were tested also on real data, using as reference the elliptic flow of charged hadrons measured by ALICE [103]. To do the test the task was modified in order to select single charged track passing a set of quality cuts instead of the D meson candidates. The main requirement the tracks must have to pass the selection cuts were $p_t > 0.5$ GeV/c (that is the single track minimum p_t applied in the D^+ analysis in peripheral collisions), $|\eta| < 0.8$, at least 70 clusters in the TPC and a distance of closest approach to the primary vertex smaller than 2.4 cm and 3 cm in the transverse plane and along the z axis respectively. These cuts were applied in order to have a track sample as close as possible as the one used for the analysis of light hadrons v_2. The test, performed in several centralities and p_t bins, showed a good agreement between the results using the D meson tools and the charged hadrons v_2

value measured using the event plane method at ALICE. As shown in figure 4.27 at high p_t ($p_t > 6$ GeV/c) some deviations are observed between the two measurements, possibly due to some differences in the track selection, but the test results is anyhow satisfactory.

4.3.3 D^+ v_2 results

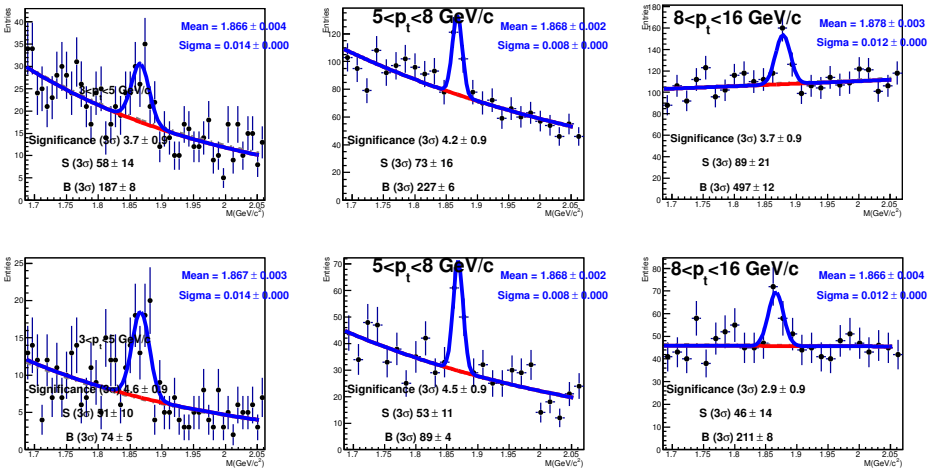

Figure 4.28: Invariant mass distributions for the D^+ candidates in-plane (top) and out-of-plane (bottom) for 3 p_t bins in the range $3 < p_t < 16$ GeV/c, for semi-peripheral events (30-50% centrality).

The results from the elliptic flow analysis of the D^+ candidates are shown in this section. The histograms with the invariant mass distribution for candidates in-plane ($\left(0, \frac{\pi}{4}\right] \cup \left(\frac{3\pi}{4}, \pi\right]$) and out-of-plane ($\left(\frac{\pi}{4}, \frac{3\pi}{4}\right]$) can be seen in figure 4.28 for three different p_t bins in 30-50% centrality. The statistical significance of the signal is generally higher than 3 but smaller than 5, leading to large statistical uncertainties on the extracted raw yield and consequently on the final v_2 values, and important systematic uncertainties due to the yield extraction. To improve the fit results the width and the mean of the gaussian peak are not left as free parameters but are fixed to the values of mean and σ obtained by fitting the $\Delta\phi$ integrated distribution, larger statistics is available to perform the fit. The two-dimensional methods do not need to split the candidates into sub-events bins, but are more sensitive to background fluctuations and to assumptions on the background v_2. Figure 4.29 shows the steps used for the v_2 estimation with the fit of the v_2 of candidates as a function of the invariant mass in the p_t bin $3 < p_t < 5$ GeV/c. In the figure, the two dimensional histogram and its projection on the invariant mass axis are shown in the top panels. In the top left panel of the figure the invariant mass distribution of D^+ candidates

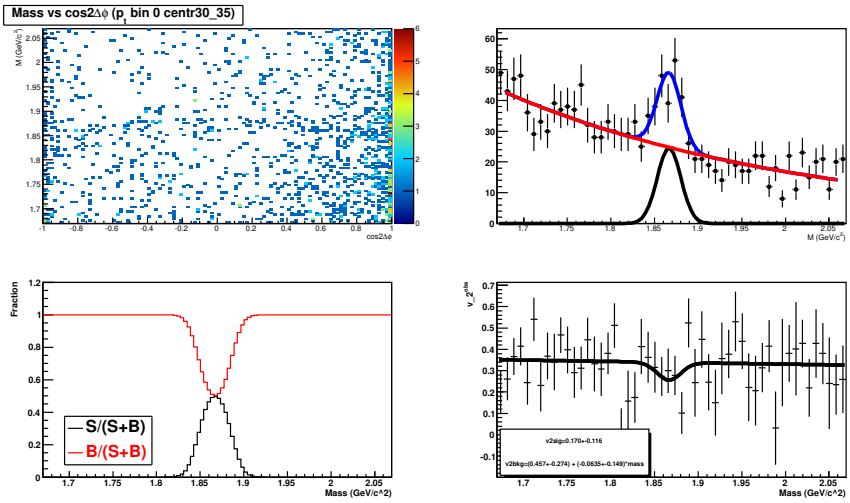

Figure 4.29: Top left panel: invariant mass distribution of D^+ candidates with $3 < p_t < 5$ GeV/c versus $\cos(2\Delta\phi)$ for events in the 30-50% centrality class and its projection on the invariant mass axis (top right panel). The invariant mass fit is shown superimposed to it, with the blue (red) line showing the signal (background) fitting function. Bottom left panel: signal and background fractions as a function of mass obtained from the fit. The bottom right panel shows the v_2 as a function of mass (eq. 4.12).

versus $\cos(2\Delta\phi)$ is shown for events in the 30-50% centrality class. The projection of the 2D distribution is shown in the top right panel, with the result of the invariant mass fit superimposed to it. From the signal and background fitting functions it is possible to compute the signal and background fractions as a function of mass (bottom left panel). The bottom right panel shows the v_2, obtained averaging $\cos(2\Delta\phi)$ for each invariant mass bin, as a function of mass. The v_2^{signal} value can be obtained using equation 4.12. The systematic uncertainties for the method based on the fit of v_2 versus mass is estimated varying the histogram binning, accounting for the error on fit parameters and using a constant function to parametrise $v_2^{\text{background}}$ instead of a linear one. For the side band subtraction method, the systematics uncertainties are estimated varying the side band and signal regions width, using different binning and comparing the results obtained using only the left or right side band with the results obtained using the average of the two. In both cases, the full spread of the different results is considered for the definition of the systematic uncertainties. No evaluation of the systematic uncertainties affecting the anisotropy method has been performed so far. The values of v_2 as a function of p_t measured with the different methods are shown in figure 4.30, together with the systematic uncertainties for the side band and v_2 fit to the mass methods. The results generally agree within the

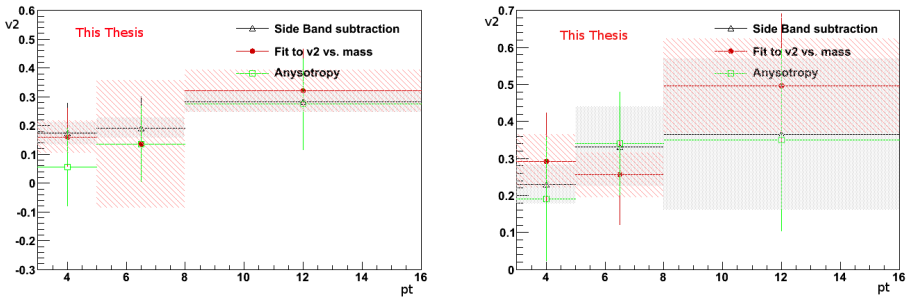

Figure 4.30: D^+ v_2 in 30-50% (left) and 50-80% (right) centrality collisions. Results from three different methods are shown: the in-plane versus out-of-plane anisotropy (green), the fit of v_2 versus invariant mass (red) and side band subtraction (black). The red and grey band are systematic uncertainties on the fit and side band subctraction methods respectively. Error bars are statistical uncertainties.

uncertainties affecting the measurement. The analysis was repeated also in the 50-80% centrality class, but in such peripheral events the small statistics of D mesons leads to even large statistical and systematic uncertainties, and therefore the measurement is not very significant. The results in 50-80% centrality are shown in the right panel of figure 4.30.

The D^+ elliptic flow in 3 p_t bins ($3 < p_t < 5$ GeV/c, $5 < p_t < 8$ GeV/c and $8 < p_t < 16$ GeV/c) is shown in figure 4.31 compared to the results for the D^0 meson and for the charged hadrons as measured by ALICE. The D^+ p_t differential v_2 measurement is compatible with the D^0 measurement and both with 0 and the light hadrons value in all the three p_t bins considered. It is therefore difficult to have a conclusive statement on the D^+ elliptic flow with the 2010 Pb-Pb statistics. Some useful informations can be obtained from the v_2 distributions integrated in $p_t > 3$ GeV/c. Figure 4.32 shows the v_2 measurement obtained with the anisotropy, fit of v_2 versus mass and side band subtraction methods for the centrality classes 30-40%, 40-50%, 50-60% and 60-70% (the very limited statistics in the 70-80% centrality class did not allow us to go towards more peripheral events) and for the wider centrality classes 30-50% and 50-80%. The 3 different methods are in good agreement within errors in all centralities except for the 60-70% centrality where in any case the statistic is limited and the fit quality very poor. The results show a positive v_2 between 1.5 and 2 σ larger than 0, suggesting a positive v_2 for centralities larger than 40% (considering only statistical uncertainties), while the v_2 observed in 30-40% centrality, although positive, is compatible with 0 within one σ. The results for 30-50% and 50-80% centrality intervals also show an hint of $v_2 > 0$. The value of v_2 seems to increase with centrality at least up to the centrality class 50-60%, while the results in 60-70% suggesting

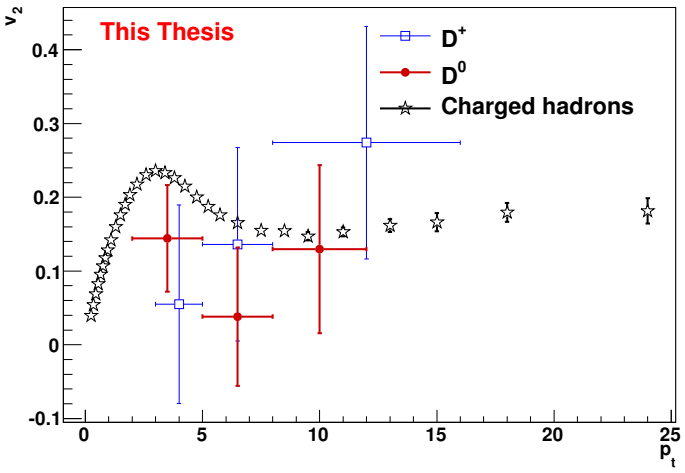

Figure 4.31: D^+ p_t differential elliptic flow measurement (blue squares) compared to D^0 (red circles) and charged hadrons from ALICE (black stars) measurement in 30-50% centrality. Statistical errors only.

that the v_2 can decrease after this value. These results are consistent with what observed for the charged hadrons v_2, for which the maximum value of p_t integrated v_2 is reached around 50% centrality, as shown in figure 1.28. Also the comparison between the results in 30-50% and 50-80% centrality, shown in the bottom panel of figure 4.32 is coherent with this picture, with the v_2 value in the more central sample lower than the value in the more peripheral one. It is useful to note that the 30-50% centrality class is dominated by candidates coming from D^+ mesons close to 30% centrality, while the 50-80% is dominated by the 50% centrality, as can be observed comparing the 50-80% result (lower panel in figure 4.32) with the results in 50-60% (upper panel).

The results obtained with the 2010 Pb-Pb statistics are affected by too large statistical and systematic uncertainties to obtain a precise measurement of the D^+ p_t differential elliptic flow, although results integrated over a broad p_t range seems to suggest a positive v_2 contribution. The results obtained are compatible with what observed for the D^0 meson. The large number of Pb-Pb collisions collected by ALICE in November 2011 should allow us to improve significantly the D^+ elliptic flow measurement. Having a clearer signal available, we aim at measure the D^+ elliptic flow in several p_t bins in different centrality classes, from semi-central (10-30% centrality class) to semi-peripheral (30-50% centrality) and peripheral (50-80% centrality) events.

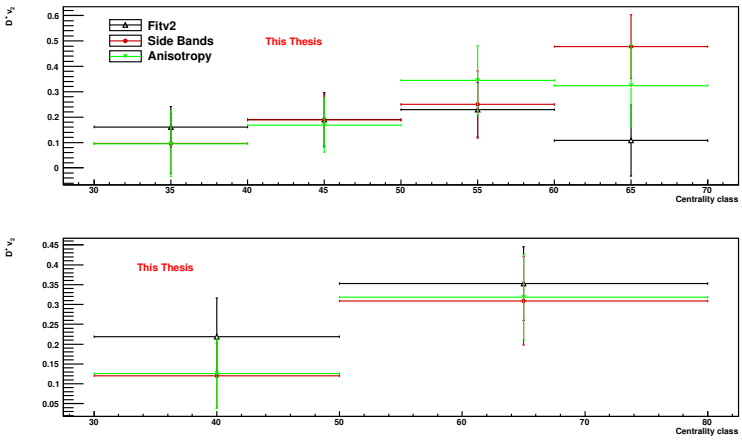

Figure 4.32: v_2 for D^+ mesons for $3 < p_t < 16$ GeV/c in the 30-40%, 40-50%, 50-60% and 60-70% centrality classes (upper panel) and for the 30-50% and 50-80% centrality classes (lower panel). The measurement has been done using the in-plane versus out-of-plane anisotropy (green downward triangles), side band subtraction (red circles) and fit to v_2 versus the invariant mass (black open triangles). Only statistical uncertainties are shown. The marker are placed in the centre of each centrality class, the horizontal error bars indicate the width of the centrality class.

5 Conclusions

Using the excellent capabilities of ALICE at the LHC, it was possible to measure the D^+ p_t differential production cross-section in proton-proton collisions in the centre of mass energies of $\sqrt{s} = 2.76$ TeV and $\sqrt{s} = 7$ TeV. The statistics collected in 2010 allowed us to measure it in 10 p_t bins for proton-proton collisions at $\sqrt{s} = 7$ TeV and 4 p_t bins at $\sqrt{s} = 2.76$ TeV. The measured cross-section are in good agreement with pQCD predictions from FONLL and GM-VFNS models within error bars, although the central values of FONLL systematically underestimate the data and the central values of GM-VFNS predictions overestimate the measurement. The total charm production at the LHC has been extrapolated from the D^+ production cross-section, averaged with the D^0 and D^* cross-section, using FONLL predictions to estimate the non-visible cross-section. Both at $\sqrt{s} = 2.76$ TeV and $\sqrt{s} = 7$ TeV The results at $\sqrt{s} = 7$ TeV are in good agreement with what measured at the LHC by the ATLAS and LHCb experiments. At both energies the results are in agreement with FONLL predictions, and follow the trend of lower energy experiments.

The measured proton-proton cross-section, scaled to the energy of $\sqrt{s} = 2.76$ TeV, has been used as reference cross-section for the measurement of D^+ R_{AA} in Pb-Pb collision at $\sqrt{s_{NN}} = 2.76$ TeV. The D^+ R_{AA} has been measured in 3 p_t bins ($6 < p_t < 8$ GeV/c, $8 < p_t < 12$ GeV/c and $12 < p_t < 16$ GeV/c) in central (0-20%) Pb-Pb collisions and in 4 p_t bins ($3 < p_t < 4$ GeV/c, $4 < p_t < 6$ GeV/c, $6 < p_t < 8$ GeV/c and $8 < p_t < 12$ GeV/c) in peripheral (40-80%) collisions. Data show a large D^+ suppression in both central and peripheral suppression, with a $R_{AA} \sim 0.3$ and $R_{AA} \sim 0.6$ in central and peripheral collisions respectively. The D^+ R_{AA} is in good agreement with that measured using the D^0 and D^* mesons. The averaged results have been compared to the charged hadrons R_{AA} measured by ALICE. The two distribution are compatible within the uncertainties, but the D mesons central values are systematically higher than those of

the charged hadrons, a fact that hints to a possible hierarchy $R^{D}_{\rm AA} > R^{h}_{\rm AA}$, expected by theoretical models. Initial state effects (shadowing) should not modify significantly the measured values of $R_{\rm AA}$ in the $\rm p_t$ range considered in the analysis, and therefore the strong observed suppression can be ascribed as a medium effect. Several theoretical models have made predictions for the D meson $R_{\rm AA}$. Those predictions are generally found to be compatible with our measurement within the uncertainties. Only a few of the models that make predictions also for the charged hadrons $R_{\rm AA}$ can predict fairly well both the distributions (GLV, CUJET1.0, WHDG).

The elliptic flow v_2 of the $\rm D^+$ meson has also been measured with the 2010 Pb-Pb data in different centralities. With the statistics collected in 2010 Pb-Pb collisions, the measurement has too large statistical and systematic uncertainties to allow us to make any statement on the $\rm p_t$ differential v_2. The $\rm D^+$ elliptic flow integrated in the $\rm p_t$ range $3 < p_t < 16$ has been studied in different centrality class. Its behaviour seems qualitatively consistent with what observed at ALICE for the v_2 of the light hadrons, with v_2 increasing towards centralities up to 50%. The $\rm p_t$ integrated data also seems to suggest a positive v_2 contribution in the considered $\rm p_t$ range. The larger statistics collected during the Pb-Pb runs of November 2011 will allow to make a more precise measurement of the $\rm D^+$ v_2.

A

Rapidity and Pseudorapidity

The rapidity y is an adimensional kinematic quantity commonly used to define the geometry of particles distribution at colliders. It is defined starting from the four momentum components $(p_0, \overrightarrow{p})$ as:

$$y = \frac{1}{2}\log(\frac{p_0 + p_z}{p_0 - p_z}). \tag{A.1}$$

It is straightforward to demonstrate that the rapidity of a particle moving toward direction z with speed β is given by:

$$y = y_\beta = \frac{1}{2}\log(\frac{1+\beta}{1-\beta}) \tag{A.2}$$

and it is easy to compute that given the transverse mass $m_t^2 \equiv m^2 + p_t^2$ then the following relation holds:

$$p_0 = m_t \cosh(y), p_z = m_t \sinh(y) \tag{A.3}$$

Rapidity is not a invariant under Lorentz transformations, but it is quite simple to compute its variation among different frames. It is possible to demonstrate the a particle with rapidity y in the reference frame F will be seen in the reference frame F$'$ where it moves at speed β with rapidity

$$y' = y + y_\beta \tag{A.4}$$

with y_β defined as in equation A.2.
The rapidity distribution of particles emitted in a heavy ion collision is compatible with the superposition of two gaussians and it is symmetric around the centre of mass rapidity value, that is basically the average of the two colliding nuclei rapidities. The value of the centre of mass rapidity is referred to as *midrapidity*, it is 0 if the collision is symmetric i.e. if the colliding objects are identical and at the same energy. At the LHC energies

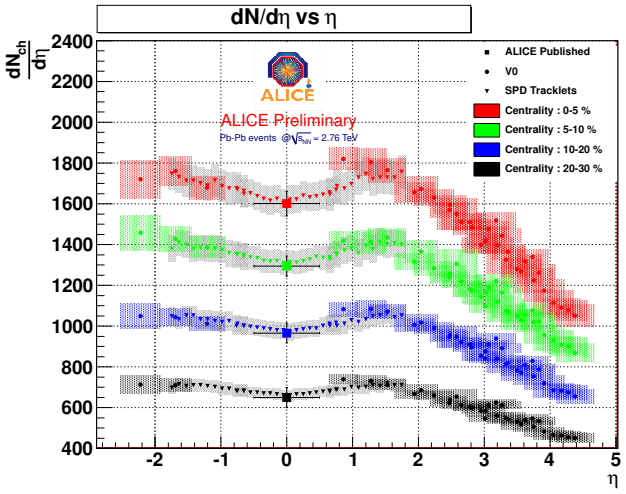

Figure A.1: Pseudorapidity distribution of charged particles in Pb-Pb collisions at $\sqrt{s_{NN}} = 2.76$ TeV in ALICE measured with the SPD and V0 detectors

it is expected the particle rapidity distribution to show a flat central region, a behaviour known as *Dirac plateau*.

The *pseudorapidity* is another kinematical often used in place of rapidity. It is defined as:

$$\eta = -\log(\frac{\theta}{2}) = -\log(\sqrt{\frac{|\overrightarrow{p}| + p_z}{|\overrightarrow{p}| - p_z}}) \tag{A.5}$$

Where θ is the angle among the particle direction and the z axis. If the particle is moving at a speed close to the speed of light c then we can assume that $|\overrightarrow{p}| \approx p_0$ and the pseudorapidity takes the same value of the rapidity. Pseudorapidity is used because its measurement only requires measure the θ angle, and therefore is a much easier measurement to perform. The pseudorapidity distribution of charged particles in Pb-Pb collisions at $\sqrt{s_{NN}} = 2.76$ TeV measured with ALICE is shown in figure A.1. The effect of the Dirac plateau is visible in the figure.

Bibliography

[1] J. Allday, *Quarks, Leptons and the Big Bang.* Bristol: Institute of Physics Pub, 2002.

[2] J. Adams *et al.*, "Experimental and theoretical challenges in the search for the quark gluon plasma: The STAR Collaboration's critical assessment of the evidence from RHIC collisions," *Nucl.Phys.*, vol. A757, pp. 102–183, 2005.

[3] K. Nakamura *et al.*, "Review of particle physics," *J.Phys.G*, vol. G37, p. 075021, 2010.

[4] G. Sterman, *An introduction to quantum field theory.* Cambridge University Press, 1993.

[5] R. Rapp and J. Wambach, "Low mass dileptons at the CERN SPS: Evidence for chiral restoration?," *Eur.Phys.J.*, vol. A6, pp. 415–420, 1999.

[6] F. Karsch, "Lattice QCD at high temperature and density," *Lect.Notes Phys.*, vol. 583, pp. 209–249, 2002.

[7] F. Karsch, "Transition temperature in QCD with physical light and strange quark masses," *J.Phys.G*, vol. G34, pp. S627–S630, 2007.

[8] M. Cheng, N. Christ, S. Datta, J. van der Heide, C. Jung, *et al.*, "The Transition temperature in QCD," *Phys.Rev.*, vol. D74, p. 054507, 2006.

[9] H.-T. Ding, A. Bazavov, P. Hegde, F. Karsch, S. Mukherjee, *et al.*, "Exploring phase diagram of $N_f = 3$ QCD at $\mu = 0$ with HISQ fermions," 2011. * Temporary entry *.

[10] P. Shukla, "Glauber model for heavy ion collisions from low-energies to high-energies," 2001.

[11] J. Bjorken, "Highly Relativistic Nucleus-Nucleus Collisions: The Central Rapidity Region," *Phys.Rev.*, vol. D27, pp. 140–151, 1983.

[12] U. W. Heinz, "Thermalization at RHIC," *AIP Conf.Proc.*, vol. 739, pp. 163–180, 2005.

[13] R. Baier, Y. L. Dokshitzer, A. H. Mueller, S. Peigne, and D. Schiff, "Radiative energy loss and p(T) broadening of high-energy partons in nuclei," *Nucl.Phys.*, vol. B484, pp. 265–282, 1997.

[14] R. Baier, Y. L. Dokshitzer, A. H. Mueller, S. Peigne, and D. Schiff, "Radiative energy loss of high-energy quarks and gluons in a finite volume quark - gluon plasma," *Nucl.Phys.*, vol. B483, pp. 291–320, 1997.

[15] S. Chatrchyan *et al.*, "Observation and studies of jet quenching in PbPb collisions at nucleon-nucleon center-of-mass energy = 2.76 TeV," *Phys.Rev.*, vol. C84, p. 024906, 2011.

[16] G. Aad *et al.*, "Observation of a Centrality-Dependent Dijet Asymmetry in Lead-Lead Collisions at sqrt(S(NN))= 2.76 TeV with the ATLAS Detector at the LHC," *Phys.Rev.Lett.*, vol. 105, p. 252303, 2010.

[17] A. Bialas, M. Bleszynski, and W. Czyz, "Multiplicity Distributions in Nucleus-Nucleus Collisions at High-Energies," *Nucl.Phys.*, vol. B111, p. 461, 1976.

[18] M. L. Mangano, P. Nason, and G. Ridolfi, "Heavy quark correlations in hadron collisions at next-to-leading order," *Nucl.Phys.*, vol. B373, pp. 295–345, 1992.

[19] M. Abreu *et al.*, "Evidence for deconfinement of quarks and gluons from the J / psi suppression pattern measured in Pb + Pb collisions at the CERN SPS," *Phys.Lett.*, vol. B477, pp. 28–36, 2000.

[20] R. Arnaldi *et al.*, "J/psi production in proton-nucleus collisions at 158 and 400 GeV," 2010.

[21] E. Andersen *et al.*, "Strangeness enhancement at mid-rapidity in Pb Pb collisions at 158-A-GeV/c," *Phys.Lett.*, vol. B449, pp. 401–406, 1999.

[22] H. Appelshauser *et al.*, "Hadronic expansion dynamics in central Pb + Pb collisions at 158-GeV per nucleon," *Eur.Phys.J.*, vol. C2, pp. 661–670, 1998.

[23] B. I. Abelev *et al.*, "Energy and system size dependence of ϕ meson production in Cu+Cu and Au+Au collisions," *Phys. Lett.*, vol. B673, pp. 183–191, 2009.

[24] P. Braun-Munzinger, K. Redlich, and J. Stachel, "Particle production in heavy ion collisions," 2003. To appear in Quark Gluon Plasma 3, eds. R.C. Hwa and Xin-Nian Wang, World Scientific Publishing.

[25] F. Becattini and J. Manninen, "Strangeness production from SPS to LHC," *J.Phys.G*, vol. G35, p. 104013, 2008.

[26] J. M. Maldacena, "The Large N limit of superconformal field theories and supergravity," *Adv.Theor.Math.Phys.*, vol. 2, pp. 231–252, 1998.

[27] P. Kovtun, D. Son, and A. Starinets, "Viscosity in strongly interacting quantum field theories from black hole physics," *Phys.Rev.Lett.*, vol. 94, p. 111601, 2005. An Essay submitted to 2004 Gravity Research Foundation competition.

[28] Y. Kats and P. Petrov, "Effect of curvature squared corrections in AdS on the viscosity of the dual gauge theory," *JHEP*, vol. 0901, p. 044, 2009.

[29] L. Landau, "On the multiparticle production in high-energy collisions," *Izv.Akad.Nauk Ser.Fiz.*, vol. 17, pp. 51–64, 1953.

[30] J.-Y. Ollitrault, "Relativistic hydrodynamics for heavy-ion collisions," *Eur.J.Phys.*, vol. 29, pp. 275–302, 2008.

[31] A. M. Poskanzer and S. Voloshin, "Methods for analyzing anisotropic flow in relativistic nuclear collisions," *Phys.Rev.*, vol. C58, pp. 1671–1678, 1998.

[32] G. Wang, "Incident-energy and system-size dependence of directed flow," *J.Phys.G*, vol. G34, pp. S1093–1098, 2007.

[33] S. Troshin and N. Tyurin, "Directed flow as effect of transient matter rotation in hadron and nucleus collisions," *Int.J.Mod.Phys.*, vol. E17, pp. 1619–1633, 2008.

[34] J. Takahashi, B. Tavares, W. Qian, R. Andrade, F. Grassi, *et al.*, "Topology studies of hydrodynamics using two particle correlation analysis," *Phys.Rev.Lett.*, vol. 103, p. 242301, 2009.

[35] A. P. Mishra, R. K. Mohapatra, P. Saumia, and A. M. Srivastava, "Using cosmic microwave background radiation analysis tools for flow anisotropies in relativistic heavy-ion collisions," *Phys.Rev.*, vol. C81, p. 034903, 2010.

[36] M. Cacciari, M. Greco, and P. Nason, "The P(T) spectrum in heavy flavor hadroproduction," *JHEP*, vol. 9805, p. 007, 1998.

[37] M. Cacciari, S. Frixione, M. Mangano, P. Nason, and G. Ridolfi, "QCD analysis of first b cross-section data at 1.96-TeV," *JHEP*, vol. 0407, p. 033, 2004.

[38] R. Aaij *et al.*, "Measurement of $\sigma(pp \to b\bar{b}X)$ at $\sqrt{s} = 7$ TeV in the forward region," *Phys.Lett.*, vol. B694, pp. 209–216, 2010.

[39] V. Khachatryan *et al.*, "Prompt and non-prompt J/psi production in pp collisions at sqrt(s) = 7 TeV," *Eur.Phys.J.*, vol. C71, p. 1575, 2011.

[40] D. Acosta *et al.*, "Measurement of prompt charm meson production cross sections in $p\bar{p}$ collisions at $\sqrt{s} = 1.96$ TeV," *Phys.Rev.Lett.*, vol. 91, p. 241804, 2003.

[41] B. Abelev *et al.*, "Erratum: Transverse momentum and centrality dependence of high-p_t non-photonic electron suppression in Au+Au collisions at $\sqrt{s_{NN}} = 200$ GeV," *Phys.Rev.Lett.*, vol. 98, p. 192301, 2007.

[42] S. Alekhin, G. Altarelli, N. Amapane, J. Andersen, V. Andreev, *et al.*, "HERA and the LHC: A Workshop on the implications of HERA for LHC physics. Proceedings, Part B," 2005.

[43] S. Wicks, W. Horowitz, M. Djordjevic, and M. Gyulassy, "Elastic, inelastic, and path length fluctuations in jet tomography," *Nucl.Phys.*, vol. A784, pp. 426–442, 2007.

[44] M. Djordjevic and M. Gyulassy, "Where is the charm quark energy loss at RHIC?," *Phys.Lett.*, vol. B560, pp. 37–43, 2003.

[45] A. Adare *et al.*, "Energy Loss and Flow of Heavy Quarks in Au+Au Collisions at s(NN)**(1/2) = 200-GeV," *Phys.Rev.Lett.*, vol. 98, p. 172301, 2007.

[46] H. van Hees, V. Greco, and R. Rapp, "Heavy-quark probes of the quark-gluon plasma at RHIC," *Phys.Rev.*, vol. C73, p. 034913, 2006.

[47] J. Adams *et al.*, "Particle type dependence of azimuthal anisotropy and nuclear modification of particle production in Au + Au collisions at s(NN)**(1/2) = 200-GeV," *Phys.Rev.Lett.*, vol. 92, p. 052302, 2004.

[48] D. Molnar, "Heavy quarks at RHIC from parton transport theory," *Eur.Phys.J.*, vol. C49, pp. 181–186, 2007.

[49] S. Adler *et al.*, "Measurement of single electron event anisotropy in Au+Au collisions at s(NN)**(1/2) = 200-GeV," *Phys.Rev.*, vol. C72, p. 024901, 2005.

[50] e. Evans, Lyndon and e. Bryant, Philip, "LHC Machine," *JINST*, vol. 3, p. S08001, 2008.

[51] G. Aad *et al.*, "The ATLAS Experiment at the CERN Large Hadron Collider," *JINST*, vol. 3, p. S08003, 2008.

[52] R. Adolphi *et al.*, "The CMS experiment at the CERN LHC," *JINST*, vol. 3, p. S08004, 2008.

[53] J. Alves, A.Augusto *et al.*, "The LHCb Detector at the LHC," *JINST*, vol. 3, p. S08005, 2008.

[54] R. Aaij *et al.*, "Evidence for CP violation in time-integrated D0 →h-h+ decay rates," 2011.

[55] K. Aamodt *et al.*, "The ALICE experiment at the CERN LHC," *JINST*, vol. 3, p. S08002, 2008.

[56] "http://press.web.cern.ch/press/PressReleases/Releases2008/PR09.08E.html."

[57] "http://lpcc.web.cern.ch/LPCC/."

[58] S. Masciocchi, "Investigation of charm and beauty production via semileptonic decays of heavy-flavour hadrons in pp at 7 TeV and Pb–Pb at 2.76 TeV with ALICE," *J.Phys.G*, vol. G38, p. 124069, 2011.

[59] "ALICE Off-line framework, AliRoot, http://aliceinfo.cern.ch/Offline."

[60] R. Brun and F. Rademakers, "ROOT: An object oriented data analysis framework," *Nucl.Instrum.Meth.*, vol. A389, pp. 81–86, 1997.

[61] T. Sjostrand, S. Mrenna, and P. Z. Skands, "PYTHIA 6.4 Physics and Manual," *JHEP*, vol. 0605, p. 026, 2006.

[62] X.-N. Wang and M. Gyulassy, "HIJING: A Monte Carlo model for multiple jet production in p p, p A and A A collisions," *Phys.Rev.*, vol. D44, pp. 3501–3516, 1991.

[63] S. Roesler, R. Engel, and J. Ranft, "The Monte Carlo event generator DPMJET-III," pp. 1033–1038, 2000.

[64] R. Brun, F. Bruyant, M. Maire, A. McPherson, and P. Zanarini, "GEANT3," 1987. Revised version.

[65] S. Agostinelli *et al.*, "GEANT4: A Simulation toolkit," *Nucl.Instrum.Meth.*, vol. A506, pp. 250–303, 2003.

[66] A. Fasso, A. Ferrari, S. Roesler, P. Sala, F. Ballarini, *et al.*, "The Physics models of FLUKA: Status and recent developments," *eConf*, vol. C0303241, p. MOMT005, 2003.

[67] P. Saiz *et al.*, "AliEn - ALICE environment on the GRID," *Nucl.Instrum.Meth.*, vol. A502, pp. 437–440, 2003.

[68] R. Fruhwirth, "Application of Kalman filtering to track and vertex fitting," *Nucl.Instrum.Meth.*, vol. A262, pp. 444–450, 1987.

[69] E. Bruna, A. Dainese, M. Masera, and F. Prino, "Vertex reconstruction for proton-proton collisions in alice," Nov 2009.

[70] C. Grigoras, L. Betev, F. Carminati, I. Legrand, and R. Voicu, "Automated agents for management and control of the ALICE computing grid," *J.Phys.Conf.Ser.*, vol. 219, p. 062050, 2010.

[71] P. Z. Skands, "The Perugia Tunes," 2009.

[72] S. V. der Meer *ISR-PO/68-31, KEK68-64.*

[73] M. Gagliardi, "Measurement of reference cross sections in pp and Pb-Pb collisions at the LHC in van der Meer scans with the ALICE detector," 2011.

[74] M. Cacciari, "private communication,"

[75] M. Cacciari, P. Nason, and R. Vogt, "QCD predictions for charm and bottom production at RHIC," *Phys.Rev.Lett.*, vol. 95, p. 122001, 2005.

[76] C. Loizides, "Measurement of charm production at central rapidity in proton-proton collisions at sqrt(s) = 7 TeV," *JHEP*, vol. 1201, p. 128, 2012. 23 pages, 5 figures.

[77] B. Kniehl, G. Kramer, I. Schienbein, and H. Spiesberger, "Reconciling open charm production at the Fermilab Tevatron with QCD," *Phys.Rev.Lett.*, vol. 96, p. 012001, 2006.

[78] P. M. Nadolsky, H.-L. Lai, Q.-H. Cao, J. Huston, J. Pumplin, *et al.*, "Implications of CTEQ global analysis for collider observables," *Phys.Rev.*, vol. D78, p. 013004, 2008.

[79] A. Adare *et al.*, "Measurement of high-p(T) single electrons from heavy-flavor decays in p+p collisions at s**(1/2) = 200-GeV," *Phys.Rev.Lett.*, vol. 97, p. 252002, 2006.

[80] B. Abelev *et al.*, "Erratum: Transverse momentum and centrality dependence of high-p_t non-photonic electron suppression in Au+Au collisions at $\sqrt{s_{NN}}$ = 200 GeV," *Phys.Rev.Lett.*, vol. 98, p. 192301, 2007.

[81] B. A. Kniehl, G. Kramer, I. Schienbein, and H. Spiesberger, "Open charm hadroproduction and the charm content of the proton," *Phys.Rev.*, vol. D79, p. 094009, 2009.

[82] K. Aamodt *et al.*, "Centrality dependence of the charged-particle multiplicity density at mid-rapidity in Pb-Pb collisions at sqrt(sNN) = 2.76 TeV," *Phys.Rev.Lett.*, vol. 106, p. 032301, 2011.

[83] A. Toia, "Bulk Properties of Pb-Pb collisions at sqrt(sNN) = 2.76 TeV measured by ALICE," *J.Phys.G*, vol. G38, p. 124007, 2011.

[84] K. Eskola, R. Vogt, and X. Wang, "Nuclear overlap functions," *Int.J.Mod.Phys.*, vol. A10, pp. 3087–3090, 1995.

[85] D. Lange, "The EvtGen particle decay simulation package," *Nucl.Instrum.Meth.*, vol. A462, pp. 152–155, 2001.

[86] R. Averbeck, N. Bastid, Z. del Valle, P. Crochet, A. Dainese, *et al.*, "Reference heavy flavour cross sections in pp collisions at $\sqrt{s}$ = 2.76 TeV, using a pQCD-driven $\sqrt{s}$-scaling of ALICE measurements at $\sqrt{s}$ = 7 TeV," 2011.

[87] S. Wicks, W. Horowitz, M. Djordjevic, and M. Gyulassy, "Heavy quark jet quenching with collisional plus radiative energy loss and path length fluctuations," *Nucl.Phys.*, vol. A783, pp. 493–496, 2007.

[88] N. Armesto, A. Dainese, C. A. Salgado, and U. A. Wiedemann, "Testing the color charge and mass dependence of parton energy loss with heavy-to-light ratios at RHIC and CERN LHC," *Phys.Rev.*, vol. D71, p. 054027, 2005.

[89] S. Chatrchyan *et al.*, "Suppression of non-prompt J/psi, prompt J/psi, and Y(1S) in PbPb collisions at sqrt(sNN) = 2.76 TeV," 2012.

[90] J. Pumplin, D. Stump, J. Huston, H. Lai, P. M. Nadolsky, *et al.*, "New generation of parton distributions with uncertainties from global QCD analysis," *JHEP*, vol. 0207, p. 012, 2002.

[91] K. Eskola, H. Paukkunen, and C. Salgado, "EPS09: A New Generation of NLO and LO Nuclear Parton Distribution Functions," *JHEP*, vol. 0904, p. 065, 2009.

[92] H. Appelshauser, "Particle Production at Large Transverse Momentum with ALICE," *J.Phys.G*, vol. G38, p. 124014, 2011.

[93] R. Sharma, I. Vitev, and B.-W. Zhang, "Light-cone wave function approach to open heavy flavor dynamics in QCD matter," *Phys.Rev.*, vol. C80, p. 054902, 2009.

[94] W. Horowitz and M. Gyulassy, "Quenching and Tomography from RHIC to LHC," *J.Phys.G*, vol. G38, p. 124114, 2011.

[95] W. Horowitz, "Testing pQCD and AdS/CFT Energy Loss at RHIC and LHC," 2011.

[96] W. Alberico, A. Beraudo, A. De Pace, A. Molinari, M. Monteno, *et al.*, "Heavy-flavour spectra in high energy nucleus-nucleus collisions," *Eur.Phys.J.*, vol. C71, p. 1666, 2011.

[97] P. Gossiaux, J. Aichelin, T. Gousset, and V. Guiho, "Competition of Heavy Quark Radiative and Collisional Energy Loss in Deconfined Matter," *J.Phys.G*, vol. G37, p. 094019, 2010.

[98] J. Uphoff, O. Fochler, Z. Xu, and C. Greiner, "Open heavy flavor at RHIC and LHC in a partonic transport model," 2011.

[99] A. Buzzatti and M. Gyulassy, "Jet Flavor Tomography of Quark Gluon Plasmas at RHIC and LHC," *Phys.Rev.Lett.*, vol. 108, p. 022301, 2012. 4 pages, 3 eps figures.

[100] V. Greco, H. van Hees, and R. Rapp, "Heavy-Quark Kinetics at RHIC and LHC," 2007.

[101] V. Greco, C. Ko, and R. Rapp, "Quark coalescence for charmed mesons in ultrarelativistic heavy ion collisions," *Phys.Lett.*, vol. B595, pp. 202–208, 2004.

[102] A. Bilandzic, R. Snellings, and S. Voloshin, "Flow analysis with cumulants: Direct calculations," *Phys.Rev.*, vol. C83, p. 044913, 2011.

[103] K. Aamodt *et al.*, "Elliptic flow of charged particles in Pb-Pb collisions at 2.76 TeV," *Phys.Rev.Lett.*, vol. 105, p. 252302, 2010.

[104] M. Masera, G. Ortona, M. Poghosyan, and F. Prino, "Anisotropic transverse flow introduction in Monte Carlo generators for heavy ion collisions," *Phys.Rev.*, vol. C79, p. 064909, 2009.